

*

NATIONAL AND KAPODISTRIAN UNIVERSITY OF ATHENS

DEPARTMENT OF PHYSICS

MASTER THESIS IN ASTROPHYSICS

EVOLUTION OF STELLAR MASS FUNCTION FOR RADIOGALAXIES UP TO $Z \sim 2.5$

SUPERVISOR

PROF. KALLIOPI DASYRA

NATIONAL AND KAPODISTRIAN UNIVERSITY OF ATHENS

MASTER'S STUDENT

DIAMANTO KOURAKOU

COMMITTEE MEMBERS

DR. ANTONIS GEORGAKAKIS

NATIONAL OBSERVATORY OF ATHENS

PROF. DESPINA HATZIDIMITRIOU

NATIONAL AND KAPODISTRIAN UNIVERSITY OF ATHENS

STUDENT ID

7110112100307

ACADEMIC YEAR

2022-2023

Acknowledgements

First and foremost I would like to thank my supervisor Kalliopi Dasyra for accepting me, trusting on me, tolerating my shortcomings and giving me the opportunity to work with an outstanding astrophysicist.

I would like to thank my advisor Antonis Georgakakis for his unconditional support, for sharing his expertise, for his thoughtful input and for being an exceptional astrophysicist and an admirable mentor.

Thank you to my advisor Despina Hatzidimitriou for the helpful conversations, for being a valued part of this project and for being the professor that introduced me to the study of galaxies.

I would like to express my gratitude to Markos Polkas for guiding me through this project, openly sharing his work, answering all my questions and being a truly brilliant researcher.

I would like to extend my gratitude to Anelise Audibert, Athanasia Gkogkou and Vasileia Masoura for the helpful conversations and advise.

A special thank you goes to Evgenia Koutsoumpou and John Kallimanis for their daily support, help and friendship during this project, as well as to Despina Karavola, Argyris Loules, Stamatis Stathopoulos, Marios Nikolaidis, Barbara Kotsiourou, Vasilis Mpisketzi and Haris Tsakonas for being the most excellent colleagues and friends. Thank you to Sofia Zerbouti who cheered for and supported everyone of us. You all made it so much more special!

Thank you to all the students and to all the people working at the University of Athens.

This work has been inspired by the research of Markos Polkas («The stellar mass content and star formation rate of radio galaxies as a function of redshift. Consequences for the growth of massive galaxies») on the project «Do massive winds induced by black-hole jets alter galaxy evolution? Evidence from galaxies in the Atacama Large Millimeter Array (ALMA) Radio-source Catalog» (PI: Kalliopi Dasyra, National Observatory of Athens).

In this work, the main data analysis tool has been the `UltraNest` software, (developed by Johannes Buchner) presented in 2021, Journal of Open Source Software, 6, 60, 3001 (DOI: [10.21105/joss.03001](https://doi.org/10.21105/joss.03001)).

This work has made use of the ARC data selection (original work by Audibert, Dasyra, Pappachristou, Fernández-Ontiveros, Ruffa, Bisigello, Combes, Salomé and Gruppioni) that was published in 2022, Astronomy & Astrophysics, 668, A67, 21 (DOI: [10.1051/0004-6361/202243666](https://doi.org/10.1051/0004-6361/202243666)).

I am grateful to the programmers who build open-source and publicly available python packages.

Περίληψη

Οι παρατηρήσεις γαλαξιών επηρεάζονται από πολλές φυσικές παραμέτρους, όπως αστρικές μάζες, ρυθμούς αστρογένεσης, ιστορικό σχηματισμού αστέρων, μεταλλικότητα, σκόνη, δραστηριότητα μελανών οπών και άλλα. Ως αποτέλεσμα, η εξαγωγή ακριβών φυσικών παραμέτρων απαιτεί πολυδιάστατα μοντέλα που αποτυπώνουν αυτή την πολυπλοκότητα.

Οι φωτομετρικές κατανομές φασματικής ενέργειας (SED) 45 ραδιογαλαξιών πλούσιων σε αέριο από την αρχειακή πλήρη φασματοσκοπική έρευνα του ALMA Radio-source Catalogue (ARC) σε ερυθρομεταπότισεις $0.06 < z < 2.5$ προσαρμόζονται και οι αστρικές μάζες τους εκτιμώνται χρησιμοποιώντας ένα φυσικό μοντέλο 21 παραμέτρων σε πλαίσιο συμπερασματολογίας Bayes. Εξετάζονται οι βασικές αρχές της στατιστικής Bayes, της πιθανοτικής δειγματοληψίας και της μοντελοποίησης SED, περιλαμβάνοντας συνιστώσα ενεργού γαλαξιακού πυρήνα (AGN) στη διαδικασία μοντελοποίησης και προσαρμογής SED.

Για ερυθρομεταπότιση $z < 0.3$ η διάμεση εκτίμηση της αστρικής μάζας είναι $1.03 \times 10^{11} M_{\odot}$, ενώ σε υψηλότερη ερυθρομεταπότιση ($z > 1$) η διάμεση εκτίμηση της αστρικής μάζας βρέθηκε να είναι υψηλότερη $6.47 \times 10^{11} M_{\odot}$, συνεπές με τους παρατηρησιακούς περιορισμούς. Η προκύπτουσα συνάρτηση αστρικής μάζας των πλούσιων σε αέριο ραδιογαλαξιών στο τοπικό Σύμπαν βρέθηκε να είναι ~ 1 dex χαμηλότερη από τη συνάρτηση αστρικής μάζας για κανονικούς ή ελλειπτικούς γαλαξίες, ενώ σε υψηλότερες ερυθρομεταπότισεις, η συνάρτηση αστρικής μάζας των πλούσιων σε αέριο ραδιογαλαξιών βρέθηκε να είναι ~ 4 dex χαμηλότερη από εκείνη των κανονικών γαλαξιών.

Σε σύγκριση με μελέτες που αφορούν κανονικούς γαλαξίες και γαλαξίες με έντονη αστρογένεση, ο λόγος μάζας αερίου προς αστρική μάζα των πλούσιων σε αέριο ραδιογαλαξιών σε υψηλότερη ερυθρομεταπότιση ($1.0 < z < 2.5$) βρέθηκε να είναι πιο κοντά σε αυτόν των κανονικών γαλαξιών, υποδηλώνοντας ότι σε υψηλότερη ερυθρομεταπότιση οι πλούσιοι σε αέριο ραδιογαλαξίες, αν και σπάνιοι, είναι πιθανό να είναι πιο κοντά στην Κύρια Ακολουθία Αστρογένεσης απ' ότι στο Κοντινό Σύμπαν.

Λέξεις-κλειδιά: Εξέλιξη Γαλαξιών, Φασματική Κατανομή Ενέργειας, Αστροστατιστική, Μοντελοποίηση Αστρονομικών δεδομένων

Abstract

Galaxy observations are influenced by many physical parameters including stellar masses, star formation rates, star formation histories, metallicities, dust, black hole activity, and more. As a result, inferring accurate physical parameters requires high-dimensional models that capture this complexity.

The photometric Spectral Energy Distributions (SEDs) of 45 gas rich radiogalaxies from the ALMA Radio-source Catalogue (ARC) archival full spectroscopic survey at $0.06 < z < 2.5$ are fit and their galaxy stellar masses are assessed using a 21-parameter physical model in Bayesian inference framework. The fundamentals of Bayesian statistics, probabilistic sampling and SED modelling are explored, including an Active Galactic Nucleus (AGN) component in the SED modelling and fitting process.

For redshift $z < 0.3$ the median stellar mass estimate is $1.03 \times 10^{11} M_{\odot}$, while at higher redshift ($z > 1$) the median stellar mass estimate is found to be higher $6.47 \times 10^{11} M_{\odot}$, consistent with the observational constraints. The resulting stellar mass function of gas rich radiogalaxies in the local Universe is found to be ~ 1 dex lower than the stellar mass function for normal or elliptical galaxies, while in higher redshifts, the stellar mass function of gas rich radiogalaxies is found to be ~ 4 dex lower than the one for normal galaxies.

In comparison with studies regarding normal and star-forming galaxies, the gas-to-stellar mass ratio of gas rich radiogalaxies at higher redshift ($1.0 < z < 2.5$) is found to be closer to the one for normal galaxies, hinting that in higher redshift gas rich radiogalaxies, although uncommon, might be closer to the Star Forming Main Sequence.

Key words: Galaxy Evolution , Spectral Energy Distribution , Astrostatistics , Astronomy Data Modeling

Contents

ΠΕΡΙΛΗΨΗ	iv
ABSTRACT	v
LIST OF FIGURES	xii
LIST OF TABLES	xvii
LISTING OF ACRONYMS	xix
1 INTRODUCTION	I
1.1 Motivation	I
1.2 Thesis Outline	2
2 STELLAR CONTENT OF GALAXIES, GALAXY EVOLUTION & COSMOLOGICAL FRAMEWORK	5
2.1 Star Formation Rate & the Main sequence	5
2.2 Stellar Mass & Stellar Mass Function	7
2.3 Cosmological measures	9
2.3.1 Scale Factor of the Universe	10
2.3.2 Comoving distance	10
2.3.3 Angular size of a galaxy	11
2.3.4 Luminosity distance	11
2.3.5 Cosmological assumptions	11
3 ARC SAMPLE OF RADIO-GALAXIES	13
3.1 Data selection of ARC galaxies	13
3.2 SED data acquisition & compilation	15
3.3 Data cleaning	15
4 SED & SED MODELLING	19
4.1 Spectral Energy Distribution of Galaxies	19
4.2 Modeling the SED of galaxies	20
4.2.1 AGN Component	20
4.2.2 Galaxy Component	22
4.3 Dust in the ISM	22

4.3.1	Dust extinction	23
4.3.2	Dust emission	24
4.3.3	Dust model & parameters	26
4.4	Stellar Populations	26
4.4.1	Simple Stellar Population	28
4.4.2	Stellar Evolution, Star Formation History & Dust Absorption	30
4.4.3	Stellar population models	32
4.5	AGN Accretion Disk	35
4.5.1	Accretion disk model & parametres	36
4.6	AGN Torus	37
4.6.1	Torus model & parameters	38
4.7	Synchrotron radio emission	38
4.7.1	Radio jet model & parametres	40
4.8	Other Components	41
4.9	Model photometry	41
5	PROBABILISTIC SED FITTING ALGORITHM	43
5.1	Bayesian Framework	43
5.2	Parametre Space, Likelihood & Priors	44
5.2.1	Likelihood	44
5.2.2	Priors	48
5.3	Sampling Method, Optimisation & Implementation	49
5.3.1	Dynamic Nested Sampling	49
5.3.2	Software & Optimal Sampling	50
5.4	Testing the Algorithm on Synthetic Data	50
5.5	Fitting SED models to Data	51
6	RESULTS	59
6.1	ARC Stellar Mass	59
6.2	ARC Gas Mass to Stellar Mass Ratio	59
6.3	ARC Stellar Mass Function	60
6.3.1	Maximum Volume	60
6.3.2	Completeness	62
6.3.3	Redshift Ranges	66
7	CONCLUSIONS	73
7.1	Stellar Mass Function Comparisons	73
7.2	Molecular Gas to Stellar Mass Ratio	75
7.3	Improvements & Future Work	75
	APPENDIX A LIST OF 44 ARC SOURCES	79

APPENDIX B PROBABILITY, BAYESIAN METHOD AND SAMPLING	87
B.1 Interpretations of Probability	87
B.2 Bayesian Statistics	89
B.3 Bayesian Sampling techniques	90
APPENDIX C POSTERIOR DISTRIBUTIONS OF FIT GALAXIES	93
APPENDIX D MASS DISTRIBUTIONS OF FIT GALAXIES	109
APPENDIX E THE FIT SEDs FOR 44 GALAXIES	125
STATEMENT OF ORIGINAL AUTHORSHIP	148
REFERENCES	173

Listing of figures

2.1	Logarithmic Star Formation Rate-Stellar Mass relation for different redshifts. Panel (a): The relation and its evolution is shown for the star-forming (left) and all galaxies (right) of the VLA-COSMOS survey. This relation for the star-forming galaxies is called Star Forming Main Sequence. Panel (b): The Main Sequences for star-forming galaxies classified as Zurich Estimator of Structural Types ¹²⁶ (ZEST) type 1 ("Early Type, ET"), ZEST types 2.0-2.1 ("Late Type with Bulges, bulgeLT"), ZEST types 2.2-2.3 ("Disk-dominated Late Type, diskLT"), and ZEST type 3 ("Irregular, irr"), the plotted lines represent each galaxy type at each plot and the Main Sequence relation is shown in the background for comparison. Images lifted from the VLA-COSMOS study of Leslie et al. (2020) ⁹⁰	8
2.2	Stellar Mass Function for quiescent and star-forming galaxies of the COSMOS and XMM-LSS surveys. Figure lifted from Adams et al. (2021) ²	9
3.1	The ARC survey. Left panel: histogram of the redshift spanning of the 120 ARC sources. Right panel: Projection of the ARC sample in the celestial sphere.	14
3.2	Raw SEDs of two ARC galaxies. Data integration by Michalis Papachristou, seen as the data points labeled "Full Data". Data reduction by Markos Polkas, the selection of the SED photometry (marked as "Reduced Data") and the upper limits for the accretion disk emission (marked as "BBB upper limit").	17
4.1	An example of a panchromatic galaxy SED. Signature band-passes are plotted in color accompanied by the name of the survey where they were used. Spectral regions and related dominant component are denoted at the bottom. Image credit: Luke J. M. Davies.	20
4.2	Schematic representation of the AGN unified model, where the accretion disk, the torus and the relativistic jet are depicted, as well as the radio loud types of sources (in the upper part of the diagram), such as those that populate the ARC survey. The type of AGN depends on the viewing angle, whether or not the AGN produces a significant jet emission, and how powerful the central engine is. Image credit: Jessica E. Thorne.	21
4.3	Difference between dust extinction and dust absorption of stellar light. Image lifted from Salim & Narayanan (2020) ¹²²	23
4.4	ISM dust emission Dale et al. (2014) ³² for different values of α_{SF}	27

4.5	Panel (a): Different types of Initial Mass Functions, the model used in the present work is the Chabrier 2003 ²⁶ Panel (b): The Padova ^{12 56 97} Stellar Isochrones for different age of the coeval population. Panel (c): Different types of Star Formation Histories, in the present work the delayed exponential decay function is used here denoted as "LinExp". Panel (d): The empirical library of MILES model spectra ^{147 147 43} is used for the Stellar Population Model of the present work. Panel (e): Different Dust attenuation laws are shown. In the Stellar Population Model of this work, the Calzetti 2000 ²⁴ law is used.	29
4.6	The Bruzual & Charlot 2003 ¹⁹ Stellar Population Models with the Chabrier 2003 ²⁶ Initial Mass function, Padova ^{12 56 97} Isochrones and a Star Formation History in the shape of delayed exponential decay, unattenuated. Panel (a): The shape changes for different age, here each spectrum has constant metallicity of $Z = Z_{\odot}$ and constant e-folding time of $\tau = 0.6$ Gyrs. Panel (b): The shape changes for different metallicity, here each spectrum has constant age of 10 Myrs and the e-folding time is $\tau = 2$ Gyrs. Panel (c): The shape changes for different e-folding time τ of the assumed Star Formation History, here each spectrum has constant age of 3.4 Gyrs and constant metallicity of $Z = Z_{\odot}$	33
4.7	Distinguishability of single-age populations with Signal-to-Noise ratio S/N=10 (dash-dotted line) and with Signal-to-Noise ratio S/N=100 (continuous line). Plot lifted from Ocvirk et al. (2006) ¹⁰⁵	34
4.8	Accretion disk emission templates by Richards et al. (2006) ¹¹⁹ for different values of reddening fraction E(B-V) _{BBB}	36
4.9	AGN clumpy torus cartoon plot. The origin represents the SMBH, the horizontal axis represents the plane of the torus, R_{in} and R_{out} are the inner and outer radius of the torus, R_{in} is essentially the sublimation radius. N_0 is the number of clouds along an equatorial line-of-sight, i is the inclination of the torus with respect to the observer and θ_0 is the half-angle that covers the torus from the equatorial plane. Image lifted from García-González et al. (2017) ⁵²	39
4.10	AGN torus emission templates generated by Markos Polkas using CAT3D ⁷⁰ . Here plotted some indicative values of viewing angle i , half-covering angle of torus θ , spectar index of dust-cloud distribution α and number of clouds along an equatorial line-of-sight N , with the same amplitude scaling.	40
5.1	Posterior distributions sampled by fitting a single component model to synthetic data from the same component. Panel (a): Stellar Population component posterior Panel (b): ISM dust component posterior. Panel (c): Accretion disk component posterior. Panel (d): AGN torus component posterior.	52
5.2	Component Residuals.	53
5.3	Posterior distribution of a full SED fit of a Mock galaxy.	53

5.4	SED model fit for synthetic data with logarithmic-Gaussian noise, representing a mock galaxy. The 20 highest posterior fits are plotted along with the synthetic data and each component is highlighted with color.	54
5.5	SED fit for The ARC galaxies J0504-1014 and J0009-3216. Plots of the SED fit for all the 44 ARC sources can be found in Appendix E.	56
5.6	SED fit for The ARC galaxies NGC 4696 and NGC 541. Plots of the SED fit for all the 44 ARC sources can be found in Appendix E.	57
6.1	The stellar mass estimate for 44 ARC sources, stellar masses are inferred in Solar Mass units (M_{\odot}) and the base-ten logarithm of them is plotted. In bold color: the median of sampled values from the Bayesian process, uncertainties are half of the (84 th -16 th) percentile range. In light color: the maximum posterior value from the Bayesian process.	69
6.2	The 44 ARC galaxies' gas-to-stellar mass ratio. Left panel: The Molecular hydrogen mass over the median total inferred stellar mass for each galaxy, the base-10 logarithm of the ratio is plotted with the base-10 logarithm of $(1 + z)$, where z is the redshift. For sources that had an upper limit estimate of the molecular hydrogen gas, a downwards pointing arrow is plotted instead of uncertainty errorbars. The plotted line represents the main sequence and is adapted from Genzel et al. (2015) ⁵⁴ . Right panel: The plot copied from Genzel et al. (2015) ⁵⁴ represents the main sequence galaxies.	70
6.3	The NVSS completeness correction so that by multiplying the final ARC source sample in different redshift intervals can reproduce the number of sources in the NVSS survey. Plot copied from Audibert et al. (2022) ⁸ for the complete ARC survey.	71
6.4	The Galaxy Stellar Mass Function with and its evolution in two redshift ranges. The color distinguishes the redshift ranges and the point size is proportional to the number of galaxies in each bin from the initial 44-ARC sample. The SMF for AGNs of the EAGLE ¹²⁷ simulation at redshift $z = 0$ is plotted for comparison.	71
7.1	Comparison of Stellar Mass Function for different surveys. Figure lifted from Leja et al. (2020) ⁸⁶ . Figure lifted from Driver et al. (2022) ³⁶	74

Listing of tables

5.1	Parametres used for modelling the ARC SEDs. The parametre and its description are in the second and third columns, respectively. The galaxy component to which they appertain is listed in the first column, the range of values and the shape of the prior distribution are listed in the fourth and fifth column.	45
6.1	Values and limits for calculating SMF of 44 ARC galaxies. The name of each source is shown in the first column, in the second column is the 1.4 GHz flux in units of Jansky, the redshift of the source and the limit case redshift are in the third and fourth column respectively, the comoving volume through the FOV at the source and at the limit case are shown in the fifth and sixth column, respectively. The median sampled base-ten logarithm of stellar mass in units of solar masses is in seventh column.	67
6.2	Values and limits for calculating SMF of 44 ARC galaxies - continued	68
A.1	List of 44 fit ARC sources	80
A.2	List of 44 fit ARC sources - continued	81
A.2	List of 44 fit ARC sources - continued	82
A.2	List of 44 fit ARC sources - continued	83
A.2	List of 44 fit ARC sources - continued	84
A.2	List of 44 fit ARC sources - continued	85

Listing of acronyms

3D-HST	3D Hubble Space Telescope spectroscopic survey
AGB	Asymptotic Giant Branch
AGN	Active Galactic Nucleus
ALMA	Atacama Large Millimetre/submillimetre Array
ARC	ALMA Radio-Source Catalog
BBB	Big Blue Bump
CO	Carbon monoxide
COSMOS	Cosmic Evolution Survey
CSP	Composite Stellar Population
DLA	Damped Lyman Alpha
DSPS	Differential Stellar Population Synthesis
EAGLE	Evolution and Assembly of Galaxies and their Environments project
E(B-V)	Color excess
FIR	Far Infrared
FIRST	The VLA Faint Images of the Radio Sky at Twenty-cm Survey
FOV	Field Of View
FUV	Far Ultraviolet
GAMA	Galaxy And Mass Assembly survey
HST	Hubble Space telescope
IGM	Inter-galactic Medium
IMF	Initial Mass Function

IR	Infrared
ISM	Inter-stellar Medium
IGM	Inter-galactic Medium
LAF	Lyman Alpha Forest
MCMC	Markov Chain Monte Carlo
MILES	Medium-resolution Isaac Newton Telescope Library of Empirical Spectra
MS	Main Sequence
NRAO	National Radio Astronomy Observatory
NVSS	NRAO VLA Sky Survey
PAH	Polycyclic Aromatic Hydrocarbon
PDF	Probability Density Function
SDSS	Sloane Digital Sky Survey
SED	Spectral Energy Distribution
SF	Star Forming
SFH	Star Formation History
SFMS	Star Formation Main Sequence
SFR	Star Formation Rate
SMBH	Super-massive Black Hole
SMBH	Stellar Mass Function
SPS	Stellar Population Synthesis
SSP	Simple Stellar Population
UV	Ultraviolet
VLA	Very Large Array
XMM	X-ray Multi-Mirror Mission

XMM-LSS XMM-Newton Large Scale Structure survey

ZEST Zurich Estimator of Structural Types

1

Introduction

The first chapter is an introductory one and its scope is to explain the motivation that stands behind the work of the present thesis and map the steps followed in the next chapters.

1.1 MOTIVATION

Regular matter in the Universe interacts with light, which allows it to convert potential or kinetic energy into radiation, lose energy by emitting light and condense into galaxies, stars and planets. The study of galaxy formation and evolution can help us understand the physics of gas and its conversion to stars.

In the local Universe, star formation in most galaxies is very inefficient. Large amounts of energy are required to counteract the growth that would otherwise naturally arise from a galaxy's gravitational pull, the primary sources of this energy (feedback) might be related to the accretion process and are a focus of research in extragalactic astrophysics.

Radio galaxies host relativistic jets in their core, produced by the accretion process and appear to be quiescent in the Local Universe¹⁴, while the cosmic time at which their stellar mass was formed or the quenching timescale have not been explored at large. Additionally, Radio galaxies with molecular gas content (which is the fuel of star formation) are very rare in the Local Universe. Retrieving information that can be linked to star formation in this type of feedback-ridden galaxies across cosmic time would be valuable for understanding star formation and quenching in the Universe.

The estimation of stellar mass content for a sample of gas rich radiogalaxies, their stellar mass function and its evolution in comparison with star-forming galaxies will be the central theme of the present thesis.

1.2 THESIS OUTLINE

The following chapters of this thesis are structured as follows:

Chapter 2: Statistical properties of galaxies are reviewed, in particular the star formation rate and galaxy stellar mass relation along with the galaxy stellar mass function. The Star Forming Main Sequence is defined, its importance as an evolutionary threshold is highlighted.

Chapter 3: The ARC survey is concisely presented and the photometric data integration and reduction is described for the working dataset of radiogalaxies.

Chapter 4: An overview of Spectral Energy Distributions of galaxies, their data assortment and information is presented. The basic structure and components of a radio loud galaxy are described. The approach after which they are modelled is described along with the radiative processes that justify and establish it. State-of-the-art models are chosen and their full parametrisation is clarified.

Chapter 5: Bayesian inference principles are briefly revised. The Bayesian SED fitting algorithm developed for the present work and adapted for the ARC sample of galaxies is described, including the SED model implementation, sampling method, likelihood and prior functions. The algorithm is tested in parts and as a whole on synthetic data and proceeded to fit the models to the working sample of galaxies' SEDs. The sampled posterior and stellar mass histograms are plotted along with 45 radiogalaxies' fit SEDs.

Chapter 6: The inferred parameters along with archival properties are manipulated in order to produce stellar mass function estimates and gas mass-to-stellar mass relations. Methods followed, techniques and assumptions are described in detail.

Chapter 7: The results are compared with literature, broadly commented and conclusions are

drawn. Possible improvements both on the computational implementation and the method are remarked.

In the present work the python 3 programming language has been used for data manipulation, analysis and visualisation, implementing numpy⁶⁰, pandas¹⁰⁹, scipy¹⁴⁹, astropy⁷, matplotlib⁷³ and UltraNest²³ packages.

2

Stellar Content of Galaxies, Galaxy evolution & Cosmological Framework

The evolution of star formation activity in galaxies over cosmic history, and the physical processes which may drive and limit such activity, have been the subject of intensive observational and theoretical study. The ultimate goal of the galaxy formation models is to represent, with fully developed cosmological simulations, the baryonic assembly of structures at different mass scales in the Universe as a function of cosmic time. This is important in order to understand the processes that govern the formation and evolution of galaxies and matter in the Universe, and the way this formation and evolution is linked to the cosmological initial and boundary conditions that determine the statistical properties of the cosmic density field.

Wide-field and deep multi-wavelength surveys have allowed detailed studies of statistically large samples of galaxies at a wide range of redshifts. Astrophysical modeling and diagnostics of galactic star formation have enabled the determination⁹⁴ of key physical quantities of galaxies from these data, such as star formation rates (SFRs) and stellar masses (M_{\star}).

2.1 STAR FORMATION RATE & THE MAIN SEQUENCE

The star formation rate (SFR) describes the rate at which a galaxy forms new stars. There are many ways in which to infer SFRs from observations of the integrated light from galaxies⁸²,

such as H _{α} emission (which arises primarily from HII regions photoionised by massive stars with short lifetimes), or UV continuum excess produced by hot young stars.

The Star Formation History (SFH) of a galaxy is the Star Formation Rate through cosmic time and it encapsulates the history of galaxy formation. Its accurate recovery is of central importance for:

- Understanding and interpreting galaxy Spectral Energy Distributions
- Direct measurement of scientifically interesting moments (such as mass-weighted age, light-weighted age and recent star formation rate)
- Measurement of total mass formed (via integration)
- Its derivative is a sensitive probe to star formation physics ¹³⁸ (gas inflows, outflows and the life-cycle of molecular clouds)

Advanced methods involving SED fitting for SFH inference will be discussed at Chapter [7](#).

STAR FORMING MAIN SEQUENCE

The stellar mass and star formation rate of galaxies are fundamental quantities that are being measured extensively from low redshifts to the highest redshifts at which galaxies have been discovered. For star-forming (SF) galaxies, these two quantities are closely correlated ⁴⁰, and this correlation has been designated the "Main Sequence" (MS) of star-forming galaxies. It is recognised ¹⁰⁴ that such a close correlation persists to at least a redshift of ~ 4 with nearly constant slope and dispersion ¹³⁶.

The slope, shape, dispersion and redshift evolution of the SFR– M_* correlation can vary from one study to another, mainly due to the selection criterion for a galaxy to qualify categorically as star-forming. Renzini and Peng (2015) ¹¹⁸ suggested the Main Sequence should be defined as the ridgeline of the star-forming peak in a 3D logarithmic diagram of SFR– M_* –number of galaxies.

The Star Formation Rate and Galaxy Stellar Mass relation for the VLA-COSMOS survey is plotted in Figure [2.1](#), this relation for star-forming galaxies represents the Star Forming Main Sequence and its evolution at different redshifts is clearly denoted.

The Star Forming Main Sequence represents the normal, star-forming galaxies in different cosmic times, and most galaxies form the majority of their mass either on the Star Forming Main Sequence or passing through the Star Forming Main Sequence ⁸⁷. Thus, comparing different

galaxies to the Main Sequence can indicate star-burst or mass quenching linked with the properties of the galaxy sample in question and can provide information on the process of its evolution.

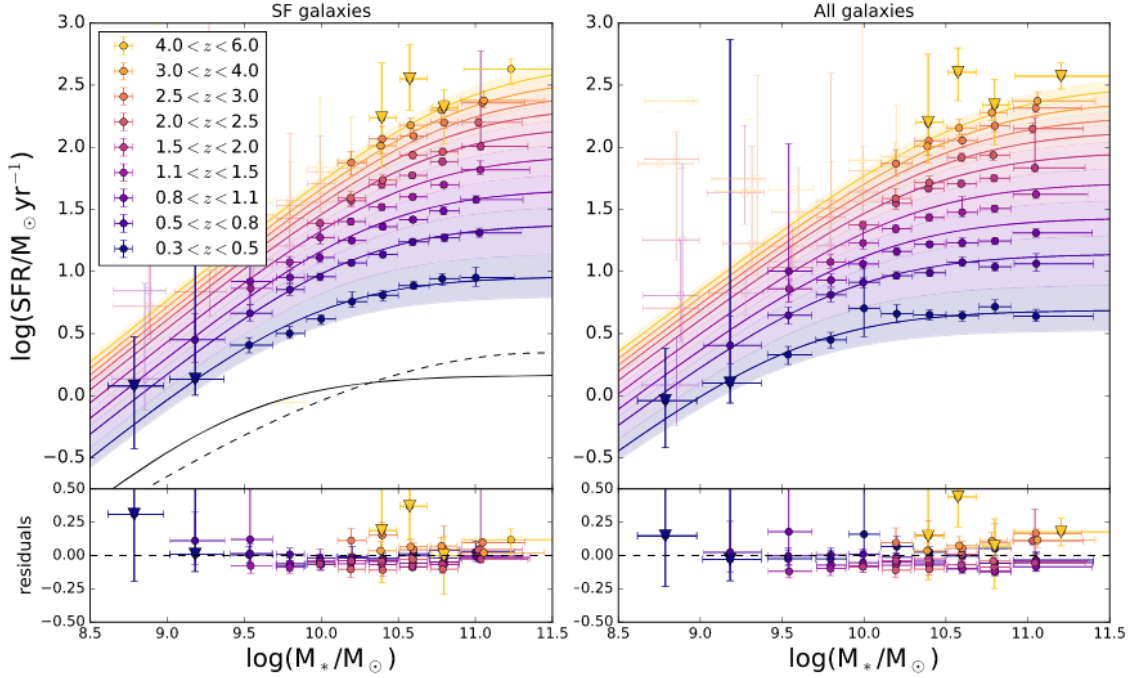
2.2 STELLAR MASS & STELLAR MASS FUNCTION

The study of the distribution of galaxies with respect to their masses (mass functions) or luminosities (luminosity functions) can provide important clues regarding the evolution of the galaxy population in the Universe.

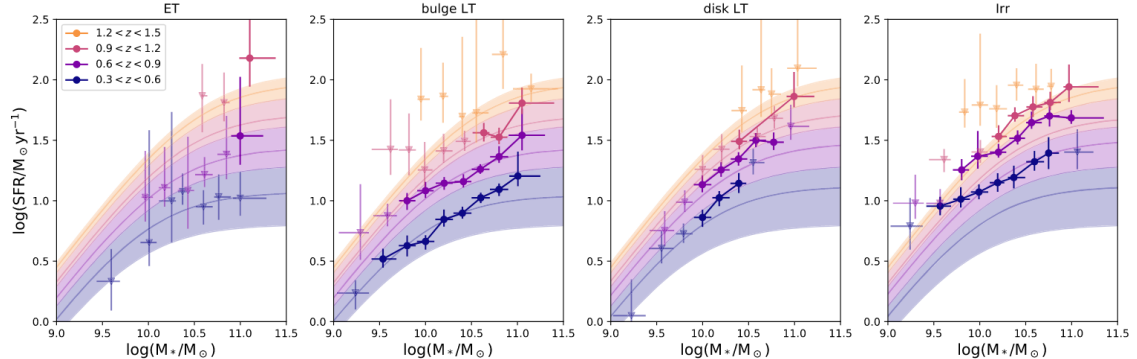
The galaxy stellar mass function (SMF) is a multivariate distribution¹⁵³ of a galaxy population which can be described by a function Φ . It represents a measurement² of the cumulative effects of physical processes that enhance or hinder star formation within galaxies. These processes include merger events, internal feedback mechanisms and environmental effects. Understanding the balance between these processes is key to understanding how galaxies have been assembled over cosmic time.

In recent years, studies¹⁵³ have shown that for star-forming galaxies the characteristic stellar mass and the low-mass end slope of the SMF stay constant out to redshifts of at least $z \sim 2$. The normalisation of the mass function is redshift dependent, and the mass function of quiescent galaxies is commonly fitted with a double Schechter¹²⁸ function, whereas star-forming galaxies are often described using a single Schechter function, as it is shown in Figure 2.2 for quiescent and starforming galaxies up to redshift $z \sim 2$ of the well-studied extragalactic legacy fields COSMOS and XMM-LSS². The stellar mass is a physical parameter that provides a useful and complementary view of galaxy evolution from the measurement of SFR. From an observational perspective, given infrared data of sufficient quality and depth, stellar mass is a more unambiguous and robust quantity to measure⁵⁸, being less subject to degenerate uncertainties. It is possible to construct⁸⁹ a star-forming sequence that is consistent with the growth of the stellar mass function, under the assumptions that mergers are negligible and there is no scatter in star formation rate, when the SMF evolution is sufficiently mapped.

The galaxy stellar mass function can convey information about the stellar mass growth and the efficiency of star formation and feedback mechanisms, an estimate of stellar mass contained within galaxies at different epochs and can provide constraints on galaxy formation models and on cosmological parameters. The latter can be used for astrophysically sound cosmological simulations.



(a) SFR- M_* for all galaxies and SF galaxies of VLA-COSMOS



(b) SFR- M_* for different galaxy types of VLA-COSMOS

Figure 2.1: Logarithmic Star Formation Rate-Stellar Mass relation for different redshifts.
 Panel (a): The relation and its evolution is shown for the star-forming (left) and all galaxies (right) of the VLA-COSMOS survey. This relation for the star-forming galaxies is called Star Forming Main Sequence. Panel (b): The Main Sequences for star-forming galaxies classified as Zurich Estimator of Structural Types¹²⁶ (ZEST) type 1 ("Early Type, ET"), ZEST types 2.0-2.1 ("Late Type with Bulges, bulgeLT"), ZEST types 2.2-2.3 ("Disk-dominated Late Type, diskLT"), and ZEST type 3 ("Irregular, irr"), the plotted lines represent each galaxy type at each plot and the Main Sequence relation is shown in the background for comparison.

Images lifted from the VLA-COSMOS study of Leslie et al. (2020)⁹⁰.

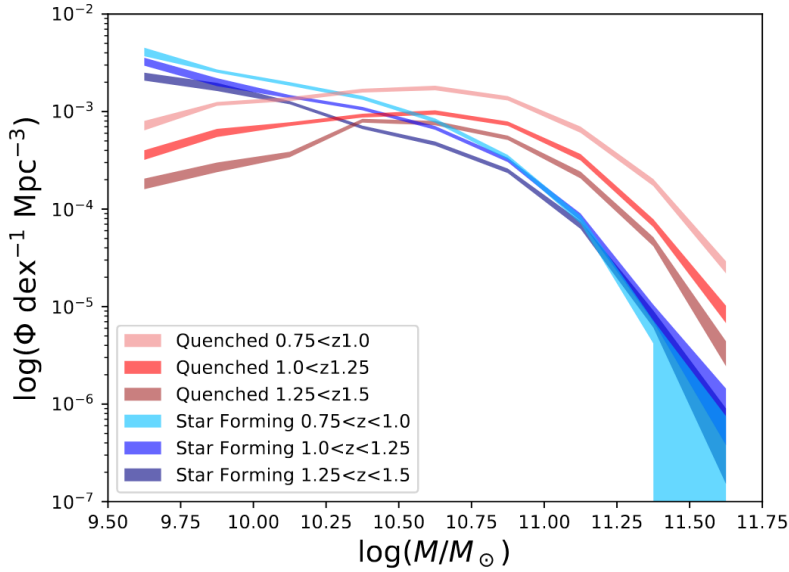


Figure 2.2: Stellar Mass Function for quiescent and star-forming galaxies of the COSMOS and XMM-LSS surveys. Figure lifted from Adams et al. (2021)².

QUASAR AND BLAZAR SMF

Quasars and blazars are types of active galaxies that are characterised by their high-energy emission, variability, and relativistic jets, they are powered by accretion of matter onto supermassive black holes at their center and their emission is dominated by non-thermal processes. AGN feedback is prominent for quasars and blazars, thus their stellar mass function and its evolution can provide insights into the emergence of feedback mechanisms across the Universe and its impact on the cosmic Star Formation Rate.

2.3 COSMOLOGICAL MEASURES

The expansion of the universe is described by the Einstein field equations which can be reduced to the fundamental Friedman equation (equation 2.1) and the conservation law (equation 2.2).

$$\dot{\alpha}^2 + K = \frac{8}{3} \pi G \rho \alpha^2 \quad (2.1)$$

$$\dot{\rho} = \frac{-3\dot{\alpha}}{\alpha} (\rho + p) \quad (2.2)$$

2.3.1 SCALE FACTOR OF THE UNIVERSE

For a Universe of curvature density $\Omega_{\kappa,0} \equiv -\frac{K}{\alpha_0^2 H_0^2}$ and a present-day-scale factor of $\alpha_0 = 1^{154}$, the differential equation that describes the scale factor of the Universe is equation 2.3

$$\dot{\alpha} = H_0 \sqrt{\Omega_{M,0} \alpha^{-1} + \Omega_{R,0} \alpha^{-2} + \Omega_{\Lambda,0} \alpha^2 + \Omega_{\kappa,0}} \quad (2.3)$$

2.3.2 COMOVING DISTANCE

The comoving radial distance is the distance that light traverses along the line-of-sight from its emission to the observing instrument in the present day and it is given by the following equation 2.5:

$$\begin{aligned} D_{\text{com}} &= \int_{\alpha_{\text{emission}}}^{\alpha_{\text{now}}=1} \frac{c}{\alpha} dt = \int_{\alpha_{\text{emission}}}^1 \frac{c}{\alpha \dot{\alpha}} d\alpha = \\ &= \int_{\alpha_{\text{emission}}}^1 \frac{c}{H_0 \alpha \sqrt{\Omega_{M,0} \alpha^{-1} + \Omega_{R,0} \alpha^{-2} + \Omega_{\Lambda,0} \alpha^2 + \Omega_{\kappa,0}}} d\alpha = \\ &= \frac{c}{H_0} \int_{\alpha_{\text{emission}}}^1 \frac{1}{\alpha \sqrt{\Omega_{M,0} \alpha^{-1} + \Omega_{R,0} \alpha^{-2} + \Omega_{\Lambda,0} \alpha^2 + \Omega_{\kappa,0}}} d\alpha \end{aligned} \quad (2.4)$$

And since $\alpha = (1+z)^{-1}$, the differential can be written $d\alpha = d(\frac{1}{1+z}) = \frac{-1}{(1+z)^2} dz$, thus:

$$\begin{aligned} D_{\text{com}} &= \frac{c}{H_0} \int_{z_{\text{emission}}}^{z_{\text{now}}=0} \frac{(-1)}{(1+z)^2} \frac{1}{(1+z)^{-1} \sqrt{\Omega_{M,0} (1+z) + \Omega_{R,0} (1+z)^2 + \Omega_{\Lambda,0} (1+z)^{-2} + \Omega_{\kappa,0}}} dz = \\ &= \frac{c}{H_0} \int_0^{z_{\text{emission}}} \frac{1}{(1+z) \sqrt{\Omega_{M,0} (1+z) + \Omega_{R,0} (1+z)^2 + \Omega_{\Lambda,0} (1+z)^{-2} + \Omega_{\kappa,0}}} dz \end{aligned} \quad (2.5)$$

Assuming a flat Universe ($\Omega_{\kappa,0} = 0$) with regular matter density of $\Omega_{M,0} = 0.3$, dark energy density of $\Omega_{\Lambda,0} = 0.7$, the speed of light being $c = 299792458 \text{ m s}^{-1}$, and the Hubble parameter in the present day being $H_0 = 70 \text{ km s}^{-1} \text{ Mpc}^{-1}$, the latter equation becomes:

$$D_{\text{com}} = \frac{299792.458 \text{ Mpc}}{70} \int_0^{z_{\text{emission}}} \frac{1}{(1+z) \sqrt{0.3(1+z) + 0.7(1+z)^{-2}}} dz \quad (2.6)$$

The transverse comoving distance (transverse to the line-of sight)⁶⁶ for a flat universe is equal to the radial comoving distance $D_{\text{com, transv}} = D_{\text{com}}$

2.3.3 ANGULAR SIZE OF A GALAXY

The angular size θ of an astrophysical light source is the angle on the celestial sphere formed by the characteristic transverse length of the source. Consequently, for a galaxy of physical rest frame diametre d_{gal} at redshift z , the angular size would be

$$\theta(z) = \frac{d_{gal}(1+z)}{D_{com}(z)} \quad (2.7)$$

2.3.4 LUMINOSITY DISTANCE

The luminosity distance D_L (luminosity distance) is defined such as to satisfy the bolometric flux-luminosity identity:

$$F = \frac{L}{4\pi D_L^2} \quad (2.8)$$

where F is the bolometric flux and L the bolometric luminosity. For a flat Universe, the emerging relation⁶⁶ between luminosity distance and comoving distance is:

$$D_L = (1+z) D_{com} \quad (2.9)$$

2.3.5 COSMOLOGICAL ASSUMPTIONS

In summary, the overall cosmological assumptions in the present work are a flat ($\Omega_{\kappa,0} = 0$) Universe with regular matter density of $\Omega_{M,0} = 0.3$ and dark energy density of $\Omega_{\Lambda,0} = 0.7$) that in present day has a scale factor of $a_0 = 1$ and a Hubble parametre of $H_0 = 70 \text{ km s}^{-1} \text{ Mpc}^{-1}$, the speed of light is a constant measured at $c = 299792458 \text{ m s}^{-1}$.

3

ARC sample of radio-galaxies

The ALMA Radio-source Catalogue (ARC) Survey, is a full spectroscopic archival survey conducted in order to study the impact relativistic jet outflows have on the evolution of radiogalaxies.

3.1 DATA SELECTION OF ARC GALAXIES

The ARC survey is been led by Kalliopi Dasyra, has been presented and exhaustively described by Anelise Audibert, Kalliopi Dasyra, Michalis Papachristou, Juan Antonio Fernández Oniveros, Ilaria Ruffa, Laura Bisigello, Françoise Combes, Philippe Salomé and Carlotta Gruppiioni in their work of Audibert et al. (2022)⁸.

For the scope of this survey, the team of Audibert et al. (2022)⁸ constructed a catalogue of radiosources which have measurements that cover the spectral region of CO molecular gas emission lines and it is representative of a large scale radio survey with regard to both flux distribution and redshift completeness. For the construction of the ARC catalogue of radiosources, several steps have been followed by the team of Audibert et al. (2022)⁸. In the first place, sources from the Atacama Large Millimetre/submillimetre Array (ALMA) archive have been assembled, including millimetre and sub-millimetre bright objects (mostly bright quasars) that can serve as flux, phase and band-pass calibrators as well as public sources from research projects. From those, only the ones which have spectroscopically determined redshift values from two or more optical lines are kept. The redshift information allows for the deduction of the spec-

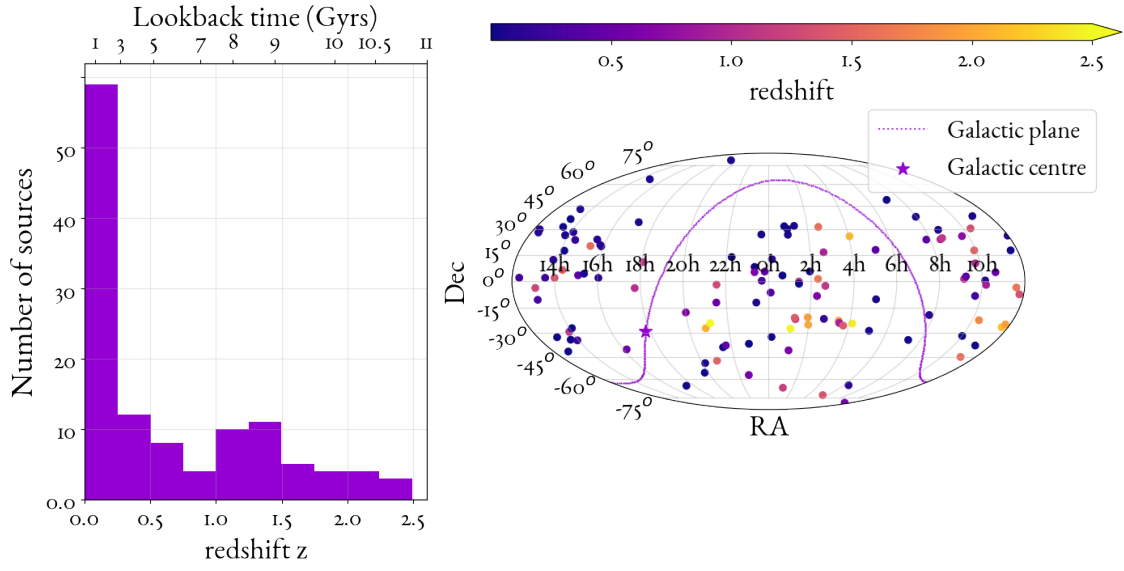


Figure 3.1: The ARC survey. Left panel: histogram of the redshift spanning of the 120 ARC sources. Right panel: Projection of the ARC sample in the celestial sphere.

tral window at which rest-frame CO emission for each source could be detected. The sources that did not have spectral measurements at their respective window have been excluded. Since the survey aims to study feedback from relativistic jet, galaxies with AGN radio emission are selected. Fulfillment of the 1.4GHz-to- $24\mu\text{m}$ criterion ¹⁶, which ensures that their radio emission is associated with Supermassive Black Hole (SMBH) accretion, led to limiting the sample to sources that have flux density at the 1.4GHz pass band above 0.4Jy. The limit flux distribution and redshift distribution of the remaining sources is compared to those of large scale surveys. Extensive statistical analysis with further exclusion of sources, described in detail in the work of Audibert et al. (2022)⁸, led to selecting the NRAO VLA Sky Survey (NVSS) 1.4GHz imaging survey as the large scale complete radio survey that is represented by the galaxy sample that finally comprises the ARC survey, resulting to a unique sample of galaxies with radiojets, information about molecular gas emission which can be studied statistically as representative of a large scale radiogalaxy survey.

In Figure 3.1, the ARC sample of 120 radiogalaxies is shown with their redshift distribution. The effective field-of-view (FOV) of the ARC survey is $\Omega_{\text{eff,ARC}} = 67\text{arcmin}^2$ which arises as the summation of the primary beam's Full Width Half Power (FWHP) for all observed sources. The team of Audibert et al. (2022)⁸ made use of the VizieR catalogue (operated at CDS, Strasbourg, France, DOI : [10.26093/cds/vizier](https://doi.org/10.26093/cds/vizier)), the SIMBAD Database (operated at CDS,

Strasbourg, France, DOI : [10.1051/aas:2000332](https://doi.org/10.1051/aas:2000332)), the NASA/IPAC Extragalactic Database (operated at Caltech, Pasadena, California, USA, DOI: [10.1007/978-94-011-3250-3_10](https://doi.org/10.1007/978-94-011-3250-3_10)) with the `astroquery`⁵⁵ access tool in the `python` programming language to collect the data.

3.2 SED DATA ACQUISITION & COMPIRATION

The acquisition of multiwavelength Spectral Energy Distribution (SED) data for each of the 120 ARC sources has been accomplished by Michalis Papachristou, with the use of the database services of the VizieR catalogue, the SIMBAD Database, the NASA/IPAC Extragalactic Database and the `astroquery`⁵⁵ access tool. The SEDs consist of all available photometric data from rest-frame far-ultraviolet (FUV) to radiofrequencies, as shown in Figure 3.2, denoted as "Full Data".

3.3 DATA CLEANING

The full multiwavelength SED data compiled include photometric observations from different telescopes with a variety of apertures taken through individual filter bands, as well as spectrograms, which offer a higher spectral resolution compared to photometry.

To ensure that each photometric data point corresponds to the integrated light of the full extend of the observed source, Athanasia Gkogkou (who worked on a small subset of these galaxies) imposed the criterion that the aperture of each photometric measurement must include the entire angular size (as described in equation 2.7) of the galaxy observed in the given redshift, assuming a representative characteristic diametre $d_{\text{gal}} = 30 \text{ kpc}$, excluding all observations with smaller aperture (since they would underestimate the flux) as well as all observations with much wider aperture (since integrated flux from nearby sources can contaminate and overestimate the flux).

Markos Polkas developed a routine in order to make a systematic selection of SED data points that are representative of each ARC galaxy's flux without assuming a 30 kpc diametre and a routine in order to select the upper limit of the AGN's accretion disk emission, as shown in Figure 3.2, denoted as "Reduced Data" and "BBB upper limit".

In the present work the end product of the compiled and cleaned SED data of ARC galaxies is used. Given the spectroscopic redshift information of every source (relevant details in

Appendix A), each SED in this work is plotted and analysed in the source's rest frame, with the SED intensity being converted to units of luminosity [erg/s].

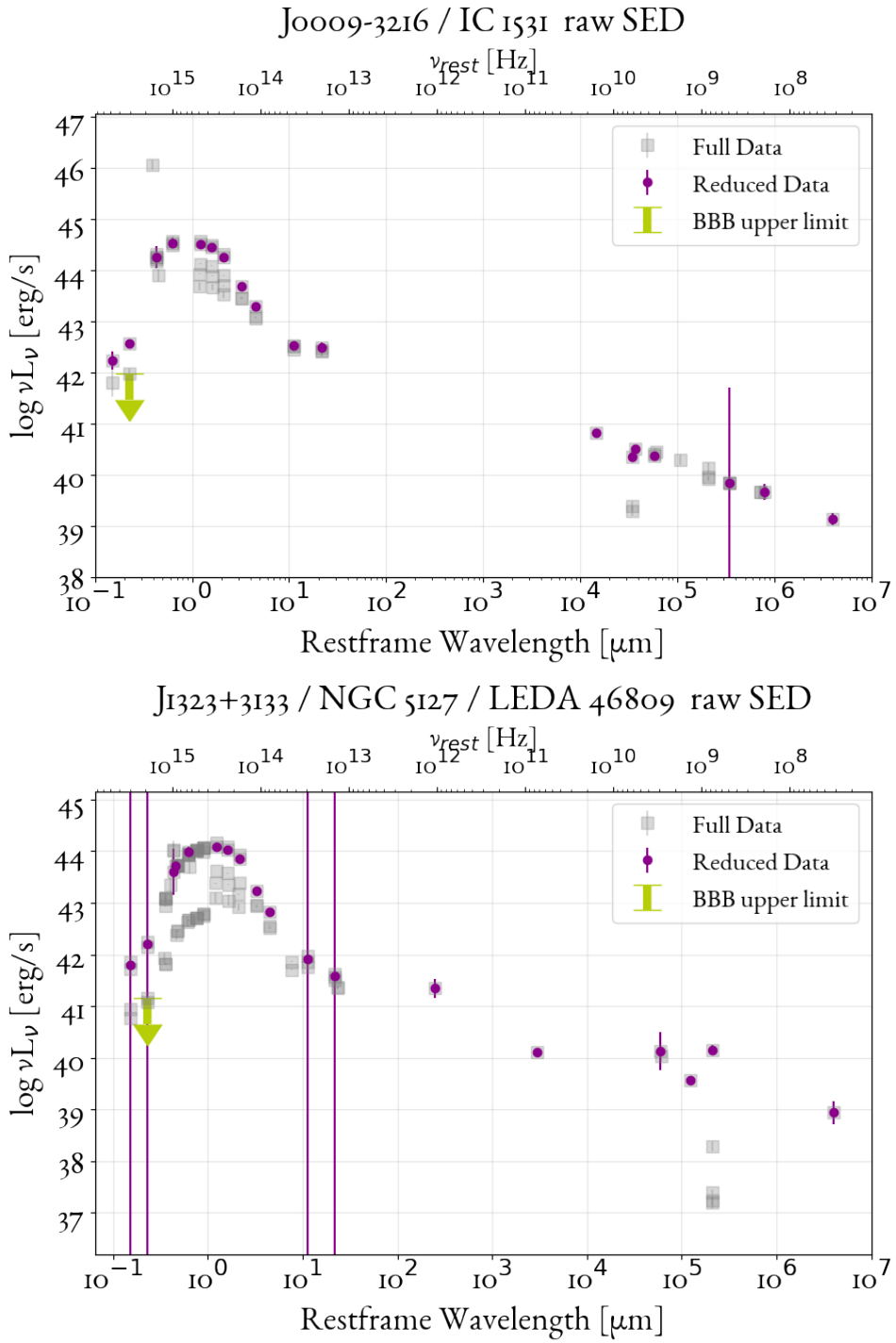


Figure 3.2: Raw SEDs of two ARC galaxies. Data integration by Michalis Papachristou, seen as the data points labeled "Full Data". Data reduction by Markos Polkas, the selection of the SED photometry (marked as "Reduced Data") and the upper limits for the accretion disk emission (marked as "BBB upper limit").

4

SED & SED Modelling

Galaxies emit radiation over the full electromagnetic spectrum, due to contributions from various components, including stars, gas, dust, and active galactic nuclei (AGN). A galaxy's Spectral Energy Distribution (SED) refers to the distribution of its emitted light across different wavelengths or frequencies.

4.1 SPECTRAL ENERGY DISTRIBUTION OF GALAXIES

Spectral Energy Distributions (SEDs) are discretely sampled functions of energy that describe the luminous output of an astronomical object. The independent variable is the photon energy of radiation, more often represented by frequency or wavelength. The dependent variable is the energy flux from the object which is the energy received from the source on the surface of the Earth assuming that is free of atmospheric or local absorption effects. This measurement is usually represented in energy units such as erg/s or Watts. Observed SEDs are usually cast in luminance units (e.g., erg/s/cm² or Watt/m²), and often in specific flux units (e.g., erg/s/cm²/μm or Watt/m²/Hz).

The Spectral Energy Distribution provides a comprehensive view of a galaxy's emission, ranging from low-energy radio waves to high-energy gamma rays, as demonstrated in Figure 4.1, and, when measured with sufficient precision and suitably analysed, offers insights about a galaxy's composition from its birth to its time of observation¹. Galaxies' SEDs can be assembled through spectrography, or constructed from the photometry of multiple surveys¹⁵¹.

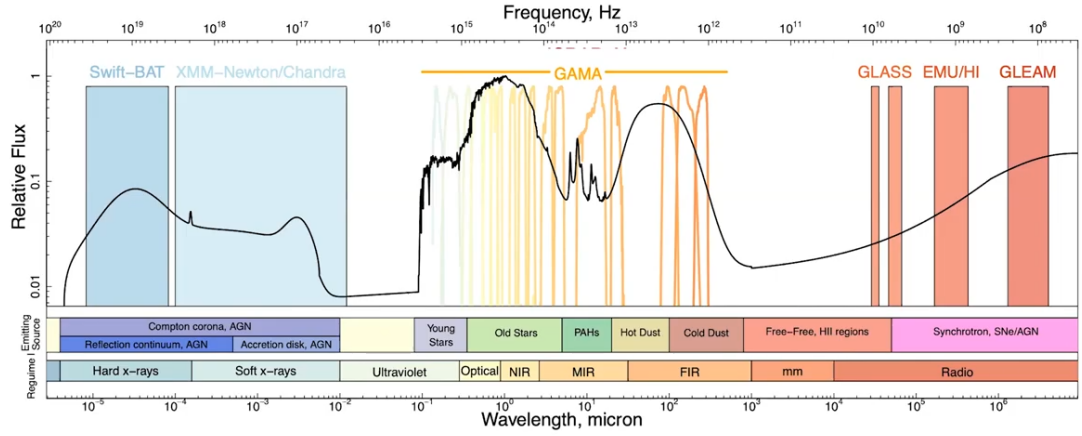


Figure 4.1: An example of a panchromatic galaxy SED. Signature band-passes are plotted in color accompanied by the name of the survey where they were used. Spectral regions and related dominant component are denoted at the bottom. Image credit: Luke J. M. Davies.

The SED of a galaxy is shaped by stellar populations, the interstellar medium (ISM), AGN torus, emission related to accretion processes such as the accretion disk, hot corona and emission from relativistic jets. In general, galaxies emit most of their energy in the form of starlight, with the dominant contribution coming from stars across different ages and masses, diffuse dust can absorb and re-emit starlight at longer wavelengths, leading to characteristic features in the infrared. However, other components can significantly affect the SED. For example, AGN, powered by accretion onto supermassive black holes at the galaxy's center, can contribute additional energy in the form of high-energy radiation, and are the dominant component for quasars. Therefore, the main aim of SED analysis is to use an observed SED to identify and constrain the contributions from these different components.

By studying the SED of galaxies across different wavelengths, insights into their physical properties, evolution, and formation mechanisms can be gained. Analyzing the SEDs of large samples of galaxies helps to build a comprehensive picture of the universe's structure and history.

4.2 MODELING THE SED OF GALAXIES

4.2.1 AGN COMPONENT

Radio sources, such as those in the ARC survey, owe their synchrotron radio emission to their radio loud AGN. Radio loud sources can be categorised, as depicted in Figure 4.2:

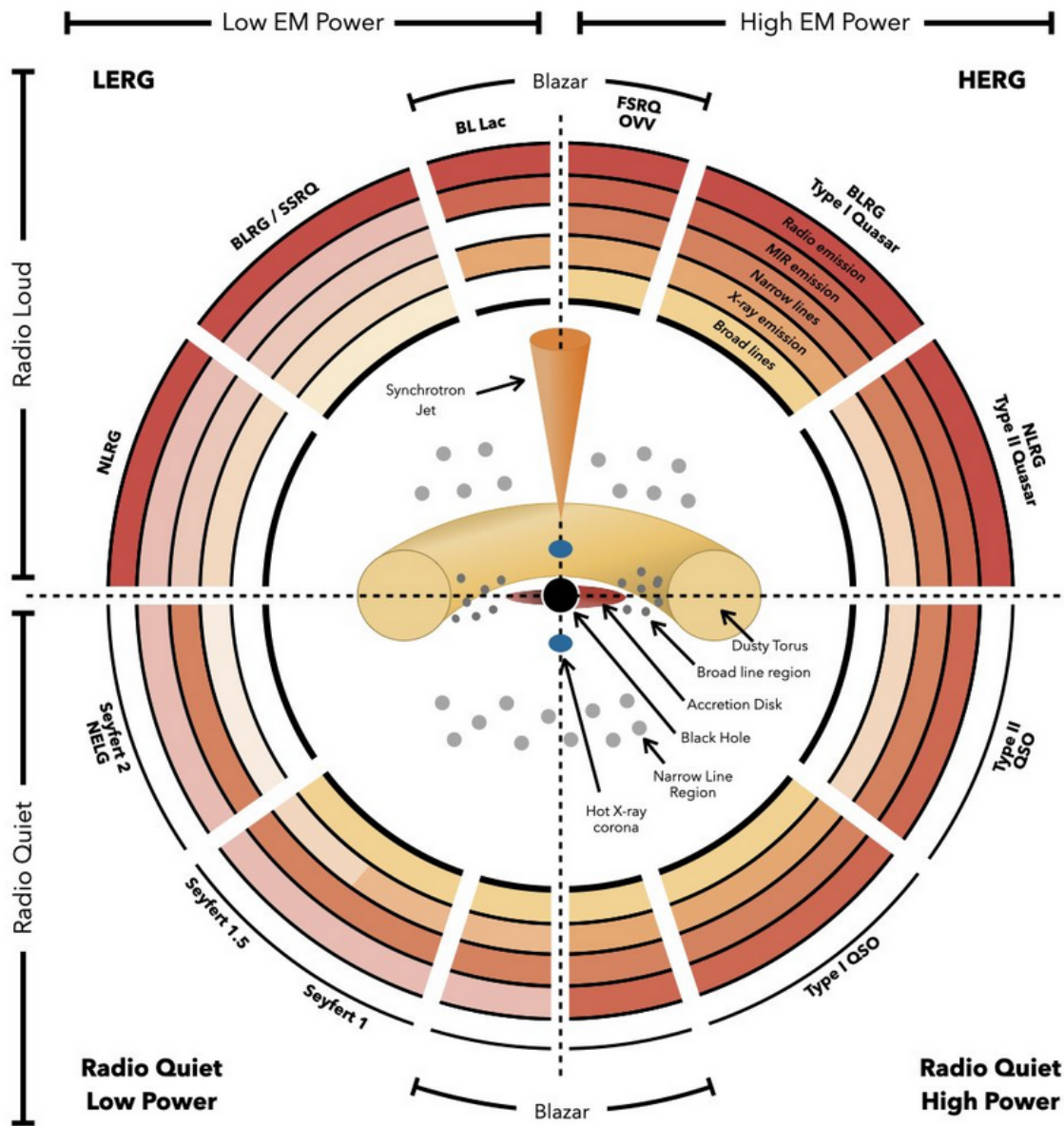


Figure 4.2: Schematic representation of the AGN unified model, where the accretion disk, the torus and the relativistic jet are depicted, as well as the radio loud types of sources (in the upper part of the diagram), such as those that populate the ARC survey. The type of AGN depends on the viewing angle, whether or not the AGN produces a significant jet emission, and how powerful the central engine is. Image credit: Jessica E. Thorne.

- Radio galaxies in which the central region is hidden but show bright radio jets and large radio luminosities. They can be divided in two groups according to their radio morphology and luminosity: the low-luminosity Fanaroff-Riley class I (FR-I) and the high-luminosity Fanaroff-Riley class II (FR-II). The FR-I galaxies show compact radio emission and their radio surface brightness profiles decrease outwards, while FR-II galaxies are dominated by radio lobes and their radio surface brightness profiles increase outwards as they reach the end of the extended structures.
- Radio loud Quasars, which were the first quasars to be discovered due to their strong radio emission. Their optical spectrum is similar to those of Seyfert galaxies and are therefore divided into type 1 and type 2.
- Radio loud Blazars, which are a special subclass of quasars, in which a relativistic jet is pointing very close to the line of sight of the observer. They have high variability and emit from radio frequencies to very high energies.

There is great variety of AGN types and to explain this diversity Antonucci (1993)⁶ proposed the first unification model, allowing the distinction between Seyferts and quasars and explaining other observational differences by orientation effects. Urry and Padovani (1995)¹⁴⁵ extended the unification model by including the relativistic jet. Figure 4.2 represents the AGN unified model, with the principal components and the type of AGN depending on the viewing angle.

4.2.2 GALAXY COMPONENT

Apart from the AGN, the host galaxy consists of the Interstellar Medium (ISM) and stars spanning a variety of spectral types³⁰. The Interstellar Medium contains dust^{38 144} and gas¹²¹, at different phases, temperatures, densities and ionisation states. Emission from gas imprints the spectral emission lines to the full galactic spectrum, but its contribution to the SED continuum is negligible. Since the main focus of the present work is based on broad band photometric SED data, the important galaxy components shaping a galaxy's SED are considered to be the stellar content of a galaxy and the diffuse ISM dust.

4.3 DUST IN THE ISM

Astrophysical dust is one of the key components of the diffuse interstellar medium of galaxies. Dust particles (“grains”) originate as a product of stellar evolution. Grains form in the atmospheres of evolved stars or remnants of supernovae, and are then released or ejected into the

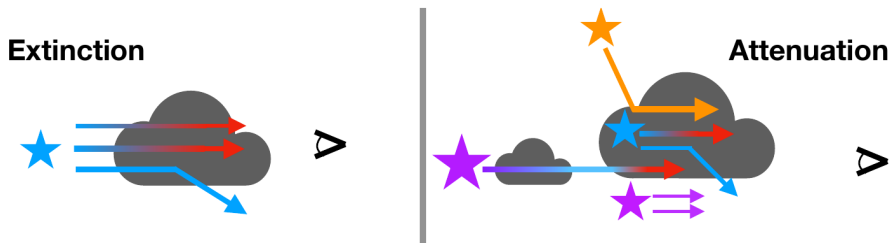


Figure 4.3: Difference between dust extinction and dust absorption of stellar light. Image lifted from Salim & Narayanan (2020)¹²².

ISM, their sizes vary from larger than $\sim 0.02 \mu\text{m}$ to nano-particle size. A robust model of dust in the diffuse ISM is proposed by Hensley & Draine (2023)⁶³. Both extinction and emission from interstellar dust are observed. Observationally, the presence of dust in galaxies is revealed by two general effects:

- dust produces emission in the infrared (IR) part of the spectrum, consisting of the dust continuum emission spectrum and various emission and absorption features
- dust modifies the light that originates from the stellar continuum at all wavelengths, in particular the ultraviolet (UV) to near-infrared (NIR) flux from stars is attenuated by dust

4.3.1 DUST EXTINCTION

Extinction represents the amount of light lost along a single line of sight through a dusty medium due to absorption or scattering away from the line of sight. The total extinction τ_λ per hydrogen column density N_H at wavelength λ for a population of randomly oriented grains is:

$$\frac{\tau_\lambda}{N_H} = \sum_{i=1}^N \int da \left(\frac{1}{n_H} \frac{dn_i}{da} \right) C_{\text{ran}}^{\text{ext}}(\lambda, i, a) \quad (4.1)$$

where N is the number of distinct components in the model, each grain component i in the model has a size distribution dn_i/da defined such that the number density of grains having an effective radius between a and $a + da$ is $(dn_i/da)da$, $C_{\text{ran}}^{\text{ext}}$ denotes the extinction cross section for randomly oriented grains.

As described in detail by Salim & Narayanan (2020)¹²², in contrast to extinction, attenua-

tion includes the effects arising from the distribution of stars and dust in the galaxy,. Attenuation includes the same mechanisms for loss of photons as extinction plus scattering back into the line of sight, as well as the contribution to the light by unobscured stars, schematically shown in Figure 4.3. In panel (e) of Figure 4.5 the radiative transfer based attenuation curve of Witt & Gordon (2000)¹⁵⁵ is shown in dashed lines, along with the average attenuation model of Calzetti (2000)²⁴ for star-forming galaxies. The evidence-based average attenuation law of Calzetti (2000)²⁴ proposes that the observed flux from stars in the presence of dust is

$$F_{\text{obs}}(\lambda) = F_{\text{intr}}(\lambda) \times 10^{-0.4A_\lambda} \quad (4.2)$$

where $F_{\text{obs}}(\lambda)$ is the observed (attenuated) stellar flux, $F_{\text{intr}}(\lambda)$ is the intrinsic (unattenuated) stellar flux and the attenuation A_λ is related to the UV-visual color excess E(B-V):

$$A_\lambda = k(\lambda) \text{ E(B-V)} \quad (4.3)$$

and the absorption coefficient $k(\lambda)$ follows:

$$k(\lambda) = \begin{cases} R_\nu + 2.659 \times \left(-2.156 + \frac{1.509}{\lambda} - \frac{0.198}{\lambda^2} + \frac{0.011}{\lambda^3} \right) & , \ 0.12 \mu\text{m} \leq \lambda \leq 0.63 \mu\text{m} \\ R_\nu + 2.659 \times \left(-1.857 + \frac{1.040}{\lambda} \right) & , \ 0.63 \mu\text{m} \leq \lambda \leq 2.2 \mu\text{m} \end{cases} \quad (4.4)$$

with $R_\nu = 4.05$ and the coefficients adjusted for λ in microns.

4.3.2 DUST EMISSION

There are two principal emission mechanisms for interstellar grains: thermal vibrational emission I_λ^{th} and rotational emission I_λ^{SpD} (“spinning dust emission”). The total dust emission per hydrogen atom I_λ/N_H is the sum of these two contributions⁶³:

$$\frac{I_\lambda}{N_H} = \frac{I_\lambda^{\text{th}}}{N_H} + \frac{I_\lambda^{\text{SpD}}}{N_H} \quad (4.5)$$

Interstellar grains absorb UV and optical starlight and reradiate the energy in the infrared, the resulting thermal vibrational emission per N_H from a population of randomly oriented dust

grains is:

$$\frac{I_{\lambda}^{\text{th}}}{N_H} = \sum_{i=1}^N \int da \left(\frac{1}{n_H} \frac{dn_i}{da} \right) \times \int dT \left(\frac{dP}{dT} \right)_{i,a} C_{\text{ran}}^{\text{abs}}(\lambda, i, a) B_{\lambda}(T) \quad (4.6)$$

where $B_{\lambda}(T)$ is the Planck function and $(dP/dT)_{i,a}$ is the grain temperature distribution of grains of composition i and effective radius a . Contribution from stimulated emission is negligible in radiation fields typical of the diffuse ISM and, thus, ignored. Assuming⁶³ a radiation field with specific energy density u_{λ} :

$$u_{\lambda} = U \left[u_{\lambda}^{\text{UV}} + \sum_{i=1}^3 \frac{4\pi}{c} W_i B_{\lambda}(T_i) \right] + \frac{4\pi}{c} B_{\lambda}(T_{\text{CMB}}) \quad (4.7)$$

where U is a frequency independent scaling factor, u_{λ}^{UV} is the UV component of the radiation field, and $T_{\text{CMB}} = 2.725$ K is the CMB temperature. The optical starlight component is modeled as three black bodies having temperatures of $T_1 = 3000$ K, $T_2 = 4000$ K and $T_3 = 7500$ K with dilution factors $W_1 = 7 \times 10^{-13}$, $W_2 = 1.65 \times 10^{-13}$ and $W_3 = 10^{-14}$. The UV component is given by

$$\frac{\lambda u_{\lambda}^{\text{UV}}}{\text{erg cm}^{-3}} = \begin{cases} 2.373 \times 10^{-14} \left(\frac{\lambda}{\mu\text{m}} \right)^{-0.6678} & , 1340 \text{ \AA} < \lambda < 2460 \text{ \AA} \\ 6.825 \times 10^{-13} \left(\frac{\lambda}{\mu\text{m}} \right) & , 1100 \text{ \AA} < \lambda < 1340 \text{ \AA} \\ 1.287 \times 10^{-13} \left(\frac{\lambda}{\mu\text{m}} \right)^{4.4172} & , 912 \text{ \AA} < \lambda < 1100 \text{ \AA} \\ 0 & , \lambda < 912 \text{ \AA} \end{cases} \quad (4.8)$$

Stimulated IR emission from the dust itself does not appreciably contribute to the heating of dust grains in radiation fields typical of the diffuse ISM and is, thus, neglected.

To ensure consistency between the power absorbed by dust (having the adopted extinction curve 4.1) and the power emitted by dust, it is required that $\log_{10} U \approx 0.2$ (yielding $U \approx 1.6$). Several factors contribute to the larger value of U and introduce constraints on IR emission and differences in the dust model.

It is remarked by Hensley & Draine (2023)⁶³ that in addition to thermal vibrational emission, rapidly rotating ultra small grains can also produce electric or magnetic dipole emission. This mechanism has been identified peaking near 30 GHz and is dependent on environmental parameters.

4.3.3 DUST MODEL & PARAMETERS

Joint AGN and star-forming SED models for dust emission are presented by Dale et al. (2014)³². The dust emission templates for the star-forming component are used in the present code, available from Daniel Dale*. In the construction of the templates, a series of “local” spectral energy distributions were created to represent the emission from dust exposed to a wide range of heating intensities $0.3 \leq U \leq 10^5$ where $U = 1$ corresponds to the local interstellar radiation field in the Solar Neighborhood. A power-law combination of these local curves can effectively mimic the spatially-integrated (“global”) dust emission:

$$dM_d \propto U^{-\alpha_{SF}} dU \quad (4.9)$$

where M_d is the dust mass heated by a radiation field at intensity U and the exponent α_{SF} represents the relative contributions of the different local spectral energy distributions. A single parameter (α_{SF}) is used to describe the full range of PAH/very small grain/large grain and overall spectral shapes for normal star-forming galaxies. The star-forming dust emission templates are based on spectral shapes of starburst galaxies from the Spitzer archives and include prominent fine-structure lines such as [Ne III] 15.6 μm , [S III] 18.7 μm , and [S III] 33.5 μm and the 17 μm PAH complex, the latter of which accounts for up to 10% of the total PAH emission in normal star-forming galaxies.

The Dale et al. (2014)³² ISM dust models for star-forming galaxies are used in the present work, parametrised with the exponential α_{SF} and the number of atoms (which contribute to the dust mass), in Figure 4.4 the templates are shown for different values of α_{SF} , while the number of particles is a scaling factor. The models are given in units of Watt and are normalised to the emission from a particle with mass equal to single hydrogen atom. For ease of use in the present work, the intensity has been transformed to erg/s and the normalisation has been converted to the luminosity of one solar mass (M_\odot).

4.4 STELLAR POPULATIONS

The visible and near-infrared (NIR) spectral windows on a galaxy’s SED are dominated by the radiation of the stars on the galaxy.

The stellar populations of a galaxy have a range of luminosities, masses, ages and metallicities

*<http://physics.uwyo.edu/~ddale/research/seds/seds.html>

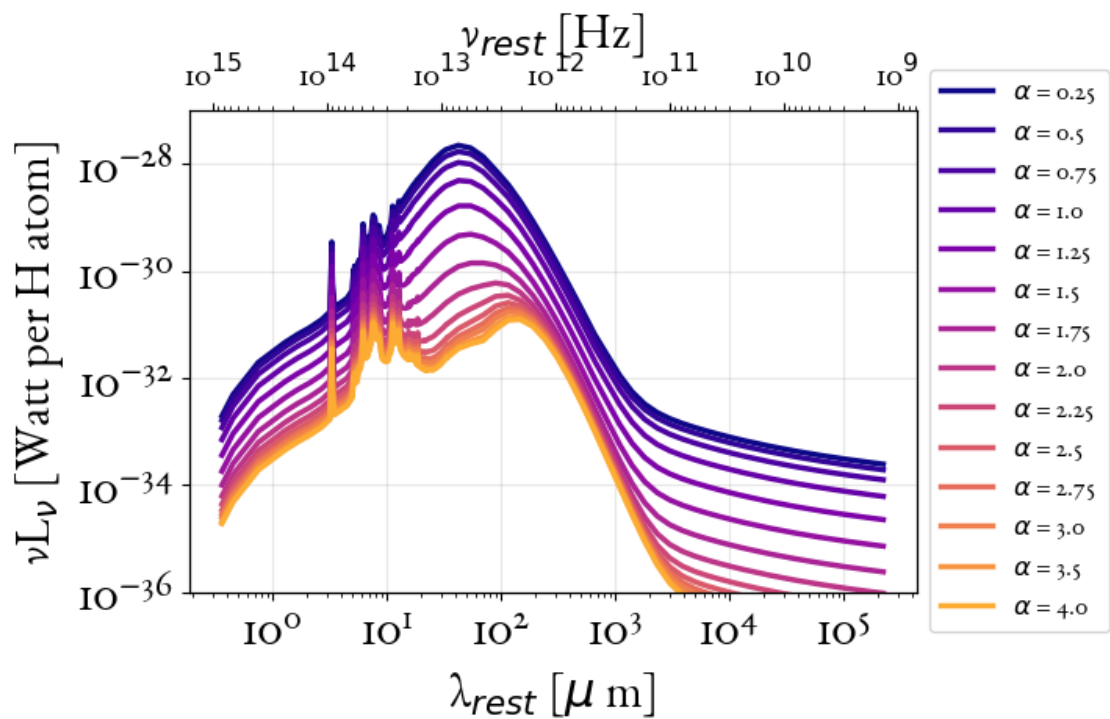


Figure 4.4: ISM dust emission Dale et al. (2014)³² for different values of α_{SF} .

with some being present from when the galaxy first formed and other being formed more recently. Stellar Population Synthesis (SPS) is a method developed for constructing a galactic spectrum from the sum of the spectra of its stars and rely on stellar evolution theory to constrain the range of possible stellar types at a given age and metallicity. Commonly, SPS models start with a Simple Stellar Population (SSP), integrated along the evolutionary track.

4.4.1 SIMPLE STELLAR POPULATION

A Single Stellar Population is the spectrum of an ideal, coeval ensemble of stars at a single metallicity and abundance pattern, based on a library of model stellar spectra. The evolution of this ensemble of stars is captured by the isochrones and its mass depends both on the initial distribution (Initial Mass Function) and the age of the ensemble. The Initial Mass Function (IMF) dictates how many stars of each spectral class exist initially, the isochrones dictate how the number of massive stars changes with time and the shape of a single star's spectrum is retrieved from the stellar spectra library.

The flux emitted per unit frequency $f_{\nu, \text{SSP}}$, of a SSP of mass M , age t , and metallicity Z is given³⁰ by the sum of the individual stars:

$$f_{\nu}^{\text{SSP}}(t, Z) = \int_{m_l}^{m_u(t)} f_{\nu}^{\text{star}}(T_{\text{eff}}(M), \log g(M); t, Z) \xi(M; t, Z) dM \quad (4.10)$$

where M is the initial (zero-age main sequence) stellar mass, $\xi(M; t, Z)$ is the stellar mass function, which is computed from the initial mass function $\xi_o(M)$ and the stellar evolution which describes when and which stars will stop contributing to the SSP spectra because they end their lives either as Supernovae or as white dwarfs¹⁵¹. f_{ν}^{star} is a stellar spectrum, and $f_{\nu}^{\text{SSP}}(t, Z)$ is the resulting time and metallicity-dependent SSP spectrum. The lower limit of integration, m_l , is typically³⁰ taken to be the hydrogen burning limit (either $0.08M_{\odot}$ or $0.1M_{\odot}$ depending on the SPS modelling), and the upper limit is dictated by stellar evolution. The isochrones specify the relation³⁰ between the effective temperature of a star T_{eff} , the measure of surface gravity $\log g$ and the mass of the star M for a given age t and metallicity Z . The creation of stellar isochrones requires¹⁵¹ a large grid of evolutionary tracks, created by modelling the evolution of stars of a given initial mass and metal content. The Padova^{12 56 97} Stellar Isochrones for some indicative SSP ages are plotted in panel (b) of Figure 4.5.

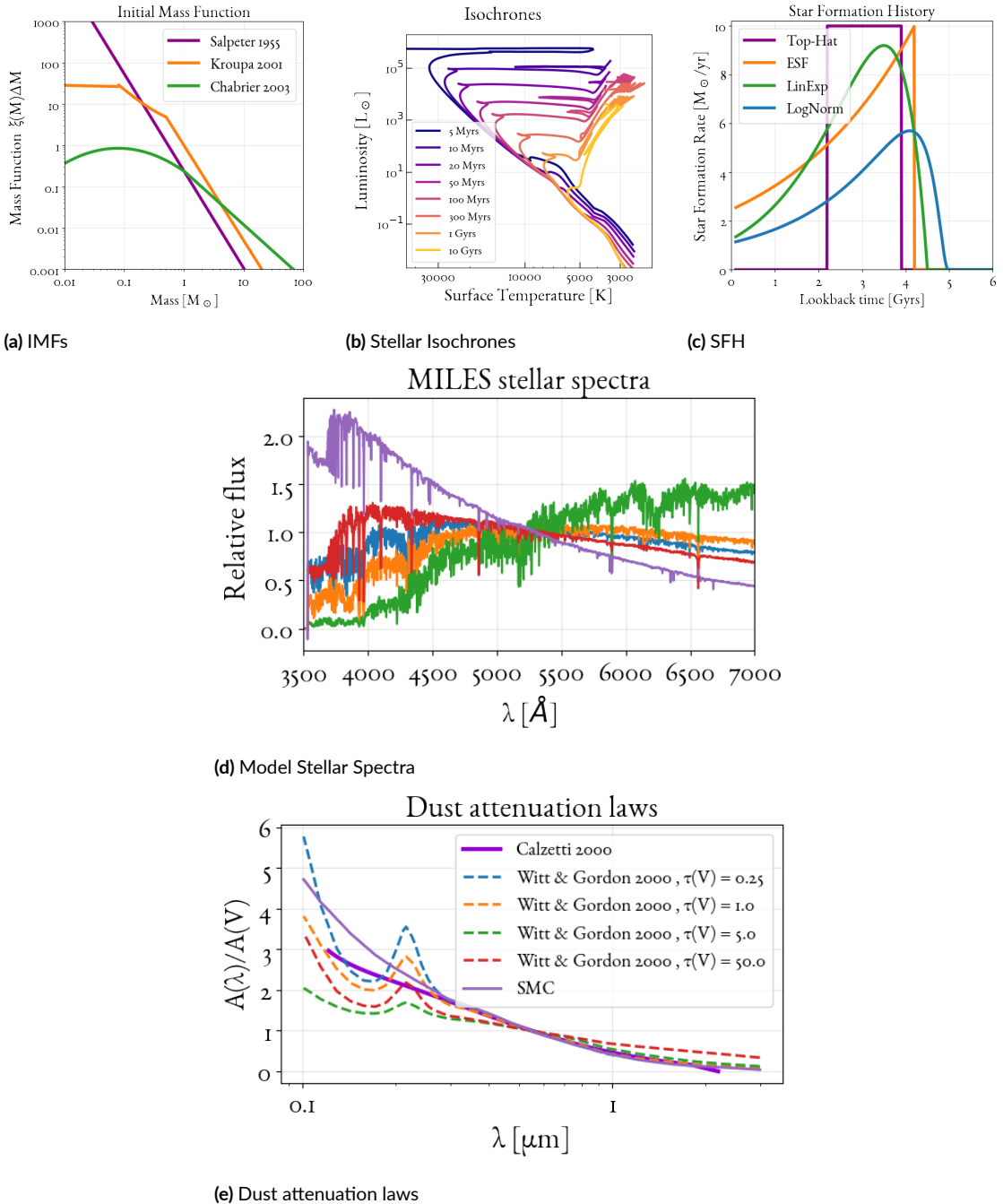


Figure 4.5: Panel (a): Different types of Initial Mass Functions, the model used in the present work is the Chabrier 2003²⁶. Panel (b): The Padova^{12 56 97} Stellar Isochrones for different age of the coeval population. Panel (c): Different types of Star Formation Histories, in the present work the delayed exponential decay function is used here denoted as "LinExp". Panel (d): The empirical library of MILES model spectra^{147 147 43} is used for the Stellar Population Model of the present work. Panel (e): Different Dust attenuation laws are shown. In the Stellar Population Model of this work, the Calzetti 2000²⁴ law is used.

4.4.2 STELLAR EVOLUTION, STAR FORMATION HISTORY & DUST ABSORPTION

The Simple Stellar Population models the flux of stars at a single specific age and metallicity. In order to represent the whole stellar population of a galaxy and combine energy and timescales of all evolutionary phases, the SSP spectrum ought to be convolved with a Star Formation History that can simulate the stellar evolution of an ensemble of stars.

STAR FORMATION HISTORY

The Star Formation History is an estimate of the galaxy's star formation rate (SFR) as a function of time, which traces its evolution and merger history⁸⁸. In Panel (c) of Figure 4.5 four common families of SFH functions are plotted:

- Top-Hat, which assumes constant star formation from a start time through the time of observation at a fixed rate

$$SFR(t; t_0, \tau) = \Theta(t - t_0) \times [1 - \Theta(t - t_0 - \tau)] \quad (4.11)$$

- ESF assumes an exponentially declining star formation rate, and performs well for local ellipticals

$$SFR(t; t_0, \tau) = \Theta(t - t_0) \times \exp\left(-\frac{t - t_0}{\tau}\right) \quad (4.12)$$

- LinExp has a functional form of a delayed exponential decay

$$SFR(t; t_0, \tau) = \Theta(t - t_0) \times \frac{t - t_0}{\tau} \times \exp\left(-\frac{t - t_0}{\tau}\right) \quad (4.13)$$

- LogNormal has a functional form that appears in many physical processes

$$SFR(t; t_0, \tau) = \Theta(t - t_0) \times \frac{1}{t} \times \exp\left[-\frac{\left(\ln(t - t_0)\right)^2}{2\tau^2}\right] \quad (4.14)$$

In all the above functional forms, Θ is the Heaviside step function, τ is the e-folding time which delineates the evolution of Star Formation Rate (governs the "width" of the episode of star formation), t_0 is the age where the galaxy star formation begins, τ and t_0 are parameters of the functional form, while t is the free variable of time.

For a Simple Stellar Population, which assumes that all of its stars form at a single lookback

time (T) and with the same metallicity (Z), the flux at a given frequency (ν), based on equation

4.10:

$$f_{\nu}^{\text{SSP}} = \int_0^{t_{\text{obs}}} f_{\nu}^{\text{SSP}}(t_{\text{obs}} - t', Z) \delta(T - t_{\text{obs}} + t') dt' \quad (4.15)$$

where δ is the Dirac functional, and for the lower integration limit we assume de facto that the time of the Big Bang is zero.

Generalising from Simple Stellar Populations (SSPs) to Composite Stellar Populations (CSPs), we can then represent the SED for a galaxy with a given star formation history ($SFH \equiv \psi(t; t_0, \tau)$) as an integral over all star formation that occurred at different times from the birth of the Universe to the time of observation:

$$f_{\nu}^{\text{CSP}} = \int_0^{t_{\text{obs}}} f_{\nu}^{\text{SSP}}(t_{\text{obs}} - t', Z) \psi(t'; t_0, \tau) dt' \quad (4.16)$$

The chosen Star Formation History in this work is the delayed exponential decay form, thus the adopted ψ satisfies the constraints outlined in equation 4.13:

$$\psi(t; t_0, \tau) = \Theta(t - t_0) \times \frac{t - t_0}{\tau} \times \exp\left(-\frac{t - t_0}{\tau}\right)$$

The star formation history (SFH) of a galaxy can sometimes be poorly constrained when assuming a predetermined functional form and parametrisation. And the sensitivity of model spectra to star formation drops approximately logarithmically with time, as remarked by Ocvirk et al. (2006)¹⁰⁵. The expanding size of galaxy catalogues available through surveys facilitates new approaches^{74,76} that aim to reconstruct the SFH from the data, using methods that include reducing the dimensionality of the parametre space using data compression methods⁸⁵, fine-binning the interval that makes the maximum contribution to flux, mapping the discretised-time photometric fitting to a linear inversion problem, or comparing against a large basis of realistic model SEDs using a Bayesian method¹⁰⁸.

DUST ATTENUATION

Dust reddening is then applied to the spectrum using the Calzetti et al. (2000)²⁴ dust attenuation law as described in Section 4.3.1, using the E(B-V) as a free parametre of the analytical function for attenuation (equation 4.2). Thus, extending the parameter space for fitting the stellar component in the presence of dusty ISM.

4.4.3 STELLAR POPULATION MODELS

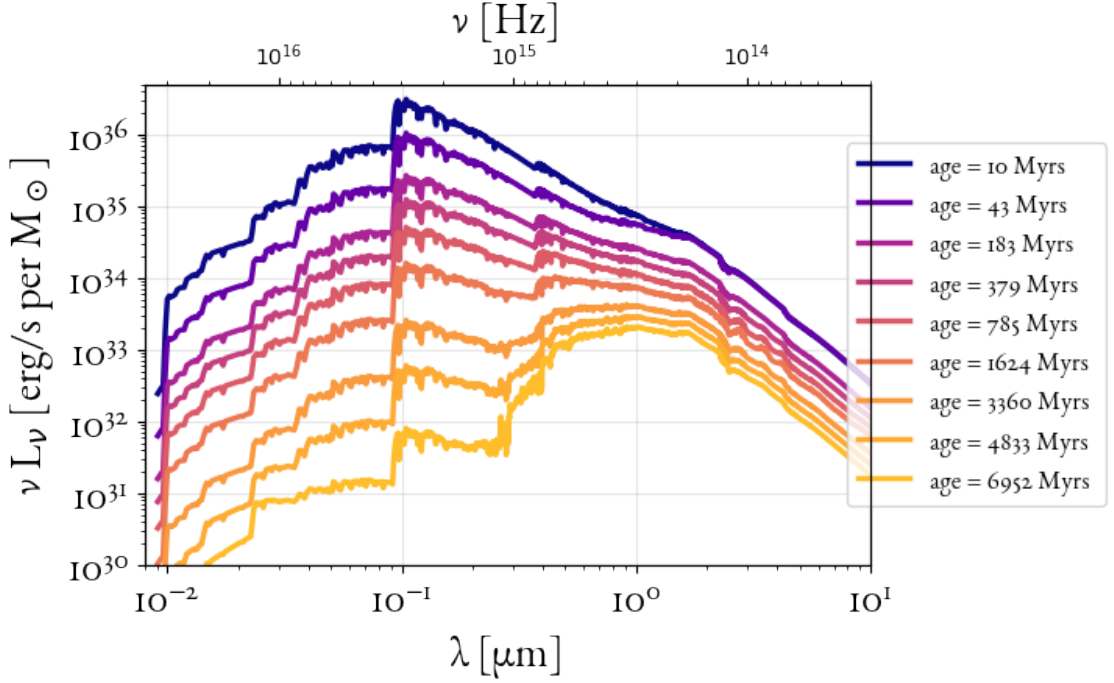
The construction of an SSP therefore requires a stellar evolution theory in the form of isochrones, stellar spectral libraries, and an IMF, each of which may.

In the present code Stellar Population Synthesis is not implemented directly, SPS models implemented in the code are the 2016 updated version of the Bruzual & Charlot (2003)¹⁹ models, using of the Medium-resolution Isaac Newton Telescope library of Empirical Spectra (MILES)^{124 147 43}. The templates were generated using Chabrier(2003)²⁶ initial mass function, spanning a range of different ages, metallicities and delayed exponential decay SFH e-folding times as depicted in Figure 4.6. The models implemented within the code are constructed using the open-source module `SMPy`, developed by Kenneth J. Duncan[†]. In order to probe a more complex Star Formation History (Section), two composite stellar populations are chosen in the SED fitting code: an old stellar population and a young stellar population, each of which are parametrised by their individual stellar mass, metallicity, age, e-folding time τ and attenuation parameter (since younger stars could still reside in their birth cloud), as deposited in Table 5.1. The two composite stellar populations are parametrised:

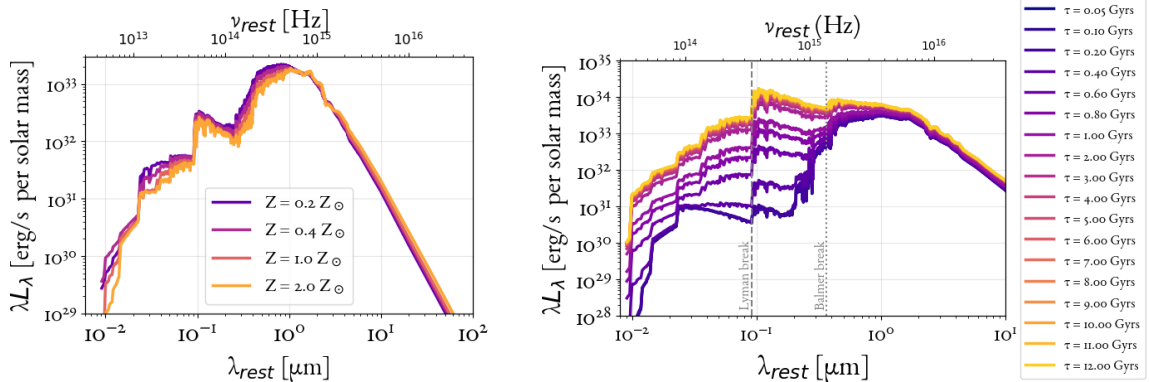
- Metallicity in units of solar metallicity (Z/Z_{\odot})
- Age t in units of Myrs
- E-folding time τ of delayed exponential decay SFH in units of Gyrs
- Stellar Mass in units of solar masses and in the logarithmic regime $\log(M_{\star}/M_{\odot})$
- E(B-V) extinction that couples the stellar component with the dust component via the attenuation law in functional form.

Interpolation to $<0.3\text{dex}$ could be performed and applied in the photometric SED model, although the templates in the produced libraries, regardless of the model are fundamentally limited could not offer distinguishable SFH information for a difference smaller than $0.3\text{-}0.4\text{ dex}$ ¹⁰⁵. Similar-age stellar populations have very similar spectra, rendering Star Formation History recovery inherently ill-conditioned⁹¹, as shown in Figure 4.7.

[†]<https://github.com/dunkenj/smpy>



(a) Composite Stellar Population with different ages



(b) Composite Stellar Population with different metallicities

(c) Composite Stellar Population with different e-folding time

Figure 4.6: The Bruzual & Charlot 2003¹⁹ Stellar Population Models with the Chabrier 2003²⁶ Initial Mass function, Padova^{12 56 97} Isochrones and a Star Formation History in the shape of delayed exponential decay, unattenuated. Panel (a): The shape changes for different age, here each spectrum has constant metallicity of $Z = Z_{\odot}$ and constant e-folding time of $\tau = 0.6$ Gyrs. Panel (b): The shape changes for different metallicity, here each spectrum has constant age of 10 Myrs and the e-folding time is $\tau = 2$ Gyrs. Panel (c): The shape changes for different e-folding time τ of the assumed Star Formation History, here each spectrum has constant age of 3.4 Gyrs and constant metallicity of $Z = Z_{\odot}$.

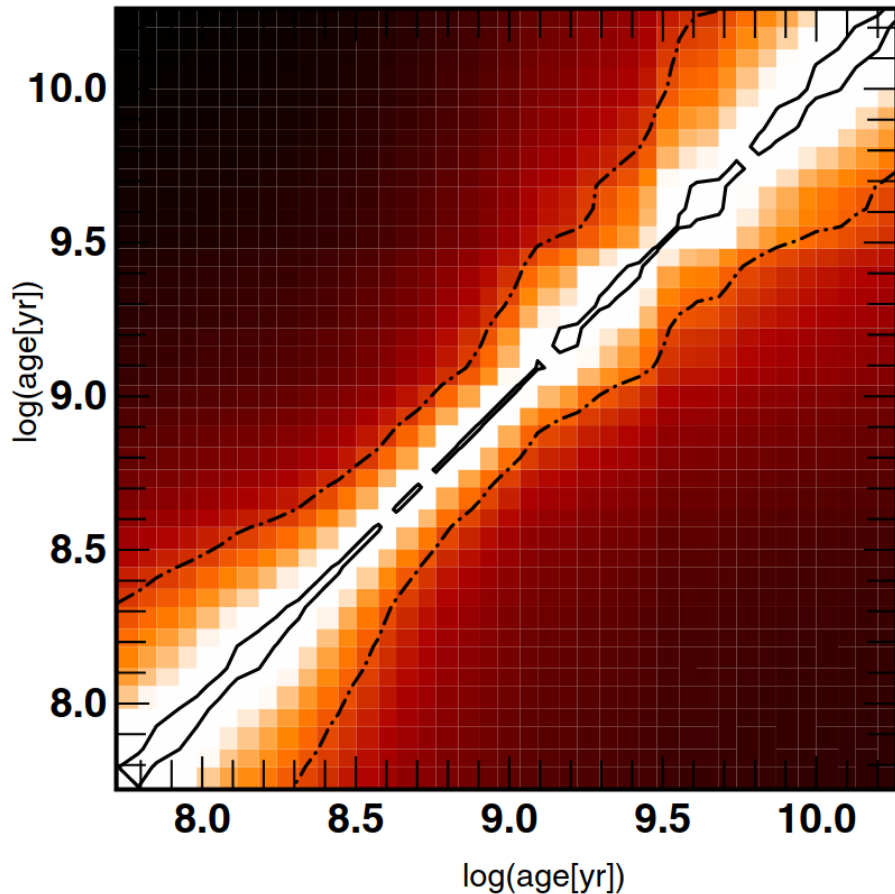


Figure 4.7: Distinguishability of single-age populations with Signal-to-Noise ratio $S/N=10$ (dash-dotted line) and with Signal-to-Noise ratio $S/N=100$ (continuous line). Plot lifted from Ocvirk et al. (2006)¹⁰⁵.

4.5 AGN ACCRETION DISK

Active galaxies host a supermassive black hole (SMBH) in their centre, which accretes the surrounding material. Because of angular momentum conservation this process leads to the formation of an accretion disk. Along with star formation, AGNs are thought to have a drastic impact on galaxy evolution. Properly disentangling the emission of AGNs from star formation is not an easy task as they can both strongly emit in the UV, and a large fraction of this emission can be reprocessed by dust and re-emitted at longer wavelengths.

Evidence of multiwavelength observations of quasar continua favor the geometrically thin optically thick accretion disk⁹⁶, schematically demonstrated in Figure 4.2. The accretion disk is made mostly out of gas and its emission is split⁹⁶ between:

- Thermal emission, since particles have Maxwellian velocity distribution due to collisions
- Non thermal bremsstrahlung (free-free) radiation with power-law energy distribution of particles¹⁰

The accretion disk emission presents a peak in the optical spectral area, which is sometimes called Big Blue Bump (BBB). According to the virial theorem, gravitational potential energy is released half into kinetic energy and half in to radiation:

$$L_{\text{BBB}} = \frac{G \dot{M} M}{2 r} \iff \frac{G \dot{M} M}{2 r} = 2\pi r^2 \sigma_{\text{SB}} T^4 \iff T(r) = \left(\frac{G \dot{M} M}{4\pi \sigma_{\text{SB}} r^3} \right)^{1/4} \quad (4.17)$$

Where, M is the mass of the accreted gas, \dot{M} is the accretion rate, r is the distance of the accreted material from the SMBH, σ_{SB} is the Stefan-Boltzmann constant and G is the universal gravity constant. In reality, the above is an approximation averaged over the disk, since energy is dissipated locally in the disk through viscosity. This yields:

$$T(r) = \begin{cases} \left[\frac{3G \dot{M} M}{8\pi \sigma_{\text{SB}} r^3} \left(1 - \sqrt{\frac{R_i}{r}} \right) \right]^{1/4} & , r \gg R_i \\ \left(\frac{3G \dot{M} M}{8\pi \sigma_{\text{SB}} R_s^3} \right)^{1/4} \times \left(\frac{r}{R_s} \right)^{-1/3} & , r \sim R_s \end{cases} \quad (4.18)$$

where R_i is the inner radius of the accretion disk and $R_s = 2GM/c^2$ is the Schwarzschild

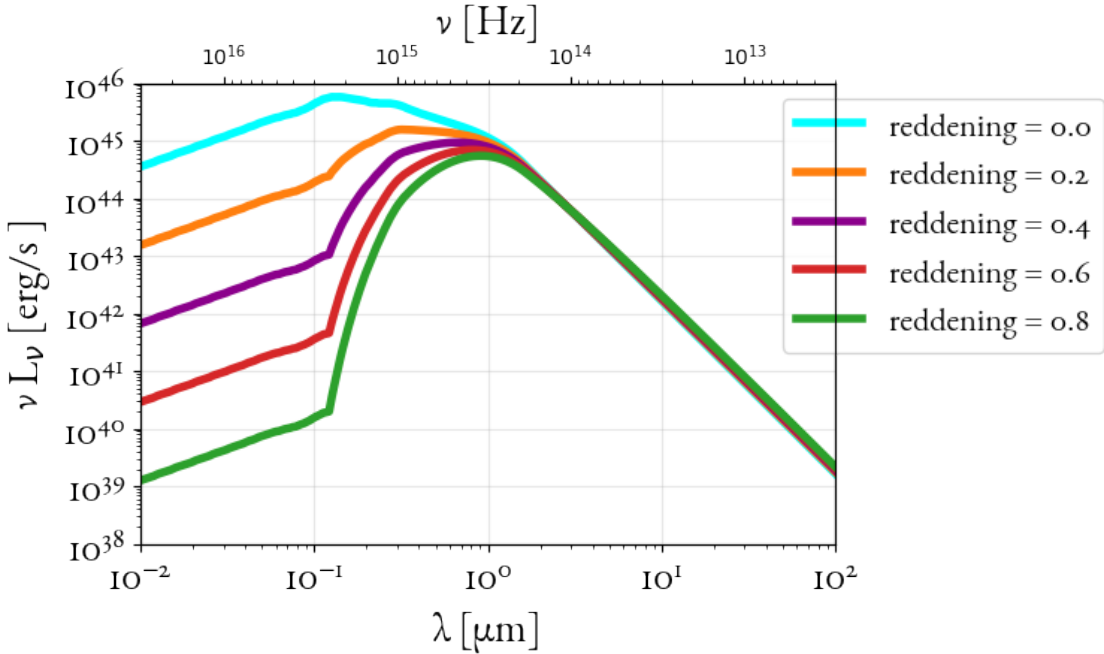


Figure 4.8: Accretion disk emission templates by Richards et al. (2006)¹¹⁹ for different values of reddening fraction $E(B-V)_{BBB}$.

radius. Hence, the accretion disk continuum spectrum is a superposition of many Black Bodies with different temperatures.

4.5.1 ACCRETION DISK MODEL & PARAMETRES

The accretion disk contribution is assumed to be mostly thermal emission from the accretion disk with $T = 10^{5\pm1}\text{K}$, accepting that locally the disk emits like a Black Body, and is parametrised by a reddening fraction (due to absorption from the dusty AGN torus) and a scaling coefficient¹¹⁹. The templates are by Richards et al. (2006)¹¹⁹ and are shown in Figure 4.8.

The attenuation law due to absorption from the dusty AGN torus follows a curve similar to that of the Small Magellanic Cloud, as studied on quasars by Hopkins et al. (2004)⁷¹. Adjacent to equation 4.2, the observed flux:

$$F_{\text{obs}}^{\text{BBB}} = F_{\text{intr}}^{\text{BBB}} \times 10^{0.4A_\lambda} \quad (4.19)$$

and the attenuation law (equations 4.3 and 4.4) is modified accordingly¹¹⁴:

$$\begin{cases} A_\lambda = k_{\text{BBB}}(\lambda) E(\text{B-V})_{\text{BBB}} \\ k_{\text{BBB}}(\lambda) = -0.38 + 1.39 \times (10^{-4}\lambda)^{-1.2} \end{cases} \quad (4.20)$$

The Accretion disk models, have two free parameters: the reddening fraction, and a scaling factor that measures the accretion disk's amplitude (shown in Table 5.1).

4.6 AGN TORUS

In a galaxy hosting an active galactic nucleus, the AGN dust torus heated by the hard radiation from the accretion disk (which, in turn, is accreting onto a supermassive black hole) emits thermal radiation that contributes to the mid-infrared (MIR) spectral band and might, even, dominate the MIR emission over that produced by the diffuse dust and stellar component for luminous AGNs. The toroidal structure and dust composition stems from the unification model⁶.

The intense radiation emitted by the disk, due to the internal friction of the gas, is then absorbed by this dust which is heated to the highest possible temperatures (around 1000-1500 K) and is then re-emitted as thermal radiation in the 2-40 μm domain⁵⁰. The AGN torus is a dust structure⁵² and dynamical studies tend to favour⁴¹ a clumpy structure rather than a uniform torus (with dust "clumps" or clouds as shown in Figure 4.9).

Assuming a dust-cloud distribution where r is the radial coordinate, Hönig & Kishimoto (2010)⁷⁰ assert that a surface filling factor $\sigma_s(r)$ can be described by the dependence

$$\sigma_s(r) \propto r^{\alpha_{\text{clouds}}} \quad (4.21)$$

Consequently, the luminosity is calculated by multiplying the surface filling factor with the source function of the clouds $S_\nu(r)$ and integrating from the inner radius (sublimation radius) to the outer radius of the torus:

$$L_\nu^{\text{Torus}} = 2\pi \int_{r_{\text{sub}}}^{R_{\text{out}}} \sigma_s(r) S_\nu(r) r dr \quad (4.22)$$

4.6.1 TORUS MODEL & PARAMETERS

As explained above (Section 4.2, the dusty torus is the essential component to explain the orientation dependence on the unified model. There are some constraints for the torus that can be inferred from indirect evidence. A large number of torus models have been presented in the literature to explain the IR observations.

The CAT3D[‡] software, described in detail by Höning & Kishimoto (2010)⁷⁰, has been run by Markos Polkas to produce AGN torus templates which are scaled for each galaxy and used in the present thesis. These are radiative transfer models of three-dimensional clumpy dust tori using optically thick dust clouds and a low torus volume filling factor, and represent the accretion disk-powered infrared luminosity.

The diffuse radiation field in the torus is approximated by a statistical approach and there are three dust compositions and grain sizes: the standard ISM (47% graphites and 53% silicates), ISM large grains (grains between 0.1 and 1 μm in size), and Gr-dominated (dominated by intermediate to larger graphite grains, 70% graphites and 30% silicates).

The parameters of this library of SEDs are (schematically depicted in Figure 4.9):

- The viewing angle i
- The number of clouds along an equatorial line-of-sight N_0
- The radial dust-cloud distribution power-law index α_{clouds}
- The half-opening angle of the distribution of clouds θ_0

An additional parameter, as already noted, is a scaling factor that adjusts the SED amplitude for each galaxy. The optical depth τ_{clouds} of the individual clouds and the outer torus radius R_{out} in units of the sublimation radius r_{sub} are used in the CAT3D code to produce the SED templates. The sublimation radius forms the inner boundary of the dust distribution (inner torus radius) where the dust becomes too hot to survive. This library includes model SEDs in the 0.01 – 36000 μm wavelength range. Some indicative templates are plotted in Figure 4.10.

4.7 SYNCHROTRON RADIO EMISSION

At radio frequencies the emission is split between:

[‡]cat3d.sungrazer.org

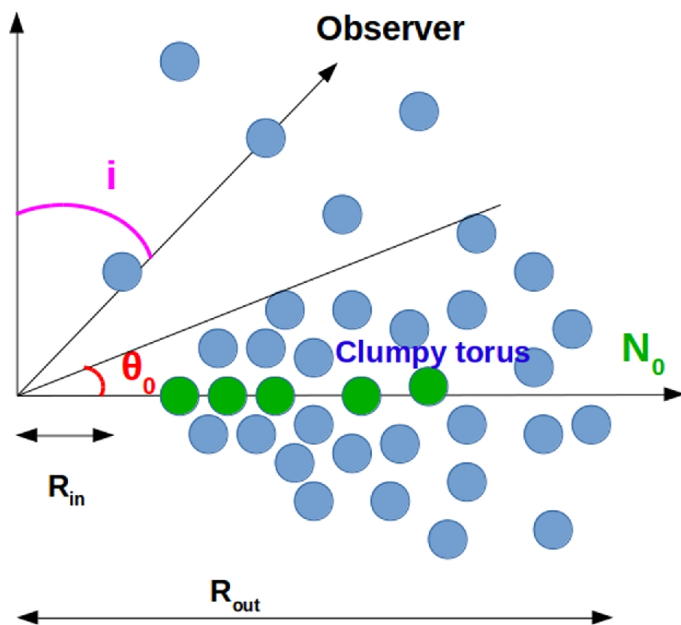


Figure 4.9: AGN clumpy torus cartoon plot. The origin represents the SMBH, the horizontal axis represents the plane of the torus, R_{in} and R_{out} are the inner and outer radius of the torus, R_{in} is essentially the sublimation radius. N_0 is the number of clouds along an equatorial line-of-sight, i is the inclination of the torus with respect to the observer and θ_0 is the half-angle that covers the torus from the equatorial plane. Image lifted from García-González et al. (2017)⁵²

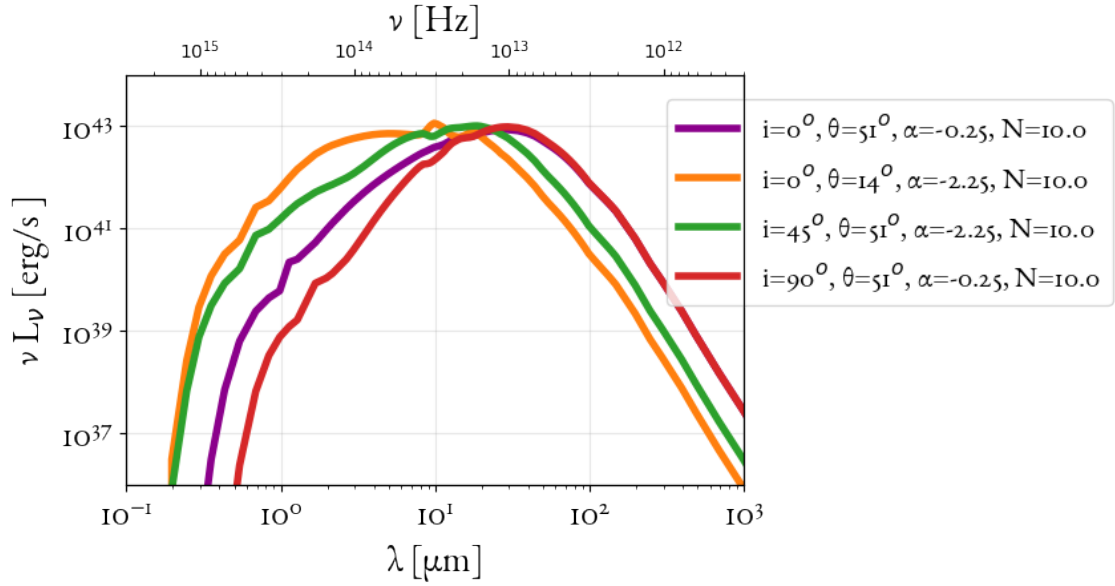


Figure 4.10: AGN torus emission templates generated by Markos Polkas using CAT3D⁷⁰.

Here plotted some indicative values of viewing angle i , half-covering angle of torus θ , spec-trar index of dust-cloud distribution α and number of clouds along an equatorial line-of-sight N , with the same amplitude scaling.

- Thermal processes: related to the ionisation of the gas by massive stars
- Non-thermal processes: related to the interaction of relativistic electrons from supernovae with local magnetic fields and free-free emission from HII regions, also synchrotron emission related to the supermassive black hole.

4.7.1 RADIO JET MODEL & PARAMETRES

The exact shape and intensity of the synchrotron spectrum depends on various parameters such as the strength of the magnetic field, the energy of the relativistic electrons propagating through it. Rather than attempting to model the synchrotron in such detail, the synchrotron component of the present code relies on a single power-law spectral slope with cutoff and on the assumption that between frequencies 10^8 Hz and 3×10^{10} Hz the spectrum is largely dominated by non-thermal (synchrotron) emission, which is ensured by design in the ARC survey. The

specific flux for the radio component is:

$$f_\nu^{\text{rad}} = A_{\text{rad}} \times \left(\frac{\nu}{10^9 \text{Hz}} \right)^{\alpha_{\text{rad}}} \times e^{-\nu/\nu_{\text{cutoff}}} \quad (4.23)$$

The model for the radio component of the SED is the analytic function of equation 4.23, where $\nu_{\text{cutoff}} = 10^{12}$ Hz, and the parametres are the spectral index α_{rad} and the scaling factor A_{rad} .

4.8 OTHER COMPONENTS

In order to construct an astrophysically sound spectral model for a galaxy, a nebular emission can be modelled (e.g. with photoionisation modeling such as the code CLOUDY⁴⁵). Since nebular emission does not contribute significantly to the continuum and only adds the spectral emission line features, in the present work it is omitted from the photometric SED models. A more complete model that can encompass different types of galaxies, could benefit from additional components, such as blazar emission model, hot corona X-ray emission, intergalactic medium (IGM), Lyman- α forest (LAF), Damped Lyman alpha (DLA) modeling and extend to joint models of morphology and SED.

Since the ARC survey contains many blazars, in the future, a model component for the blazar sequence ought to fortify and extend the SED modelling.

4.9 MODEL PHOTOMETRY

In order to model the observed photometry, the models described above can be projected into the data space with filter projections. In photometry, a filter band describes the response of the astronomical observation (composed of the atmosphere, telescope, instrument, and detector) to the light from the source. Therefore, it encapsulates the actual spectral information inherent in the corresponding photometry from the SED. The average flux through a filter band (and consequently the one used to calculate rest-frame luminosity of each SED data point) is

$$\langle F \rangle_b = \frac{\int R_\gamma^b f_\nu d\nu}{\int (\nu/\nu_b)^\beta R_\gamma^b d\nu} \quad (4.24)$$

where b denotes the band pass corresponding to the selected filter, f_ν is the observed flux, R_γ^b is the relative response of the filter b per photon (γ). The factor (ν/ν_b) in the denominator is for

calibration purposes, for UV, optical and near-IR $\beta = 0$, while for IR photometry $\beta = 1$ and some far-IR instruments adopt $\beta = 2$.

The transmission profiles $R_\gamma^b(\nu)$ (usually in units of relative response per photon) of many surveys' filters can be found at <http://svo2.cab.inta-csic.es/svo/theory/fps/>.

The aforementioned service couldn't provide the transmission curves for all band passes of the ARC SEDs, thus, in the present work, no filters were used, assuming $\langle F \rangle_b \approx f_{\langle \nu \rangle_b} \langle \nu \rangle_b$, where $\langle \nu \rangle_b$ is the dominant frequency of filter band b , effectively assuming monochromatic energy of the radiation for each SED point. In the future, a more diligent search for transmission curves and the corresponding application of those curves on the modelled SEDs would provide a more robust model photometry.

5

Probabilistic SED Fitting Algorithm

Probability calculus is the unique language within which models that have predictive capability can be developed. Probability calculus is uniquely defined¹³⁰ as the preferred language of inference. The SED fitting technique implemented in the present thesis is established on Bayesian statistics.

5.1 BAYESIAN FRAMEWORK

In Bayesian statistics, the knowledge concerning the relative probability of various parametre values Θ under the hypothesis \mathcal{H} in the absence of any data is encoded in the prior probability density distribution $\mathcal{P}_{\text{prior}}(\Theta|\mathcal{H})$ on the space of all possible parametres Θ . The probability of a particular value of Θ given a specific data set D under hypothesis \mathcal{H} is written as a posterior probability density function (according to Bayes' theorem) as:

$$\mathcal{P}_{\text{posterior}}(\Theta|D, \mathcal{H}) = \frac{\mathcal{P}_{\text{prior}}(\Theta|\mathcal{H}) \mathcal{L}(D|\Theta, \mathcal{H})}{\mathcal{E}(D|\mathcal{H})} \quad (5.1)$$

where $\mathcal{L}(D|\Theta, \mathcal{H})$ the probability of obtaining the new data under the assumption of a certain set of parametre values, and it is called the likelihood. The Bayesian evidence, or marginal likelihood $\mathcal{E}(D|\mathcal{H})$ is the probability of the hypothesis explaining the data. The hypothesis consists of the SED model parameterisation that encompasses the model components discussed

in Chapter 4. The posterior probability density function can be used to obtain a best estimate and credibility interval for any model property $Y(\Theta)$. The probability of the derived parameter $Y(\Theta)$ given the data is then

$$\mathcal{P}_{posterior}(Y|D) dY = \int_Y \mathcal{P}_{posterior}(\Theta|D) d\Theta \quad (5.2)$$

where the integral extends over all Θ for which Y lies in a specified bin $\pm dY/2$. The most probable value of Y can then be taken as the peak of this distribution and the most typical value as its median. The 95 per cent (symmetric) credibility interval of the distribution for scalar Y can be defined and yields the uncertainty. The parametre investigated in the present work is the total stellar mass of each galaxy, in order to construct the stellar mass function. More details regarding Bayesian methods can be found on Appendix B.

5.2 PARAMETRE SPACE, LIKELIHOOD & PRIORS

The parametre space describing the total galaxy emission is 21-dimensional, as given by the number of parameters listed in Table 5.1. It is composed by two different types of parametres: shape parameters, which determine the shape of the templates and hence represent non-linear dependencies, and amplitude parameters, on which the model depends linearly and which scale the contribution strength of each component. The ranges that we assume for each parametre are listed in the fourth column of Table 5.1.

As shown in Table 5.1, two composite stellar population models of delayed exponential decay SFH are used, differing in age, so that a more complex SFH function could be modeled. Hereby called Old Stellar Population and Young Stellar Population, the Old Stellar Population models a delayed exponential decay SFH that started between the Big Bang (age of the universe at galaxy's redshift) and 1 Gyr ago and the Young Stellar Population models a delayed exponential decay SFH that started between 1 Gyr and 1 Myr ago. The stellar mass of both stellar populations is fit and both are taken into account for the inference of galaxy stellar mass.

5.2.1 LIKELIHOOD

The model photometry of each component, with the according parametres (as shown in Table 5.1) will be represented as:

- $\text{ModelPhot}_{\text{old stellar}}(Z_o, t_o, \tau_o, \log M_{*,o}, EBV_o)$

Table 5.1: Parametres used for modelling the ARC SEDs. The parametre and its description are in the second and third columns, respectively. The galaxy component to which they appertain is listed in the first column, the range of values and the shape of the prior distribution are listed in the fourth and fifth column.

Component	Parametre	Description	Range	Prior
Old Stars	M_*/M_\odot	Stellar Mass	$[10^7, 10^{15}]$	logUniform
	Z_*/Z_\odot	Metallicity	$[0, 5]$	Uniform
	t/Myrs	age of CSP	$[1000, \text{Age of Universe at } z]$	logUniform
	τ/Gyrs	Stellar Metallicity	$[0.01, 14]$	logUniform
	E(B-V)	color excess	$[0, 1]$	Uniform
Young Stars	M_*/M_\odot	Stellar Mass	$[10^7, 10^{15}]$	logUniform
	Z_*/Z_\odot	Metallicity	$[0, 5]$	Uniform
	t/Myrs	age of CSP	$[1, 1000]$	logUniform
	τ/Gyrs	Stellar Metallicity	$[0.01, 14]$	logUniform
	E(B-V)	color excess	$[0, 1]$	Uniform
ISM dust	M_{dust}/M_\odot	dust Mass	$[10^0, 10^{20}]$	logUniform
	α_{SF}	dust index	$[0, 4.5]$	Uniform
BBB	A_{BBB}	BBB amplitude	$[10^{-10}, 10^5]$	logUniform
	$E(\text{B-V})_{\text{BBB}}$	reddening	$[0, 1]$	Uniform
AGN torus	A_{AGN}	AGN amplitude	$[10^{-10}, 10^8]$	logUniform
	i_{view}	inclination from observer	$[0^\circ, 90^\circ]$	Uniform
	θ_{clouds}	half opening angle	$[14^\circ, 51^\circ]$	Uniform
	$N_{\text{o,AGN}}$	equatorial number of clouds	$[5, 10]$	Uniform
	α_{AGN}	powerlaw index	$[-2.25, -0.25]$	Uniform
radio	A_{radio}	synchrotron amplitude	$[10^{13}, 10^{60}]$	logUniform
	α_{radio}	spectral index	$[-3, 3]$	Uniform

- $\text{ModelPhot}_{\text{young stellar}}(Z_y, t_y, \tau_y, \log M_{\star,y}, EBV_y)$
- $\text{ModelPhot}_{\text{ISM dust}}(\alpha_{\text{SF}}, \log M_{\text{dust}})$
- $\text{ModelPhot}_{\text{BBB}}(A_{\text{BBB}}, EBV_{\text{BBB}})$
- $\text{ModelPhot}_{\text{AGN torus}}(A_{\text{AGN}}, i_{\text{view}}, \theta_{\text{clouds}}, N_{\text{o,AGN}}, \alpha_{\text{AGN}})$
- $\text{ModelPhot}_{\text{radio}}(A_{\text{radio}}, \alpha_{\text{radio}})$

The total SED model photometry is the following linear combination of each component:

$$\begin{aligned}
\text{ModelSEDphot} & \left(Z_o, t_o, \tau_o, \log M_{\star,o}, EBV_o, Z_y, t_y, \tau_y, \log M_{\star,y}, EBV_y, \alpha_{\text{SF}}, \log M_{\text{dust}}, \right. \\
& \quad \left. A_{\text{BBB}}, EBV_{\text{BBB}}, A_{\text{AGN}}, i_{\text{view}}, \theta_{\text{clouds}}, N_{\text{o,AGN}}, \alpha_{\text{AGN}}, A_{\text{radio}}, \alpha_{\text{radio}} \right) = \\
& = \text{ModelPhot}_{\text{old stellar}}(Z_o, t_o, \tau_o, \log M_{\star,o}, EBV_o) + \\
& + \text{ModelPhot}_{\text{young stellar}}(Z_y, t_y, \tau_y, \log M_{\star,y}, EBV_y) + \\
& + \text{ModelPhot}_{\text{ISM dust}}(\alpha_{\text{SF}}, \log M_{\text{dust}}) + \\
& + \text{ModelPhot}_{\text{BBB}}(A_{\text{BBB}}, EBV_{\text{BBB}}) + \\
& + \text{ModelPhot}_{\text{AGN torus}}(A_{\text{AGN}}, i_{\text{view}}, \theta_{\text{clouds}}, N_{\text{o,AGN}}, \alpha_{\text{AGN}}) + \\
& + \text{ModelPhot}_{\text{radio}}(A_{\text{radio}}, \alpha_{\text{radio}})
\end{aligned} \tag{5.3}$$

The parametres used (shown in Table 5.1) can be denoted as Θ for illustration purposes, that is:

$$\begin{aligned}
\Theta & = (Z_o, t_o, \tau_o, \log M_{\star,o}, EBV_o, Z_y, t_y, \tau_y, \log M_{\star,y}, EBV_y, \alpha_{\text{SF}}, \log M_{\text{dust}}, \\
& \quad A_{\text{BBB}}, EBV_{\text{BBB}}, A_{\text{radio}}, \alpha_{\text{radio}}, A_{\text{AGN}}, i_{\text{view}}, \theta_{\text{clouds}}, N_{\text{o,AGN}}, \alpha_{\text{AGN}})
\end{aligned} \tag{5.4}$$

In this brief notation the total model photometry of equation 5.3 can be represented as:

$$\begin{aligned}
\text{ModelSEDphot} & \left(Z_o, t_o, \tau_o, \log M_{\star,o}, EBV_o, Z_y, t_y, \tau_y, \log M_{\star,y}, EBV_y, \alpha_{\text{SF}}, \log M_{\text{dust}}, \right. \\
& \quad \left. A_{\text{BBB}}, EBV_{\text{BBB}}, A_{\text{AGN}}, i_{\text{view}}, \theta_{\text{clouds}}, N_{\text{o,AGN}}, \alpha_{\text{AGN}}, A_{\text{radio}}, \alpha_{\text{radio}} \right) = \\
& = \text{ModelSEDphot}(\Theta)
\end{aligned} \tag{5.5}$$

The likelihood can also be written in this brief notation:

$$\begin{aligned} \mathcal{L}(D|\Theta) &= \mathcal{L}(D|Z_o, t_o, \tau_o, \log M_{\star,o}, EBV_o, Z_y, t_y, \tau_y, \log M_{\star,y}, EBV_y, \alpha_{SF}, \log M_{dust}, \\ &\quad A_{BBB}, EBV_{BBB}, A_{radio}, \alpha_{radio}, A_{AGN}, i_{view}, \theta_{clouds}, N_{o,AGN}, \alpha_{AGN}) \iff \\ \iff \ln \mathcal{L}(D|\Theta) &= \ln \mathcal{L}(D|Z_o, t_o, \tau_o, \log M_{\star,o}, EBV_o, Z_y, t_y, \tau_y, \log M_{\star,y}, EBV_y, \alpha_{SF}, \log M_{dust}, \\ &\quad A_{BBB}, EBV_{BBB}, A_{radio}, \alpha_{radio}, A_{AGN}, i_{view}, \theta_{clouds}, N_{o,AGN}, \alpha_{AGN}) \end{aligned} \quad (5.6)$$

The likelihood function assumes Gaussian uncertainties, thus, for N number of SED photometry data points:

$$\mathcal{L}(D|\Theta) = \frac{1}{\sigma_i \sqrt{2\pi}} \exp \sum_{i=1}^N \frac{[ModelSEDphot_i(\Theta) - ObsPhot_i]^2}{2\sigma_i^2} \quad (5.7)$$

where i counts the SED data points, N is the total number of SED data points (observations), $ModelSEDphot_i$ is the modelled SED of the i -th data point as described in Chapter 4, $ObsPhot_i$ is the i -th observed SED data point for each galaxy and σ_i is the measurement uncertainty for i -th data point.

The basic ln-likelihood calculation is effectively a χ^2 calculation for the photometric data. This gives the following expression for the ln-likelihood:

$$\ln \mathcal{L}(D|\Theta) = \sum_{i=1}^N \frac{[ModelSEDphot_i(\Theta) - ObsPhot_i]^2}{2\sigma_i^2} - \frac{1}{2} \ln (2\pi\sigma_i^2) \quad (5.8)$$

By default, known and independent Gaussian flux uncertainties are assumed. Under this assumption, the ln-likelihood for the photometric terms is simply χ^2 . More complex noise models can be applied in order to adjust a variety of instrumental artifacts or to allow for properties of the noise itself to be inferred, or for the presence of correlated noise to be modeled. This can be accomplished through a flexible noise covariance matrix construction. The ln-likelihood for the more complex noise model is

$$\ln \mathcal{L}(D|\vec{\Theta}) = -\frac{1}{2} \left[n_i \mathbf{C}_{ij}^{-1}(\vec{\gamma}) n_j + \ln \|2\pi\mathbf{C}(\vec{\gamma})\| \right] \quad (5.9)$$

where $\vec{\Theta}$ represents the total parameters of the SED model n_i is the noise model, \mathbf{C} is the correlation matrix (identity matrix in case of Gaussian noise, diagonal matrix in case of stationary noise) and $\vec{\gamma}$ are the parameters which model the noise:

$$n_i = \text{ObsPhot}_i - \text{ModelSEDphot}_i(\vec{\Theta}) \quad (5.10)$$

5.2.2 PRIORS

In Bayesian inference the prior model provides a valuable opportunity to incorporate astrophysical knowledge into the inferences. Every parameter specified in the construction of the full SED model, as described in Chapter 4, can be fit using the code. When fitting a parameter, a prior probability distribution is specified, consisting of an upper and lower limit on the parameter value, and a functional form for the prior probability density between these limits. As shown in Table 5.1, the priors used are Uniform or logarithmic Uniform priors. The parameters of the components synthesising the SED spectrum of a galaxy have a large dynamic range, thus, a uniform prior in log space is chosen for the parameters that span many orders of magnitude.

The conjugate prior to a Gaussian likelihood is the Dirichlet distribution, which mostly resembles the Uniform distribution, and since Gaussian likelihoods are used for every SED model component, a case can be made¹⁵ in favour of Dirichlet priors for computational efficiency. Although the work presented here has made use of the aforementioned priors in Table 5.1.

CONDITIONS AS NON-LINEAR PRIORS

In order to impose a condition based on astrophysical knowledge or an observational constraint it is possible in principle to specify joint priors on several parameters or achieve those conditions through parameter transformations. In the present work the energy balance of ISM dust absorption and re-emission or AGN dusty torus absorption and re-emission is imposed. Those conditions function as non-linear priors and can play a central role in determining the shape of the posterior probability distribution in the often highly degenerate space of SED modeling. The BBB emission upper limit discussed in Section 3.3 as a proxy of the AGN fraction of the ARC sources, is also a non linear prior that can be used in a version of the code, although it is not implemented for the runs presented in the present thesis, since a more scrutinous curation of the Hubble Space Telescope data and, consequently, selection of accretion disk upper limits is due.

5.3 SAMPLING METHOD, OPTIMISATION & IMPLEMENTATION

The sampling method chosen is the dynamic nested sampling which allows for efficient exploration of higher-dimensional, multimodal and highly degenerate parameter spaces¹³¹. This is invaluable in many circumstances relevant to spectral fitting, notably when dealing solely with broad band photometric observations, where the age-metallicity-dust degeneracy often leads to poorly constrained and highly degenerate parameter estimates, several widely spaced local minima in parameter space, any of which can trap traditional numerical functional minimisation routines or Markov Chain Monte Carlo (MCMC) methods.

5.3.1 DYNAMIC NESTED SAMPLING

Nested sampling¹³¹ is a Monte Carlo algorithm based on successive draws from the prior distribution at increasing values of the likelihood. It uses²² the change in the effective prior volume of isolikelihood contours as a function of likelihood to estimate the Bayesian evidence (\mathcal{E} in equation 5.1). The successive draws (cornered "live points"), along with their associated weights, give a direct estimate of the density of states and can be used to estimate the posterior distribution of the parameters as a by-product.

Because of the way the prior volume is sampled, nested sampling is well suited to posteriors that are multimodal. Furthermore, no optimisation is required before sampling begins, and stopping criteria based on estimates of the remaining evidence can be defined. Posterior samples from nested sampling approximate the true posterior for continuous and discontinuous functions, respectively²⁰.

Dynamic Nested Sampling is a modification of the nested sampling algorithm by dynamically varying the number of live points in order to maximise the accuracy of a calculation for some number of posterior samples, subject to practical constraints. Compared to standard nested sampling, dynamic nested sampling is particularly effective for parameter estimation because standard nested sampling typically spends most of its computational effort iterating towards the posterior peak. This produces posterior samples with negligible weights which make little contribution to parameter estimation calculations. Dynamic nested sampling, also, significantly improves⁶⁴ the accuracy of evidence calculations, and shows both evidence and parameter estimation can be improved simultaneously.

5.3.2 SOFTWARE & OPTIMAL SAMPLING

The sampling software used as the main tool of the SED fitting algorithm of the present thesis is the `UltraNest`* package, developed by Johannes Buchner (2021)²³ which uses the Nested Sampling algorithm MLFriends described in the work of Buchner (2016, 2019)^{20 21}.

The `UltraNest` code uses Reactive Nested Sampling, which is a generalisation of the Dynamic Nested Sampling that uses a tree structure for adding live points. The root of the tree represents the entire prior volume, and the branch nodes are samples from the entire prior. The tree formulation of Reactive Nested Sampling makes implementing error propagation and variable number of live points unambiguous.

SLICE SAMPLING

For problems with high dimensionality or many degeneracies, the computational efficiency is low. This can be overcome by using several types of Monte Carlo random walks supported by the `UltraNest` software. Nested Sampling with Slice Sampler⁵⁹ utilises slice sampling at each iteration to sample within the hard likelihood constraint of nested sampling. It can identify and evolve separate modes of a posterior semi-independently.

5.4 TESTING THE ALGORITHM ON SYNTHETIC DATA

In order to ensure that the SED fitting procedure produces reliable results, extensive tests were performed. At first, each model component is tested, followed by generating a synthetic galaxy SED and fitting all components in aggregate.

The number of the `UltraNest` sampler live points in every run of this work is set to 800. A finer sampling of parameter space can be achieved by increasing the number of live points to higher value (e.g. 3000 live points). This will increase the reliability of the maximum likelihood values obtained, though the time to perform a fit will become longer.

*<https://johannesbuchner.github.io/UltraNest/>

INDIVIDUAL COMPONENT FITS

The Reactive Nested Sampling with Slice Sampler is benchmarked against the pure Reactive Nested Sampling as shown in Figure 5.1. The differences are minimal, thus, the Reactive Nested Sampling with Slice Sampler is the chosen sampling method of the Bayesian SED fitting algorithm of this thesis, since it reduced the time for fitting an all-component SED model to an observed ARC galaxy SED from ~ 2 hours to ~ 20 minutes. Solely the models for the stellar population, ISM dust, accretion disk and AGN dusty torus are shown, since they are the ones that are involved in the conditional priors, are the root of the degeneracies and have a direct impact on the Stellar Mass inference (which is a parameter of the stellar population model). Furthermore, they are of interest since the models used are based on templates, instead of analytic functions.

Each component is fit and residuals are plotted in Figure 5.2, clearly delineating that most sampled fits differ from the true (synthetic) values less than 1%.

MOCK GALAXY FITS

Mock galaxy SEDs are generated by intentionally combining model parameters with known physical properties and parameters, then adding Gaussian noise (in base-ten logarithmic scale). When fit with the algorithm, the posterior is plotted in Figure 5.3, ascertaining the fit converged, 20 SEDs that correspond to the parameters of the 20 samples with the highest posterior value are plotted in Figure 5.4, along with the synthetic data. The residuals indicate a remarkably high accuracy.

5.5 FITTING SED MODELS TO DATA

44 ARC galaxies are fit reliably using the code developed in this thesis. The sources that are explicitly labeled as blazars from the team of Audibert et al.⁸ are excluded from the fit, while a converging sampling for the posterior distribution is a prerequisite for accepting the sampled fit. The most important factor impeding the algorithm to fit more galaxies is the absence of a blazar component, which can be improved in the future.

In Appendix C each of the 44 ARC galaxies' mapped posterior distribution histogram is plotted in full scale and in the concentration region, verifying that each fit converged.

In Appendix D each of the 44 ARC galaxies' sampled mass of young stellar population and old stellar population histograms are plotted clearly demarcating the median sampled value,

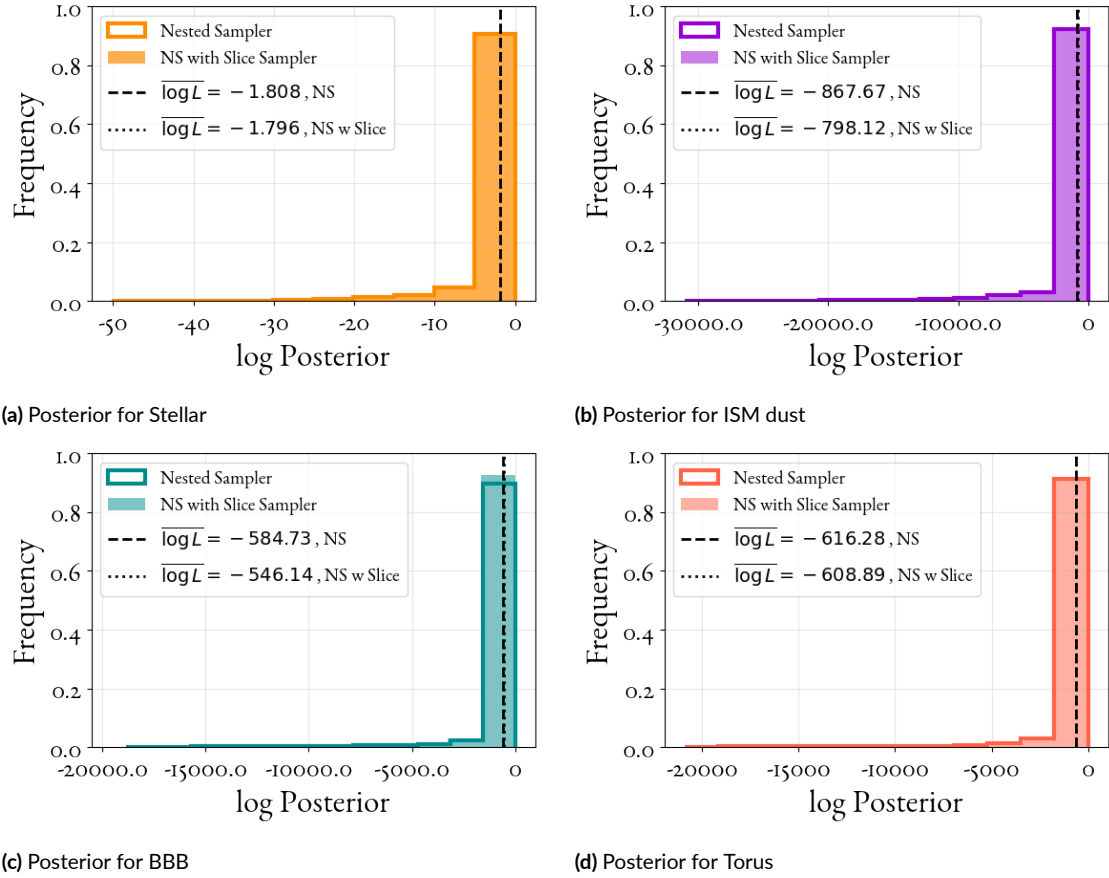


Figure 5.1: Posterior distributions sampled by fitting a single component model to synthetic data from the same component. Panel (a): Stellar Population component posterior Panel (b): ISM dust component posterior. Panel (c): Accretion disk component posterior. Panel (d): AGN torus component posterior.

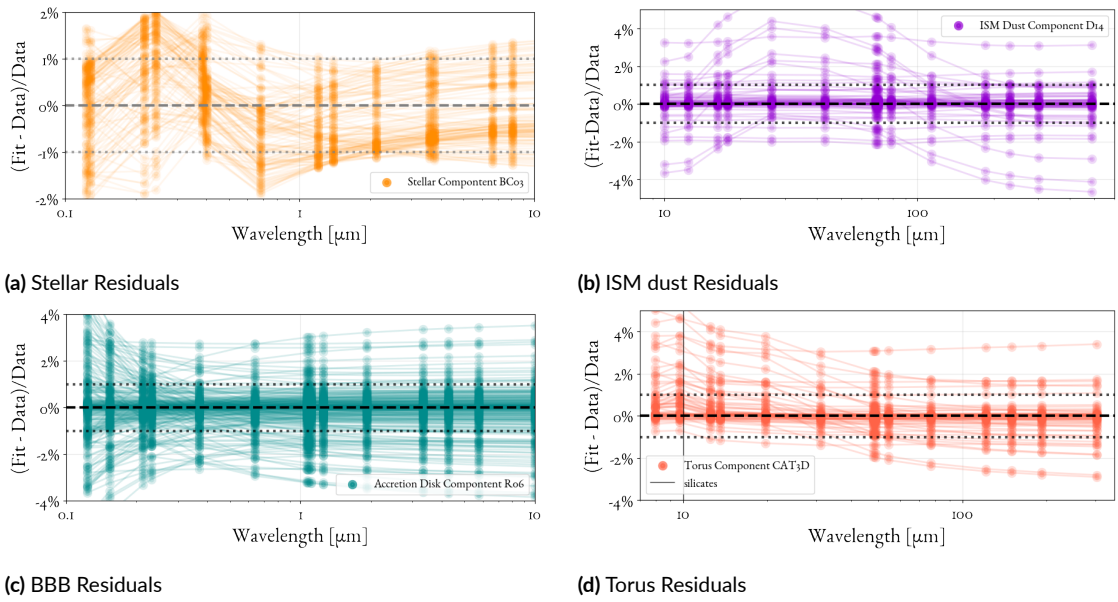


Figure 5.2: Component Residuals.

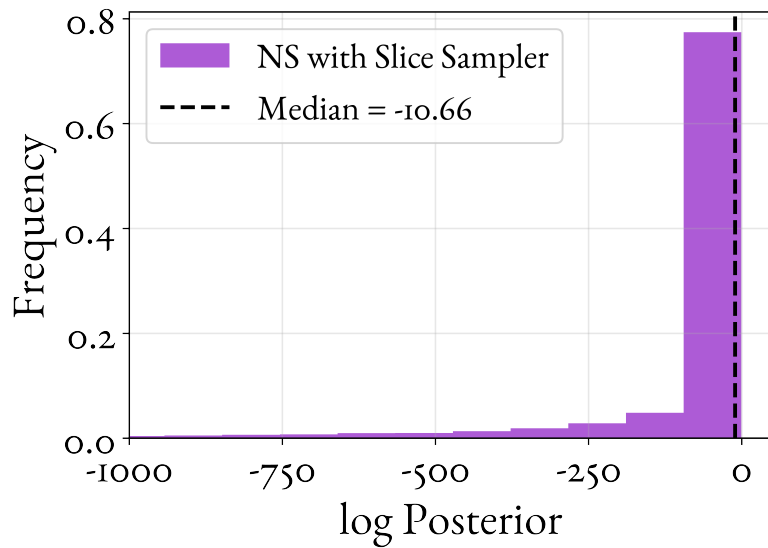


Figure 5.3: Posterior distribution of a full SED fit of a Mock galaxy.

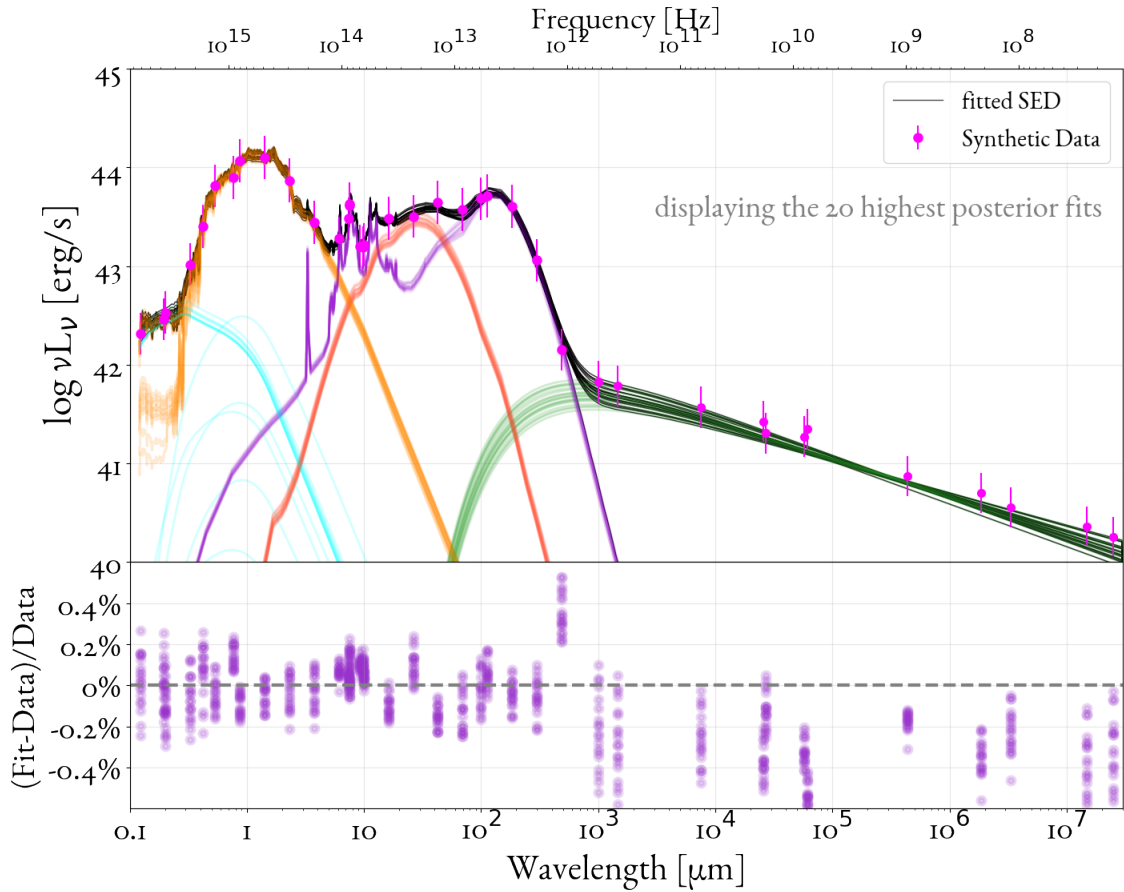


Figure 5.4: SED model fit for synthetic data with logarithmic-Gaussian noise, representing a mock galaxy. The 20 highest posterior fits are plotted along with the synthetic data and each component is highlighted with color.

the 16th and the 84th percentile of the sampled values, which are the credibility interval for the mass estimation. The masses are inferred in logarithmic scale, and the total inferred mass is

$$M_{\star,\text{tot}} = 10^{\mathcal{M}_{\star,\text{old}}} M_{\odot} + 10^{\mathcal{M}_{\star,\text{young}}} M_{\odot}$$

where

$$\begin{cases} \mathcal{M}_{\star,\text{old}} = \log_{10} M_{\star,\text{old}} \\ \mathcal{M}_{\star,\text{young}} = \log_{10} M_{\star,\text{young}} \end{cases}$$

In Appendix E each of the 44 ARC galaxies' SED is plotted with the fit SED models which correspond to 1% highest values of the sampled posterior distribution (posterior samples larger than the 99th posterior percentile), along with the residuals, while the median total stellar mass inferred is denoted. Four indicative fit galaxies are shown in Figures 5.5 and 5.6. All SEDs are portrayed in each galaxy's restframe. For most galaxies the fitted model is representative of the data, with the residuals in less than 2%.

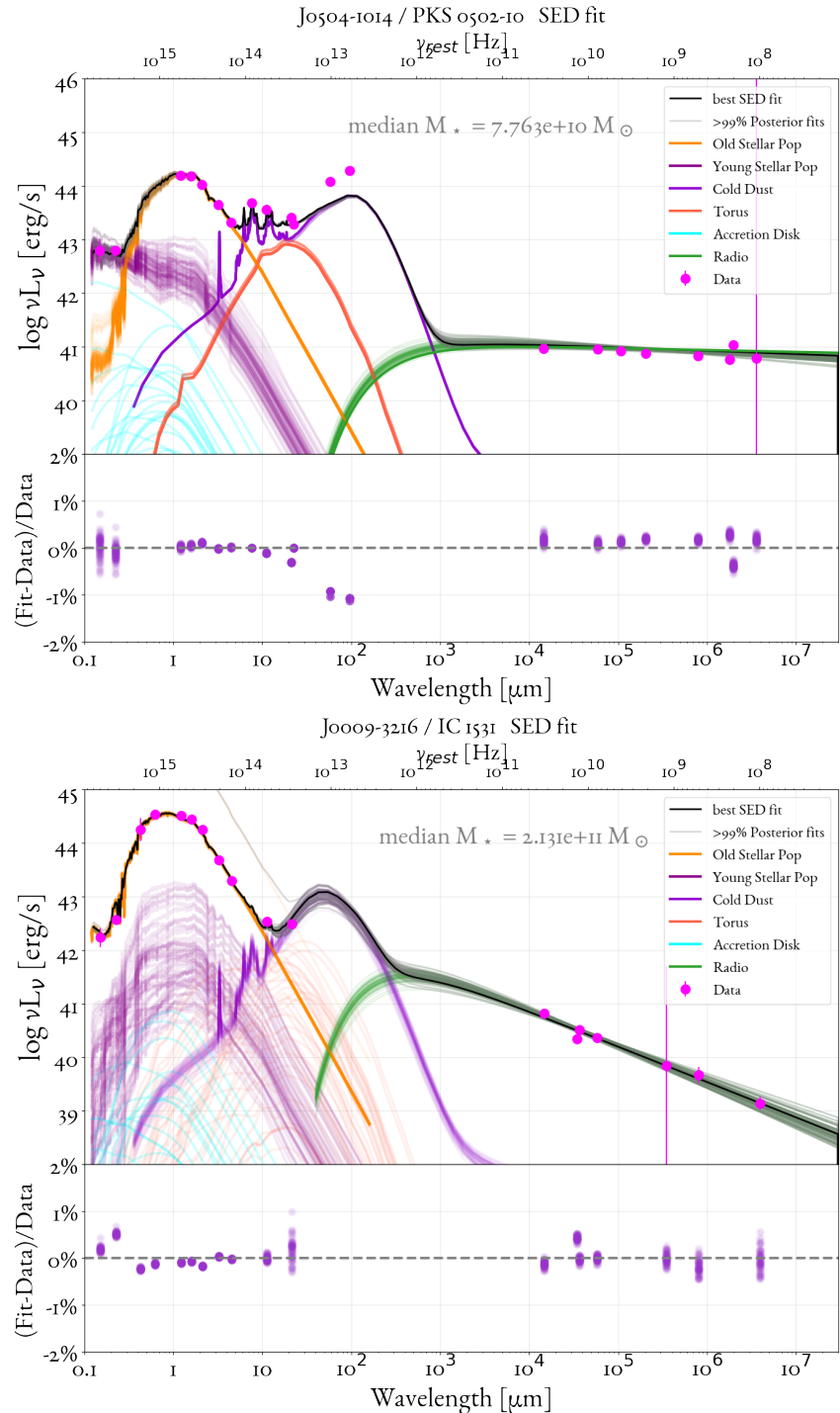


Figure 5.5: SED fit for The ARC galaxies J0504-1014 and J0009-3216. Plots of the SED fit for all the 44 ARC sources can be found in Appendix E.

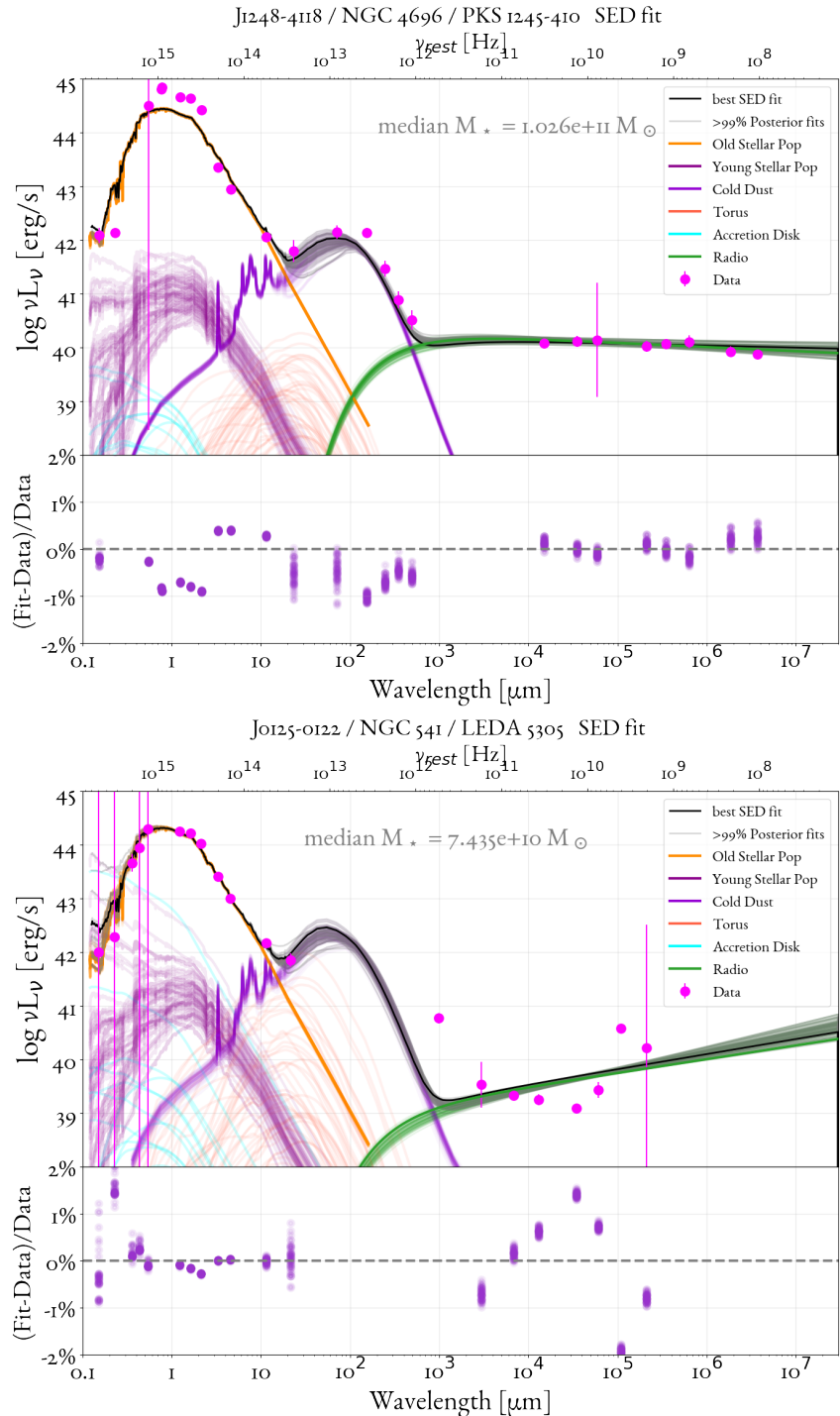


Figure 5.6: SED fit for The ARC galaxies NGC 4696 and NGC 541. Plots of the SED fit for all the 44 ARC sources can be found in Appendix E.

6

Results

6.1 ARC STELLAR MASS

In Figure 6.1 the inferred stellar masses for each galaxy are plotted with the redshift (and look-back time). The sample fit and plotted concerns 44 of the total 120 ARC galaxies making it $\sim 36.7\%$ of the full ARC survey.

Both the median sampled value and maximum posterior value of total stellar mass are plotted for comparison of the sampling results, although the median value is used for science and the uncertainties are half of the (84th-16th) percentile range, as state-of-the-art practice⁸⁶.

As shown in Figure 6.1, for the redshift range of $0 < z < 0.3$ the median galaxy stellar mass is estimated at $1.03 \times 10^{11} M_{\odot}$ and the maximum galaxy stellar mass is estimated at $7.64 \times 10^{11} M_{\odot}$, while at higher redshifts ($z > 1.0$) the median stellar mass is found to be higher at $6.47 \times 10^{11} M_{\odot}$ with the maximum being $1.38 \times 10^{13} M_{\odot}$. This is reasonable, since at higher redshift galaxies with lower stellar mass can be too faint for detection, while the most massive ones can be more easy to observe.

6.2 ARC GAS MASS TO STELLAR MASS RATIO

The molecular hydrogen (H_2) mass, probed by carbon monoxide (CO) gas emission all galaxies in the ARC survey has been calculated by the team of Audibert et al. (2022)⁸. The gas mass-

to-stellar mass ratio has been plotted in Figure 6.2 for the 44-ARC sample. The plotted line is adapted from the work of Genzel et al. (2015)⁵⁴ and it represents the main sequence galaxies.

6.3 ARC STELLAR MASS FUNCTION

There are two main ways to estimate the stellar mass function for a complete galaxy sample⁸⁶, the first one is the $1/V_{\max}$ method, introduced by Schmidt (1968)¹²⁹ and refined by Avni & Bahcall (1980)⁹ which calculates the number density of galaxies in bins of stellar mass with

$$\Phi_j = \frac{1}{\Delta \log M_{\star j}} \sum_{i=1}^N \frac{1}{V_{\max}} \quad (6.1)$$

where Φ_j is the number density of galaxies in bin j , $\Delta \log M_{\star j}$ is the width in logarithmic scale of bin j , N is the number of sources inside the bin and V_{\max} is the maximum comoving volume out to which these objects could be detected at the survey's limit. The second approach to estimate the stellar mass function is introduced by Sandage et al. (1979)¹²⁵ and is a parametric maximum likelihood estimator that typically assumes the functional form of a Schechter¹²⁸ function. The double Schechter function has the following form:

$$\Phi(\mathcal{M}) = \ln(10) \times 10^{(\mathcal{M}-\mathcal{M}^*)} \times \left[\phi_1^* 10^{\alpha_1(\mathcal{M}-\mathcal{M}^*)} + \phi_2^* 10^{\alpha_2(\mathcal{M}-\mathcal{M}^*)} \right] \times e^{-[-10^{(\mathcal{M}-\mathcal{M}^*)}]} \quad (6.2)$$

where $\mathcal{M} = \log(M/M_{\odot})$, $\mathcal{M}^* = \log(M^*/M_{\odot})$. The Schechter coefficients ϕ_1^* , ϕ_2^* are explicitly related⁸⁹ to the Star Formation Rate, the Schechter parameters α_1 , α_2 , \mathcal{M}^* are explicitly related⁸⁹ to the redshift evolution.

6.3.1 MAXIMUM VOLUME

The V_{\max} in equation 6.1 represents the maximum volume at which a source is detectable within the framework of the ARC survey.

CALCULATING THE MAXIMUM COMOVING DISTANCE FOR A SOURCE

As shown in equation 2.9: $D_L = (1 + z) D_{\text{com}}$

And from the definition of redshift:

$$\nu_{\text{obs}} = \frac{\nu_{\text{emitted, restframe}}}{1 + z_{\text{source}}} \quad (6.3)$$

Virtually redshifting an isotropic source to z_{limit} , the observed photons at frequency $\nu_{\text{limit}} = 1.4\text{GHz}$ were emitted at frequency $\nu_{\text{limit}} = (1 + z_{\text{limit}}) \times 1.4\text{GHz}$, the same holds for the observed redshift of the source, thus:

$$\begin{aligned} & \left\{ \begin{array}{l} L_{\text{bolom}} \Big|_{\text{observed}} = L_{\nu}((1 + z_{\text{source}})1.4\text{GHz}) \times (1 + z_{\text{source}})1.4\text{GHz} \\ L_{\text{bolom}} \Big|_{\text{limit}} = L_{\nu}((1 + z_{\text{limit}})1.4\text{GHz}) \times (1 + z_{\text{limit}})1.4\text{GHz} \end{array} \right. \xrightarrow{2.8} \\ & \xrightarrow{2.8} \left\{ \begin{array}{l} L_{\text{bolom}} \Big|_{\text{observed}} = f_{\nu, \text{obs}}(1.4\text{GHz}) \times (1.4\text{GHz}) \times 4\pi \times D_L^2(z_{\text{source}}) \\ L_{\text{bolom}} \Big|_{\text{limit}} = f_{\nu, \text{limit}}(1.4\text{GHz}) \times (1.4\text{GHz}) \times 4\pi \times D_L^2(z_{\text{limit}}) \end{array} \right. \end{aligned}$$

And since the bolometric luminosity of the source on its current redshift should be the same as its bolometric luminosity on the limit redshift (since there is no Doppler redshift from relativistic motion), the following is an identity:

$$\begin{aligned} & L_{\text{bolom}} \Big|_{\text{observed}} = L_{\text{bolom}} \Big|_{\text{limit}} \Rightarrow \\ & f_{\nu, \text{obs}}(1.4\text{GHz}) \times D_L^2(z_{\text{source}}) = f_{\nu, \text{limit}}(1.4\text{GHz}) \times D_L^2(z_{\text{limit}}) \xrightarrow{2.9} \\ & \xrightarrow{2.8} (1 + z_{\text{limit}})^2 \times D_{\text{com}}^2(z_{\text{limit}}) = \frac{f_{\nu, \text{obs}}(1.4\text{GHz})}{f_{\nu, \text{limit}}(1.4\text{GHz})} \times (1 + z_{\text{source}})^2 \times D_{\text{com}}^2(z_{\text{source}}) \end{aligned} \quad (6.4)$$

In equation 6.4, the right-hand-side is comprised entirely by known quantities:

- z_{source} is the spectroscopic redshift of each galaxy
- $f_{\nu, \text{obs}}(1.4\text{GHz})$ is the observed flux at 1.4GHz of each galaxy (bound to be greater or equal to 0.4Jy, as a selection criterion of the ARC survey)

- $f_{v, \text{limit}}(1.4\text{GHz})$ is the limit flux at 1.4GHz, which is equal to 0.4Jy, for a galaxy to be marginally part of the ARC survey.

Solving the equation 6.4 for z_{limit} , it is trivial to calculate the limit comoving distance $D_{\text{com}}(z_{\text{limit}})$.

CALCULATING THE MAXIMUM VOLUME FOR A SOURCE

As discussed in section 2.3.2, the transverse comoving distance for a flat Universe is equal to the radial one $D_{\text{com, transv}} = D_{\text{com}}$.

The total volume of the solid angle layer spanned when virtually moving a galaxy from z_{source} to z_{limit} is

$$\begin{aligned} V_{s \rightarrow \text{lim}} &= V_{\text{lim}} - V_s = \\ &= \frac{4\pi}{3} \times [D_{\text{com}}^3(z_{\text{limit}}) - D_{\text{com}}^3(z_{\text{source}})] \end{aligned} \quad (6.5)$$

The effective FOV of an ARC galaxy spans a solid angle $\Omega_{\text{eff, ARC}} = 67\text{arcmin}^2 \approx 5.669 \times 10^{-6}$ steradian (as discussed in Section 3.1), thus the maximum comoving volume spanned by the FOV of an ARC galaxy is

$$\begin{aligned} V_{\text{max}} &= \frac{\Omega_{\text{eff, ARC}}}{4\pi} \times \frac{4\pi}{3} \times [D_{\text{com}}^3(z_{\text{limit}}) - D_{\text{com}}^3(z_{\text{source}})] = \\ &= \frac{\Omega_{\text{eff, ARC}}}{3} \times [D_{\text{com}}^3(z_{\text{limit}}) - D_{\text{com}}^3(z_{\text{source}})] = \\ &= \frac{5.669 \times 10^{-6}}{3} \times [D_{\text{com}}^3(z_{\text{limit}}) - D_{\text{com}}^3(z_{\text{source}})] \end{aligned} \quad (6.6)$$

In Tables 6.1 and 6.2 the measured flux at 1.4 GHz (in units of Jansky) for each of the 44 sources is shown in the second column, the limit case redshift is shown on the fourth column for each source, the comoving volume through the FOV at the source in units of Mpc^3 is shown in the fifth column and the comoving volume through the FOV at the limit of each source in units of Mpc^3 is shown in the sixth column, according to the above calculations.

6.3.2 COMPLETENESS

Estimating the Stellar Mass Function (which encompasses galaxy densities) is complicated by the presence of observational selection effects, for example due to detection thresholds. Statistical tools and techniques have been developed to identify, characterise and correct or remove the impact of observational selection effects from galaxy surveys.

Completeness corrections, as well as corrections for effects of statistical cosmology are needed so that the galaxy number density can be more representative of the complete Universe.

In the present work the completeness treatment follows closely the regime of Audibert et al. (2022)⁸, since in their work the CO luminosity function (which also encompasses galaxy densities) of ARC radiogalaxies for different redshifts is examined.

NVSS COMPLETENESS CORRECTION

Equation 6.1 holds for complete samples of galaxies. The ARC survey (as discussed in Section 3.1) has been built as representative of a "parent" survey, that is the NVSS survey. The reason for it is so that the analysis performed on the ARC sources can be projected on a larger sample of galaxies and probe the galaxy number density of a sample more representative of a complete survey.

In order to estimate the stellar mass function the $1/V_{\max}$ method is adopted here and, for the purposes of completing the ARC survey with respect to the NVSS survey, equation 6.1 is modified to

$$\Phi_j = \frac{1}{\Delta \log M_{*j}} \sum_{i=1}^N \frac{\omega(\delta z)}{V_{\max}} \quad (6.7)$$

where $\omega(\delta z)$ is a weight corresponding to the completeness correction with respect to the NVSS survey, that is:

$$\omega(\delta z) = \frac{\text{Number of NVSS sources with } z \text{ in } \delta z \text{ slice per sterad}}{\text{Number of ARC sources with } z \text{ in } \delta z \text{ slice per sterad}} = \frac{\frac{N_{\text{NVSS}}(\delta z)}{\Omega_{\text{NVSS}}}}{\frac{N_{\text{ARC}}(\delta z)}{\Omega_{\text{eff,ARC}}}} \quad (6.8)$$

where $\Omega_{\text{eff,ARC}}$ is the ARC survey's effective field of view (as discussed in Section 3.1), Ω_{NVSS} is the NVSS survey's coverage of the celestial sphere, $N_{\text{ARC}}(\delta z)$ is the total number of ARC sources in a redshift region δz and $N_{\text{NVSS}}(\delta z)$ is the number of NVSS sources with spectroscopically confirmed redshift in the same redshift region.

The effective field of view is constructed as a sum of the FWHP of the primary beam of the observations, thus, for sources of a certain redshift it should be modified to the primary beam FWHP sum of those sources (instead of the full sample). For the ARC survey:

- $\Omega_{\text{eff,ARC}}(0 < z < 0.3) = 0.49 \times 67 \text{arcmin}^2$ for $z \in [0, 0.3]$
- $\Omega_{\text{eff,ARC}}(1.0 < z < 2.5) = 0.35 \times 67 \text{arcmin}^2$ for $z \in [1, 2.5]$

The NVSS survey²⁹ covers the sky north of -40° , that is

$$\Omega_{\text{tot, NVSS}} = \int_0^{2\pi} d\varphi \int_{-2\pi/9}^{\pi} \cos \theta d\theta = 2\pi \times (1 + \sin \frac{2\pi}{9}) \text{ steradian} = 3.28\pi \text{ steradian}$$

The team of Audibert et al. (2022)⁸ calculated the number of NVSS sources that have spectroscopically confirmed redshift and fulfill the flux density limit of the ARC survey ($f_\nu(1.4\text{GHz}) > 0.4\text{Jy}$) within two redshift intervals of interest $z \in [0, 0.3]$ and $z \in [1, 2.5]$, and found it to be:

- $N_{\text{NVSS}}(0 < z < 0.3) = 371$ for $z \in [0, 0.3]$
- $N_{\text{NVSS}}(1.0 < z < 2.5) = 804$ for $z \in [1, 2.5]$

The total number of ARC sources in these redshift ranges are:

- $N_{\text{ARC}}(0 < z < 0.3) = 59$ for $z \in [0, 0.3]$
- $N_{\text{ARC}}(1.0 < z < 2.5) = 34$ for $z \in [1, 2.5]$

Thus, the NVSS completeness correction for these redshift ranges is (based on equation 6.8):

$$\begin{aligned} \omega(0 < z < 0.3) &= \frac{N_{\text{NVSS}}(0 < z < 0.3)}{\Omega_{\text{NVSS}}} \times \frac{\Omega_{\text{eff,ARC}}(0 < z < 0.3)}{N_{\text{ARC}}(0 < z < 0.3)} = \\ &= \frac{371}{3.28\pi \text{ sterad}} \times \frac{0.49 \times 5.669 \times 10^{-6} \text{ sterad}}{59} = \\ &= 1.695 \times 10^{-6} \end{aligned} \quad (6.9)$$

$$\begin{aligned} \omega(1.0 < z < 2.5) &= \frac{N_{\text{NVSS}}(1.0 < z < 2.5)}{\Omega_{\text{NVSS}}} \times \frac{\Omega_{\text{eff,ARC}}(1.0 < z < 2.5)}{N_{\text{ARC}}(1.0 < z < 2.5)} = \\ &= \frac{804}{3.28\pi \text{ sterad}} \times \frac{0.35 \times 5.669 \times 10^{-6} \text{ sterad}}{34} = \\ &= 4.554 \times 10^{-6} \end{aligned} \quad (6.10)$$

REDSHIFT COMPLETENESS

The analysis of survey data is performed for sources with spectroscopic redshift information, consequently it excludes the number of galaxies observed that have no spectroscopic redshift measurement. In order to correct for this, the fraction of all galaxies over the spectroscopic redshift-confirmed galaxies of a survey on the same field of view in the is used.

The team of Audibert et al. (2022)⁸ used the total number of NVSS sources that fulfill the flux density limit ($f_\nu(1.4\text{GHz}) > 0.4\text{Jy}$) of the ARC survey $N_{\text{NVSS, tot}} = 9331$ over the number of NVSS sources with spectroscopic redshift that fulfill the flux density limit ($f_\nu(1.4\text{GHz}) > 0.4\text{Jy}$) of the ARC survey $N_{\text{NVSS, z}} = 2104$, resulting to a correction coefficient:

$$\text{RedCompl} = \frac{N_{\text{NVSS, tot}}}{N_{\text{NVSS, z}}} = \frac{9331}{2104} \approx 4.435 \quad (6.11)$$

which is applied for $z > 0.3$, since it is assumed that lack of redshift measurement might be more prominent for higher redshifts, according to the team of Audibert et al. (2022)⁸.

FURTHER COMPLETENESS CORRECTIONS

Apart from the NVSS completeness and the redshift completeness, there are several issues that affect the accuracy with which the Stellar Mass Function can be determined. Further corrections for probing the galaxies of the complete Universe include

- k-correction, which allows the transformation from the observed wavelength, λ_{obs} when measured through a particular filter (or bandpass) at z , into the emitted wavelength, λ_{emit} in the rest frame at $z = 0$ ⁶⁷, $k(z) = \frac{\nu_{\text{emit}} L(\nu_{\text{emit}})}{\nu_{\text{obs}} L(\nu_{\text{obs}})}$
- Flux completeness⁷⁹, which corrects for the fact that fainter galaxies cannot be detected and can lead to significant biasing.
- Mass completeness^{86 139} corrects for the fact that towards lower stellar masses, galaxies become intrinsically less luminous, which ultimately leads to a regime where the detection limits of the data are reached and galaxy number counts begin to fall as they are lost to noise.
- Correction for merger evolution, since number evolution assumes that galaxies were more numerous in the past but have since merged.
- Cosmic variance, since structure formation causes galaxies to be distributed in clumps and voids, and galaxies over a discrete volume can be subject to significant sample variance.

6.3.3 REDSHIFT RANGES

Following the regime of Audibert et al. (2022)⁸ the 44 ARC sample is divided in three redshift ranges of $0.006 < z < 0.3$, $0.3 < z < 1.0$ and $1.0 < z < 2.5$, respectively. 30 out of 44 galaxies fall into the first redshift range ($0.006 < z < 0.3$), and are dividend in three mass bins of mean Stellar Mass in base-ten logarithmic scale of 10.516, 11.006 and 11.554 containing 8, 12 and 10 galaxies respectively. The redshift ranges of $0.3 < z < 1.0$ and $1.0 < z < 2.5$ gather 5 and 9 galaxies respectively. For the $0.3 < z < 1.0$ redshift range the mean Stellar Mass is $10^{11.525} M_{\odot}$ and for $1.0 < z < 2.5$ redshift range the mean Stellar Mass is $10^{11.788} M_{\odot}$. As discussed in Section 6.3.2, the $0.3 < z < 1.0$ redshift range is excluded, following the regime of Audibert et al. (2022)⁸.

The following table shows all relevant values used for constructing the Stellar Mass Function, while the Stellar Mass Function is plotted and shown in Figure 6.4

	Redshift range	N	Mean [$\log M_{\star}/M_{\odot}$]	$\Delta \log M_{\star}$	Φ
bin 1	$0 < z < 0.3$	8	10.516	1.1843	1.69×10^{-3}
bin 2	$0 < z < 0.3$	12	11.006	0.2028	7.26×10^{-5}
bin 3	$0 < z < 0.3$	10	11.554	0.7928	3.40×10^{-5}
binned all	$1.0 < z < 2.5$	9	11.788	2.9204	5.32×10^{-9}

Where N is the number of galaxies in each bin, and Φ is the galaxy density with the corrections discussed in Segment 6.3.2 and Segment 6.3.2 for each bin. In the final plot (Figure 6.4) each bin is represented by one point, the color distinguishes the redshift ranges and the point size is proportional to the number of galaxies of the initial sample in each bin.

Table 6.1: Values and limits for calculating SMF of 44 ARC galaxies. The name of each source is shown in the first column, in the second column is the 1.4 GHz flux in units of Jansky, the redshift of the source and the limit case redshift are in the third and fourth column respectively, the comoving volume through the FOV at the source and at the limit case are shown in the fifth and sixth column, respectively. The median sampled base-ten logarithm of stellar mass in units of solar masses is in seventh column.

Source name	$f_{1.4\text{GHz, source}}$	z_{source}	z_{limit}	$V_{\text{com, source}}$	$V_{\text{com, limit}}$	$\log M_{\star, \text{source}}$
J0006-0623	1.754	0.347	0.644	10621412470	53619010921	11.973
J0009-3216	0.505	0.026	0.029	5451077	7667186	11.329
J0048+3157	0.401	0.015	0.015	1106755	1110842	10.434
J0057+3021	1.715	0.017	0.034	1518505	12811912	11.554
J0106-4034	0.801	0.584	0.776	42025675299	84426729631	10.708
J0112-6634	0.431	1.189	1.226	218963612672	233195025541	12.224
J0119+3210	2.502	0.059	0.140	65948906	826594905	11.074
J0125-0005	1.467	1.076	1.821	177158540511	495526195715	11.933
J0327-2239	0.459	1.898	2.007	532781704065	585503176478	11.196
J0504-1014	1.461	0.040	0.075	21020608	132875955	10.890
J0758+3747	1.734	0.041	0.083	21772604	174619443	11.883
J0840+2949	0.514	0.065	0.073	85292621	121422757	11.041
J0914+0245	0.576	0.427	0.497	18591860833	27803371016	11.947
J1000-3139	0.534	0.009	0.010	222904	342648	10.333
J1008+0029	0.434	0.098	0.102	286702369	320847780	11.135
J1248-4118	3.922	0.010	0.030	313986	9075331	11.011
J1301-3226	1.227	0.017	0.030	1609884	8337450	11.001
J1336-3357	4.372	0.013	0.040	637246	21216550	11.037
J1348+2635	0.700	0.064	0.084	84285576	184699036	11.580
J1407-2701	0.708	0.022	0.029	3357927	7742971	11.163
J1602+0157	8.286	0.105	0.405	352065728	16146030943	10.678
J1945-5520	0.679	0.015	0.020	1132482	2470867	10.827
J2131-3837	0.764	0.018	0.025	2057386	5319099	10.951
J2134-0153	1.880	1.285	2.413	256903577664	785233255541	13.141
J2257-3627	0.840	0.006	0.009	71176	214877	10.781
J2320+0812	0.627	0.011	0.014	478432	930838	11.090

Table 6.2: Values and limits for calculating SMF of 44 ARC galaxies - continued

Source name logM _{*,limit}	$f_{\text{1.4GHz, source}}$	z_{source}	z_{limit}	V _{com,source}	V _{com,limit}	logM _{*,source}
J2325-1207	1.627	0.083	0.159	177577734	1187583652	11.000
Jo125-0122	0.826	0.018	0.026	1879930	5456446	10.871
Jo156+0537	0.635	0.019	0.024	2138230	4217506	11.555
Jo709+4836	0.512	0.019	0.022	2329418	3345999	10.993
J2214+1350	2.216	0.026	0.060	5780173	68352752	10.598
J1348+2635	0.925	0.063	0.093	77671998	250804892	11.558
J1321+4235	1.687	0.790	1.415	88089040027	310812208203	11.593
J1531+2404	3.352	0.095	0.250	262964983	4287716737	11.160
Jo747-1917	2.003	0.102	0.213	326279961	2739578035	11.841
J0009+1244	1.528	0.156	0.283	1118836863	6099733607	11.028
Jo11651-2052	3.723	1.410	3.524	308966929051	1325168544618	10.221
Jo234+3134	0.909	1.575	2.201	381597436448	680202950647	11.811
Jo408-2418	0.629	2.433	2.934	795973831784	1042737809694	11.636
J2106-2405	0.447	2.491	2.609	824465074464	882462629500	11.217
Jo242-2132	1.013	0.312	0.463	7954274949	23099299235	11.402
J1305-1033	0.843	0.291	0.401	6551933406	15702640284	10.832
Jo403+2600	1.285	2.109	3.417	635471606586	1274807911997	12.714
J1347+1217	5.375	0.122	0.387	548578299	14305603664	11.011

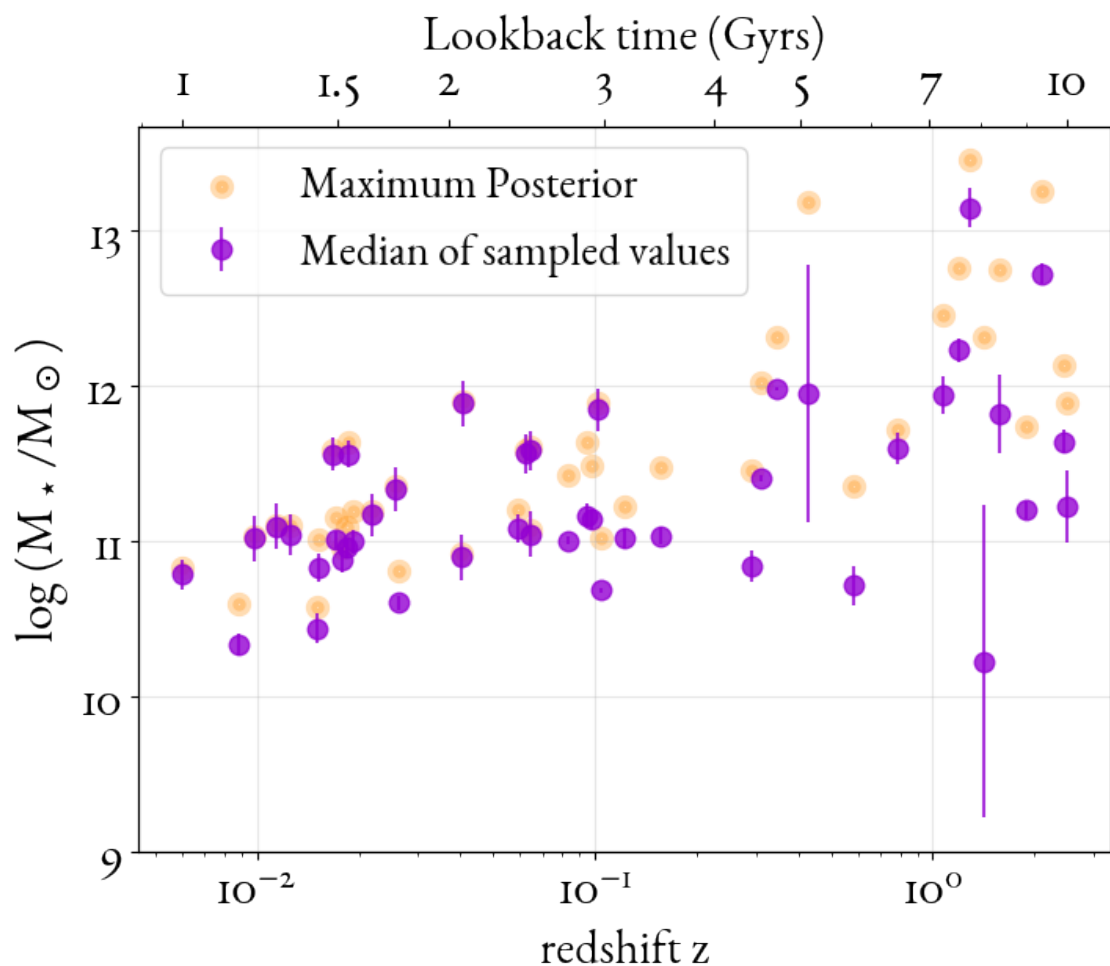


Figure 6.1: The stellar mass estimate for 44 ARC sources, stellar masses are inferred in Solar Mass units (M_\odot) and the base-ten logarithm of them is plotted. In bold color: the median of sampled values from the Bayesian process, uncertainties are half of the (84th-16th) percentile range. In light color: the maximum posterior value from the Bayesian process.

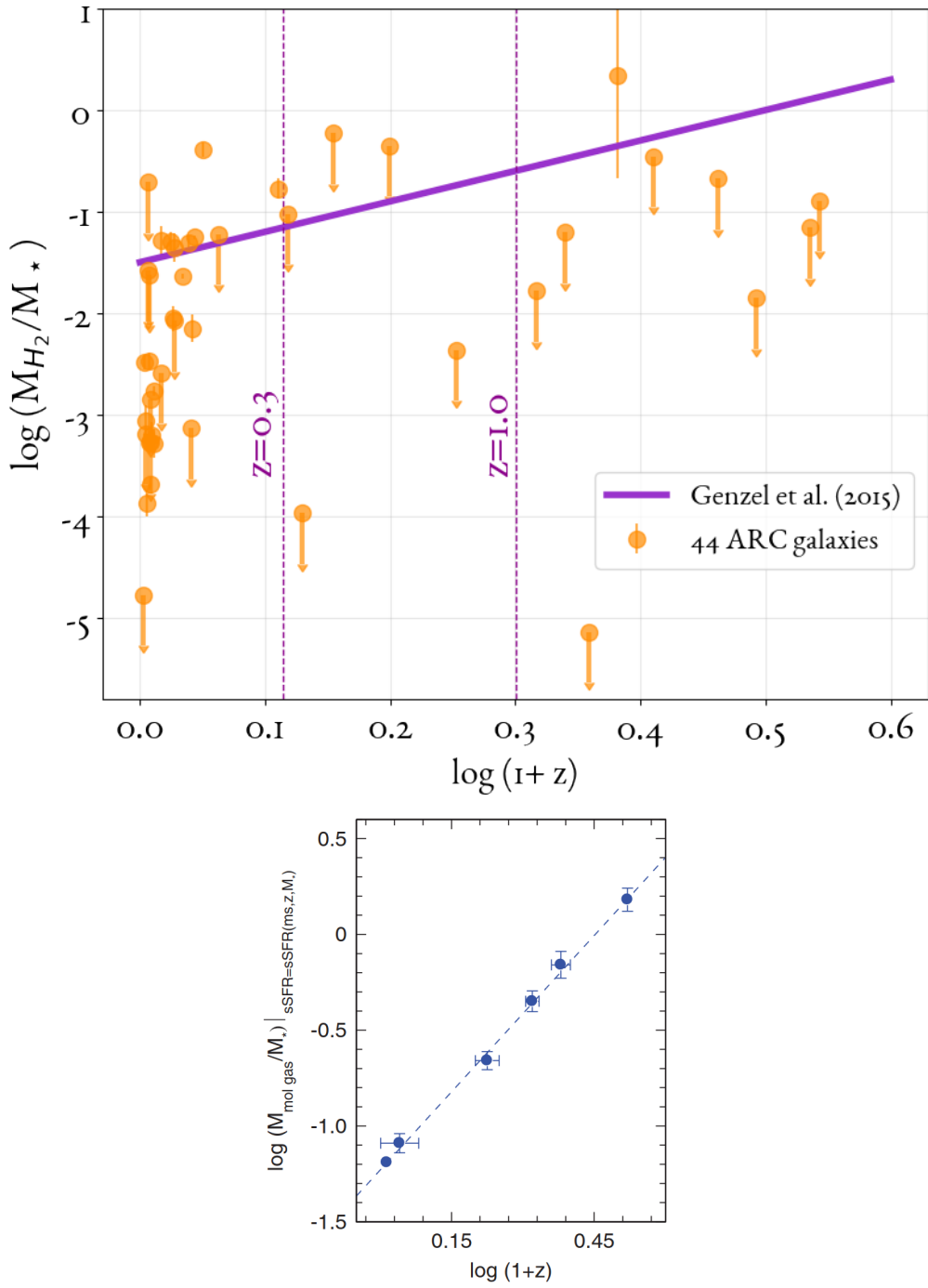


Figure 6.2: The 44 ARC galaxies' gas-to-stellar mass ratio. Left panel: The Molecular hydrogen mass over the median total inferred stellar mass for each galaxy, the base-10 logarithm of the ratio is plotted with the base-10 logarithm of $(1 + z)$, where z is the redshift. For sources that had an upper limit estimate of the molecular hydrogen gas, a downwards pointing arrow is plotted instead of uncertainty errorbars. The plotted line represents the main sequence and is adapted from Genzel et al. (2015)⁵⁴. Right panel: The plot copied from Genzel et al. (2015)⁵⁴ represents the main sequence galaxies.

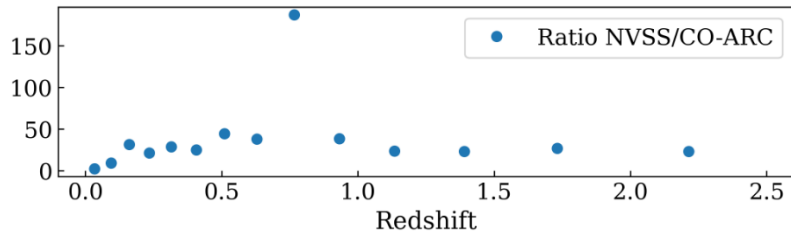


Figure 6.3: The NVSS completeness correction so that by multiplying the final ARC source sample in different redshift intervals can reproduce the number of sources in the NVSS survey. Plot copied from Audibert et al. (2022)⁸ for the complete ARC survey.

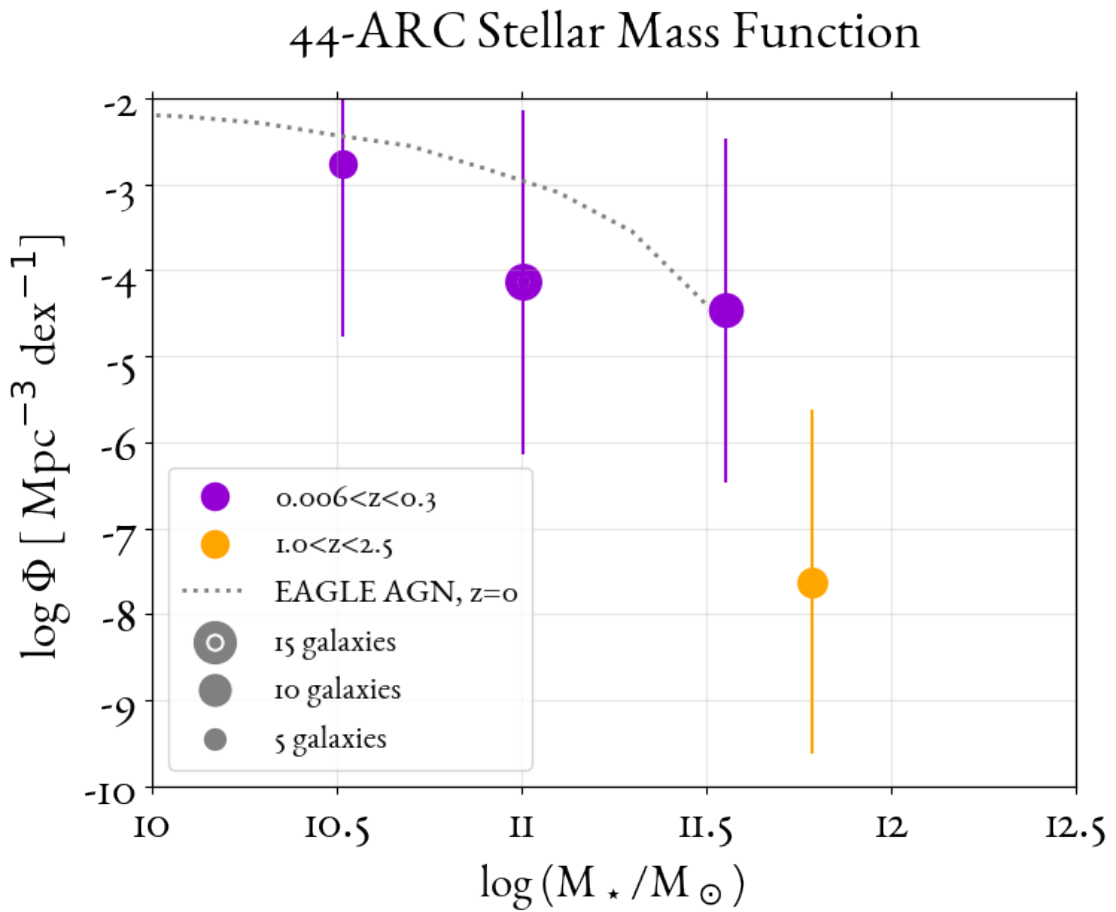


Figure 6.4: The galaxy Stellar Mass Function with its evolution in two redshift ranges. The color distinguishes the redshift ranges and the point size is proportional to the number of galaxies in each bin from the initial 44-ARC sample. The SMF for AGNs of the EAGLE¹²⁷ simulation at redshift $z = 0$ is plotted for comparison.

7

Conclusions

The ARC Stellar Mass Function plot at Figure 6.4 can give indicative information for order of magnitude since there are too little points for fitting a Schechter profile. For comparison, in Figure 7.1 the resulting Stellar Mass Function and its evolution for galaxies of the 3D-HST^{18 101} and COSMOS2015⁸⁴ surveys are shown on the left panel⁸⁶ and the local Universe SMF for the galaxies of the GAMA³⁷ survey are shown on the right panel³⁶, separately according to morphological type and in aggregate. GAMA is one of the most complete surveys with low median redshift, and the combined 3D-HST and COSMOS2015 surveys provide a very high completeness up to redshift $z = 6$.

7.1 STELLAR MASS FUNCTION COMPARISONS

For the Local Universe, the NVSS-corrected ARC sample indicates a Φ of $\sim 10^{-4}$ galaxies per Mpc^3 for galaxy stellar mass of $\sim 10^{11} M_\odot$, which compared to the morphological SMF of the local Universe in Figure 7.1 is ~ 1 dex lower than the local elliptical galaxies and ~ 1 to 2 dex lower than all the local galaxies of the GAMA survey. It is an indication that in the local Universe radiogalaxies with stellar masses $> 10^{11} M_\odot$ are not as common as normal or elliptical galaxies, although at lower stellar masses ($\sim 10^{10.5} M_\odot$) the Stellar Mass function is higher and could be perceived as an increase consistent with studies¹⁴² that support a rapid buildup for the lower mass quiescent sequence, potentially linking them to red quasars.

For the redshifts of $1.0 < z < 2.5$ the NVSS-corrected ARC sample indicates a Φ of $\sim 10^{-9}$ galaxies per Mpc^3 for galaxy stellar mass of $\sim 10^{12} M_\odot$, which, compared to the SMF of according redshift in the left panel of Figure 7.1, is roughly ~ 4 dex lower, hinting that in higher redshift ARC-like radiogalaxies are even less common. Though, higher redshift galaxy density estimation is more sensitive to poor completeness due to detection limits (flux completeness). It is important to highlight that this estimate is crude, since no exact values are compared, the ARC SMF was not corrected with respect to the effects discussed in Section 6.3.2, the literature results are not corrected to a Chabrier IMF to match the treatment of the ARC data, and it is not examined whether these studies are mass complete in the Chabrier IMF regime.

In Figure 6.4, the disparity between the ARC galaxy density at different redshifts might be interpreted such that galaxies that evolve to be ARC-like quasars undergo this stage of evolution in the last ~ 4 Gyrs ($z < 0.3$) of the Universe. Although, it is of central importance to remark that the completeness correction preformed in Section 6.3.2 is a vast simplification, and more rigorous treatment is due that ought to take into account the impact of detection limit biases, cosmic variance, merger effects and integrate K-correction⁶⁸ to the Bayesian process.

A case can also be made for the redshift bins since they include a wide interval of cosmic time, ~ 3 or 4 Gyrs each, where many (not independent) stages of evolution are included.

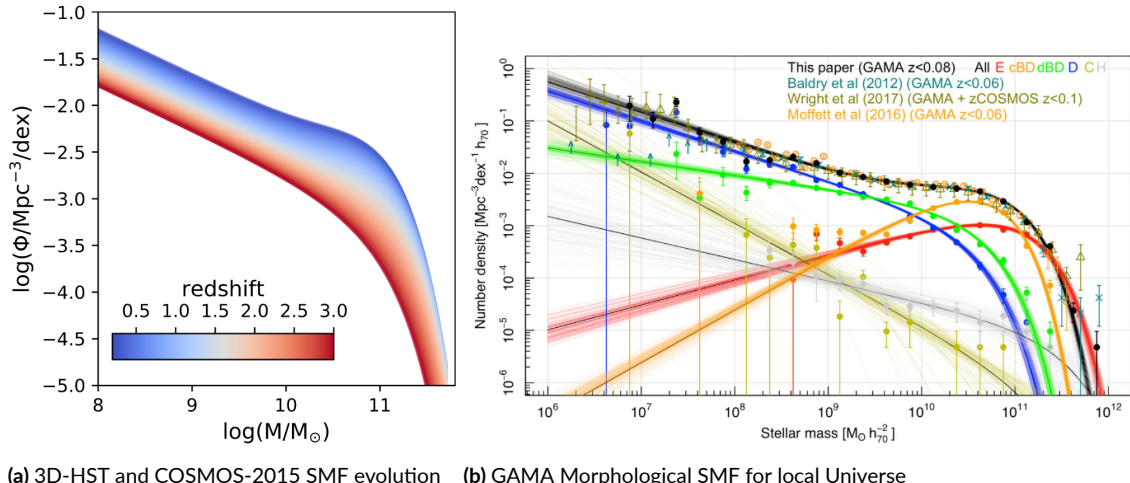


Figure 7.1: Comparison of Stellar Mass Function for different surveys. Figure lifted from Leja et al. (2020)⁸⁶. Figure lifted from Driver et al. (2022)³⁶

7.2 MOLECULAR GAS TO STELLAR MASS RATIO

In Figure 6.2 the molecular hydrogen gas mass-to-stellar mass ratio is plotted. This relation between gas and stars reveals the connection of star forming activity to its immediate fuel, and it is the more immediate and rigorous result of the present thesis. The molecular gas mass is estimated by the Audibert et al. (2022)⁸ from the CO spectroscopy. Where molecular hydrogen mass upper limit is used, it is denoted with a downwards arrow. As shown in Figure 6.2, the molecular gas mass-to-stellar mass ratio for the majority of the local ARC galaxies is well below the relation of the CO-based molecular gas mass to stellar mass ratio at the main-sequence from the work of Genzel et al.(2015)⁵⁴, confirming that most radiogalaxies in the local universe have already formed the majority of their stellar mass. Although in higher redshifts (i.e. $z > 1.0$, corresponding to 8 or more Gyrs ago) they seem to be a lot closer to the main sequence hinting that they might be closer to their peak of star formation.

7.3 IMPROVEMENTS & FUTURE WORK

IMPROVEMENTS ON THE MODELLING

The projection of the modelled SED to model photometry is described in Section 4.9, and includes the use of filter curves, which are excluded from the present work. A careful selection of every filter curve corresponding to the observational data will contribute to a more rigorous treatment of SED fitting.

As highlighted in Section 4.4.3, modeling the Star Formation History with a functional form is prone to inaccurate modelling of a galaxy's SED. As shown in Table 5.1, two composite stellar population models of delayed exponential decay SFH are used, differing in age, so that a more complex SFH function could be modeled, although there is vast room for improvement. A basis of nonparametric⁷⁵ Star Formation Histories can be built by training with a well motivated selection of SFH families⁷⁴ or generate stochastic SFHs. This can result to a more complete formulation of SFH and the use of one well-informed composite stellar population component which means a robust estimation⁹¹ of not only Star Formation Rate, but also mass-weighted ages.

As discussed in Section 4.8, the implemented SED models in the present work lack a blazar component, which is crucial for improvement of the routine since many of the ARC galaxies are radio loud balzars and including the appropriate modelling can expand the current sample

of reliably fitted galaxies. Blazar SED components can be fitted with robust modeling¹¹¹, and is a central priority for the amelioration of the present code.

IMPROVEMENTS ON THE FITTING ALGORITHM

Imposing priors of the separate AGN torus parametres can lead to a more careful SED fitting, especially if blazars are going to be fitted, in which case physical quantities such as inclination can be coupled with the blazar emission component (as demonstrated in Figure 4.2).

Imposition of a prior on the accretion disk emission upper limit from HST observations of the central region of the resolved sources, which is a proxy of the AGN fraction, makes the SED modelling astrophysically sounder. Although it has been tested, a more thorough selection of upper limits is due and will be implemented in an improved version of the code, as mentioned in Section 5.2.2.

In dust attenuation equation 4.2 the 0.4 attenuation for local universe is adopted, while 0.93 for $z \sim 1$ is proposed by Puglisi et al. (2016)¹¹⁵, although Narayanan et al. (2023)¹⁰² and Lower et al. (2023)⁹² remark that the choice of attenuation law contributes to the stellar component shape significantly less than the assumed Star Formation History.

Advanced methods for Stellar Population Synthesis could be an update for the future, such as Differentiable Stellar Population Synthesis(DSPS)⁶² or use of emulators⁸³ along with nonparametric prescriptions for the SFH (already discussed).

As demonstrated in Section 5.2.1, in the formulation of the Bayesian likelihood the covariance matrix can be specified as a sum of weighted kernels for noise models, which is useful if spectroscopic data form galaxies should be used. Some of the ARC galaxies have IR spectral data from Spitzer/IRS, which have not been used for the analysis of the present thesis. Careful noise modeling ought to be invoked when spectrograms are included.

IMPROVEMENTS ON POST-PROCESSING FOR STELLAR MASS FUNCTION

A rigorous study and careful implementation of corrections applied to the galaxy density can probe radiogalaxies in the complete Universe. Following the corrections stated in Segment 6.3.2, and implementing them with analytical modelling (for k-correction) or routines such as those of Rauzy et al. (2001)¹¹⁶, Johnston et al. (2007)⁷⁹, Tal et al. (2014)¹³⁹ or gaussian processes (for flux and mass completeness and merger densities).

SUMMARY OF CENTRAL IMPROVEMENTS

Methodical modelling of SFH can lead to the estimation of Star Formation Rate at any given time, and better assessment of the radiogalaxy evolution in the last ~ 11 Gyrs. The Stellar Mass Function could be better corrected for completeness, and stellar masses can be inferred for a larger sample when including a blazar component. The stellar mass and dust mass will be inferred more robustly with one composite stellar population and thorough SFH modelling. Scaling relations such as molecular gas mass-to-stellar mass ratio evolution and inferred dust mass-to-stellar mass ratio can be produced and studied with representative uncertainties. In conclusion, improvement on the fitting method, in particular

- the Star Formation History modelling and computational implementation
- correct filter integration and application
- extension of the model to include a rigorous blazar component fit
- rigorous corrections (mass/flux completeness and statistical cosmology)

can lead to more robust results without resorting to the request of high resolution spectroscopy or needing to include more galaxies to the studied sample.

A more careful treatment of the post processing methods, such as the flux and mass completeness correction, inclusion of cosmic variance and Bayesian inference integrated K-correction can vastly improve the conclusiveness of the results and the comparison with literature.

A

List of 44 ARC sources

In the present thesis a sub sample of 44 out of 120 ARC galaxies are used. The following table includes all of those 44 sources' name, redshift value and coordinates as a complete identifier of every source.

Table A.1: List of 44 fit ARC sources

Source name	Redshift	Coordinates (J2000.0)		Redshift reference	Coordinate reference
		RA	Dec		
J0006-0623 / PKS 0003-06	0.34668	00 ^h 06 ^m 13.89 ^s 1.55789 ^o	-06 ^d 23 ^m 35.34 ^s -6.39315 ^o	Jones et al. (2004) ⁸¹ Jones et al. (2009) ⁸⁰	Johnston et al. (1995) ⁷⁸
J0009-3216 / IC 1531	0.02564	00 ^h 09 ^m 35.58 ^s 2.39824 ^o	-32 ^d 016 ^m 06.48 ^s -32.27701 ^o	Bottinelli et al. (1993) ¹⁷	Evans et al. (2010) ⁴²
J0048+3157 / NGC 262	0.01503	00 ^h 48 ^m 47.14 ^s 12.196423 ^o	+31 ^d 57 ^m 25.09 ^s 31.956968 ^o	Huchra et al. (1999) ⁷²	Fey et al. (2004) ⁴⁶
J0057+3021 / NGC 315	0.016485	00 ^h 57 ^m 48.88 ^s 14.45368 ^o	+30 ^d 21 ^m 08.82 ^s 30.35245 ^o	Trager et al. (2000) ¹⁴³	Fey et al. (2004) ⁴⁶
J0106-4034 / [HB89] 0104-408	0.584	01 ^h 06 ^m 45.11 ^s 16.68795 ^o	-40 ^d 34 ^m 19.96 ^s -40.57221 ^o	Gattano et al. (2018) ⁵³	Johnston et al. (1995) ⁷⁸
J0112-6634 / PKS 0110-668	1.1888	01 ^h 12 ^m 18.91 ^s 18.0788 ^o	-66 ^d 34 ^m 45.19 ^s -66.57922 ^o	Titov et al. (2011) ¹⁴¹	Fey et al. (2006) ⁴⁷
J0119+3210 / 4C +31.04	0.0602	01 ^h 19 ^m 35.00 ^s 19.89585 ^o	+32 ^d 10 ^m 50.05 ^s 32.18057 ^o	García-Burillo et al. (2007) ⁵¹	Fey et al. (2006) ⁴⁷
J0125-0005 / UM 321	1.074533	01 ^h 25 ^m 28.84 ^s 21.37018 ^o	-00 ^d 05 ^m 55.93 ^s -0.09887 ^o	Albareti et al. (2017) ⁴	Beasley et al. (2002) ¹¹

Table A.2: List of 44 fit ARC sources - continued

Source name	Redshift	Coordinates (J2000.0)		Redshift reference	Coordinate reference
		RA	Dec		
J0327-2239 / PKS 0324-228	1.894	03 ^h 27 ^m 04.44 ^s 51.7685°	-22 ^d 39 ^m 42.59 ^s -22.66183°	Falkendal et al. (2019) ⁴⁴	McCarthy et al. (1991) ¹⁰⁰
J0504-1014 / PKS 0502-10	0.040345	05 ^h 04 ^m 53.00 ^s 76.22082°	-10 ^d 14 ^m 51.25 ^s -10.24757°	Jones et al. (2004) ⁸¹ Jones et al. (2009) ⁸⁰	Douglas et al. (1996) ³³
J0758+3747 / NGC 2484	0.040825	07 ^h 58 ^m 28.11 ^s 119.61712°	+37 ^d 47 ^m 11.80 ^s 37.78661°	Albareti et al. (2017) ⁴	Fomalond et al. (2003) ⁴⁸
J0840+2949 / CGCG 150-014	0.06484	08 ^h 40 ^m 02.37 ^s 130.00986°	+29 ^d 49 ^m 02.64 ^s 29.8174°	Best et al. (2012) ¹³	Adelman-McCarthy+ (2008) ³
		09 ^h 14 ^m 37.91 ^s 138.65797°	+02 ^d 45 ^m 59.26 ^s 2.76646°		
J0914+0245 / PKS 0912+029	0.426622	10 ^h 00 ^m 40.84 ^s 150.17015°	-31 ^d 39 ^m 52.34 ^s -31.66454°	Albareti et al. (2017) ⁴	Fey et al. (2004) ⁴⁶
J1000-3139 / NGC 3100	0.008813	10 ^h 08 ^m 11.44 ^s 152.04766°	+00 ^d 30 ^m 00.00 ^s 0.5°	Ogando et al. (2008) ¹⁰⁷	Petrov et al. (2005) ¹¹²
J1008+0029 / PKS 1005+007	0.0979	12 ^h 48 ^m 49.25 ^s 192.20521°	-41 ^d 18 ^m 38.99 ^s -41.31083°	Colless et al. (2003) ²⁸	Adelman-McCarthy+ (2008) ³
J1248-4118 / NGC 4696	0.009904			Bottinelli et al. (1993) ¹⁷	Mahony et al. (2010) ⁹⁵

Table A.2: List of 44 fit ARC sources - continued

Source name	Redshift	Coordinates (J2000.0)		Redshift reference	Coordinate reference
		RA	Dec		
J1301-3226 / PKS 1258-321	0.017042	13 ^h 01 ^m 00.79 ^s 195.25328°	-32 ^d 6 ^m 28.72 ^s -32.44131°	Smith et al. (2000) ¹³³	Evans et al. (2010) ⁴²
J1336-3357 / IC 4296	0.012465	13 ^h 36 ^m 39.03 ^s 204.16262°	-33 ^d 57 ^m 56.99 ^s -33.96583°	Allison et al. (2014) ⁵	Healey et al. (2007) ⁶¹
J1348+2635 / 4C 26.42	0.063309	13 ^h 48 ^m 52.54 ^s 207.2189°	+26 ^d 35 ^m 33.65 ^s 26.59268°	Albareti et al. (2017) ⁴	Cava et al. (2009) ²⁵
J1407-2701 / IC 4374	0.021798	14 ^h 07 ^m 29.76 ^s 211.87401°	-27 ^d 01 ^m 04.30 ^s -27.01786°	Allison et al. (2014) ⁵	Beasley et al. (2002) ¹¹
J1602+0157 / 3C 327	0.1048	16 ^h 02 ^m 27.37 ^s 240.61406°	+01 ^d 57 ^m 56.16 ^s 1.9656°	Hill et al. (1996) ⁶⁵	Evans et al. (2010) ⁴²
J1945-5520 / NGC 6812	0.015451	19 ^h 45 ^m 24.22 ^s 296.35092°	-55 ^d 20 ^m 48.48 ^s -55.3468°	Wegner et al. (2003) ¹⁵²	Costa et al. (1996) ³¹
J2131-3837 / NGC 7075	0.018479	21 ^h 31 ^m 32.98 ^s 322.88742°	-38 ^d 37 ^m 04.51 ^s -38.61792°	Wegner et al. (2003) ¹⁵²	Skrutskie et al. (2006) ¹³²
J2134-0153 / [HB89] 2131-021	1.285	21 ^h 34 ^m 10.31 ^s 323.54296°	-01 ^d 53 ^m 17.23 ^s -1.88812°	Drinkwater et al. (1997) ³⁵	Johnston et al. (1995) ⁷⁸

Table A.2: List of 44 fit ARC sources - continued

Source name	Redshift	Coordinates (J2000.0)		Redshift reference	Coordinate reference
		RA	Dec		
J ₂₂₅₇₋₃₆₂₇ / IC 1459	0.006011	22 ^h 57 ^m 10.61 ^s 344.2942°	-36 ^d 27 ^m 43.99 ^s -36.46222°	Wong et al. (2006) ¹⁵⁶	Fomalont et al. (2003) ⁴⁸
J ₂₃₂₀₊₀₈₁₂ / NGC 7626	0.011358	23 ^h 20 ^m 42.55 ^s 350.17728°	+08 ^d 13 ^m 01.09 ^s 8.21697°	Trager et al. (2000) ¹⁴³	Jackson et al. (2007) ⁷⁷
J ₂₃₂₅₋₁₂₀₇ / PKS 2322-12	0.082991	23 ^h 25 ^m 19.72 ^s 351.33216°	-12 ^d 07 ^m 26.76 ^s -12.1241°	Pollack et al. (2005) ¹¹³	Drinkwater et al. (2010) ³⁴
J ₀₁₂₅₋₀₁₂₂ / NGC 541	0.018086	01 ^h 25 ^m 44.31 ^s 21.43462°	-01 ^d 22 ^m 46.49 ^s -1.37958°	Smith et al. (2000) ¹³³	Evans et al. (2010) ⁴²
	0.018294	01 ^h 56 ^m 21.03 ^s 29.08764°	05 ^d 37 ^m 44.18 ^s 5.62894°	van den Bosch et al. (2015) ¹⁴⁶	Venkatesan et al. (1994) ¹⁴⁸
J ₀₇₀₉₊₄₈₃₆ / NGC 2329	0.01933	07 ^h 09 ^m 08.01 ^s 107.28337°	+48 ^d 36 ^m 55.55 ^s 48.61543°	Smith et al. (2000) ¹³³	Snellen et al. (1995) ¹³⁴
J ₂₂₁₄₊₁₃₅₀ / NGC 7236	0.026186	22 ^h 14 ^m 44.99 ^s 333.68746°	+13 ^d 50 ^m 47.44 ^s 13.84651°	Albareti et al. (2017) ⁴	Adelman-McCarthy+ (2008) ³
J ₁₃₄₈₊₂₆₃₅ / 4C 26.42	0.063309	13 ^h 48 ^m 52.54 ^s 207.2189°	+26 ^d 35 ^m 33.65 ^s 26.59268°	Albareti et al. (2017) ⁴	Cava et al. (2009) ²⁵

Table A.2: List of 44 fit ARC sources - continued

Source name	Redshift	Coordinates (J2000.0)		Redshift reference	Coordinate reference
		RA	Dec		
J ₁₃₂₁₊₄₂₃₅ / 3C 285	0.079385	13 ^h 21 ^m 17.88 ^s 200.32449 ^o	+42 ^d 35 ^m 15.14 ^s 42.58754 ^o	Albareti et al. (2017) ⁴	Evans et al. (2010) ⁴²
J ₁₅₃₁₊₂₄₀₄ / 3C 321	0.096456	15 ^h 31 ^m 43.51 ^s 232.9313 ^o	+24 ^d 04 ^m 18.84 ^s 24.0719 ^o	Albareti et al. (2017) ⁴	Evans et al. (2010) ⁴²
J ₀₇₄₇₋₁₉₁₇ / PKS 0745-191	0.102804	07 ^h 47 ^m 31.32 ^s 116.88052 ^o	-19 ^d 17 ^m 39.95 ^s -19.29443 ^o	Bottinelli et al. (1993) ¹⁷	Taylor et al. (1994) ¹⁴⁰
J ₀₀₀₉₊₁₂₄₄ / 4C +12.03	0.156	00 ^h 09 ^m 52.60 ^s 2.46917 ^o	+12 ^d 44 ^m 04.88 ^s 12.73469 ^o	Perryman et al. (1984) ¹¹⁰	Skrutskie et al. (2006) ¹³²
J ₀₁₁₆₅₁₋₂₀₅₂ / PKS 0114-21	1.41533	01 ^h 16 ^m 51.44 ^s 19.21435 ^o	-20 ^d 52 ^m 06.71 ^s -20.86853 ^o	Nesvadba et al. (2017) ¹⁰³	Wright et al. (1990) ¹⁵⁷
J ₀₂₃₄₊₃₁₃₄ / 3C 068.2	1.575	02 ^h 34 ^m 23.86 ^s 38.5994 ^o	+31 ^d 34 ^m 17.47 ^s 31.57152 ^o	Reddy et al. (2021) ¹¹⁷	Douglas et al. (1996) ³³
J ₀₄₀₈₋₂₄₁₈ / MRC 0406-244	2.44	04 ^h 08 ^m 51.47 ^s 62.21445 ^o	-24 ^d 18 ^m 16.49 ^s -24.30458 ^o	McCarthy et al. (1996) ⁹⁸	Rush et al. (1997) Rush et al.
J ₂₁₀₆₋₂₄₀₅ / MRC 2104-242	2.4917	21 ^h 06 ^m 58.16 ^s 316.74234 ^o	-24 ^d 05 ^m 11.26 ^s -24.08646 ^o	Nesvadba et al. (2017) ¹⁰³	McCarthy et al. (1990) ⁹⁹

Table A.2: List of 44 fit ARC sources - continued

Source name	Redshift	Coordinates (J2000.0)		Redshift reference	Coordinate reference
		RA	Dec		
J0242-2132 / PKS 0240-217	0.17	02 ^h 42 ^m 35.91 ^s 40.64962 ^o	-21 ^d 32 ^m 25.94 ^s -21.54054 ^o	O'Donnell et al. (2022) ¹⁰⁶	Beasley et al. (2002) ¹¹
J1305-1033 / PG 1302-102	0.2784	13 ^h 05 ^m 33.01 ^s 196.38756 ^o	-10 ^d 33 ^m 19.44 ^s -10.5554 ^o	Spoon et al. (2022) ¹³⁷	Johnston et al. (1995) ⁷⁸
J0403+2600 / [HB89] 0400+258	2.109	04 ^h 03 ^m 05.58 ^s 60.77327 ^o	+26 ^d 00 ^m 01.51 ^s 26.00042 ^o	Cheng et al. (2020) ²⁷	Johnston et al. (1995) ⁷⁸
J1347+1217 / 4C +12.50	0.12174	13 ^h 47 ^m 33.36 ^s 206.88901 ^o	+12 ^d 17 ^m 24.25 ^s 12.29007 ^o	Holt et al. (2003) ⁶⁹	Ma et al. (1998) ⁹³

B

Probability, Bayesian Method and Sampling

The following sections that review probability and illuminate Bayesian statistics are heavily based on the lecture notes of Elena Sellentin*.

B.I INTERPRETATIONS OF PROBABILITY

Multiple concepts of "probability" have emerged over the centuries and can be unified on a mathematical level by measure theory.

σ -ALGEBRAS

For set S , the powerset \mathcal{S} is the set of all subsets of S (including the $\{\emptyset\}$). A σ -Algebra indicates countability or measurability (it is an extended notion of counting) and is defined:

- Let $\mathcal{A} \subseteq \mathcal{S}(S)$ be some subset of the powerset of S
- \mathcal{A} is a σ -Algebra if:
 1. \emptyset and $S \in \mathcal{A}$ (indicates the notion of nothing and all)
 2. for all $A \in \mathcal{A} \Rightarrow \bar{A} := S/A \in \mathcal{A}$ (\bar{A} is the complement of A , indicating consistency)

*<https://github.com/elenasellentin/Modern-Astrostatistics>

3. for $A_i \in \mathcal{A}$ with $i \in \mathbb{N}$, then $\left(\bigcup_{i=1}^{\infty} A_i \right) \in \mathcal{A}$ (conjunctions of elements are countable, indicates countability)

- If \mathcal{A} is a σ -Algebra, then all $A_i \in \mathcal{A}$ are " \mathcal{A} -measurable" subsets of S
- For set S and \mathcal{A} a σ -Algebra on it, (S, \mathcal{A}) is called a "measurable space".

It follows that if S some set, I some range of integers $I = [1, 2, \dots, N]$ and many \mathcal{A}_j ($j \in I$) are σ -Algebras on S , then

$$\bigcap_{j=1}^N \mathcal{A}_j \text{ is a } \sigma\text{-Algebra on } S$$

which means that combined posteriors (Bayesian updating) of a probability measure of many experiments are again a probability.

MEASURES

A measure can be a generalised notion of volume, and is defined:

- If (S, \mathcal{A}) a measurable space using set S and σ -Algebra \mathcal{A} , then

$$\mu : \mathcal{A} \mapsto [0, \infty]$$

μ is called a "measure" if $[0, \infty]$ is \mathbb{R}^+ , including ∞ , and μ satisfies:

1. $\mu(A_i) \geq 0 \quad \forall A_i \in \mathcal{A}$ (positive definite, generalisation of the first Kolmogorov axiom for probability measures)
2. $\mu(\emptyset) = 0$ (empty set has measure zero, generalisation of the second Kolmogorov axiom for probability measures)
3. for $A_i, A_k \in \mathcal{A}$, when $A_i \cap A_k = \emptyset \quad \forall i \neq k$, then

$$\sum_{i=1}^{\infty} \mu(A_i) = \mu\left(\bigcup_{i=1}^{\infty} A_i\right)$$

(indicating σ -additivity, generalisation of the third Kolmogorov axiom for probability measures)

- If (S, \mathcal{A}) a measurable space, then (S, \mathcal{A}, μ) a measure space
- Let (S, \mathcal{A}, μ) a measure space, μ is a probability measure

$$\text{if } \mu(S) = 1$$

LEBESGUE INTEGRATION

The Riemann integral is commonly used in physics where the function $f(x)$ integrated is of interest (instead of its domain of definition, which is usually the \mathbb{R}^n space) and where usually the integrated function is sufficiently differentiable.

In statistics, integration of a function needs to be performed with respect to a measure, and the data space can be Euclidean (\mathbb{E}^n) since it includes discrete events and continuous events alike, thus \mathbb{R}^n is insufficient. Additionally, in statistics, parametres Θ span a manifold (e.g. $\vec{\Theta} \otimes N$), and functions $f(x)$ can be degenerate distributions or have non-existent densities. The Lebesgue integral was introduced to handle such cases. The Lebesgue integral is an integral that runs over the a working set \mathcal{X} with respect to a measure $\mu : \mathcal{A} \mapsto [0, \infty]$ of measure space $(\mathcal{X}, \mathcal{A}, \mu)$, using σ -Algebra \mathcal{A}

$$\int_{\mathcal{X}} f d\mu.$$

In Bayesian statistics, priors are probability measures against which Bayesian likelihoods are integrated (in the Lebesgue regime). Set S is the sample space of Bayesian methods.

B.2 BAYESIAN STATISTICS

Equation 5.1 is called Bayes' theorem but it does not encode what is known as 'Bayesian statistics', it simply follows from the laws of probability manipulations.

The aim of Bayesian statistics is to infer non-trivial conclusions given observables and domain expertise by marginalising on conditional probabilities. Bayesian Inference assigns "credibility" on non-observable quantities. Thence, the likelihood \mathcal{L} factors signal and describes noise processes, the posterior $\mathcal{P}_{\text{posterior}}$ describes an attempt of inferring the parameter values from observed data x (inverse workflow of the likelihood), priors $\mathcal{P}_{\text{prior}}$ constrain the introduced parametres and the Bayesian evidence \mathcal{E} is central for model selection. Uniform priors are not

necessarily uninformative, since they do not stay flat under non-linear transformations. The posterior distribution can be marginalised over in order to extract information and constraining the parameters with the data essentially accomplishes the mapping of the posterior. Samples whose number density is proportional to the posterior probability

$$n(\Theta) \propto \mathcal{L}(\vec{D}|\Theta) \mathcal{P}_{\text{prior}}(\Theta)$$

provide a guess for a Gaussian approximation $\mathcal{G}_p(\Theta)$ to the posterior and can be used to make integration trivial. Thus, integration/marginalisation can be performed for all parameters the models as well as the observables.

B.3 BAYESIAN SAMPLING TECHNIQUES

Bayesian sampling is achieved with numerical methods and many algorithms have been developed to achieve numerical feasibility for high dimensional posteriors. Brute Force Bayesian search, Markov Chain Monte Carlo (such as Gibbs sampling, Metropolis-Hastings sampling), Nested Sampling are some of those algorithms.

The samples need to be representative of the distribution, otherwise biases are introduced. This means that only converged sampling sequences should be used and that (for Markov chains) random (instead of neighbouring) chainlinks must be selected for post-processing.

Relevant software which implements Bayesian sampling algorithms that can be used in SED fitting codes such as the one developed for the present thesis are

- emcee[†] software⁴⁹, which implements the Affine-Invariant Ensemble Sampler⁵⁷
- ptemcee[‡] software¹⁵⁰, which implements the Adaptive Parallel Tempering Ensemble Sampler^{123 39}
- dynesty[§] software¹³⁵ which implements the Dynamic Nested Sampling algorithm⁶⁴
- UltraNest[¶] software²³, which implements the Reactive Nested Sampling algorithm^{20 21}

Nested Sampling algorithms are optimised to achieve a good approximation of the evidence and shape of the posterior with the most efficient possible sampling of parameter space. Un-

[†]<https://ascl.net/1303.002>

[‡]<https://ascl.net/2101.006>

[§]<https://zenodo.org/record/7995596>

[¶]<https://ascl.net/1611.001>

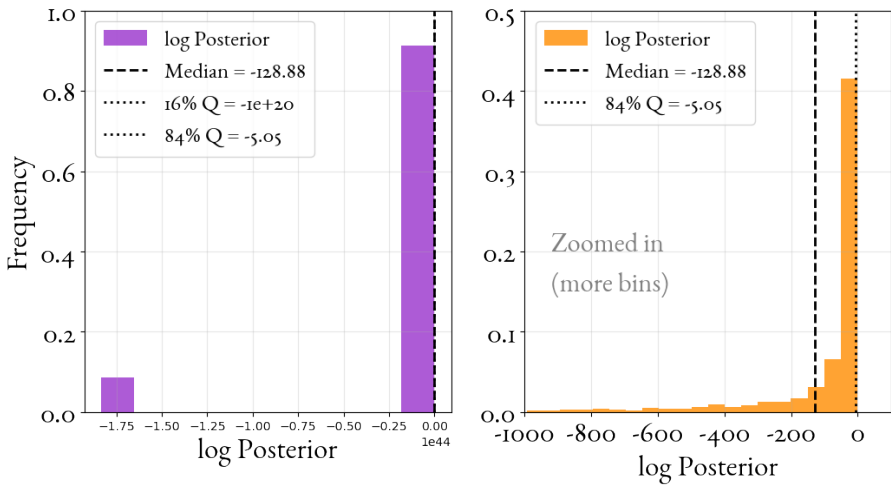
like more traditional algorithms (e.g. MCMC), the primary aim is not to sample in detail the parameter space, although for a large number of live points this can be achieved.

C

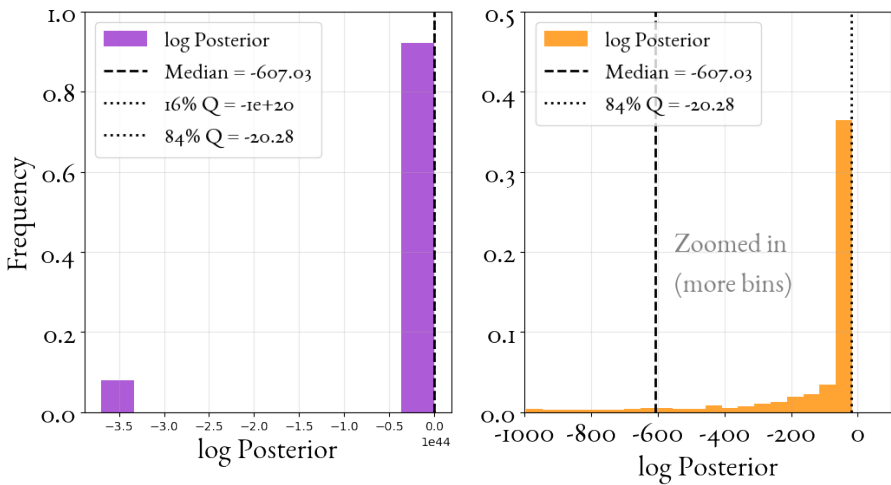
Posterior Distributions of Fit Galaxies

The sampled posterior histograms are plotted for every source from the 44 fit sources. The title of each plot corresponds to the name identifier of the ARC radiogalaxy, on the left panels is the full sampled histogram, while on the right panels the histogram has been zoomed in the region close to the median value, with a lot more bins. The median posterior value and the 16th and 84th percentiles have been clearly marked and the values are shown in the legend.

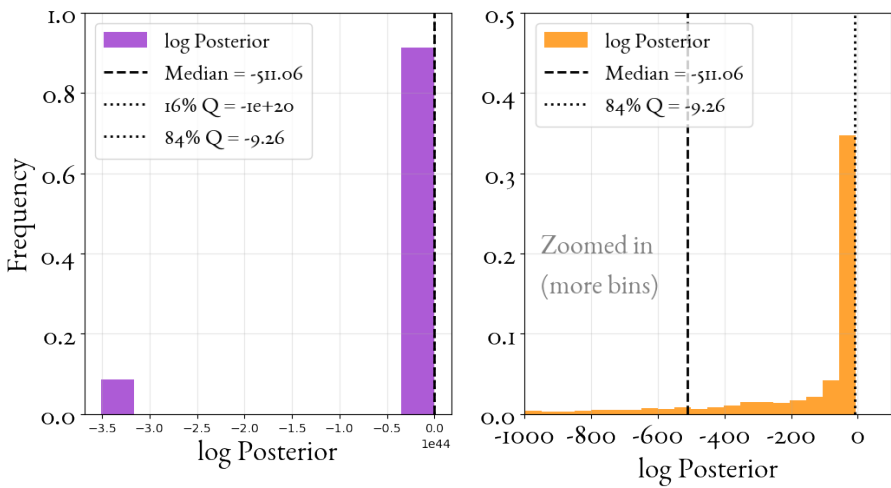
J0006-0623 / PKS 0003-066



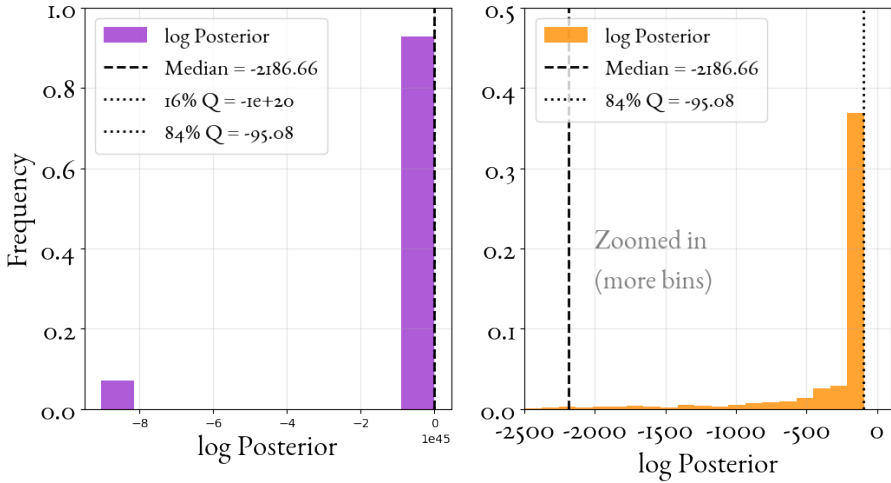
J0009-3216 / IC 1531



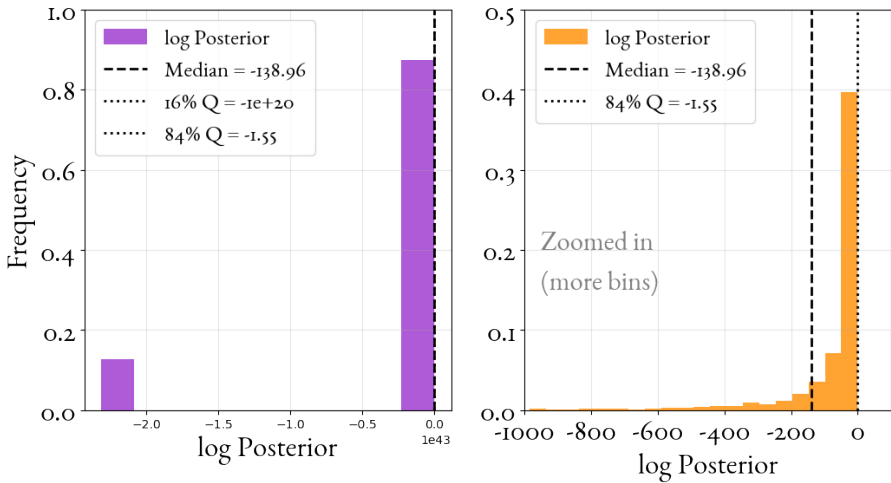
J0048+3157 / NGC 262



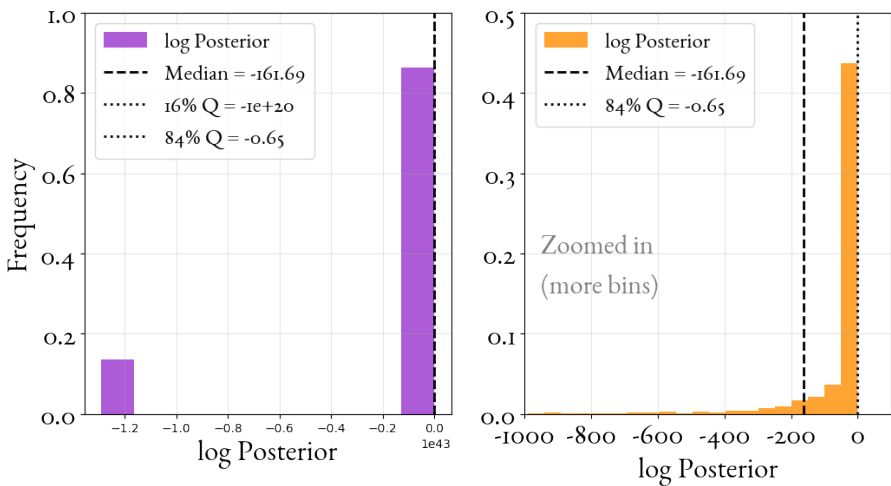
J0057+3021 / NGC 315



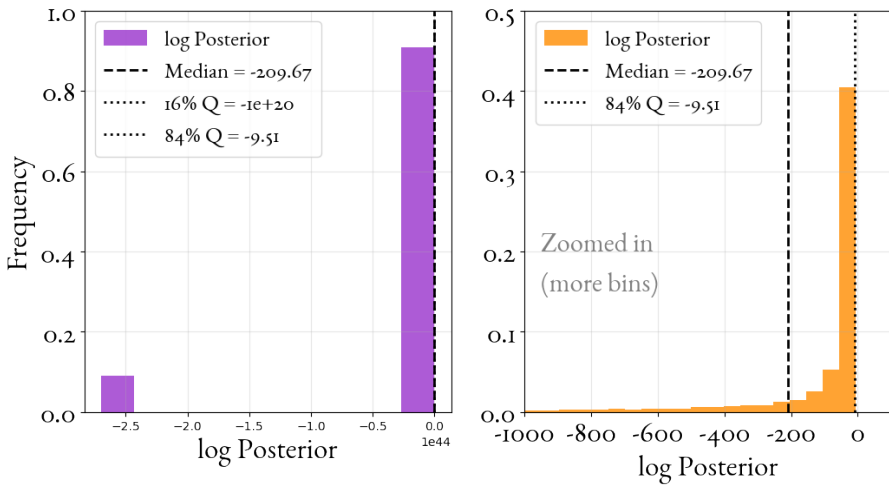
J0106-4034 / PKS 0104-408



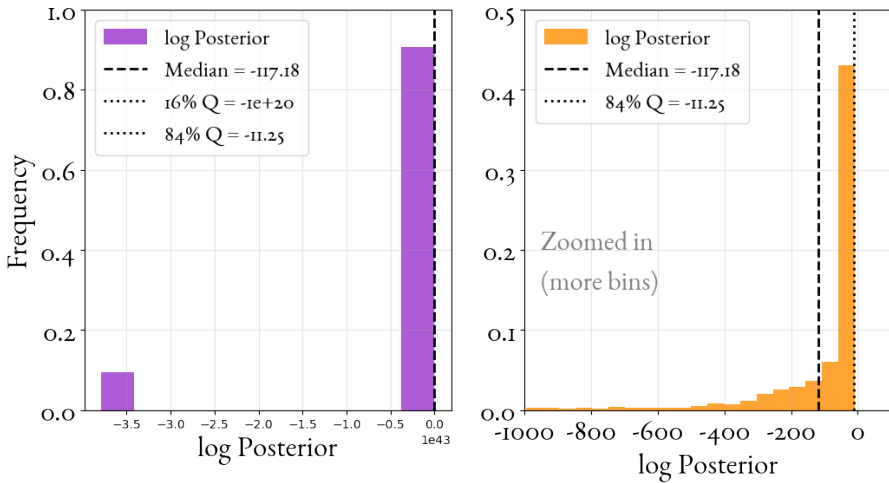
J0112-6634 / PKS 0110-668



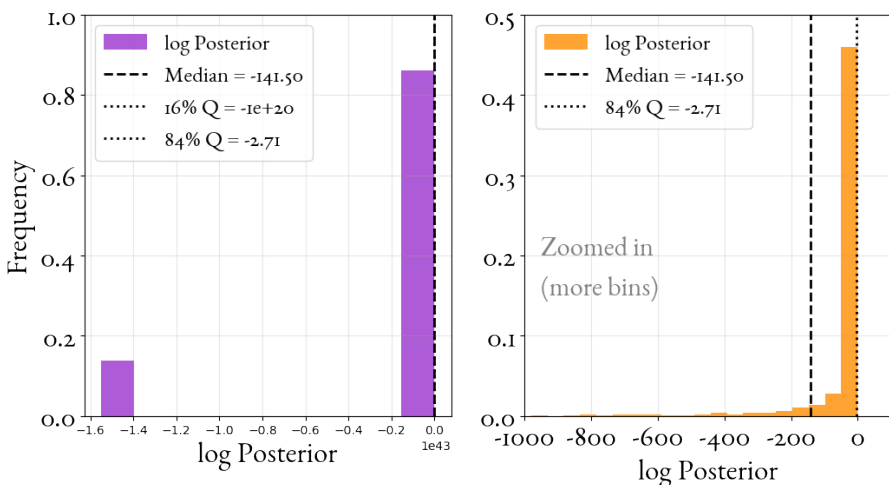
J0119+3210 / 4C +31.04 / QSO B0116+319



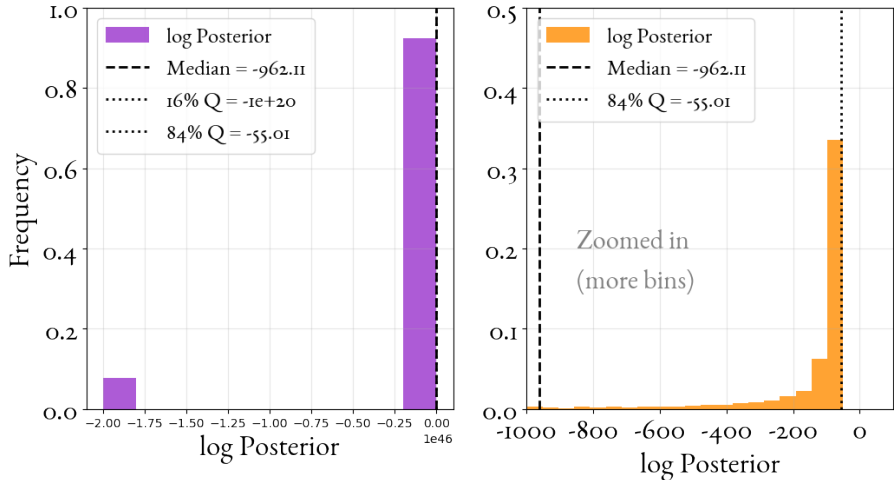
J0125-0005 / PKS 0122-003



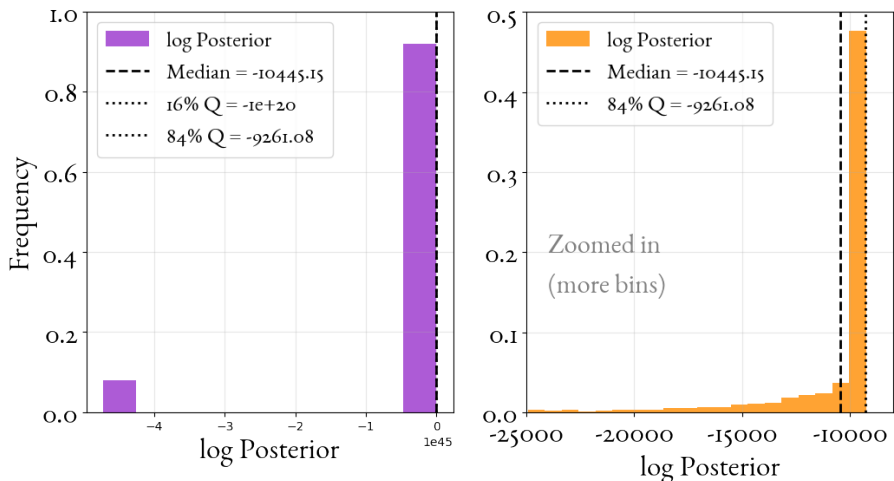
PKS 0324-228



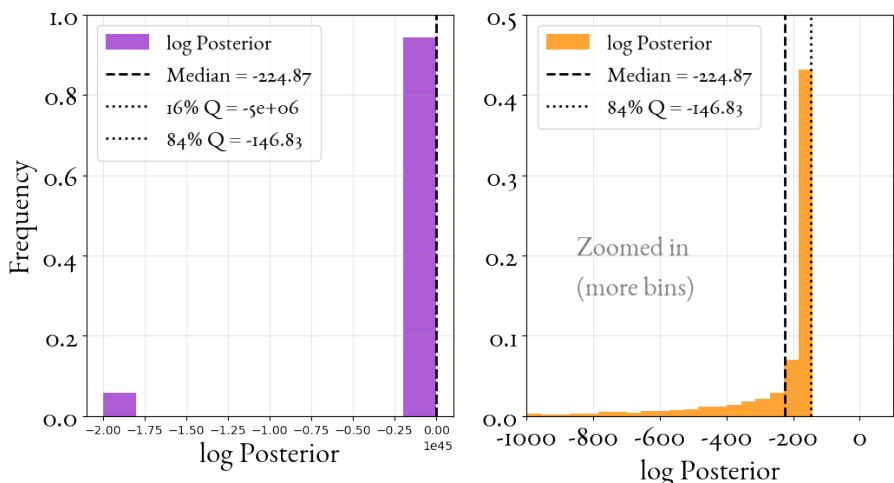
Jo504-1014 / PKS o502-10



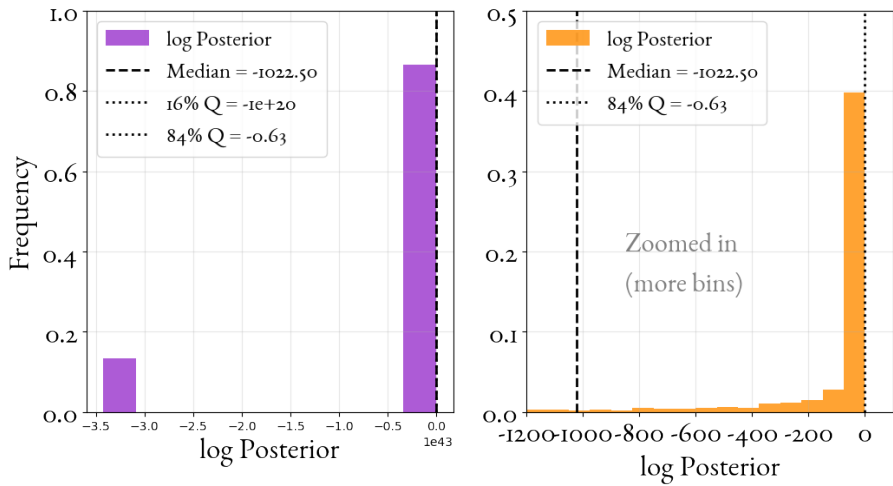
Jo758+3747 / 3C 189 / NGC 2484



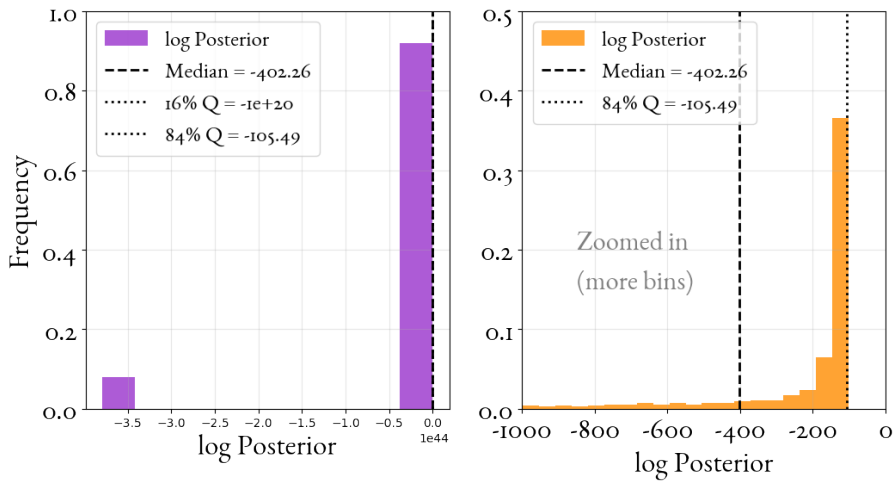
Jo840+2949 / 4C +29.30 / CGCG 150-014



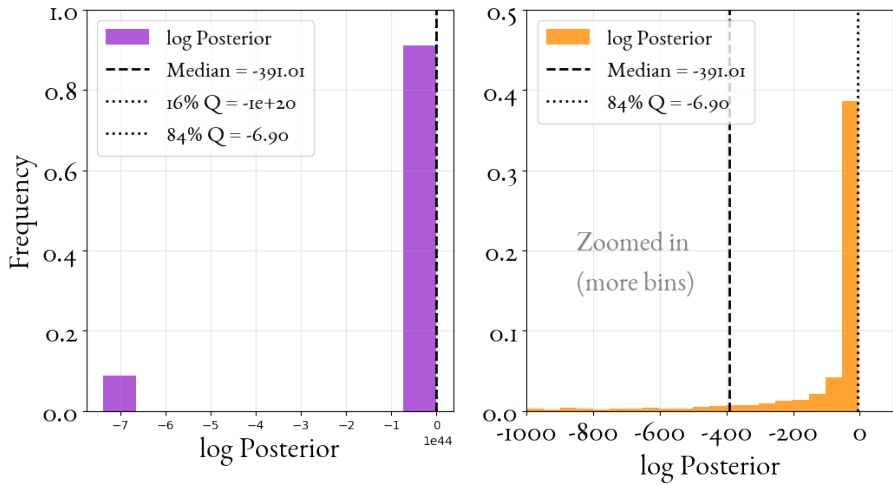
J0914+0245 / PKS 0912+029



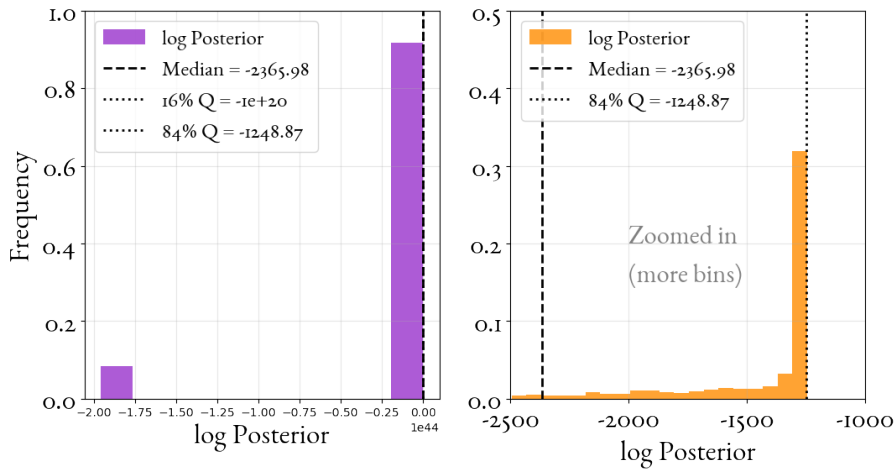
J1000-3139 / NGC 3100



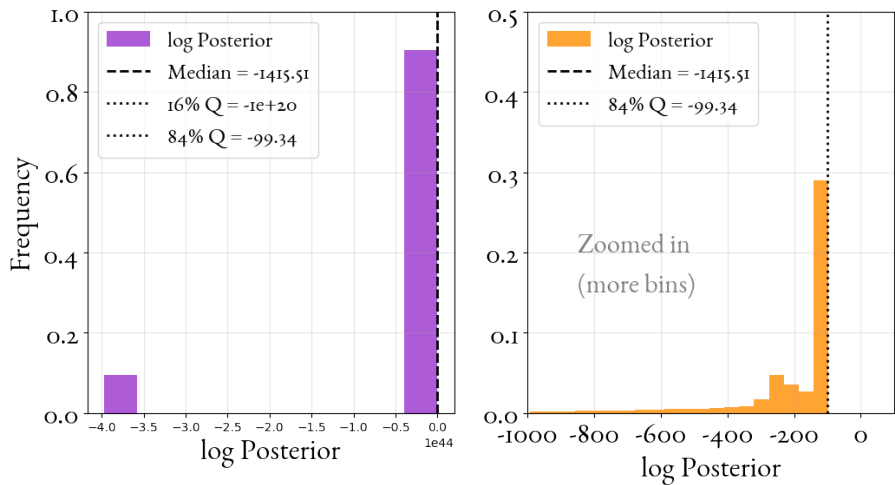
J1008+0029 / PKS 1005+007



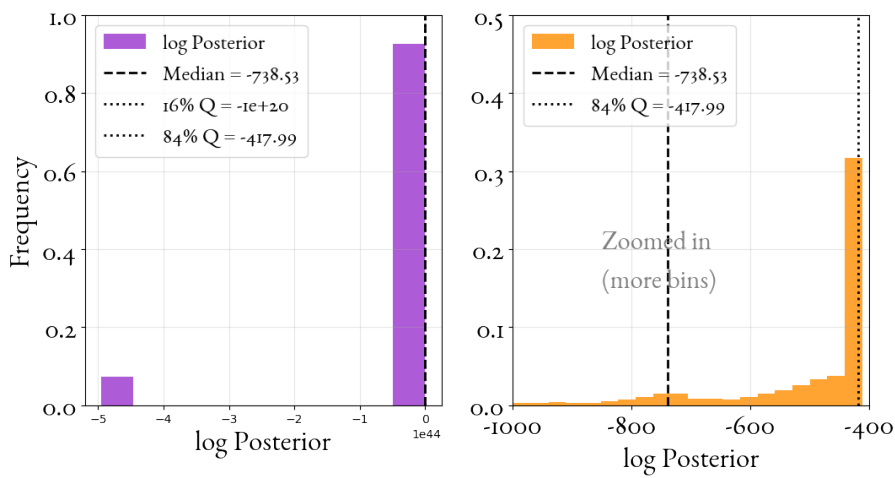
J1248-4118 / NGC 4696 / PKS 1245-410



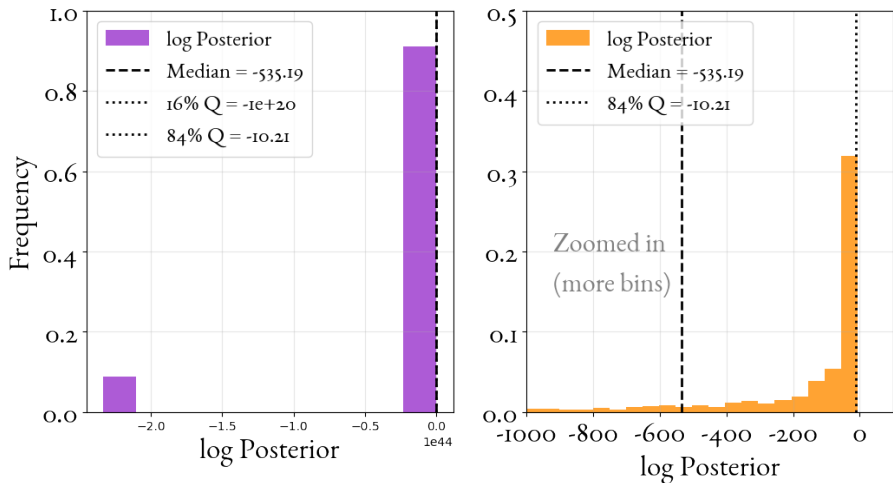
J1301-3226 / PKS 1258-321



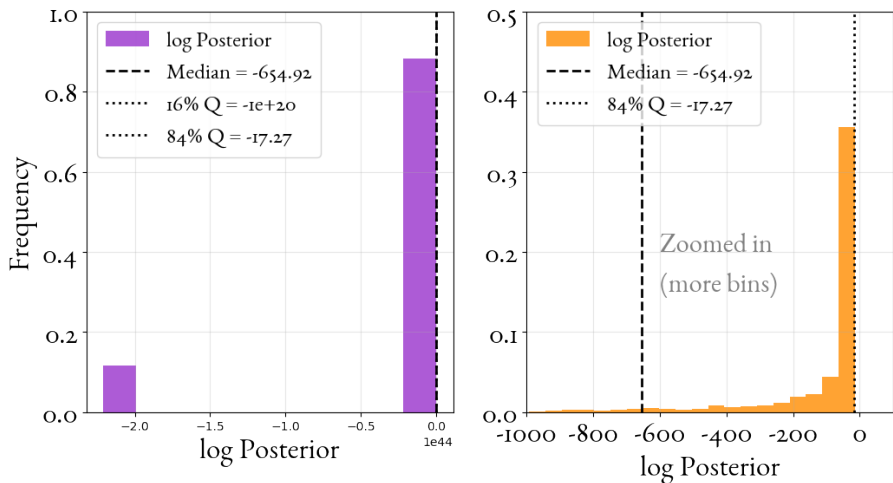
J1336-3357 / IC 4296 / PKS 1333-336



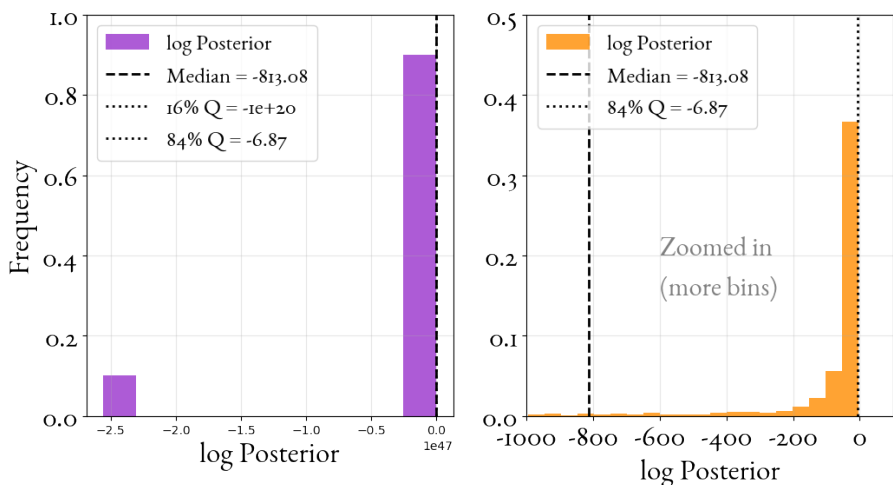
J1348+2635 / 4C 26.42 / PKS 1346+268



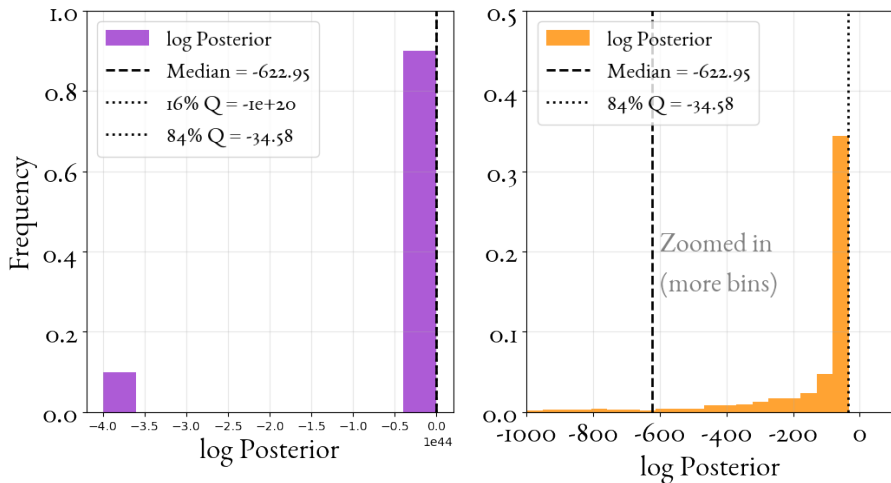
J1407-2701 / IC 4374 / PKS 1404-267



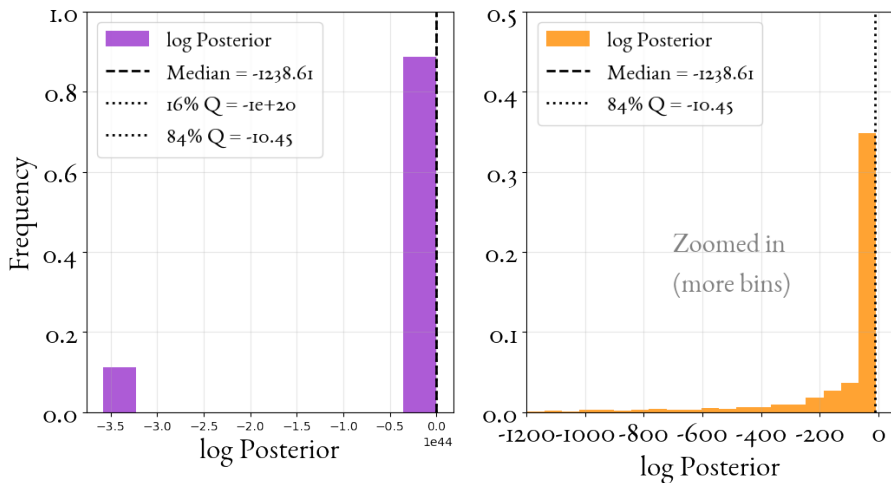
J1602+0157 / 3C 327 / PKS 1559+021



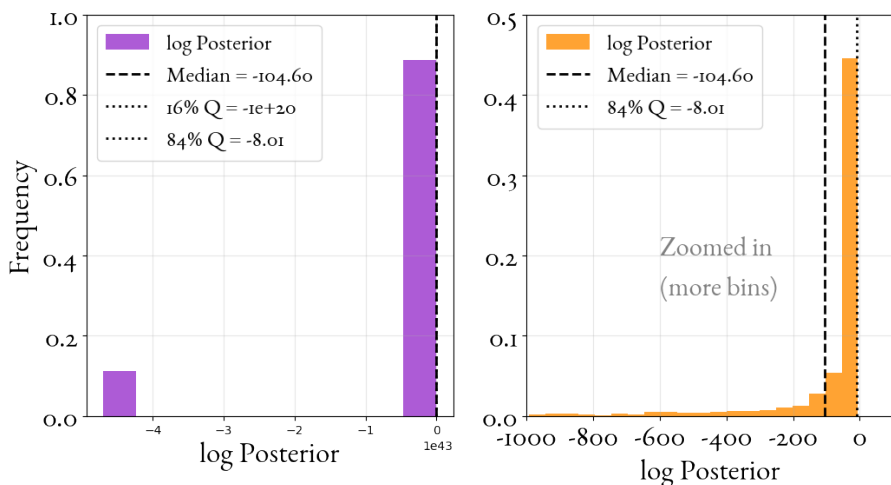
J1945-5520 / NGC 6812 / PKS 1941-554



J2131-3837 / NGC 7075 / PKS 2128-388

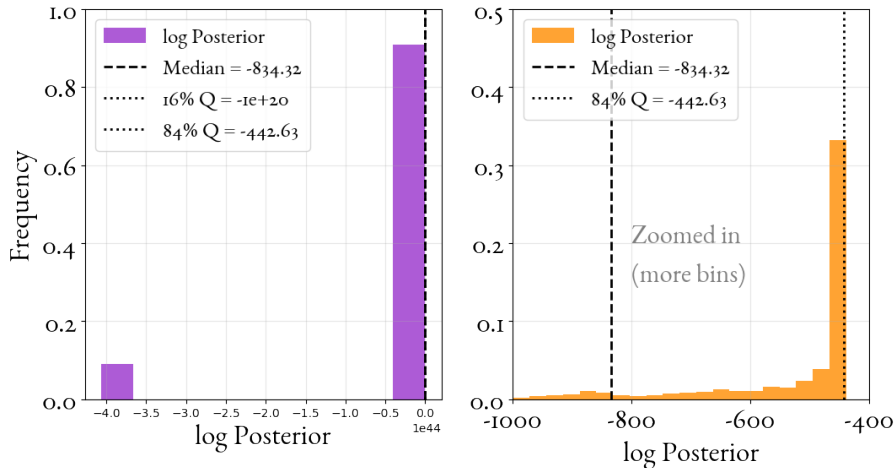


J2134-0153 / 4C -02.81 / PKS 2131-021

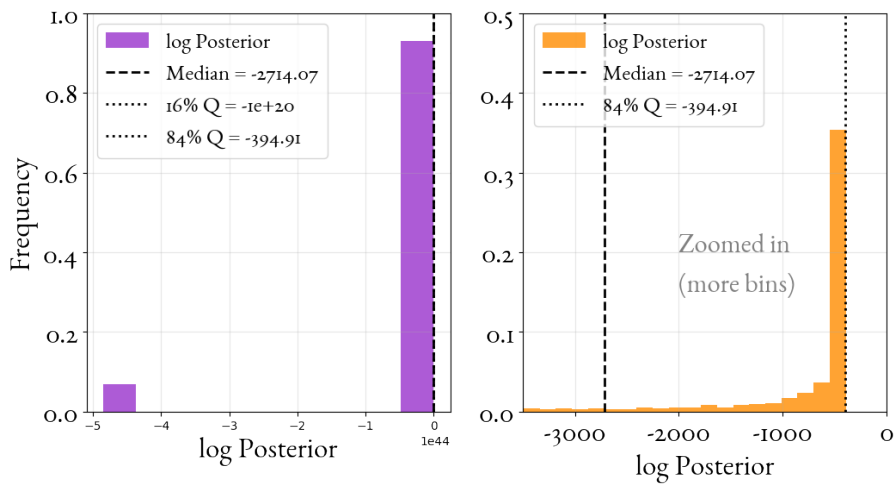


TOI

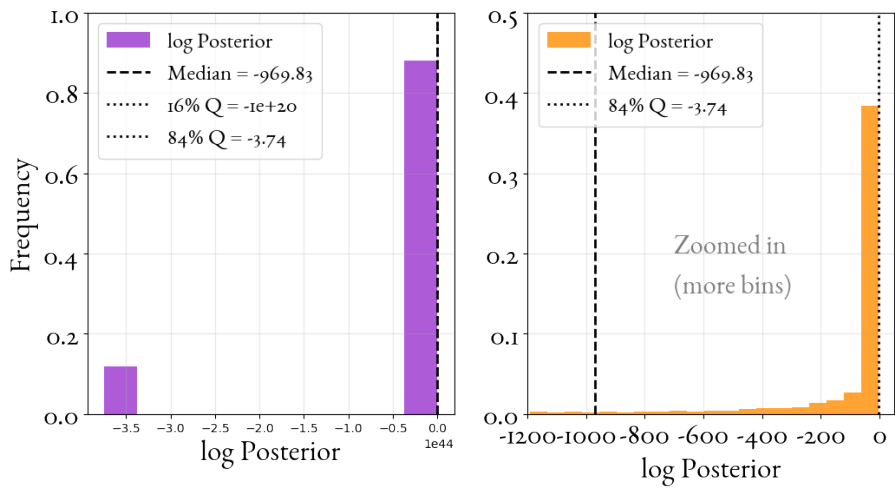
J2257-3627 / IC 1459 / PKS 2254-367



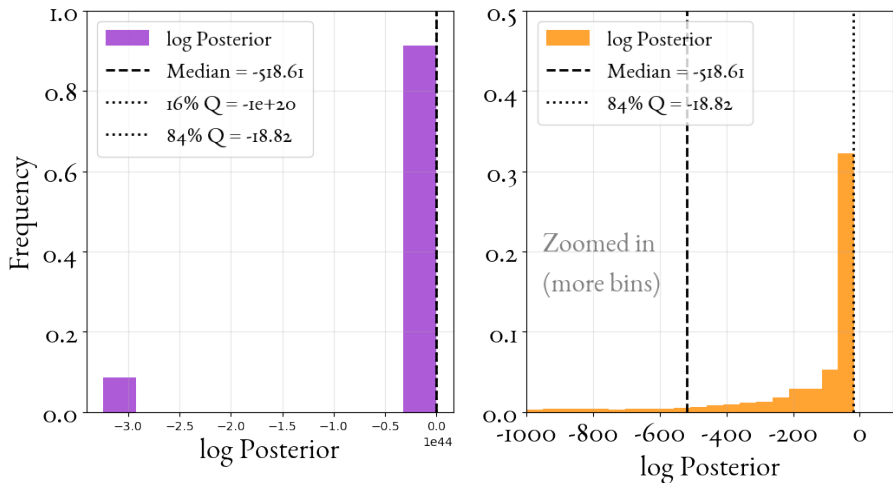
J2320+0812 / NGC 7626 / PKS 2318+079



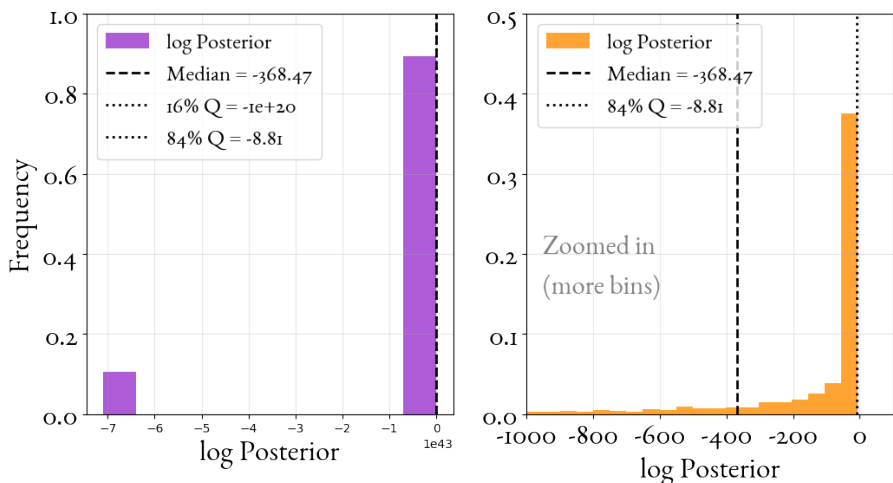
J2325-1207 / PKS 2322-123



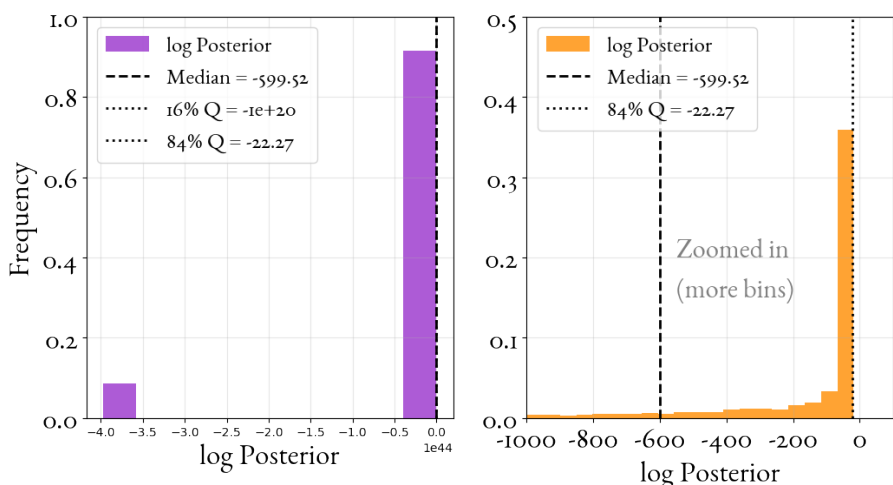
Jo125-0122 / NGC 541 / LEDA 5305



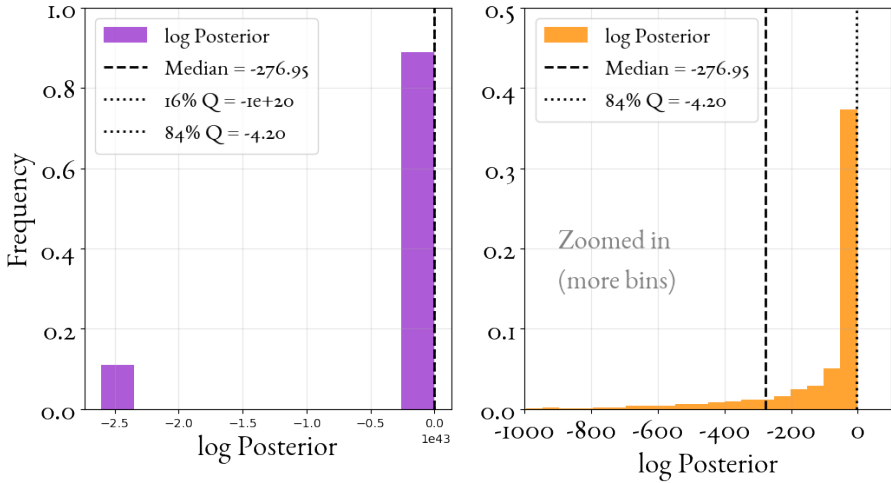
Jo156+0537 / NGC 741 / PKS 0153+053



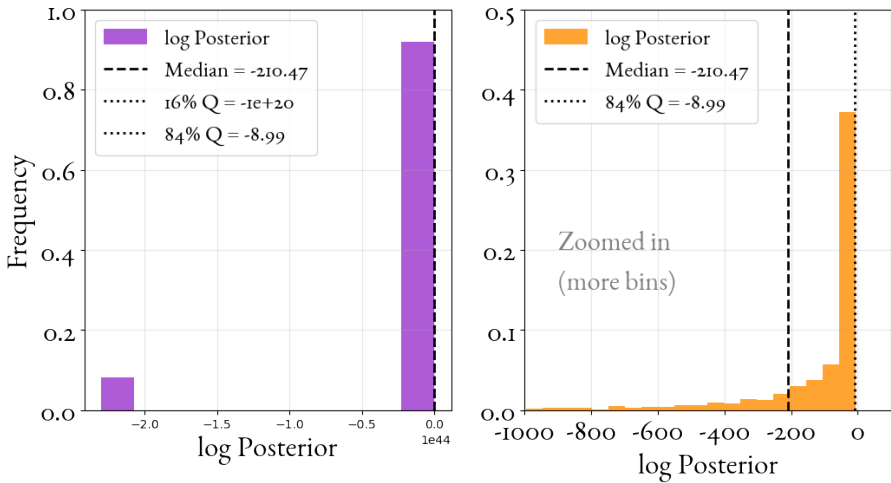
Jo709+4836 / NGC 2329



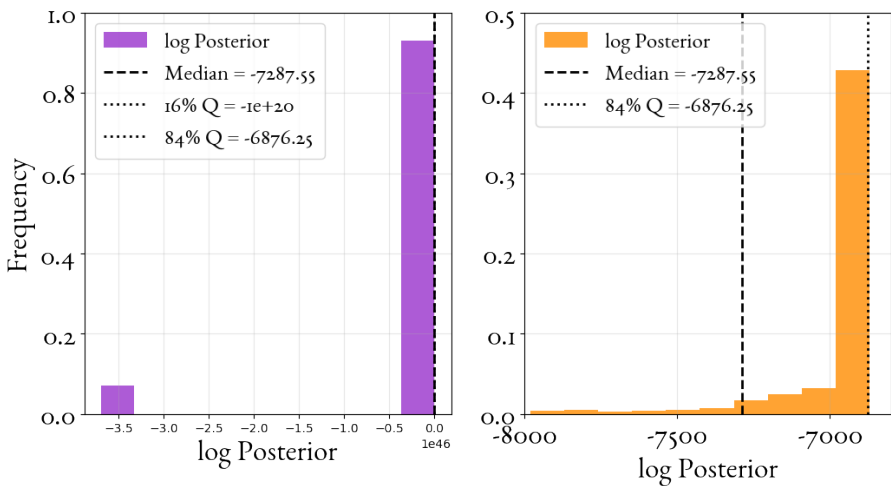
J₂₂₁₄₊₁₃₅₀ / NGC 7236 / PKS 2212+135



J₁₃₄₈₊₂₆₃₅ / 4C 26.42 / PKS 1346+268

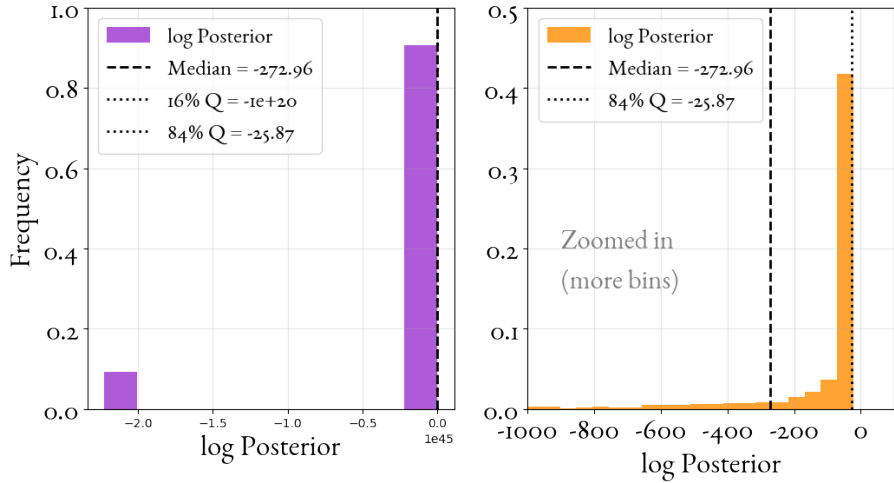


J₁₃₂₁₊₄₂₃₅ / 3C 285 / LEDA 46625

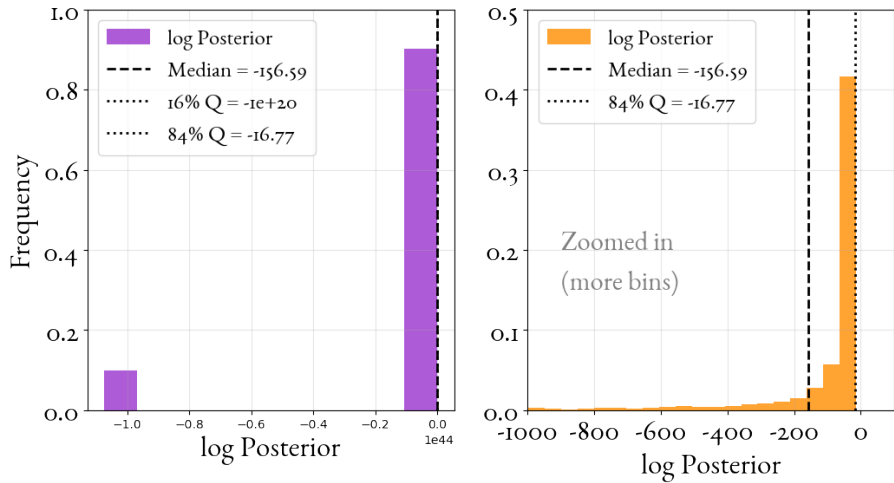


104

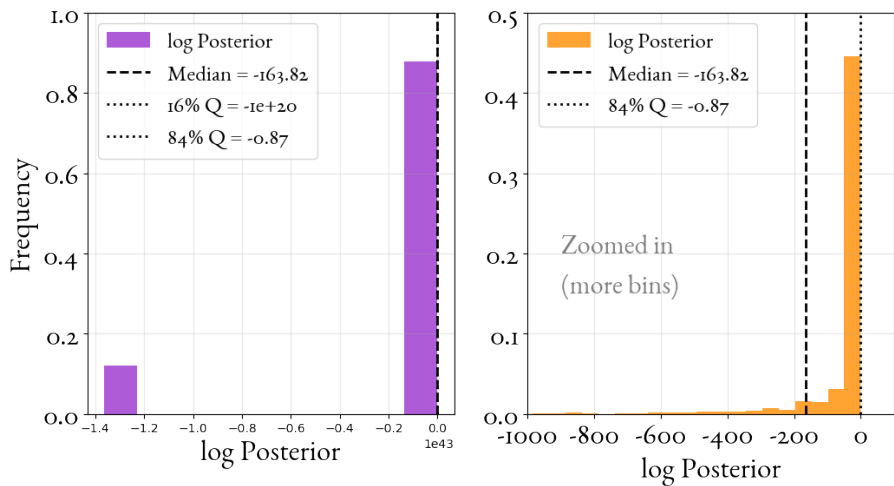
J1531+2404 / 3C 321 / PKS 1529+242



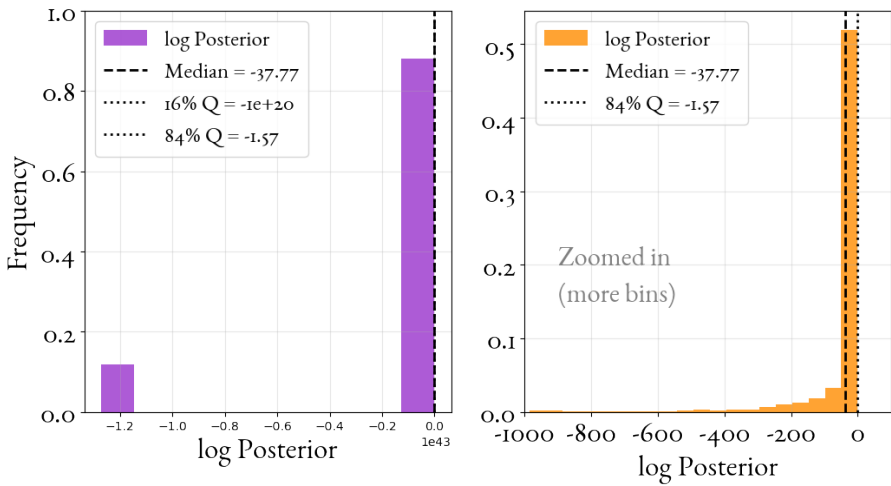
J0747-1917 / PKS 0745-191



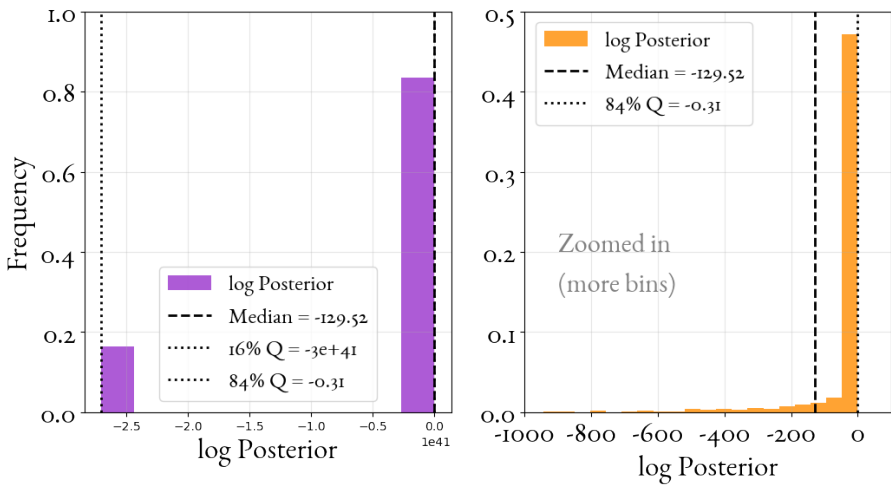
J0009+1244 / 4C 12.03 / PKS 0007+124



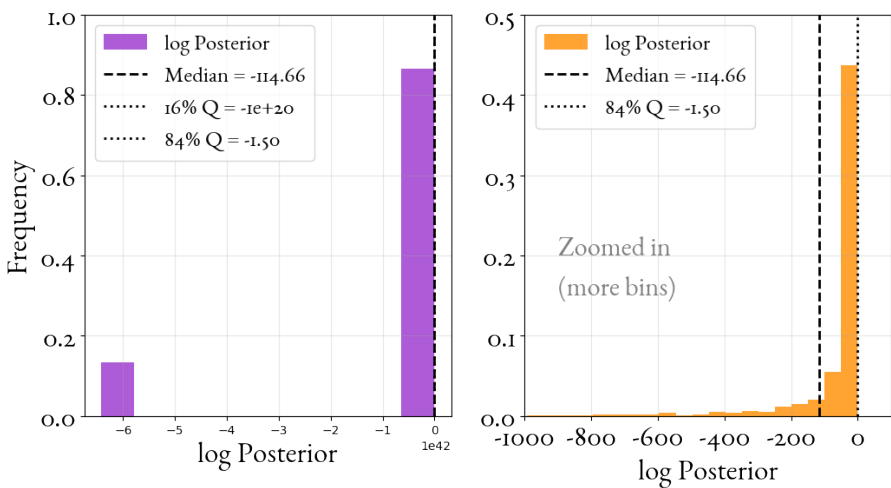
J011651-2052 / PKS 0114-21



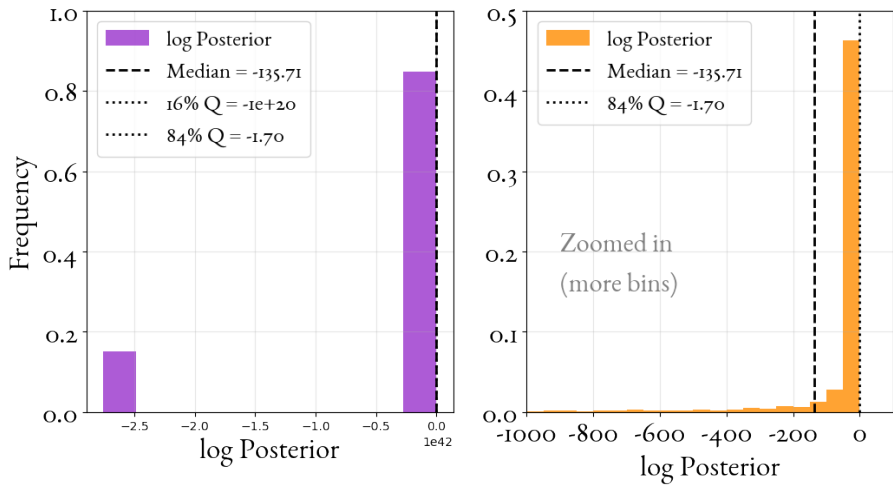
J0234+3134 / 3C 68.2 / LEDA 2820169



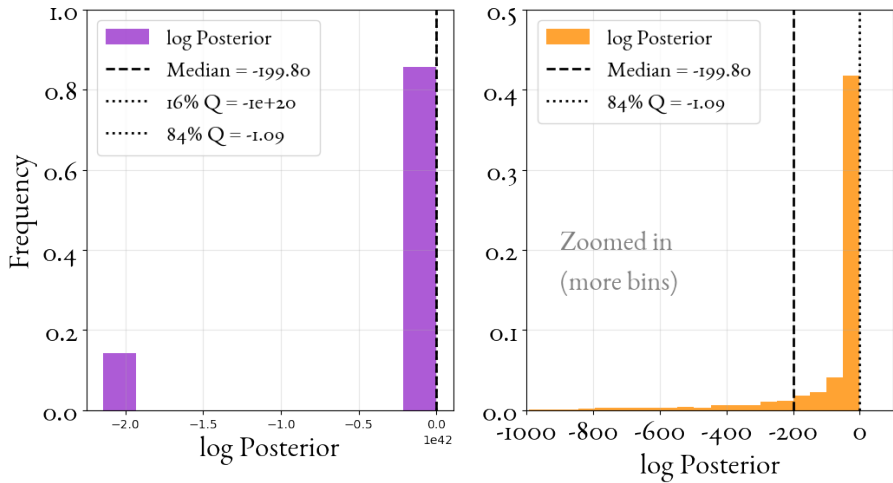
J0408-2418 / LEDA 2823818 / MRC 0406-244



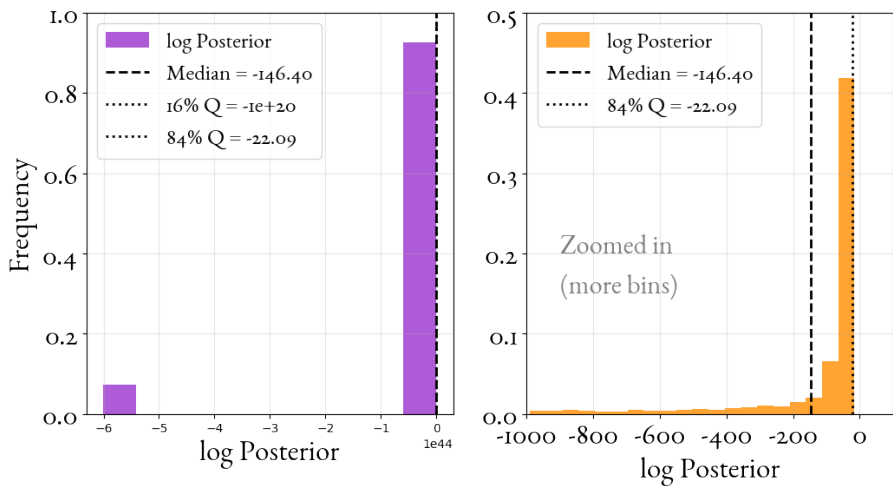
J2106-2405 / LEDA 2830749 / MRC 2104-242



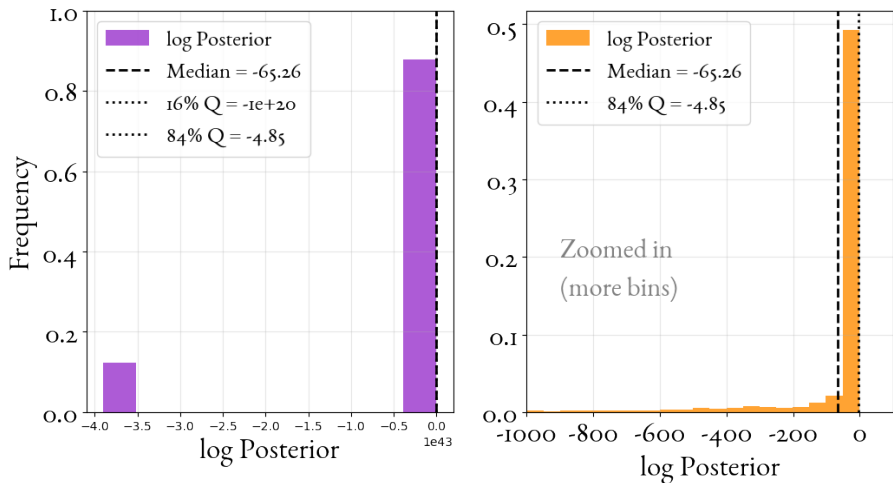
J0242-2132 / PKS 0240-217



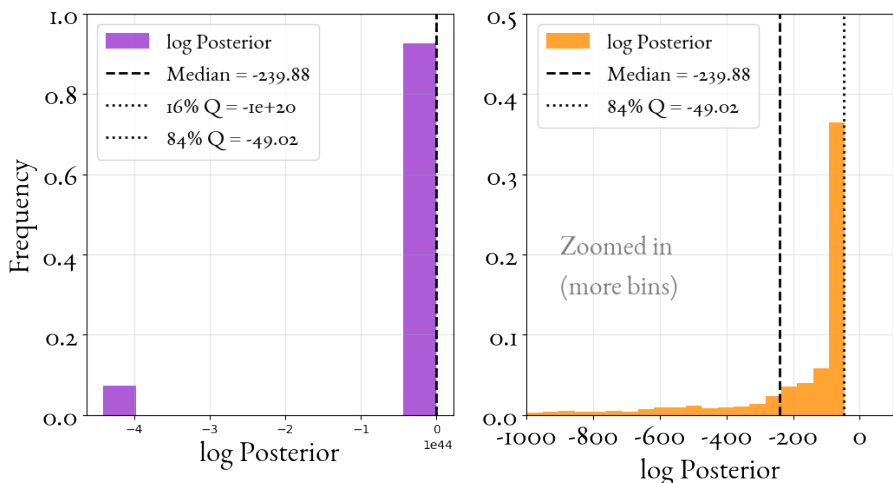
J1305-1033 / PKS 1302-103



J0403+2600 / PKS 0400+258



J1347+1217 / 4C 12.50 / PKS 1345+125

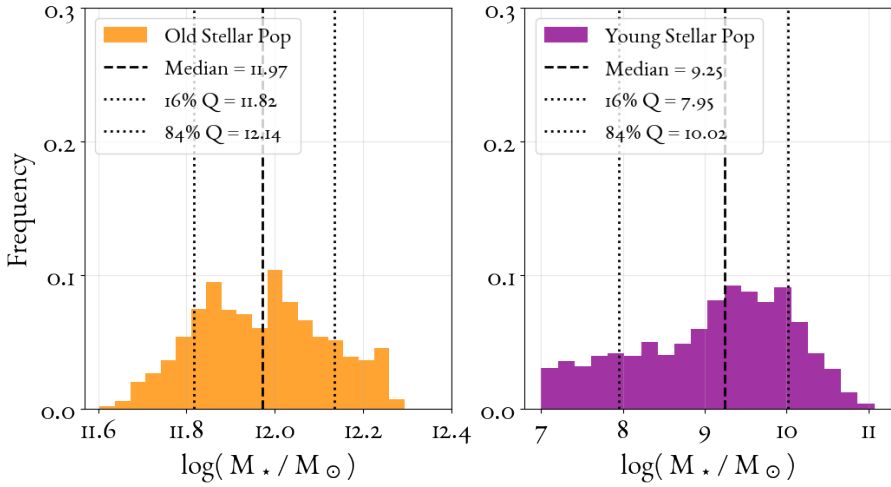


D

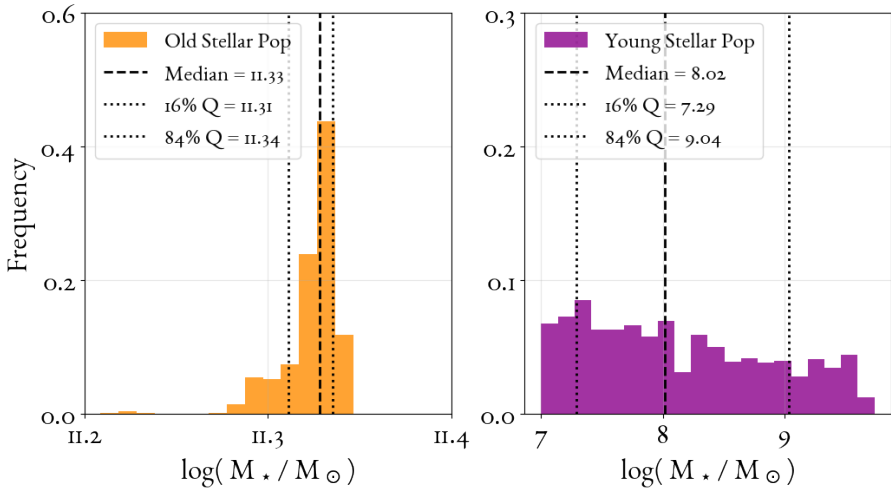
Mass Distributions of Fit Galaxies

The Stellar Mass probability distributions for each one of the 44 galaxies, product of the Bayesian sampling process. Multimodality is clear for certain cases. In the following figures, the left panel represents the old stellar population sampling (with ages between 1 Gyr and the age of the Universe at the galaxy's redshift) and the right panel represents the young stellar population sampling (with ages between 10 Myrs and 1 Gyr). The base-ten logarithm of stellar mass in units of M_{\odot} is plotted, the median value is clearly denoted, as well as the 16th and 84th percentile.

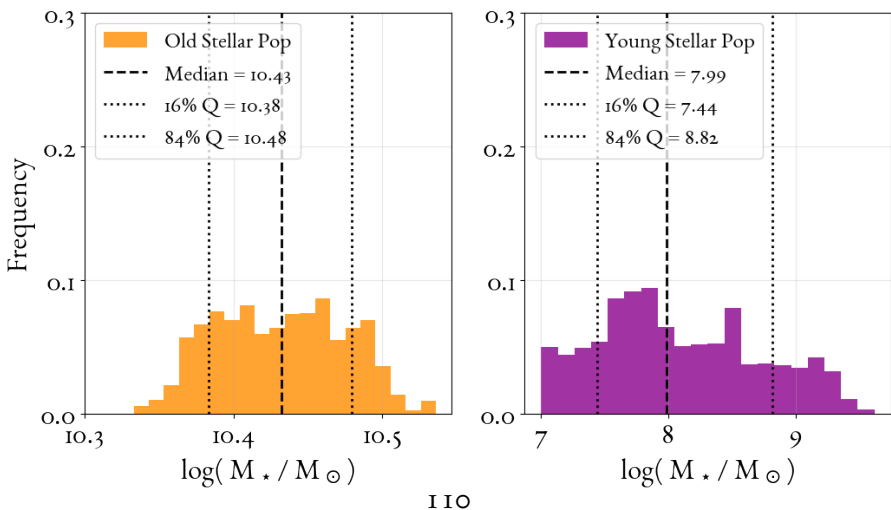
J0006-0623 / PKS 0003-066 Stellar Mass Distribution



J0009-3216 / IC 1531 Stellar Mass Distribution

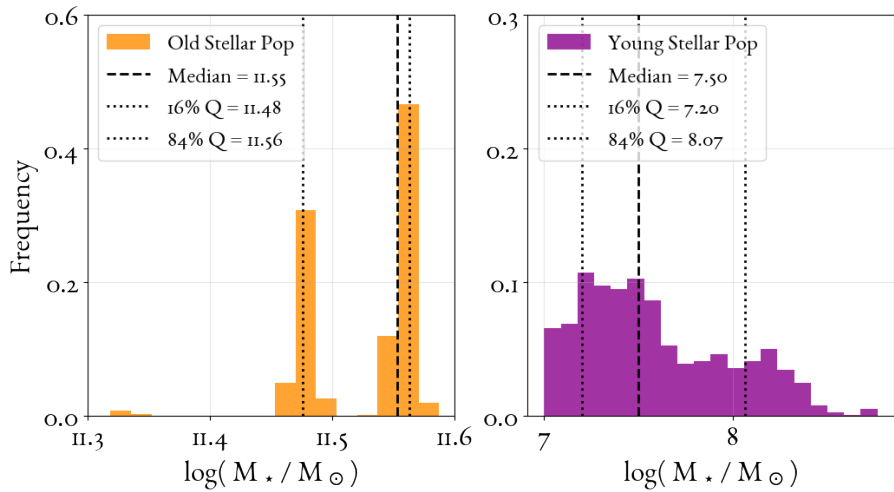


J0048+3157 / NGC 262 Stellar Mass Distribution

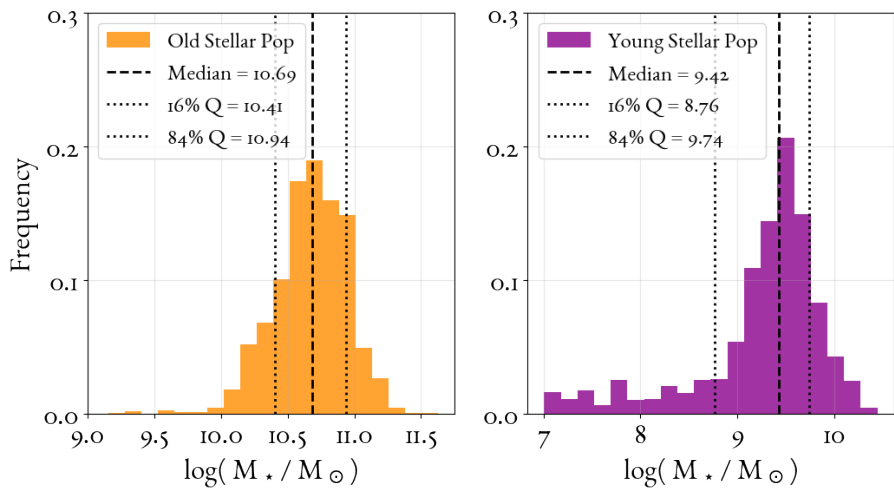


110

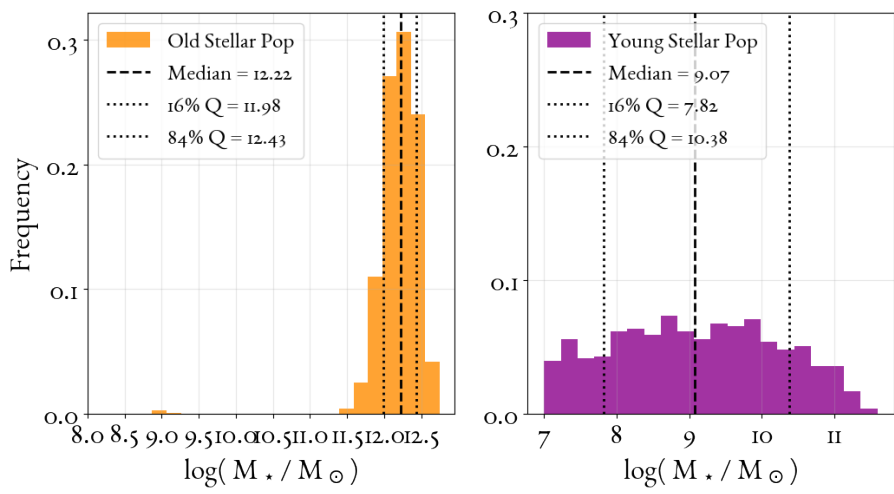
J0057+3021 / NGC 315 Stellar Mass Distribution



J0106-4034 / PKS 0104-408 Stellar Mass Distribution

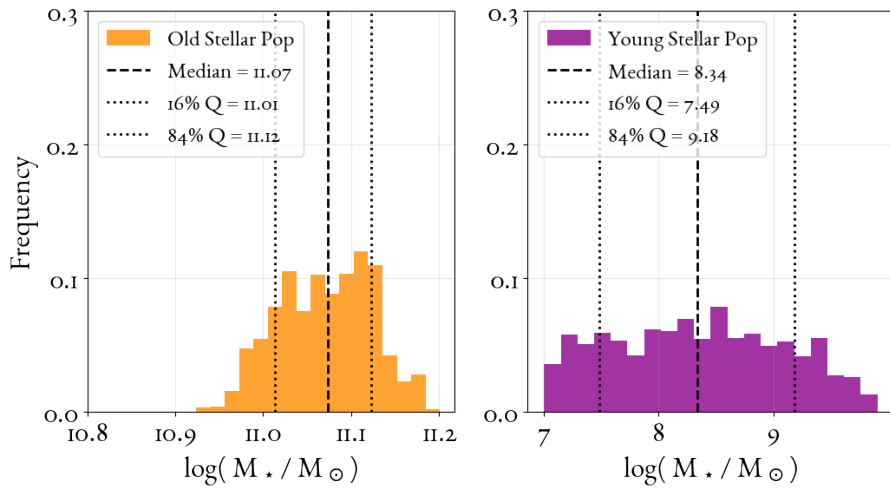


J0112-6634 / PKS 0110-668 Stellar Mass Distribution

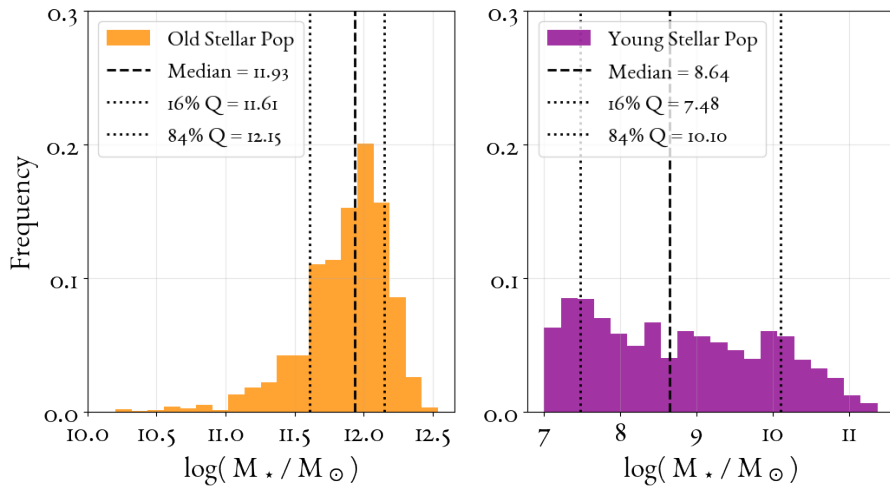


III

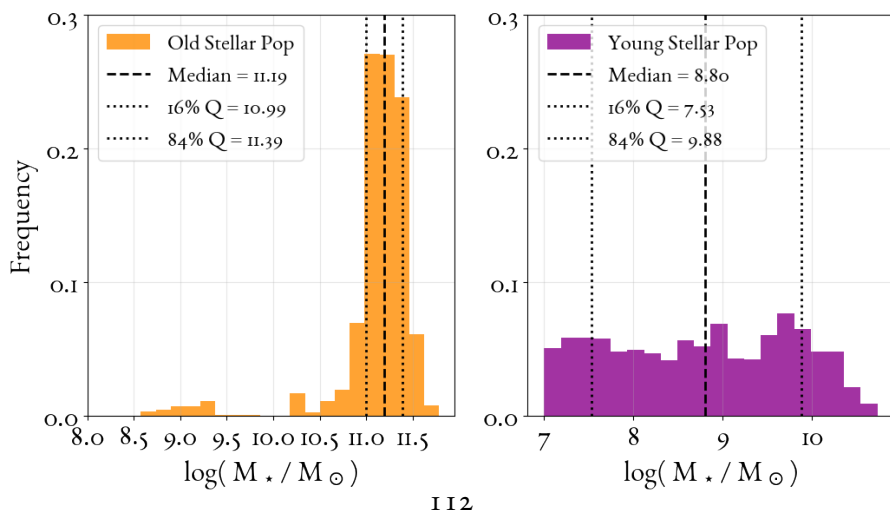
J0119+3210 / 4C +31.04 / QSO Bon16+319 Stellar Mass Distribution



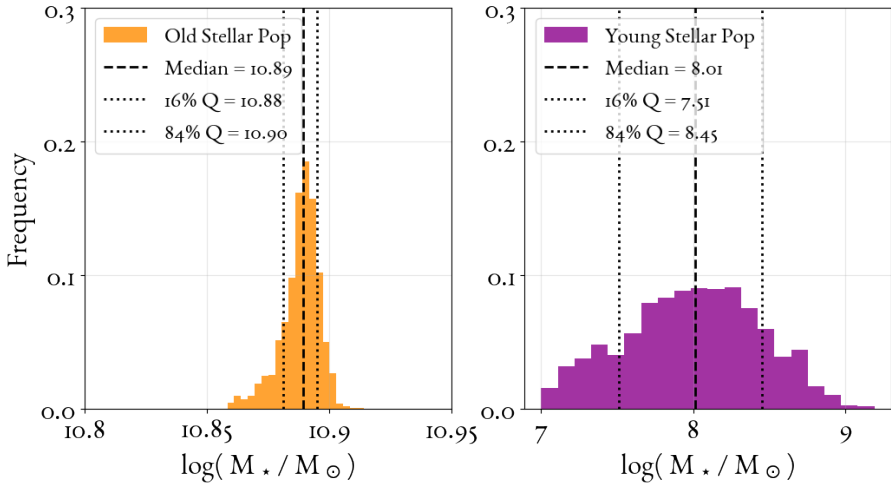
J0125-0005 / PKS 0122-003 Stellar Mass Distribution



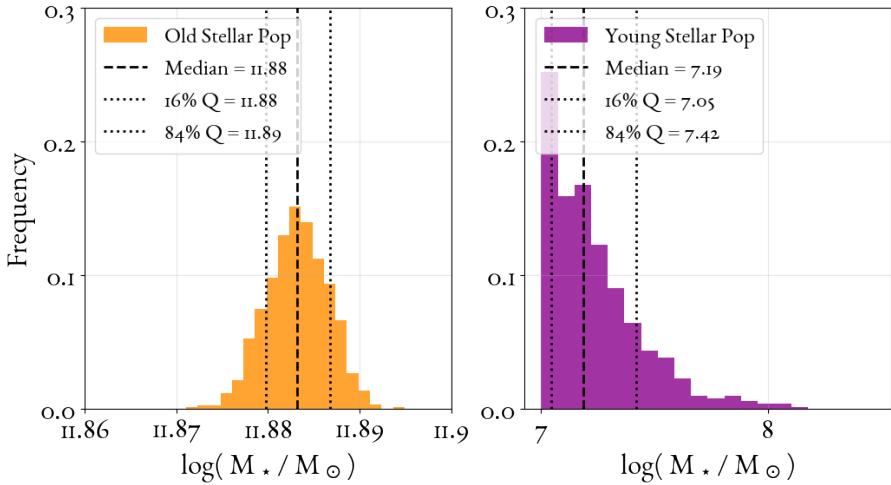
PKS 0324-228 Stellar Mass Distribution



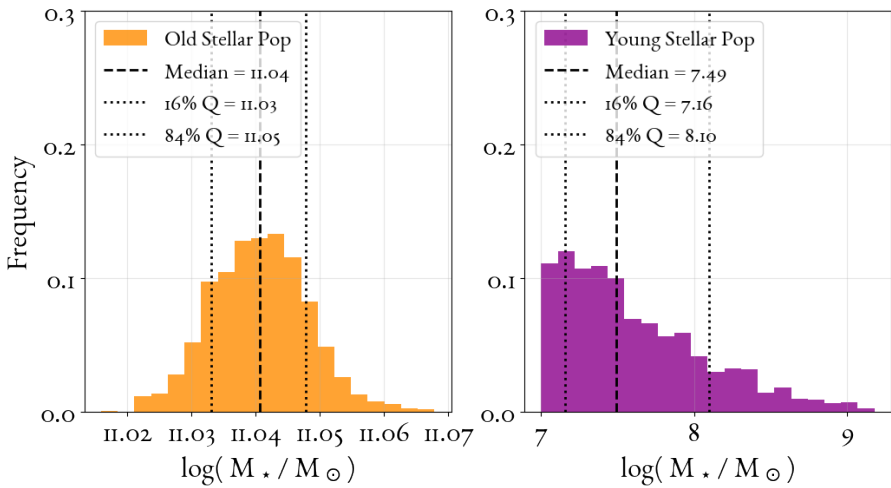
J0504-1014 / PKS 0502-10 Stellar Mass Distribution



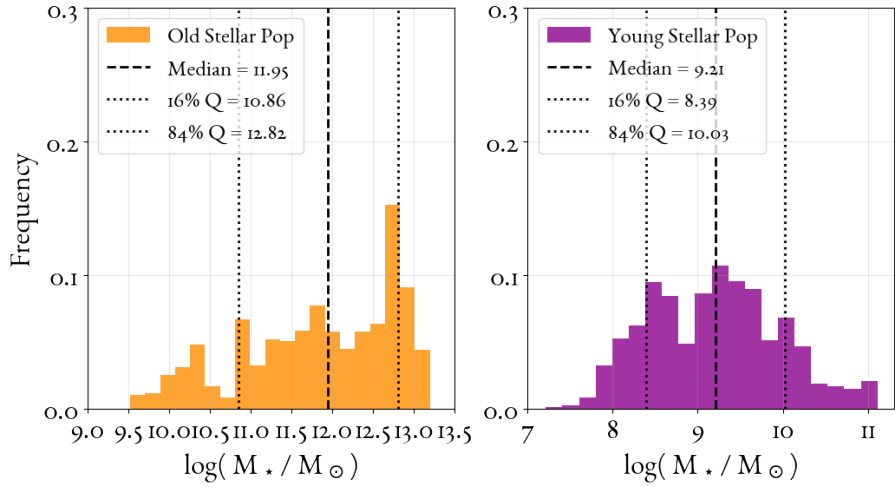
J0758+3747 / 3C 189 / NGC 2484 Stellar Mass Distribution



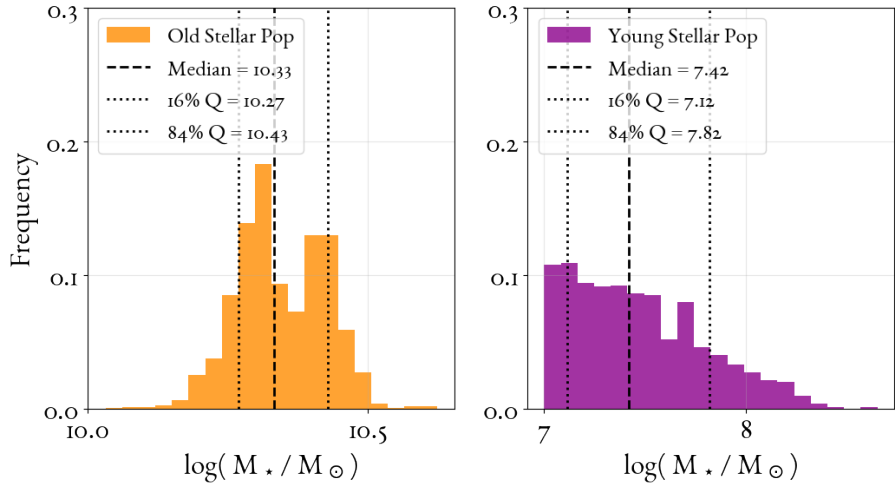
J0840+2949 / 4C +29.30 / CGCG 150-014 Stellar Mass Distribution



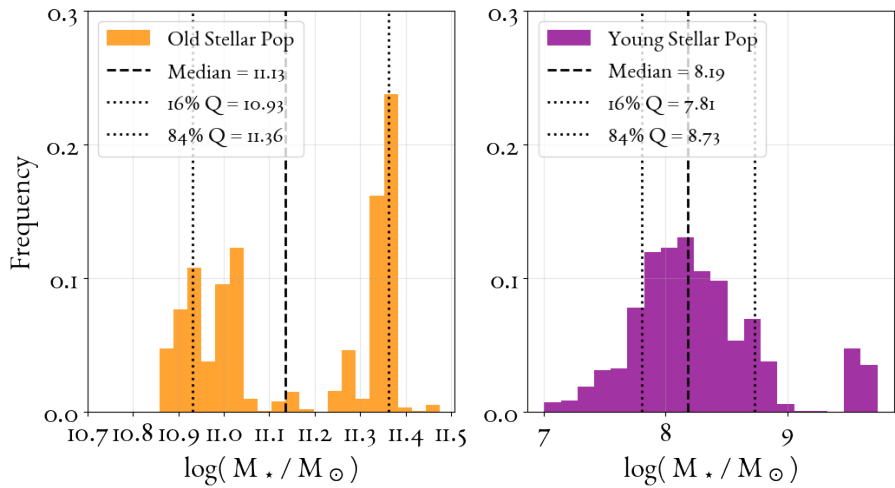
J0914+0245 / PKS 0912+029 Stellar Mass Distribution



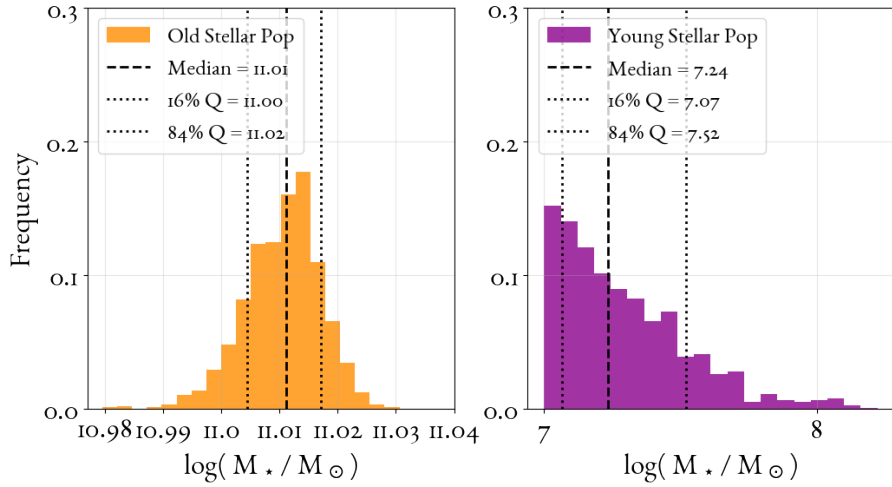
J1000-3139 / NGC 3100 Stellar Mass Distribution



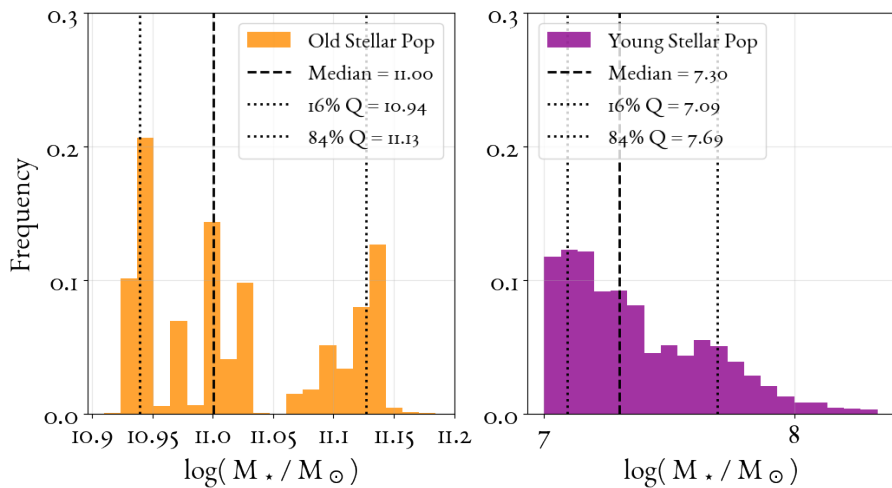
J1008+0029 / PKS 1005+007 Stellar Mass Distribution



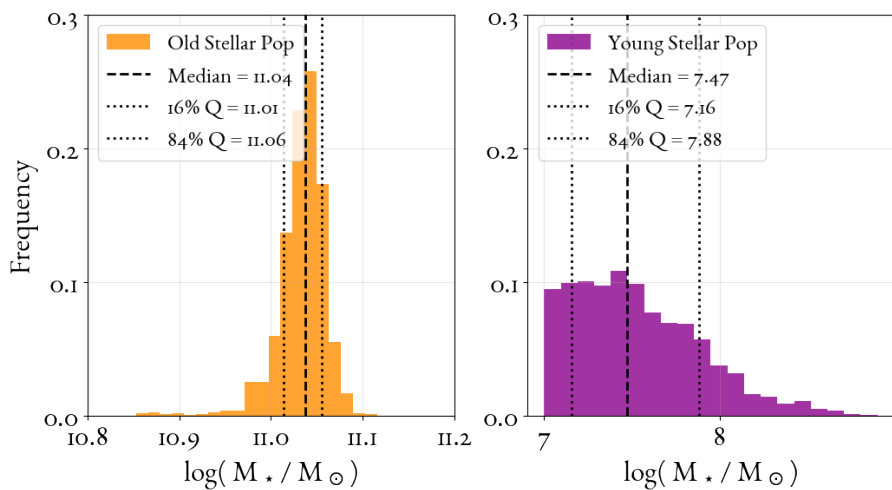
J1248-4118 / NGC 4696 / PKS 1245-410 Stellar Mass Distribution



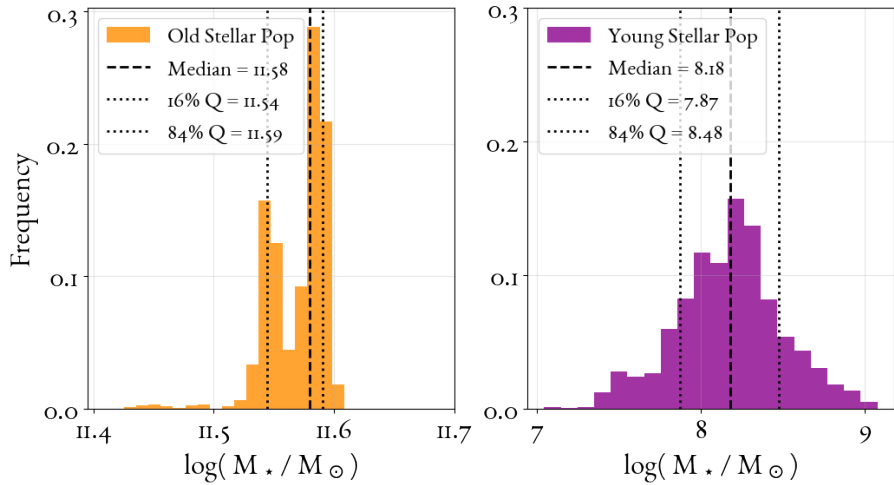
J1301-3226 / PKS 1258-321 Stellar Mass Distribution



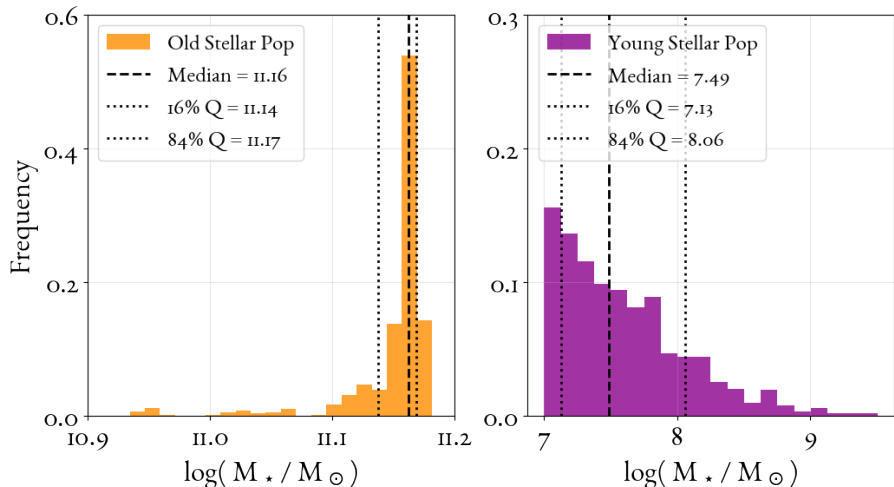
J1336-3357 / IC 4296 / PKS 1333-336 Stellar Mass Distribution



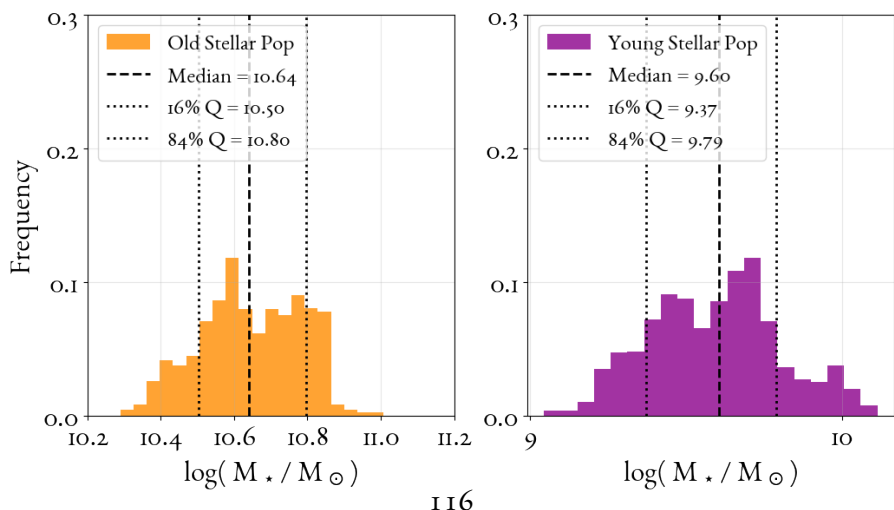
J1348+2635 / 4C 26.42 / PKS 1346+268 Stellar Mass Distribution



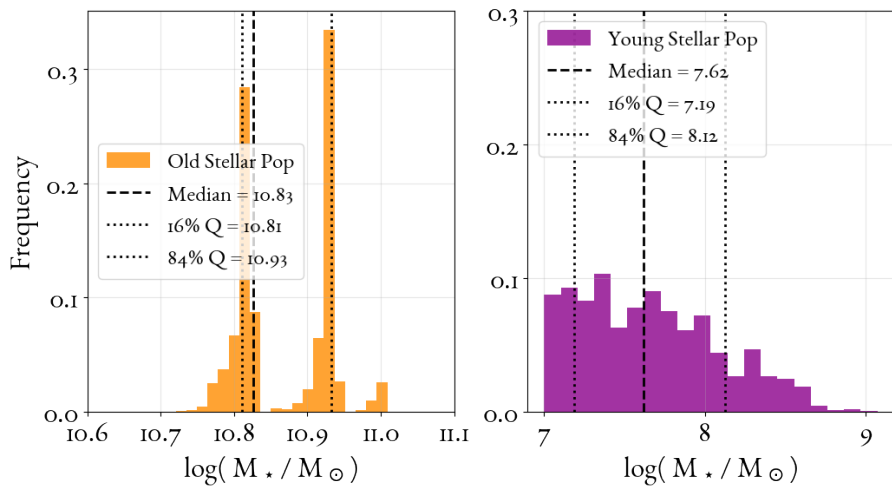
J1407-2701 / IC 4374 / PKS 1404-267 Stellar Mass Distribution



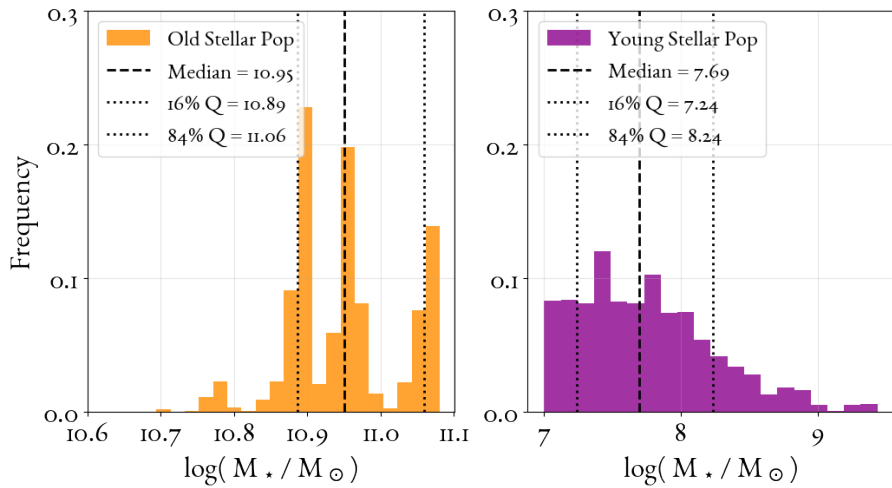
J1602+0157 / 3C 327 / PKS 1559+021 Stellar Mass Distribution



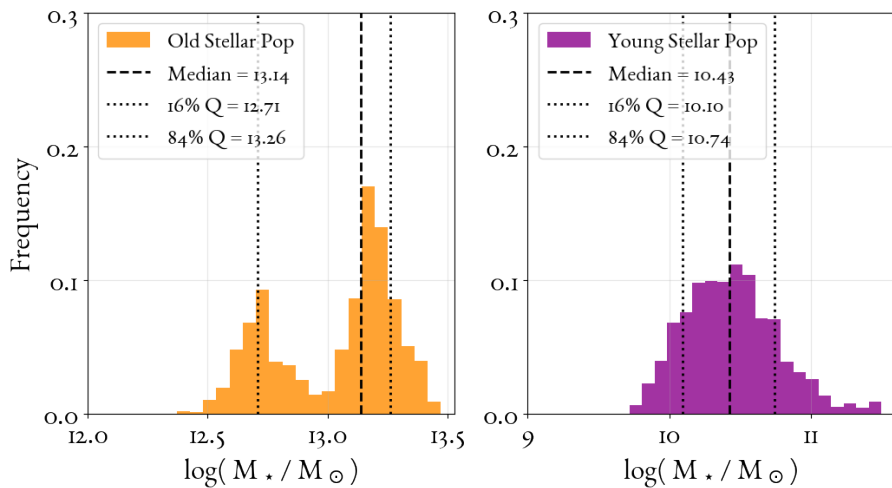
J1945-5520 / NGC 6812 / PKS 1941-554 Stellar Mass Distribution



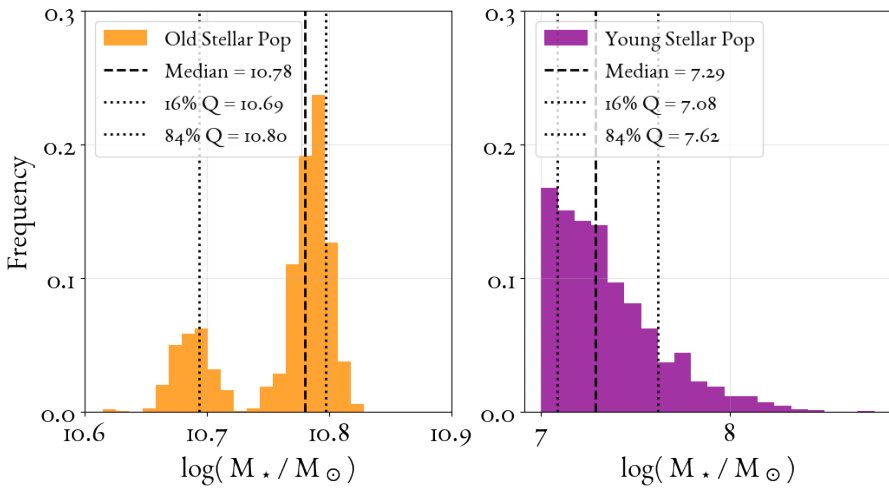
J2131-3837 / NGC 7075 / PKS 2128-388 Stellar Mass Distribution



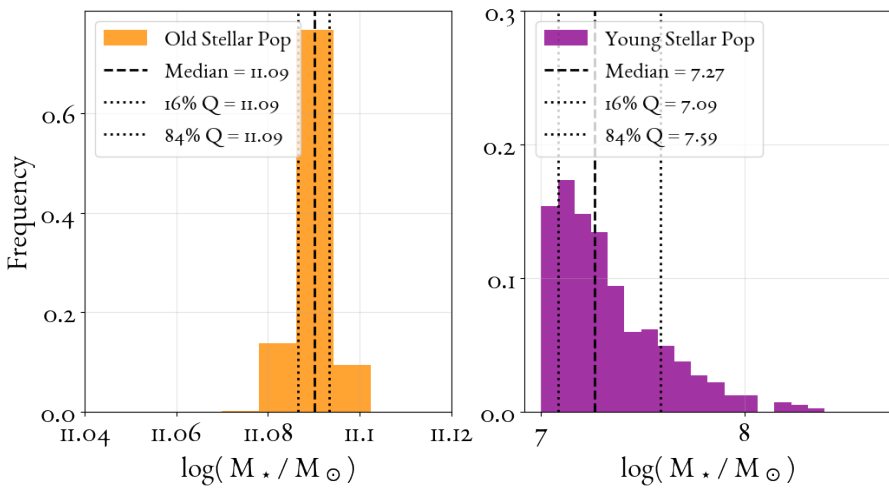
J2134-0153 / 4C -02.81 / PKS 2131-021 Stellar Mass Distribution



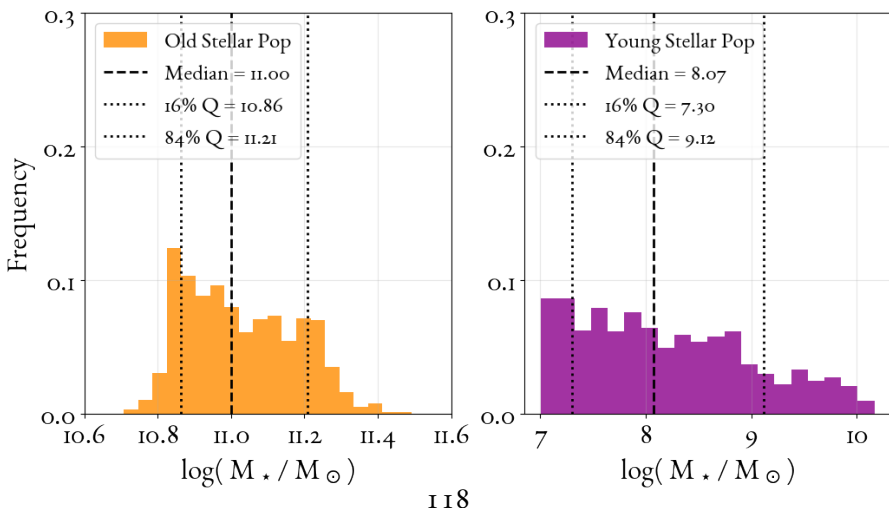
J2257-3627 / IC 1459 / PKS 2254-367 Stellar Mass Distribution



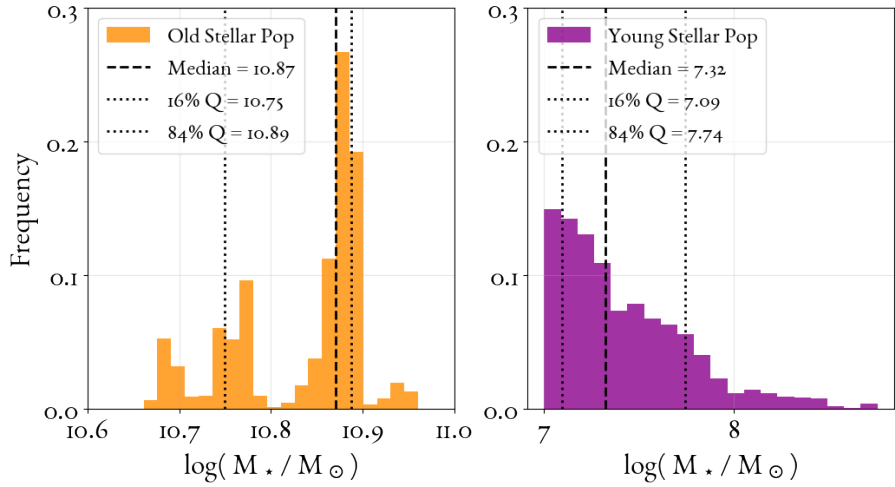
J2320+0812 / NGC 7626 / PKS 2318+079 Stellar Mass Distribution



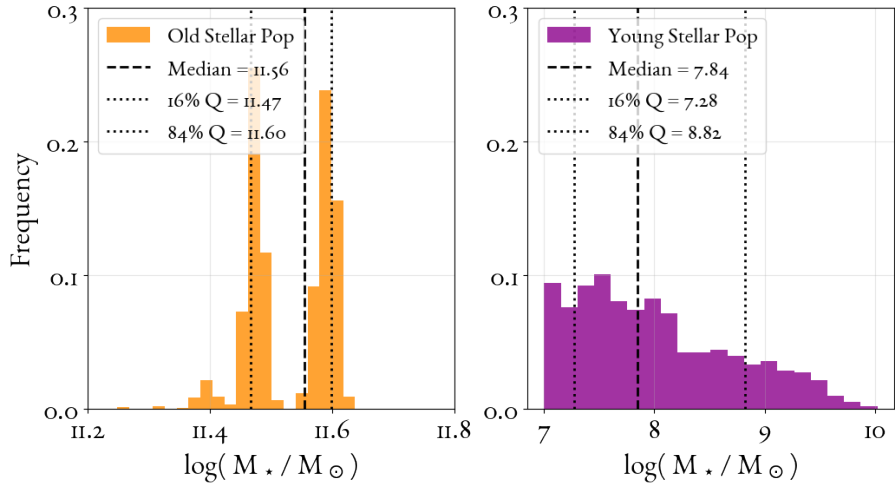
J2325-1207 / PKS 2322-123 Stellar Mass Distribution



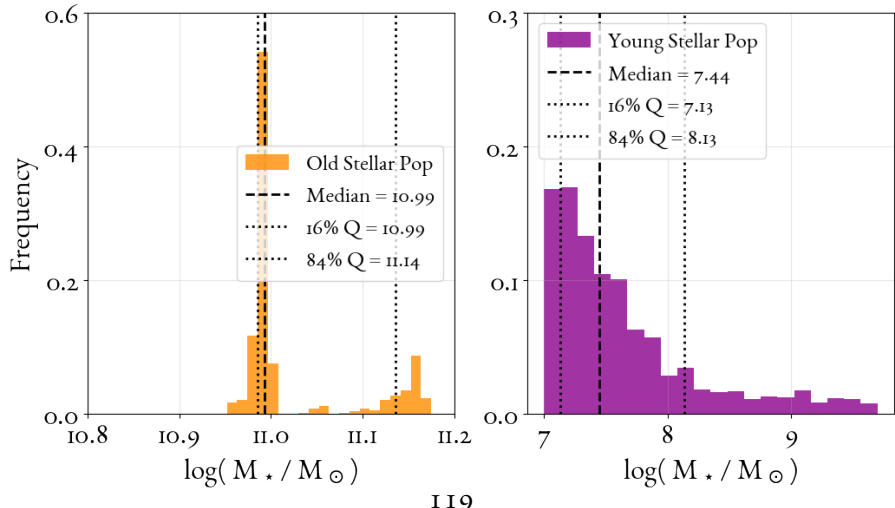
Jo125-0122 / NGC 541 / LEDA 5305 Stellar Mass Distribution



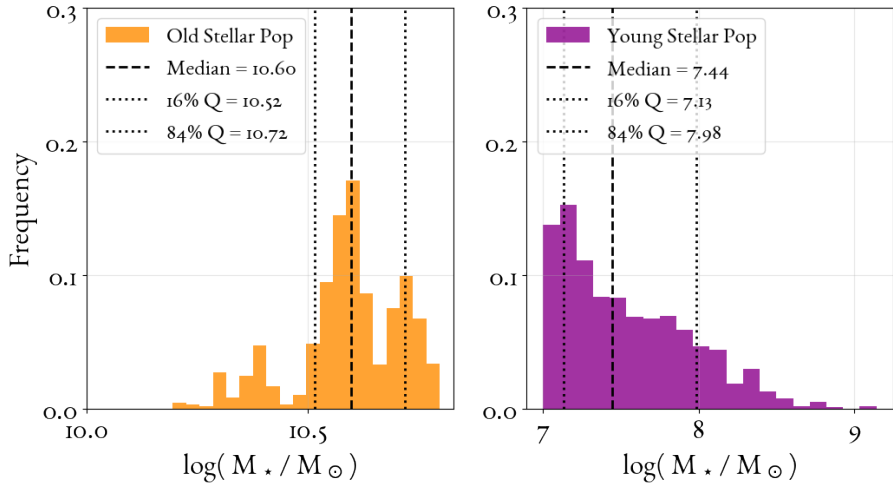
Jo156+0537 / NGC 741 / PKS 0153+053 Stellar Mass Distribution



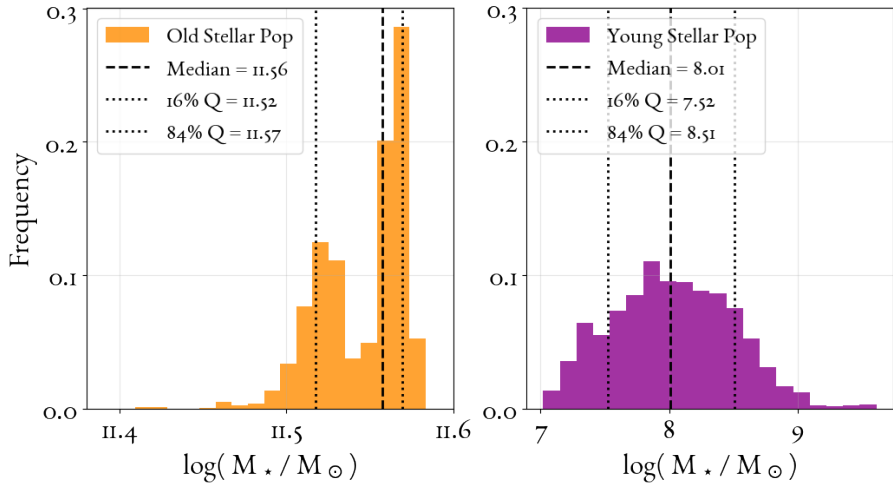
Jo709+4836 / NGC 2329 Stellar Mass Distribution



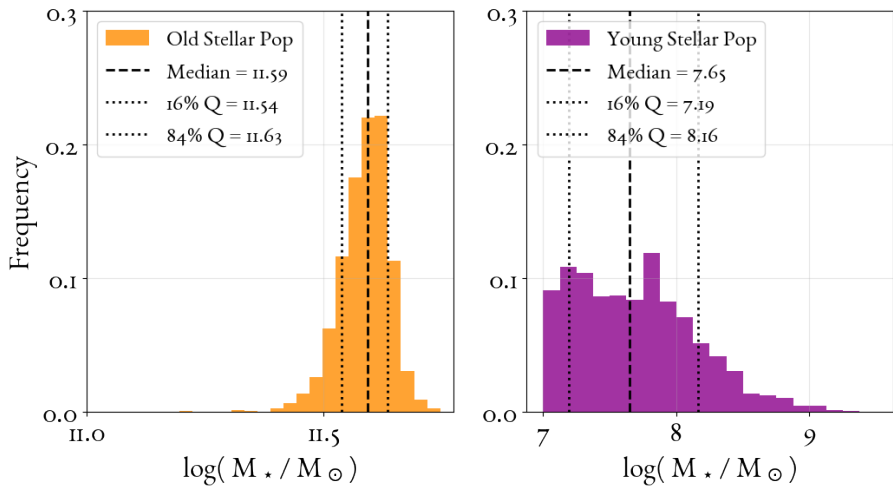
J2214+1350 / NGC 7236 / PKS 2212+135 Stellar Mass Distribution



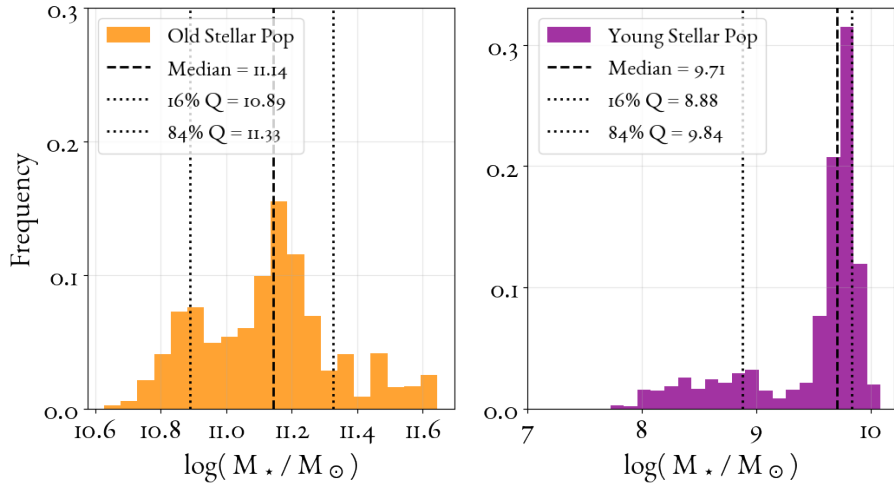
J1348+2635 / 4C 26.42 / PKS 1346+268 Stellar Mass Distribution



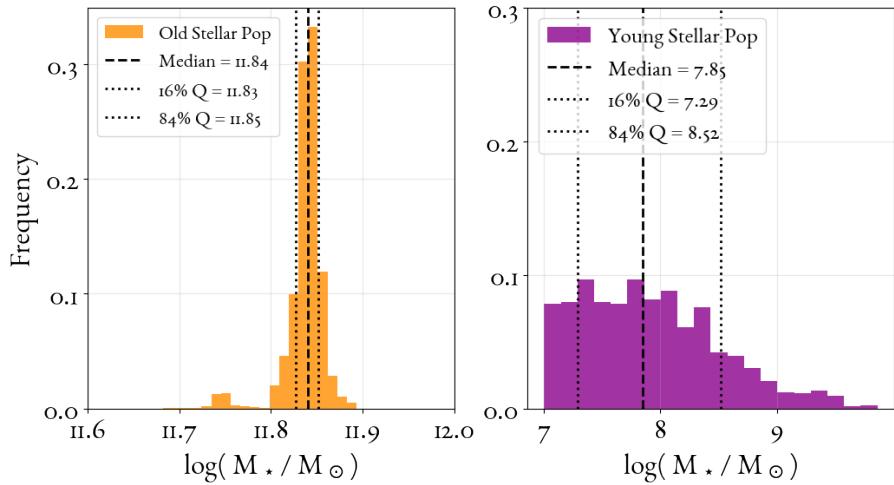
J1321+4235 / 3C 285 / LEDA 46625 Stellar Mass Distribution



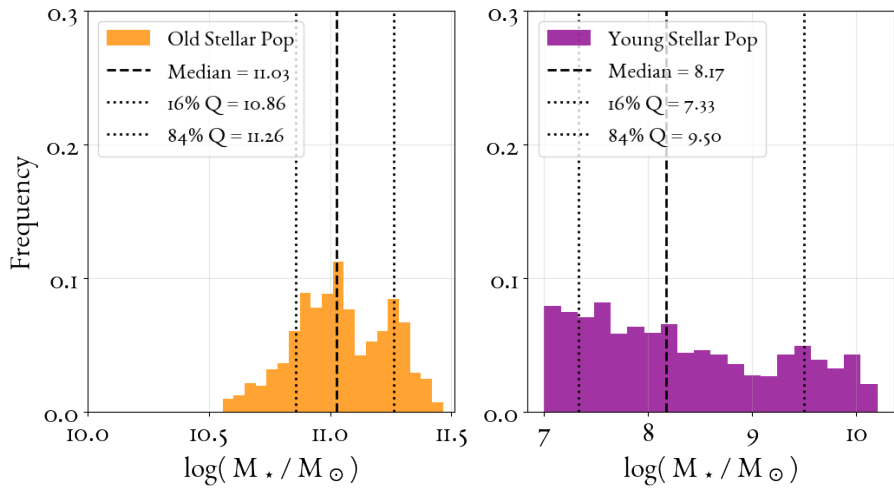
J1531+2404 / 3C 321 / PKS 1529+242 Stellar Mass Distribution



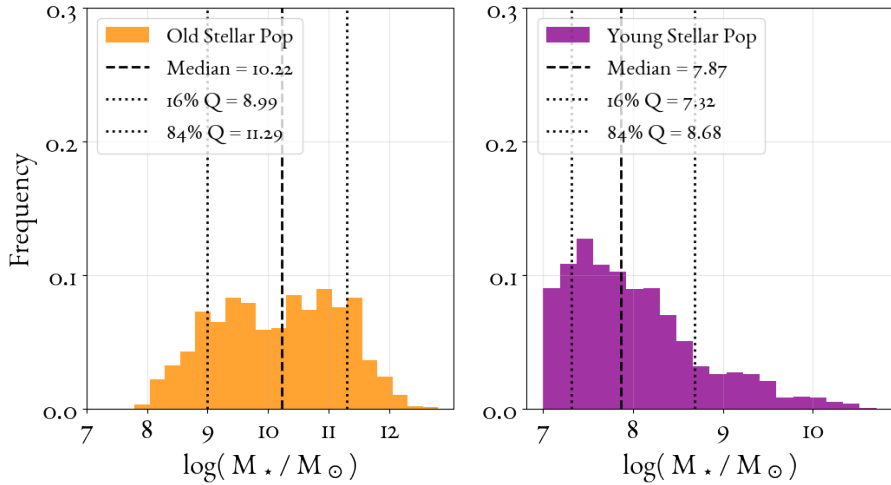
J0747-1917 / PKS 0745-191 Stellar Mass Distribution



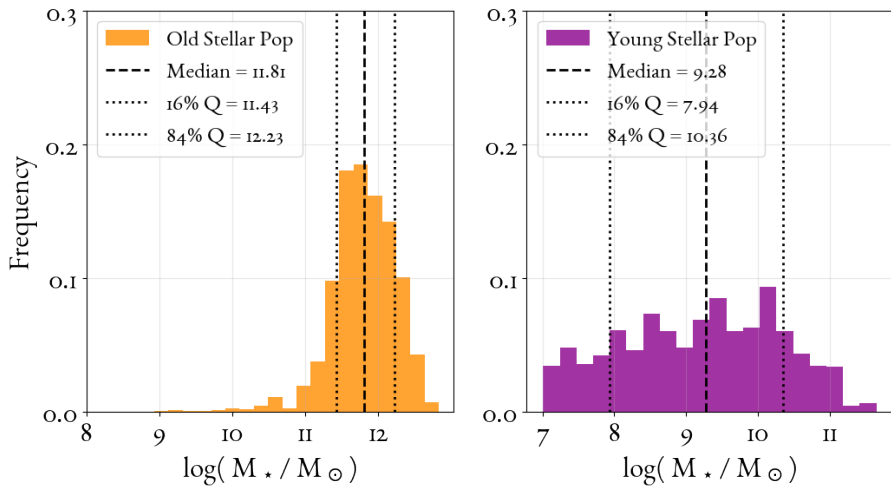
J0009+1244 / 4C 12.03 / PKS 0007+124 Stellar Mass Distribution



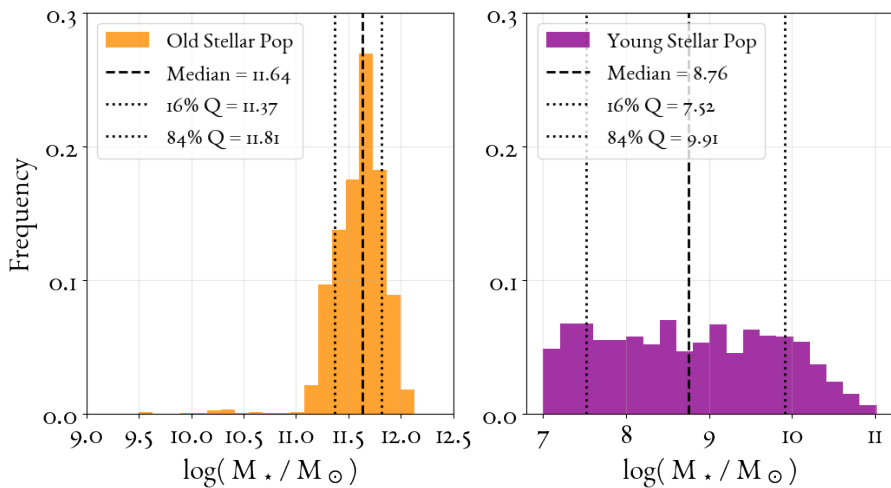
J011651-2052 / PKS 0114-21 Stellar Mass Distribution



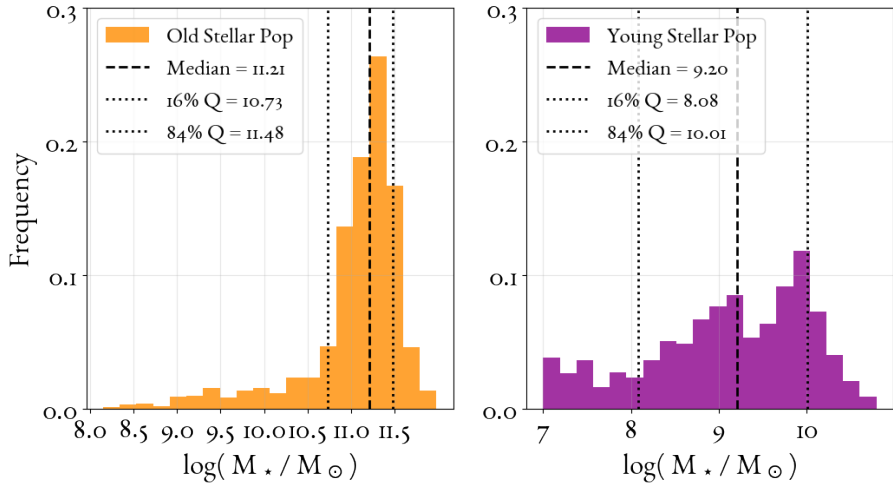
J0234+3134 / 3C 68.2 / LEDA 2820169 Stellar Mass Distribution



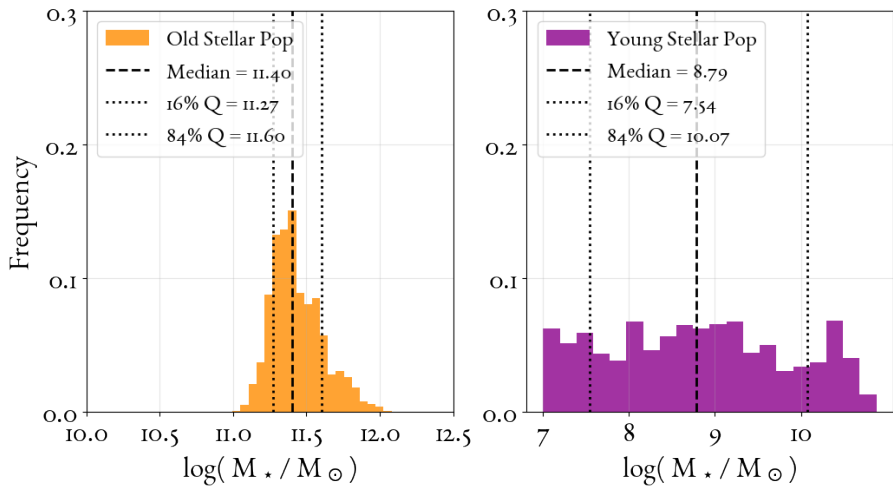
J0408-2418 / LEDA 2823818 / MRC 0406-244 Stellar Mass Distribution



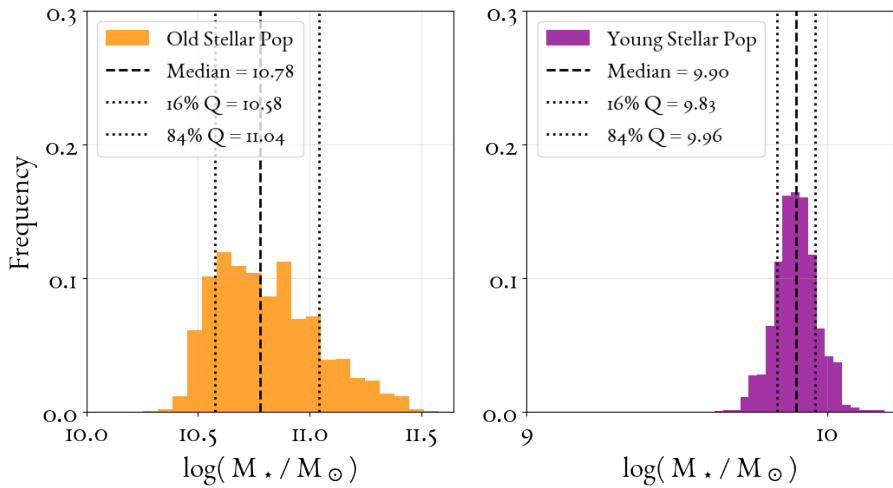
J2106-2405 / LEDA 2830749 / MRC 2104-242 Stellar Mass Distribution



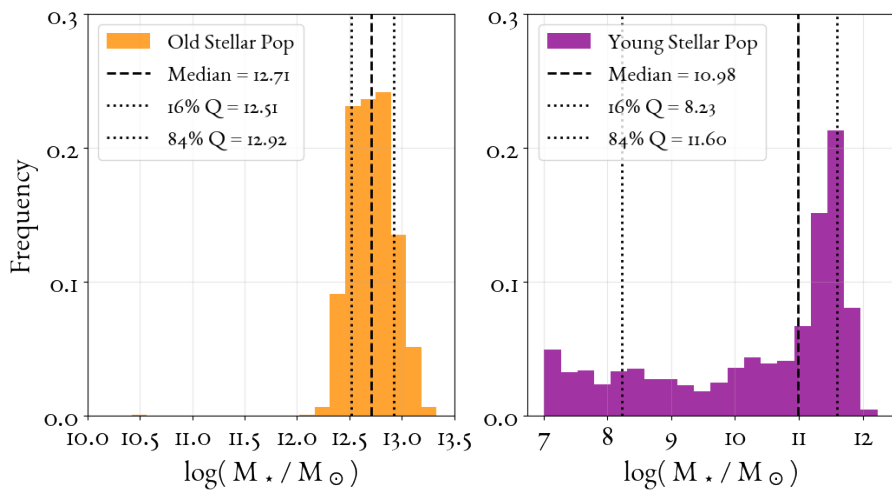
J0242-2132 / PKS 0240-217 Stellar Mass Distribution



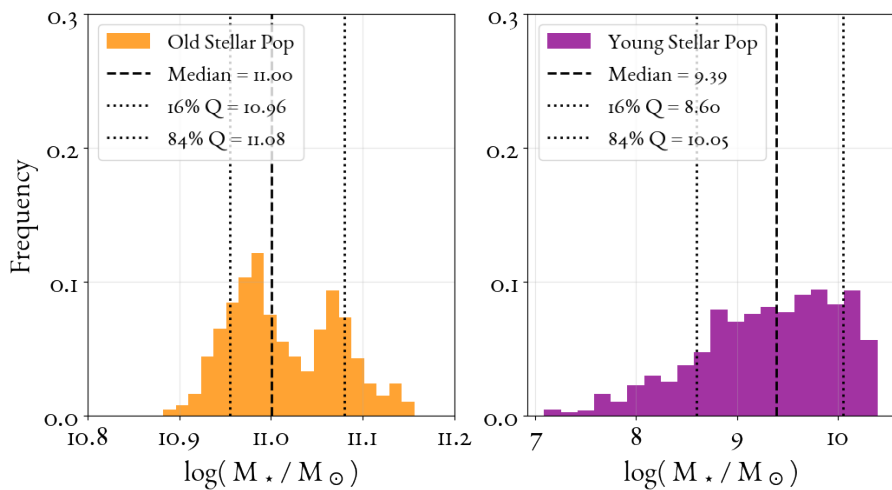
J1305-1033 / PKS 1302-103 Stellar Mass Distribution



J0403+2600 / PKS 0400+258 Stellar Mass Distribution



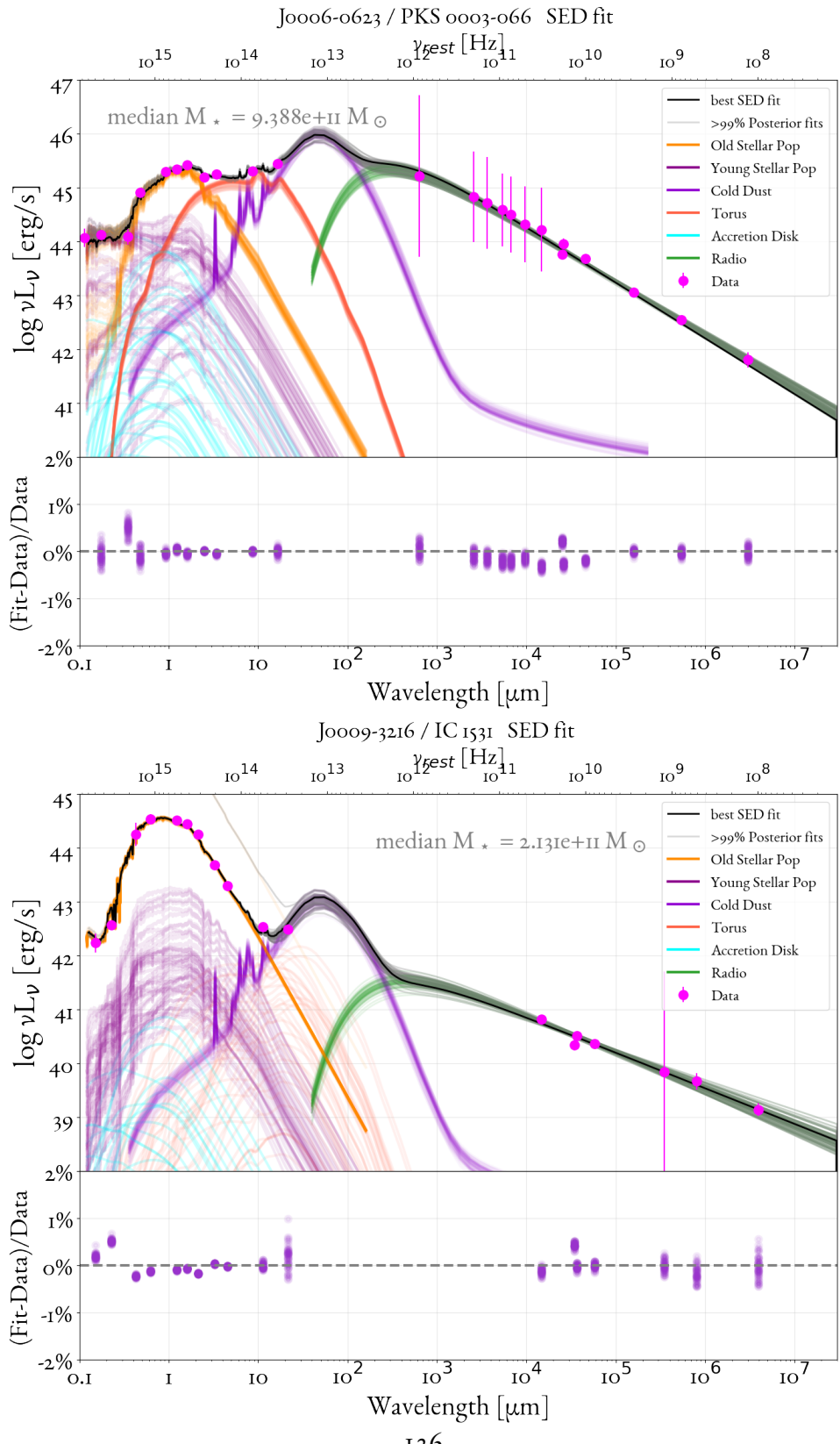
J1347+1217 / 4C 12.50 / PKS 1345+125 Stellar Mass Distribution

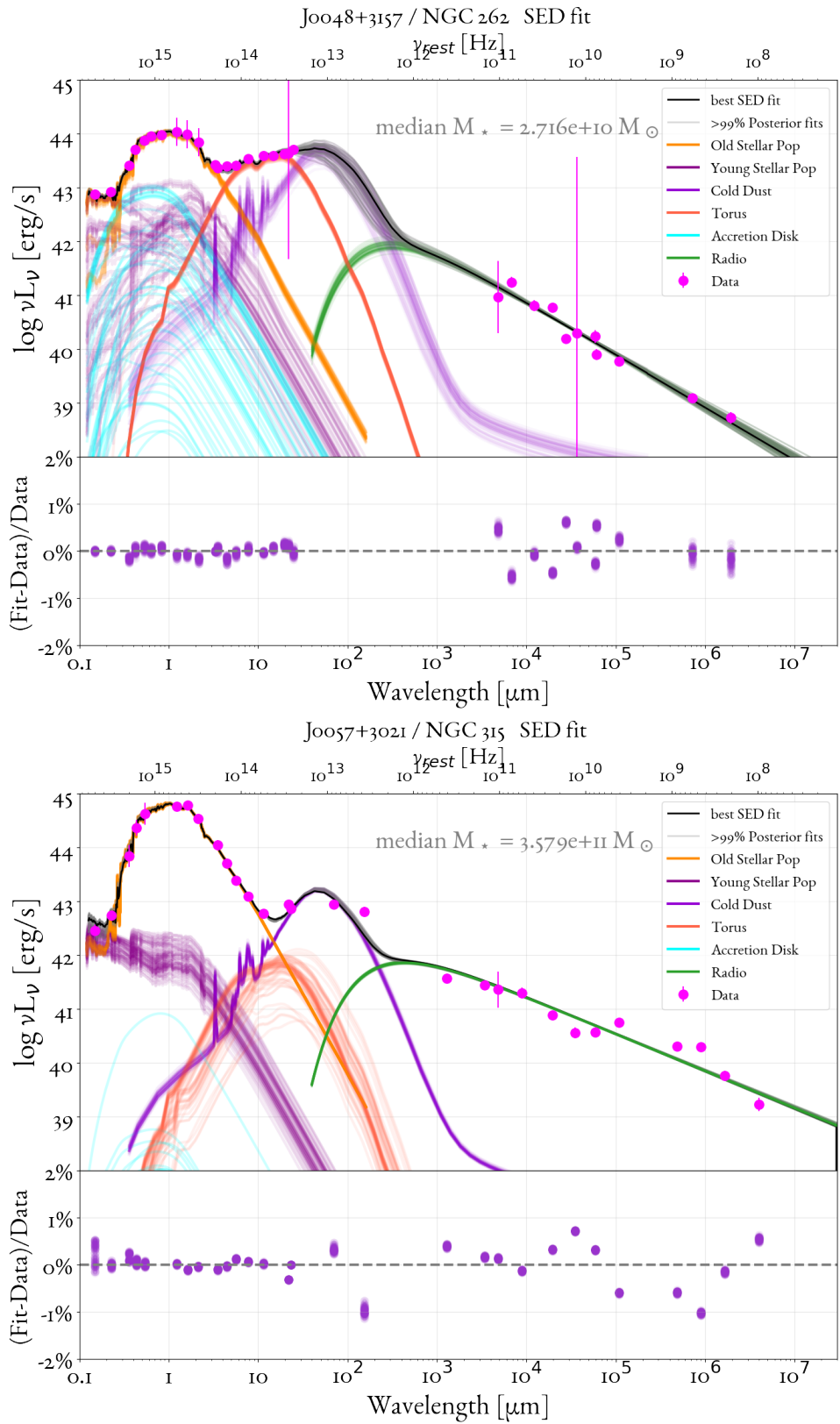


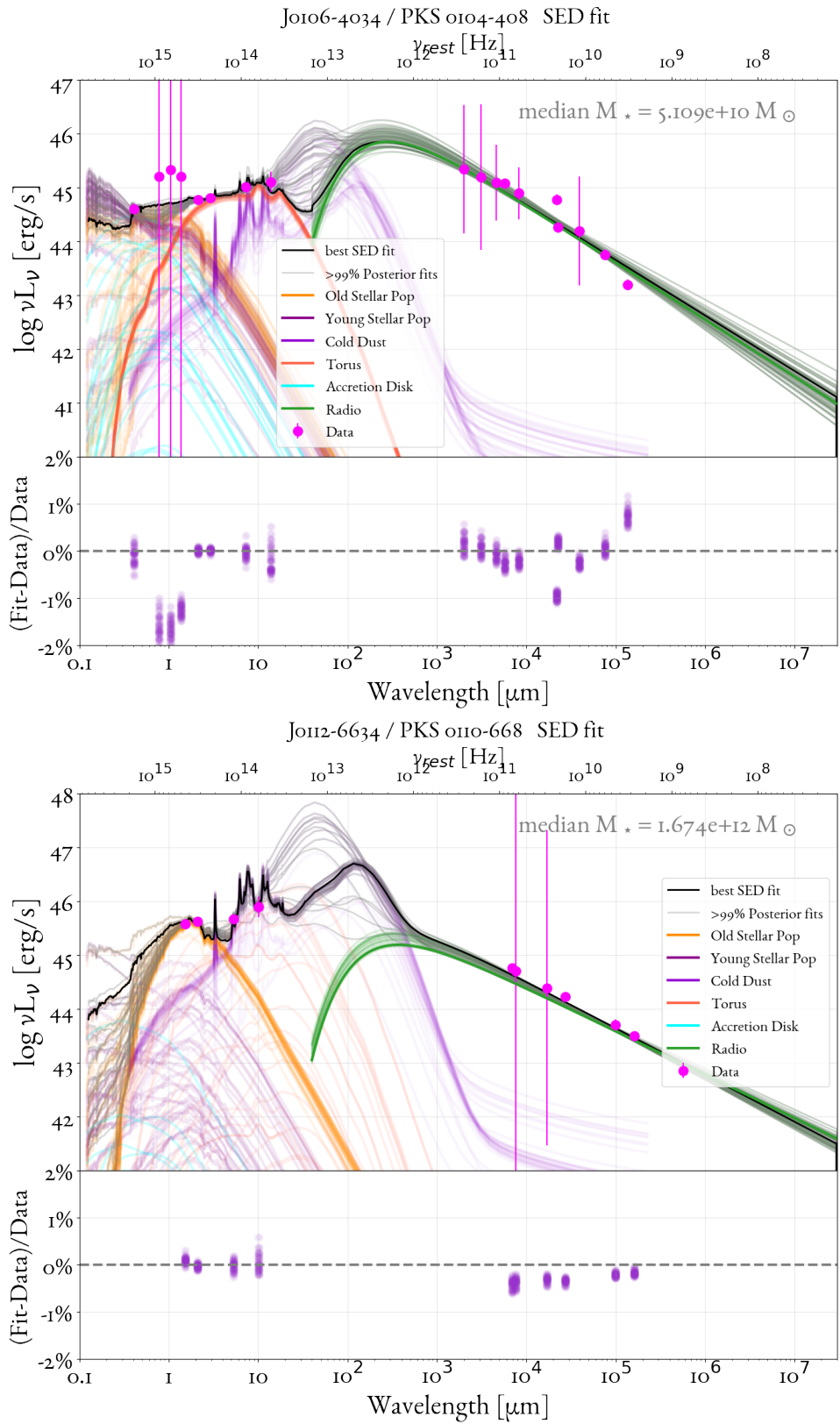
E

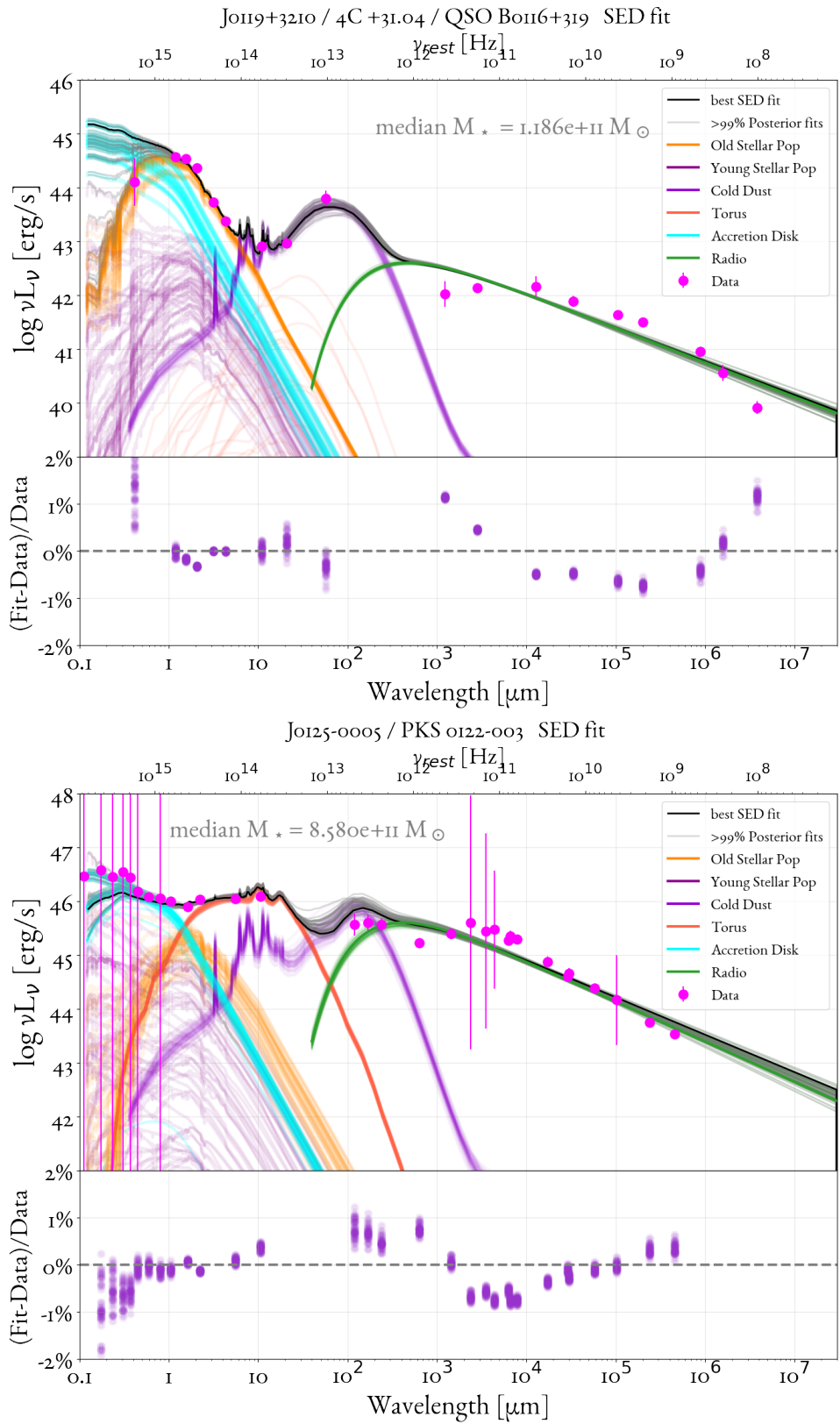
The Fit SEDs for 44 galaxies

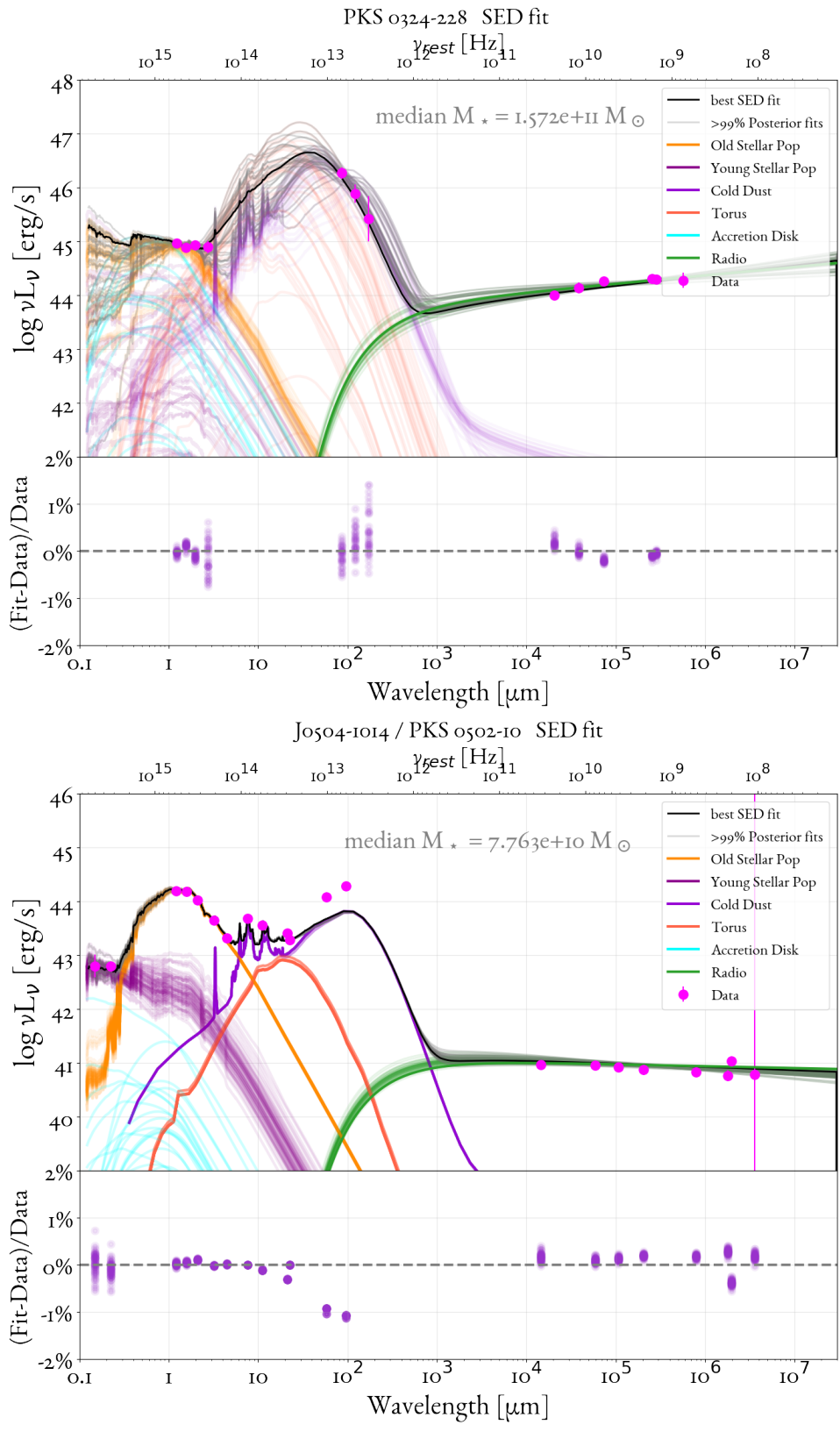
The SED observational data are plotted, along with the sampled SEDs (gray color) that correspond to Posterior higher than the 99% percentile of the sampled Posterior (i.e. the 1% highest sampled Posterior) and their components (in different vivid colors). The best fit corresponds to the highest posterior fit and is denoted with a black line. All SEDs are portrayed in each galaxy's restframe. For most galaxies the fit model is representative of the data, with the residuals in less than 2%.

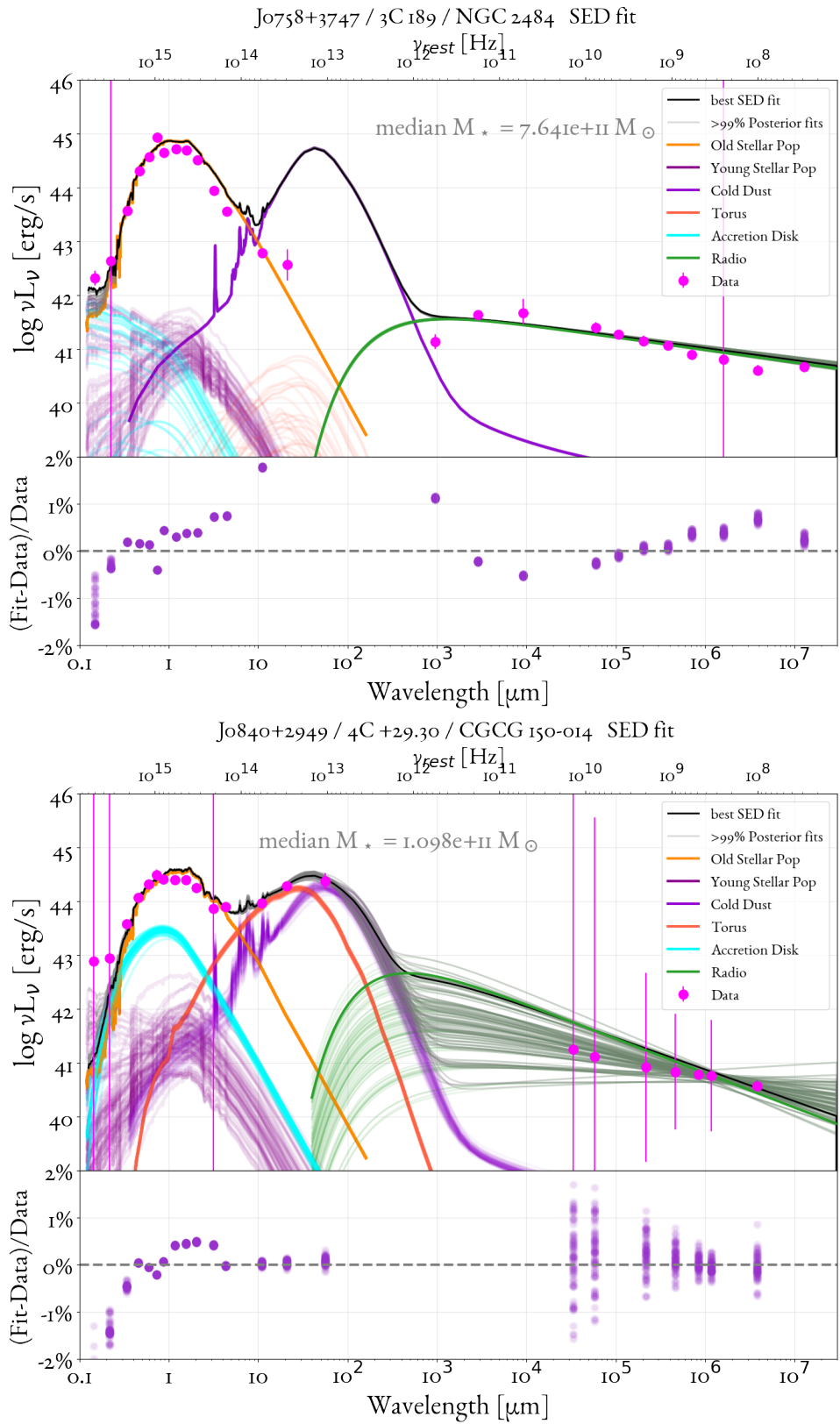


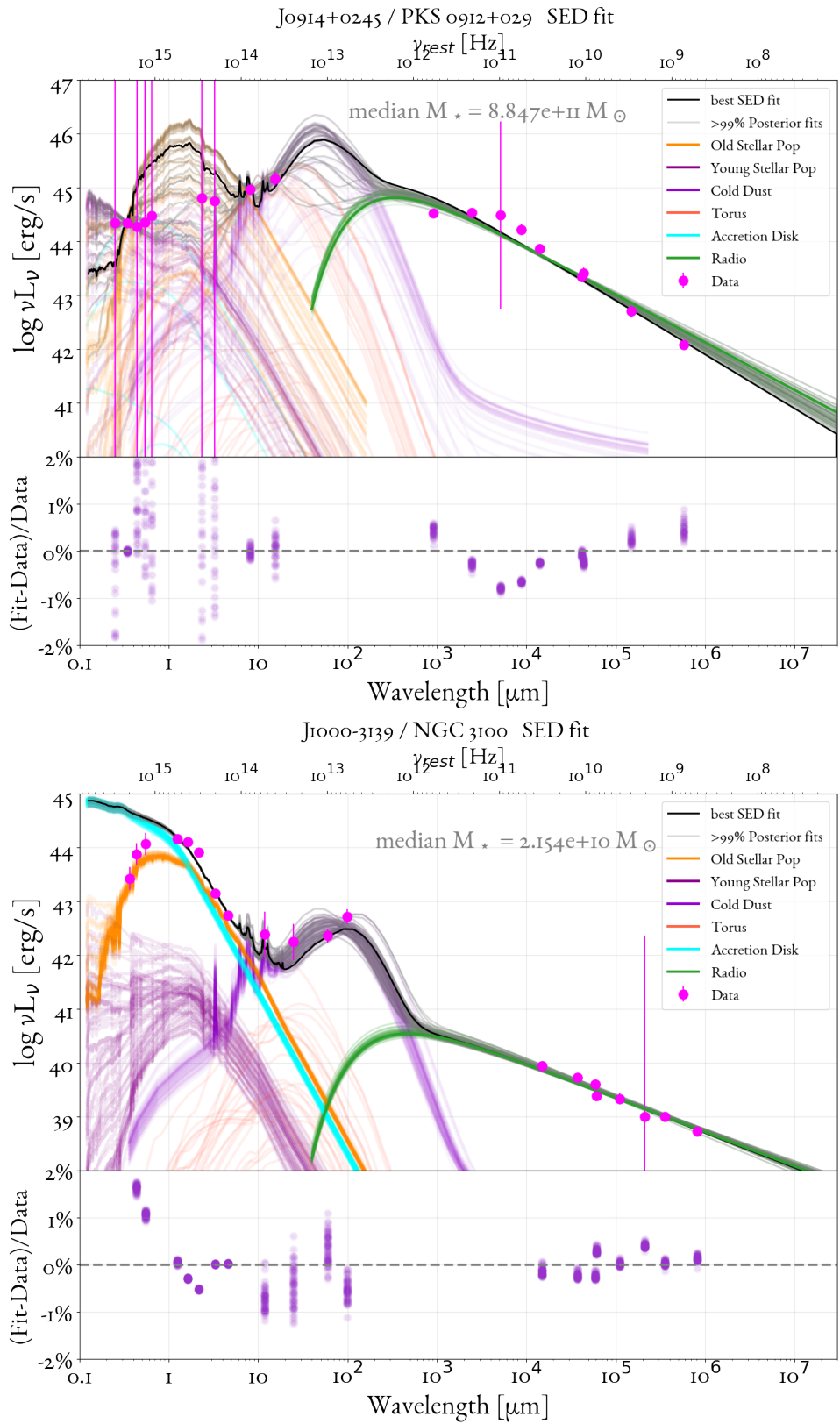


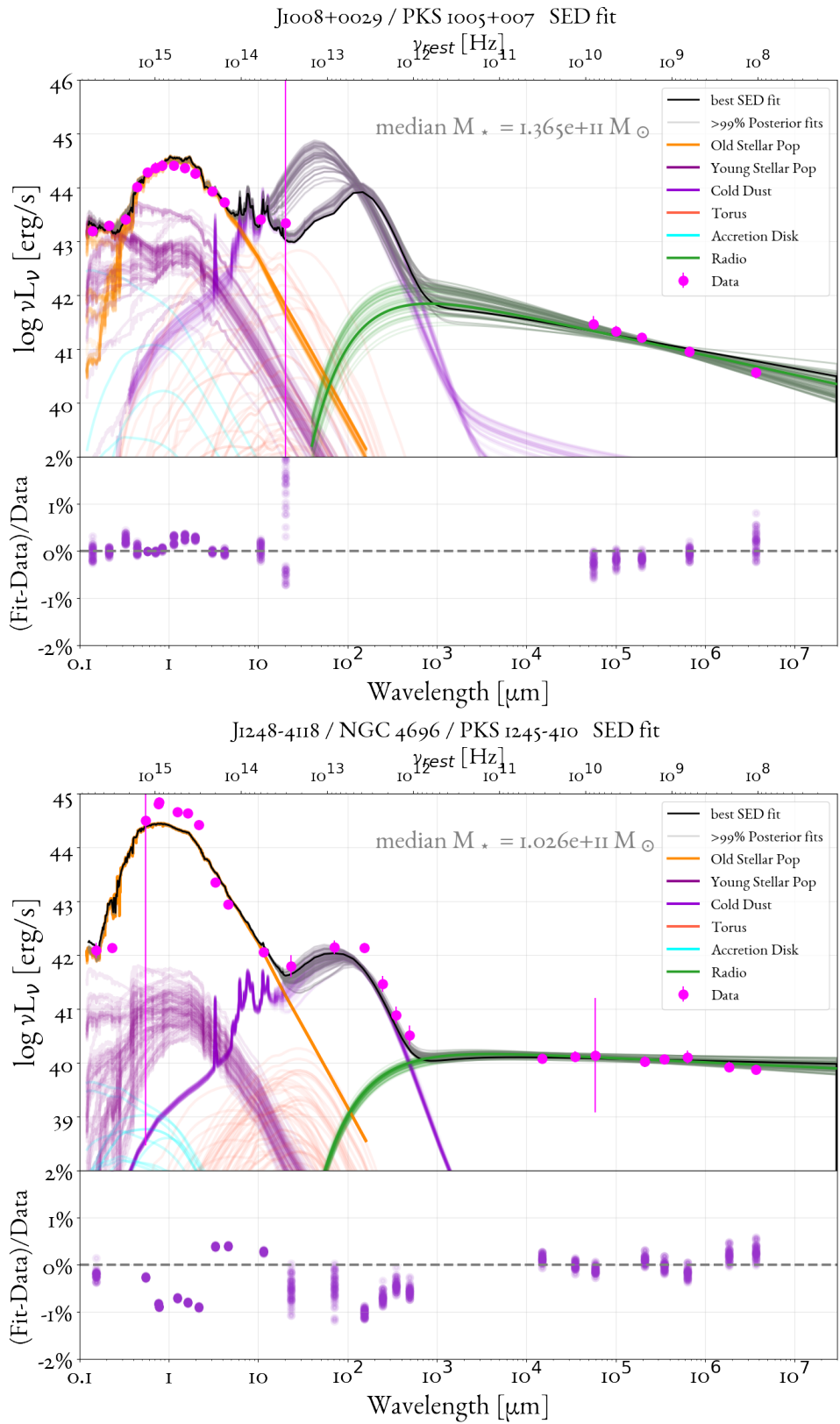


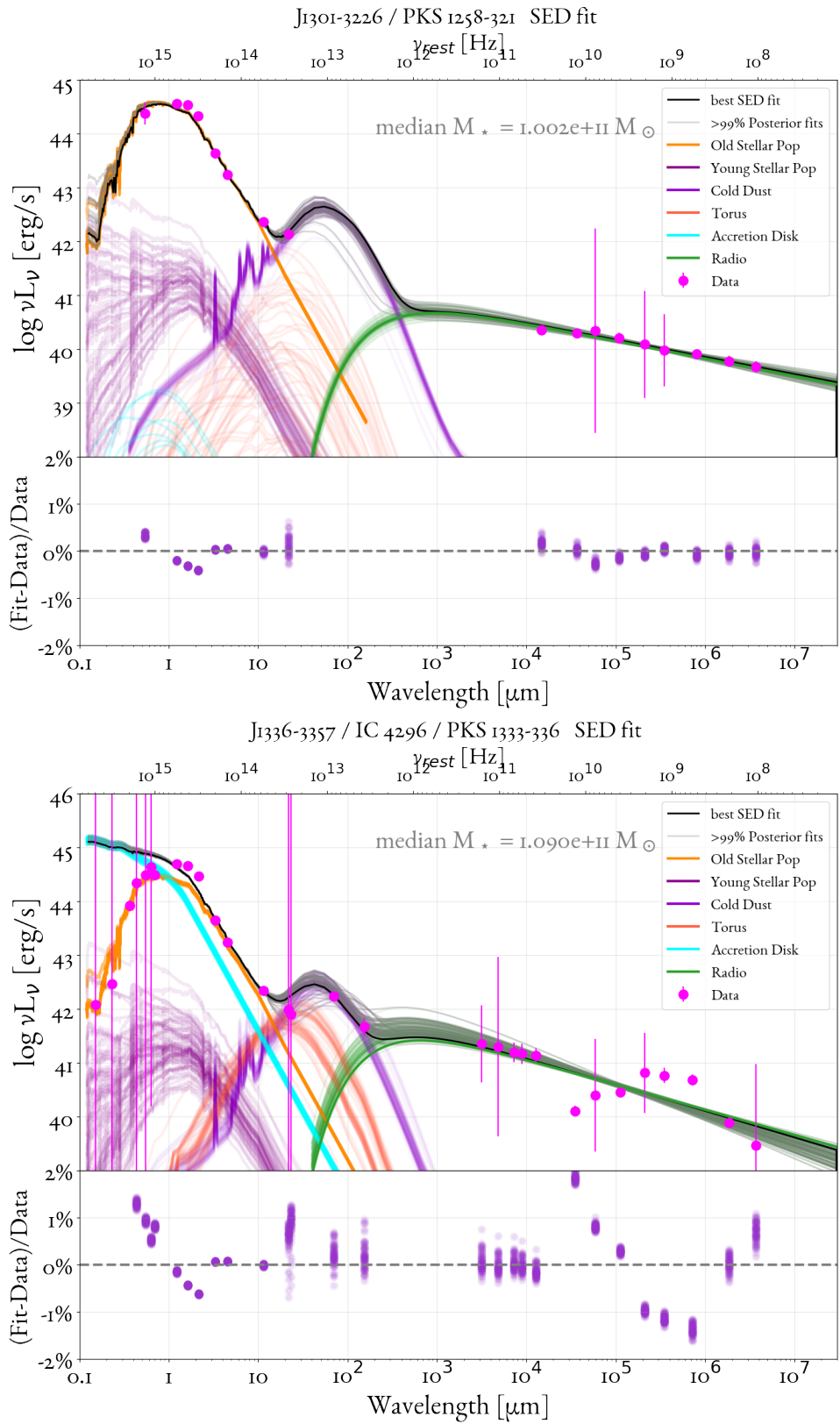


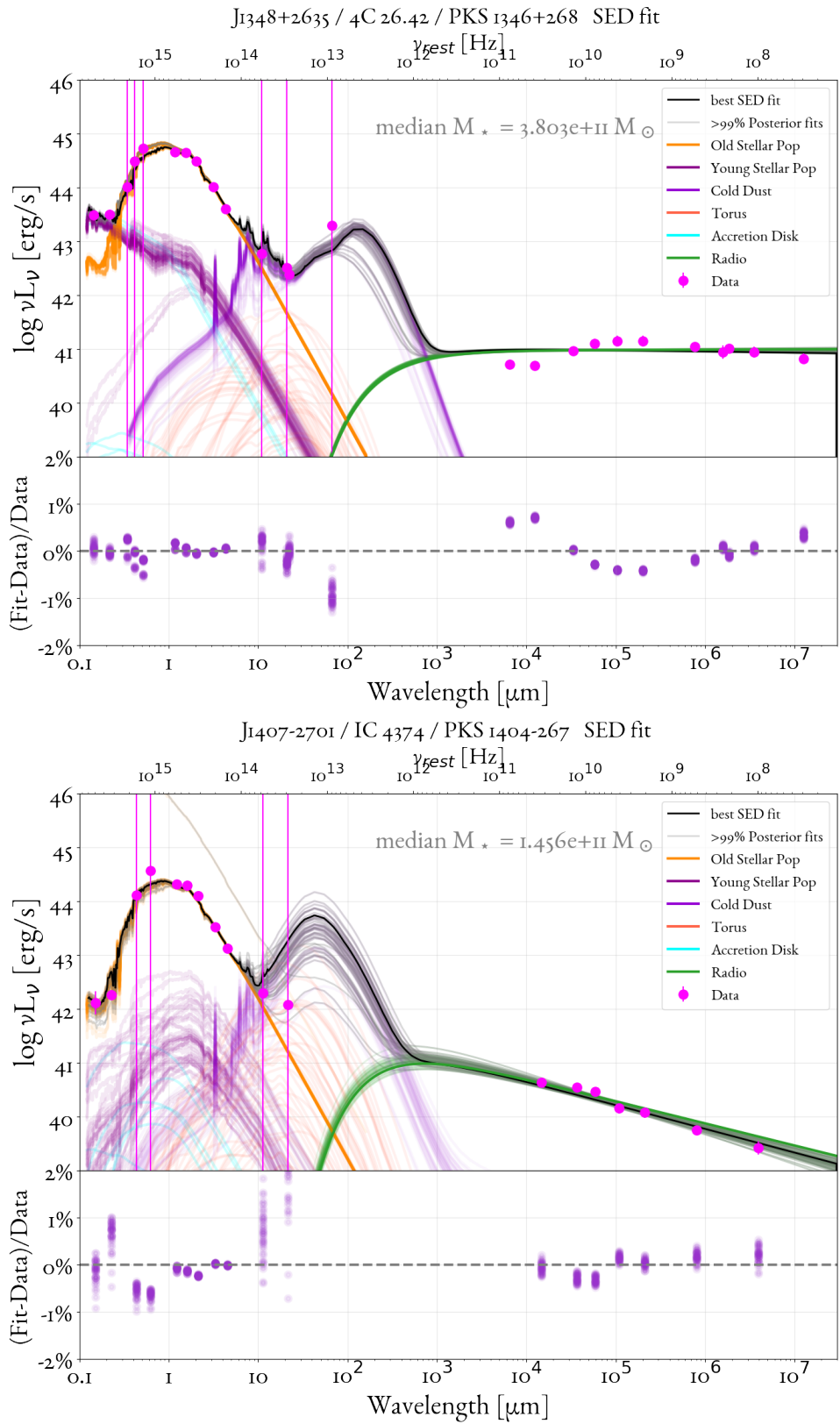


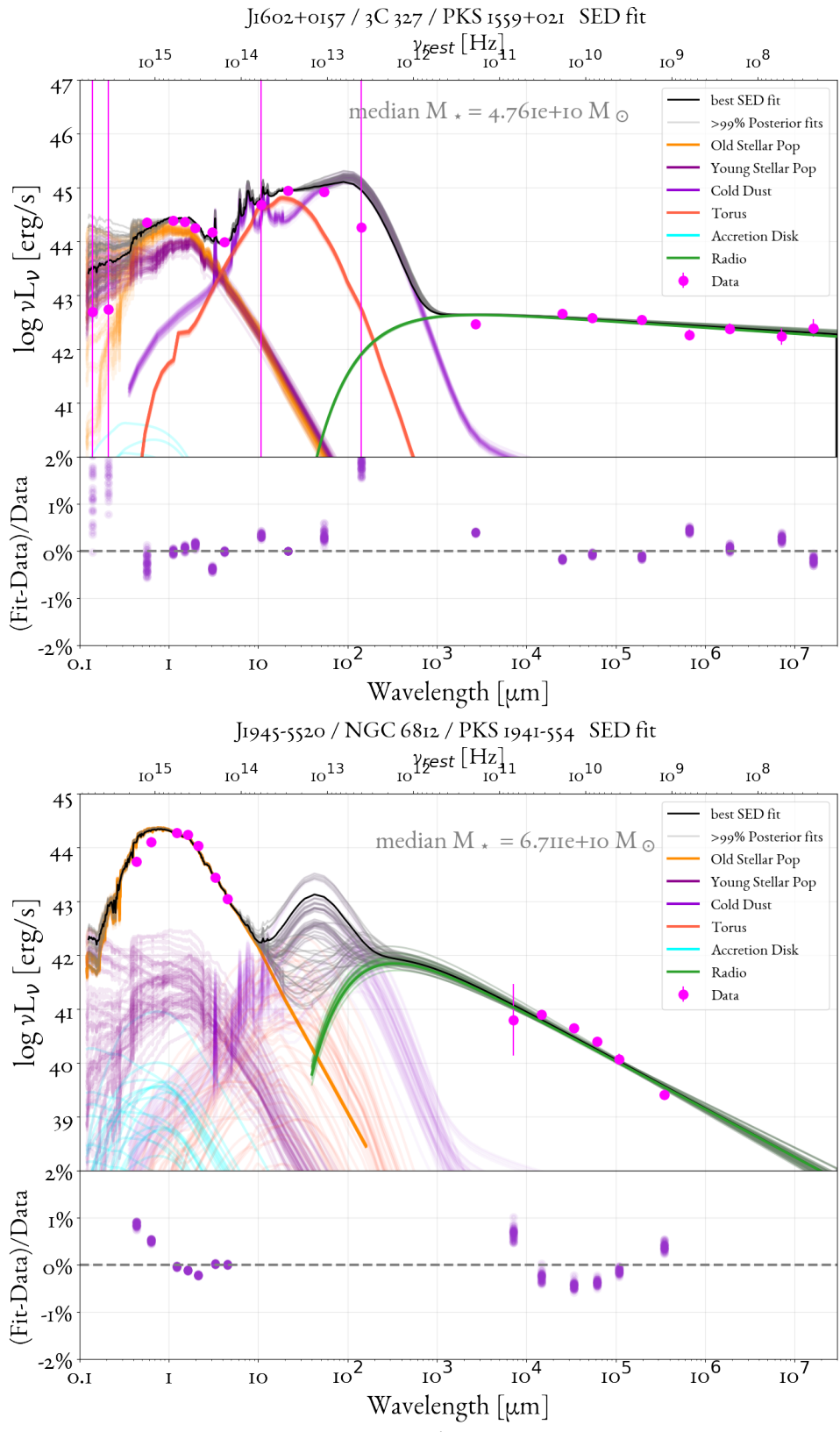


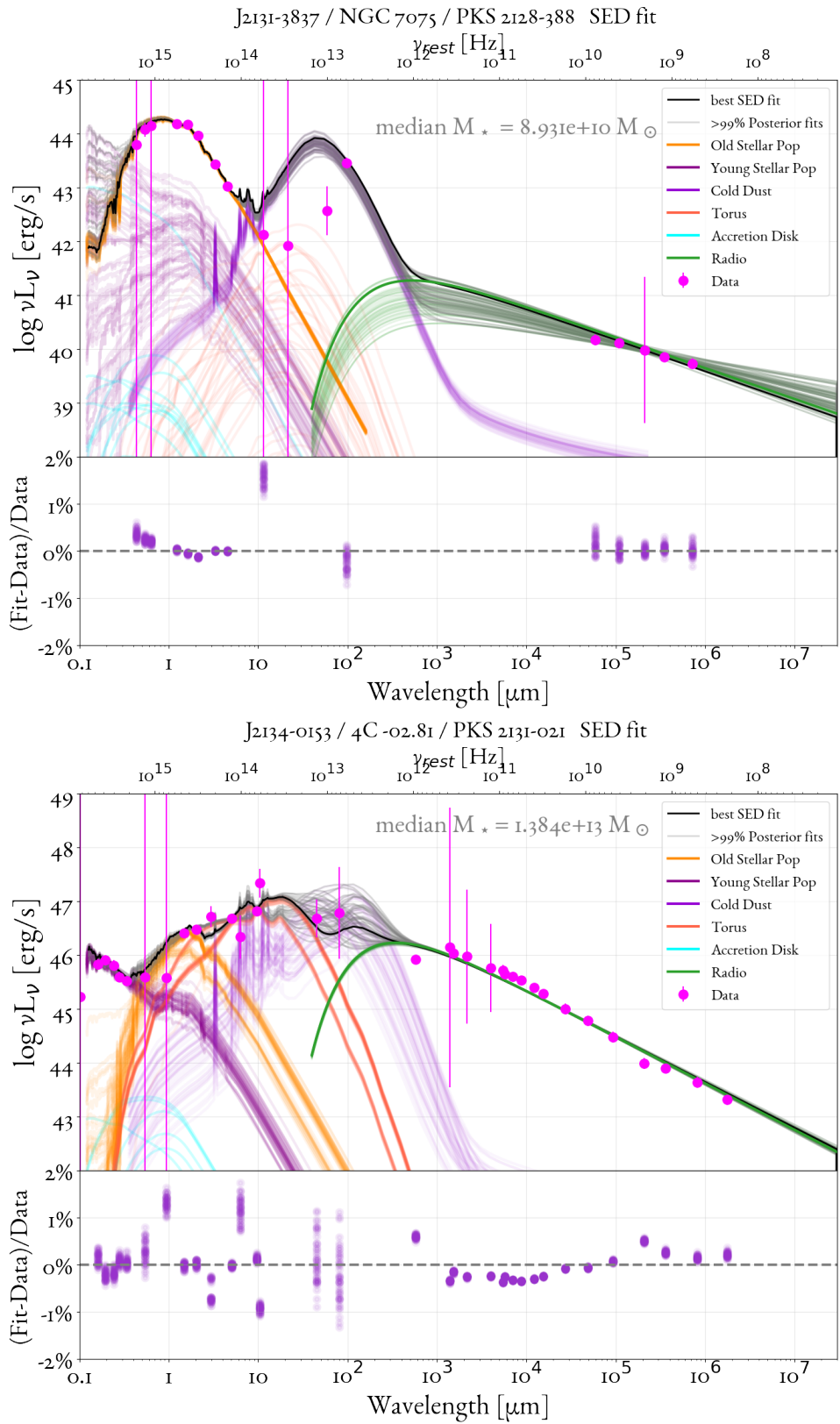


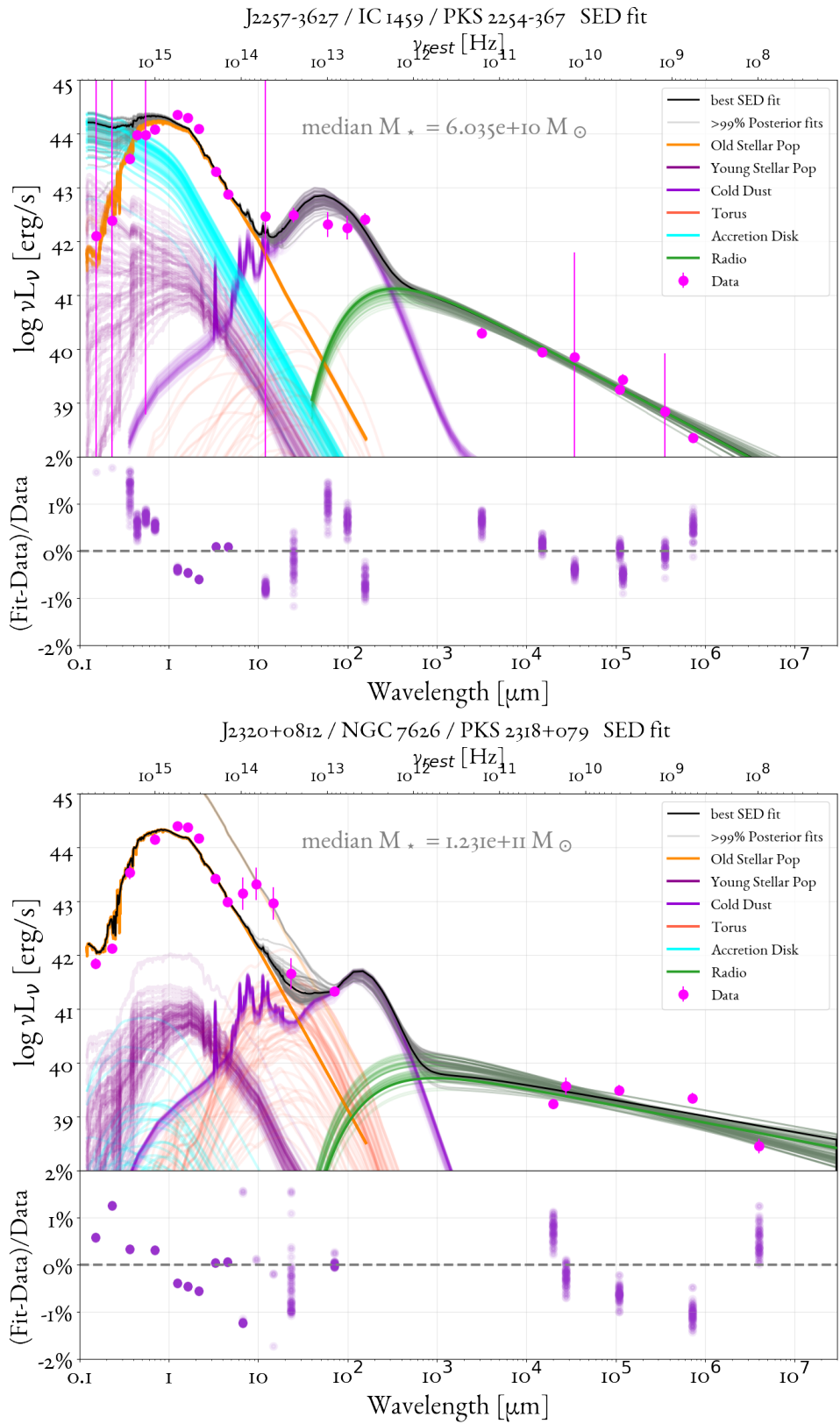


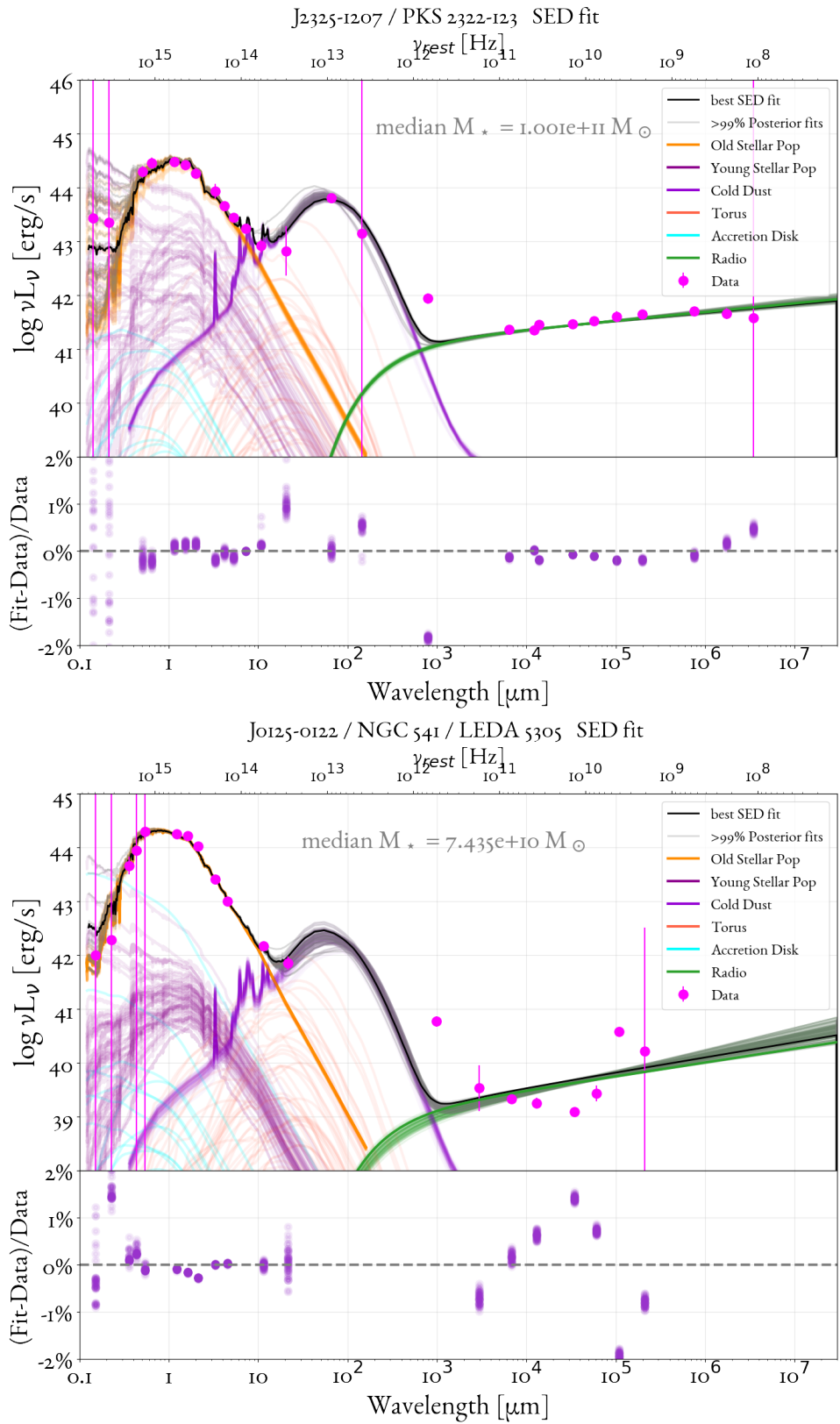


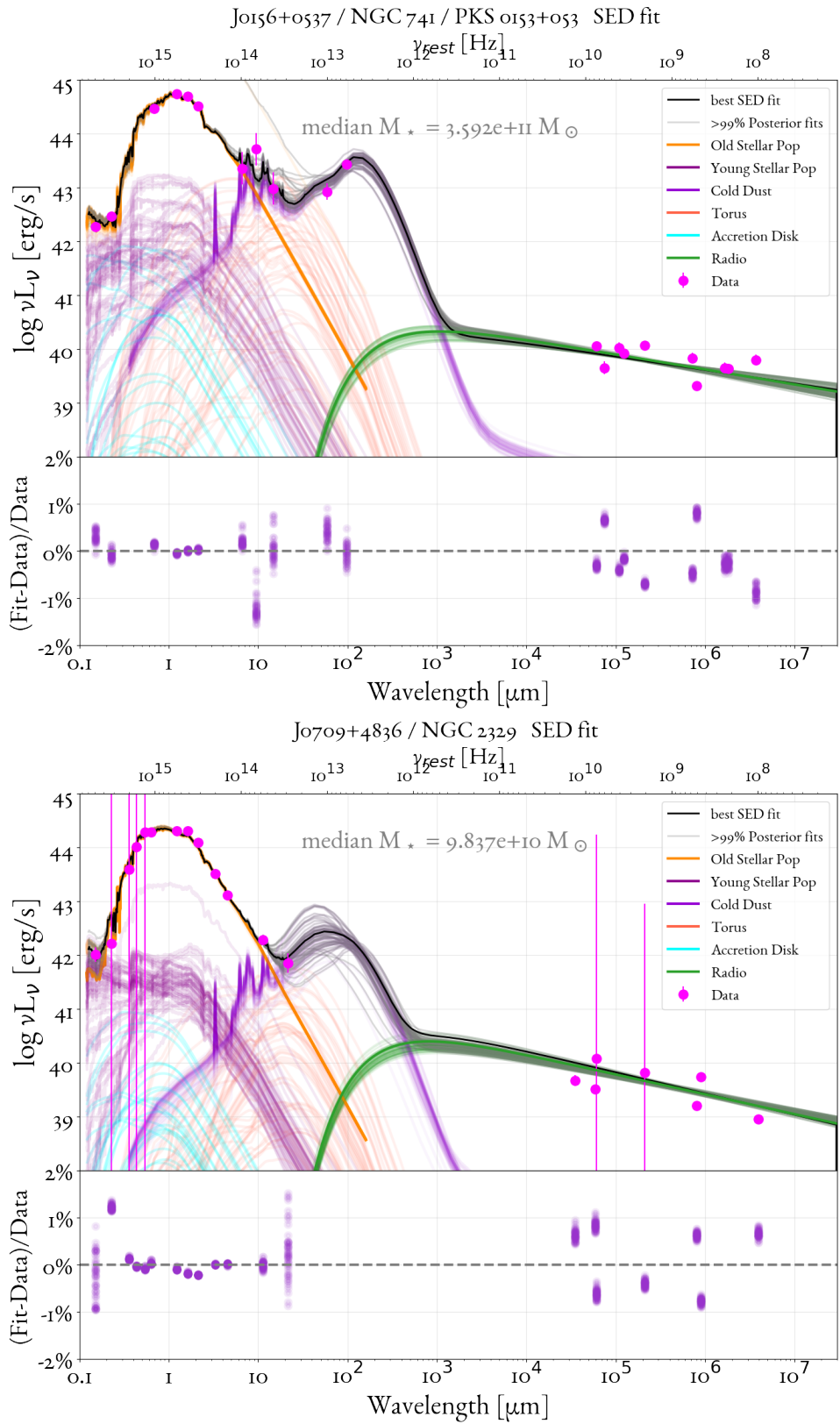


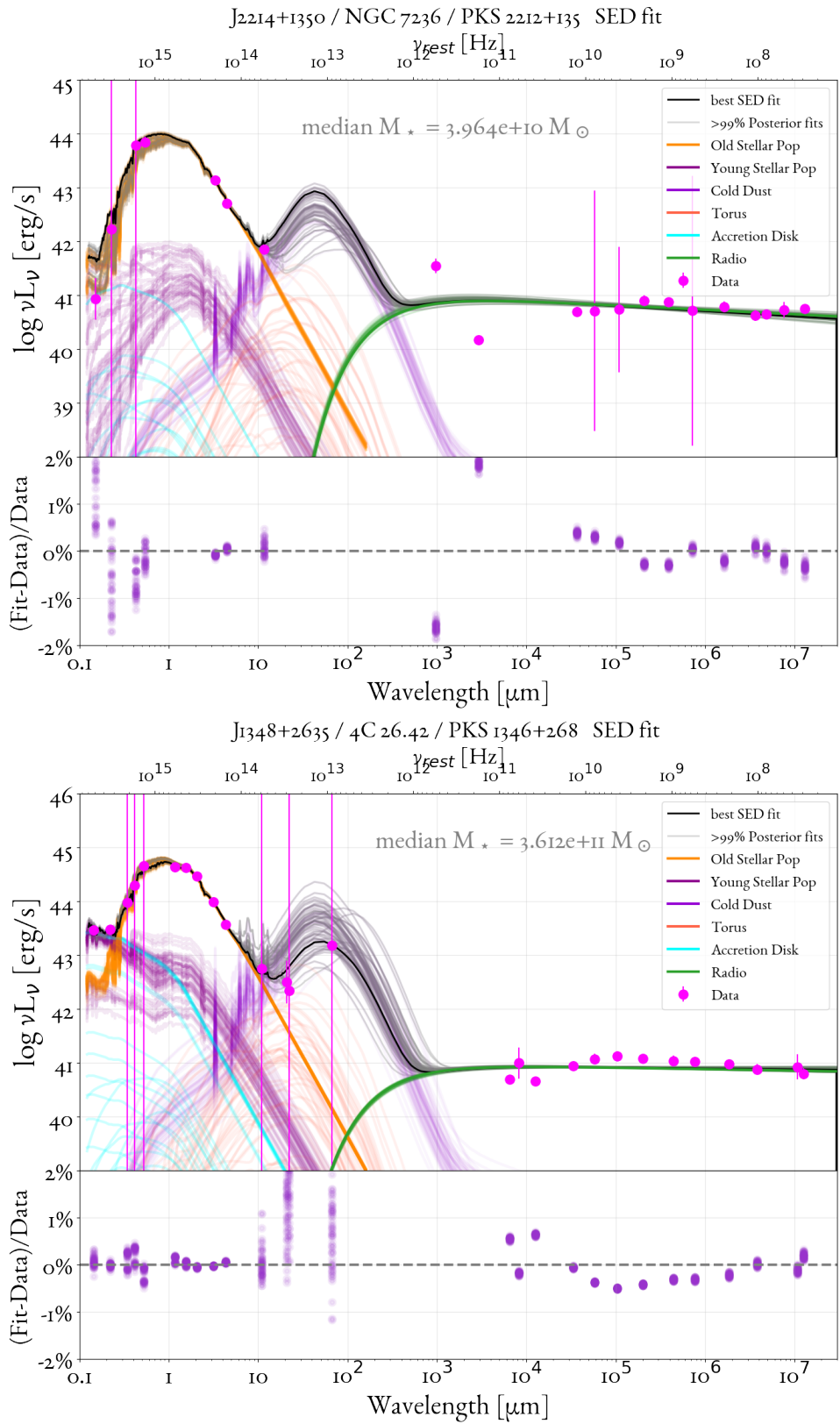


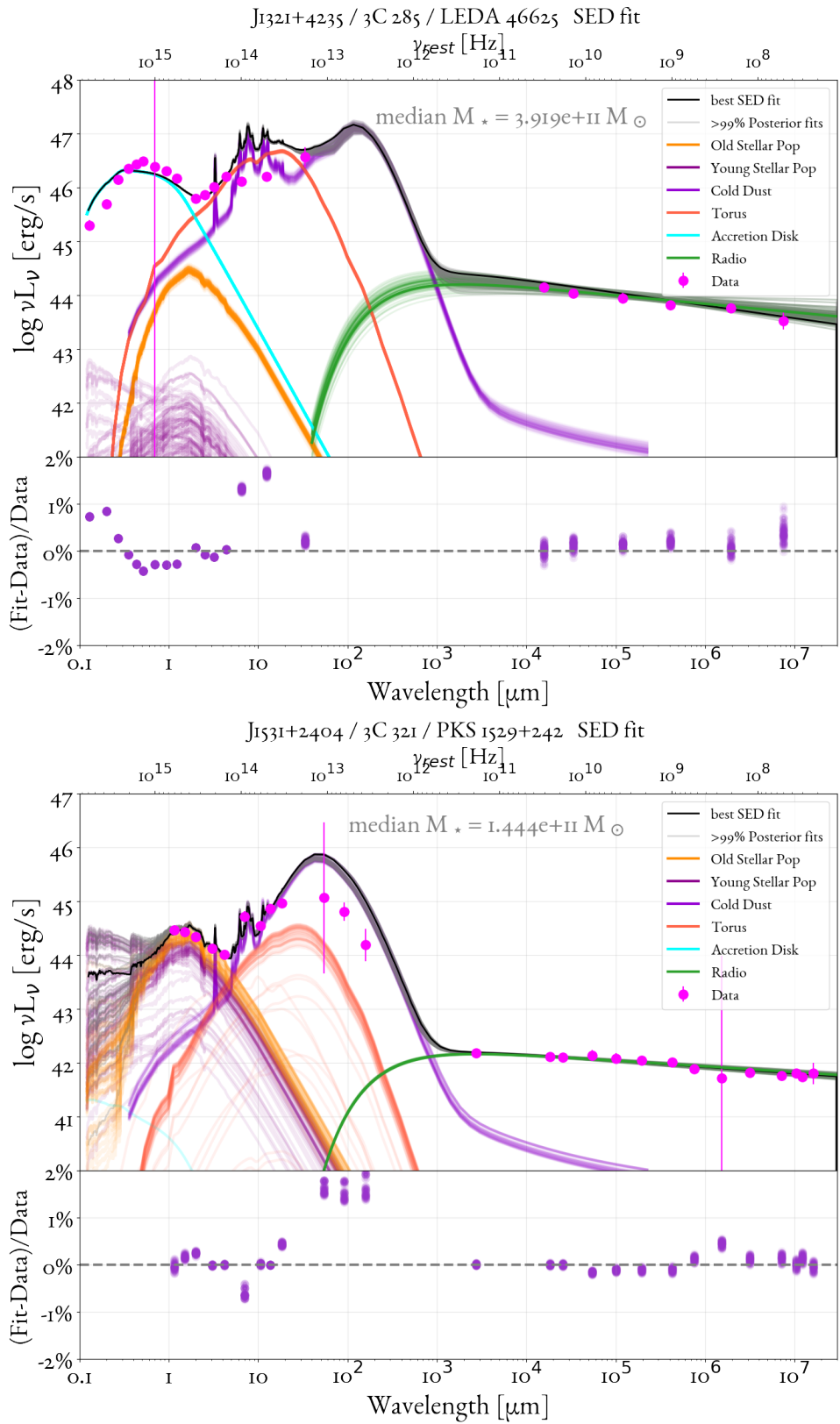


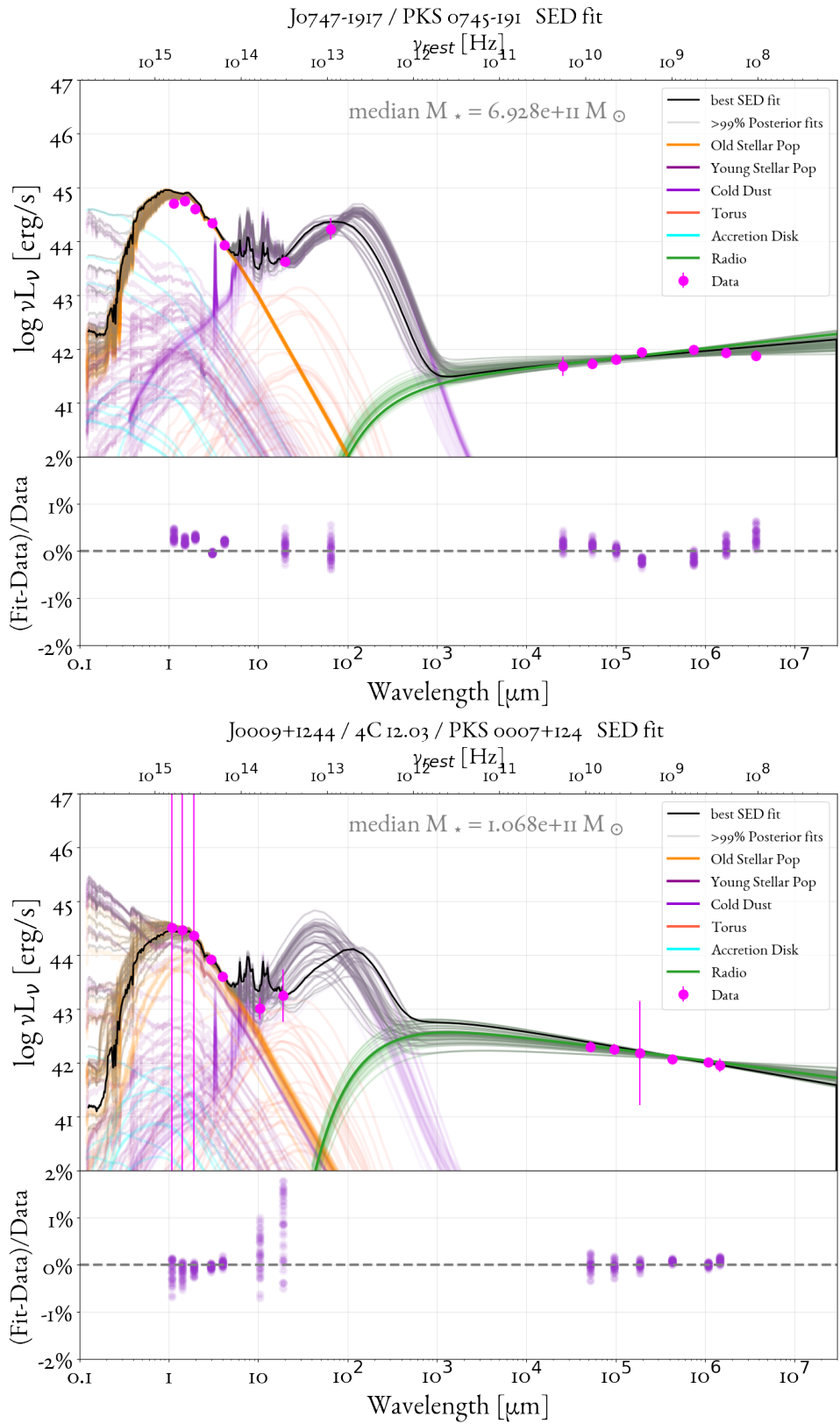


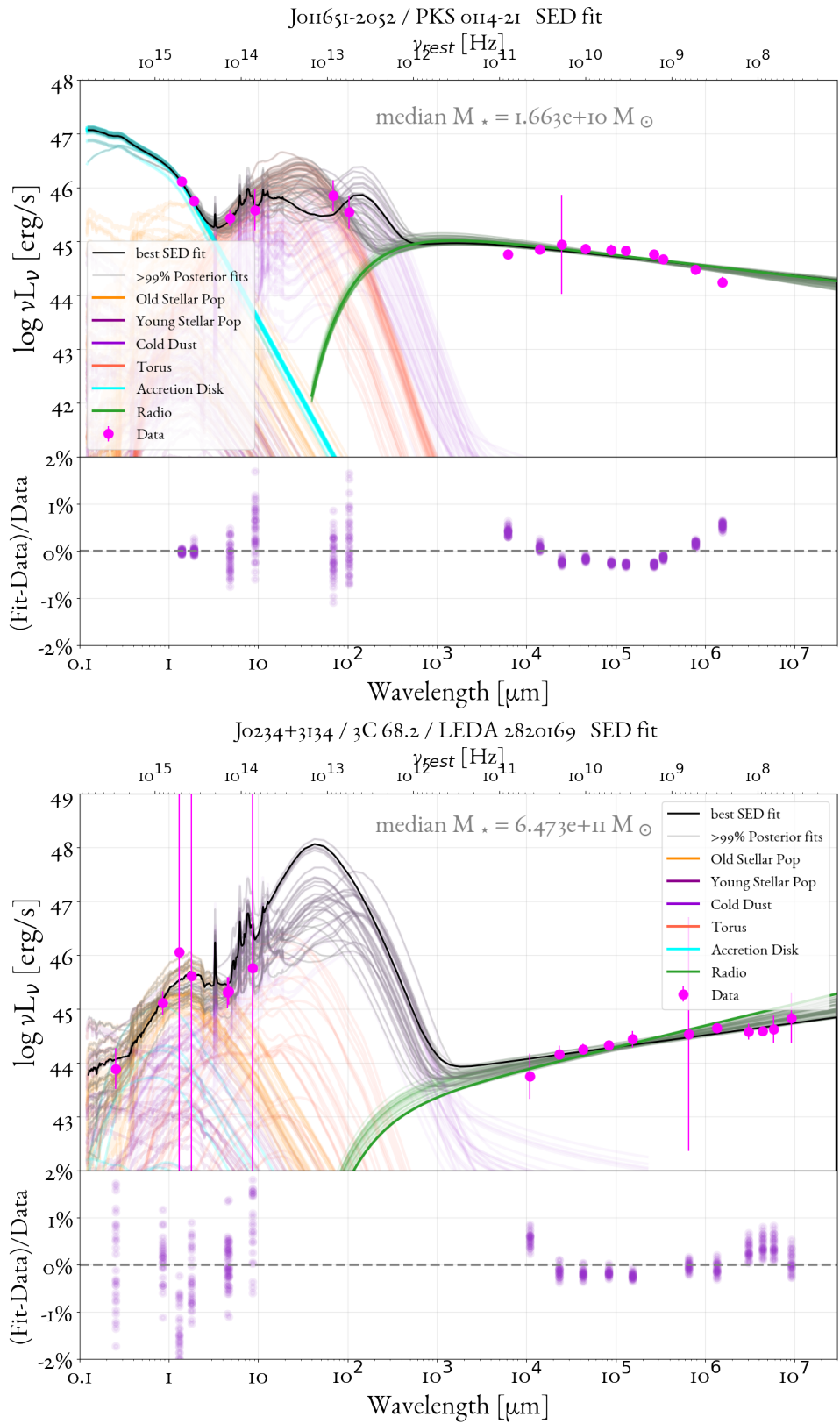


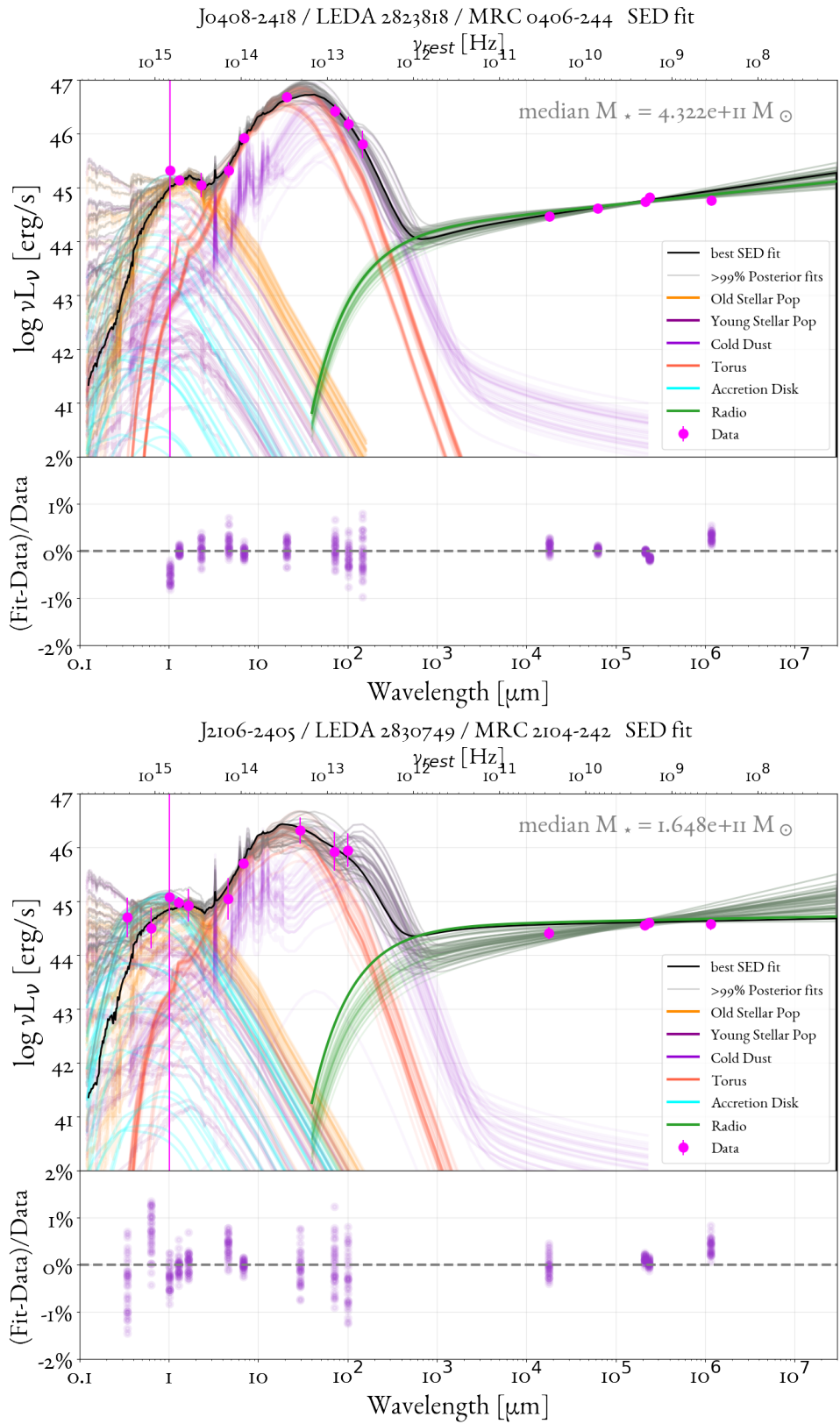


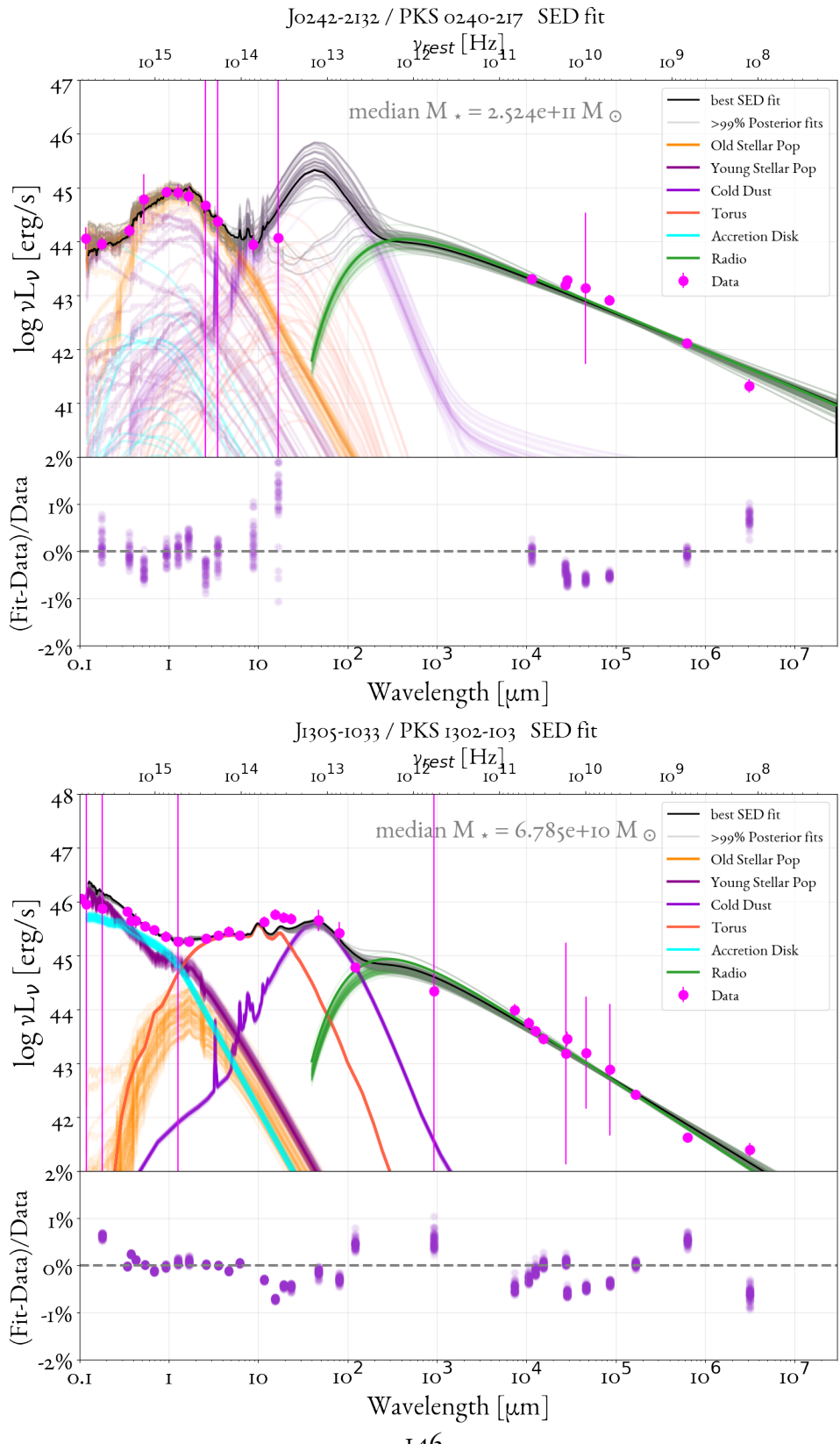


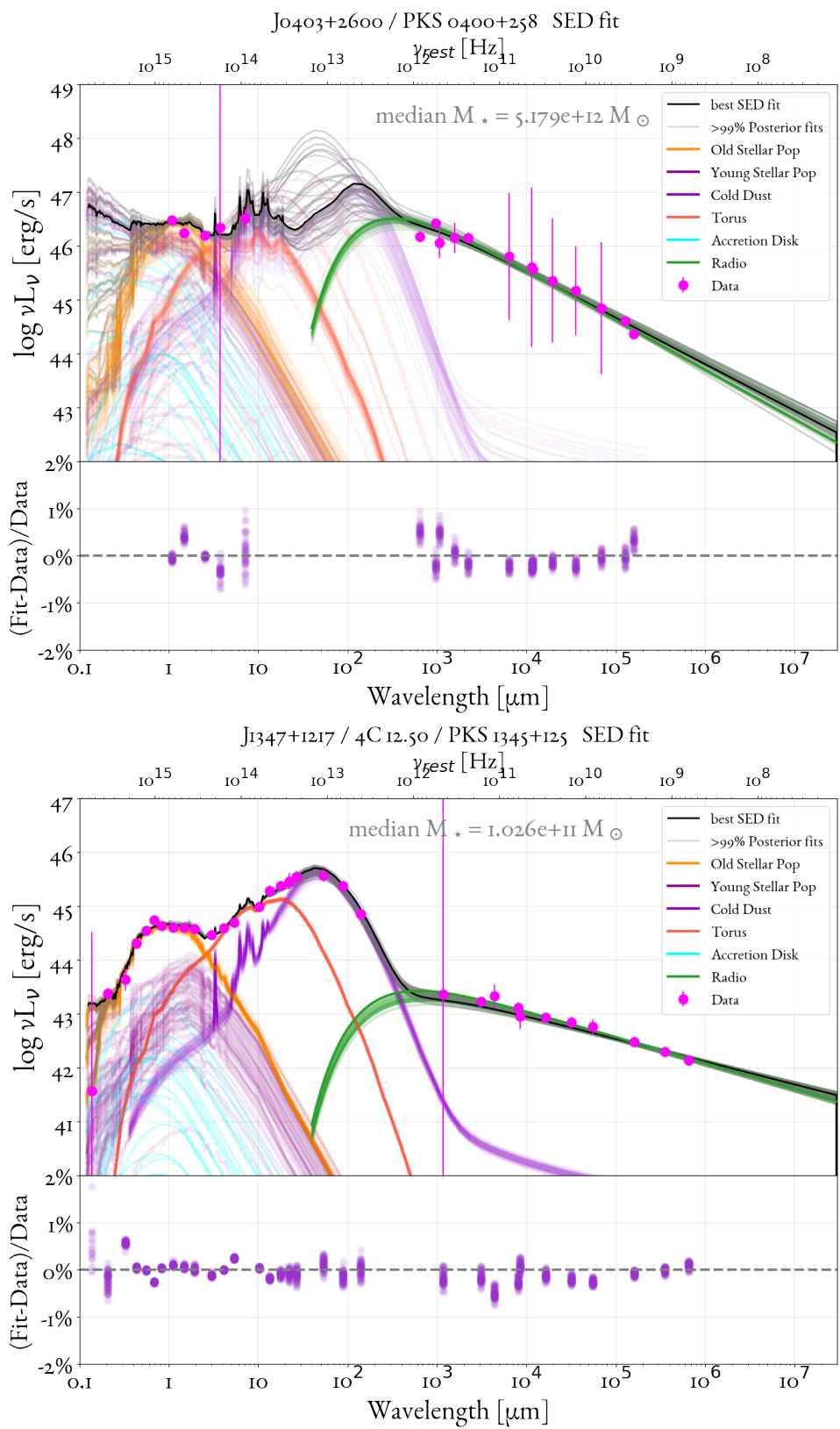












Declaration of authorship

I hereby confirm that this Master's thesis and the work presented in it is written independently and without the use of other than the stated aids. All passages taken verbatim or in spirit from published and unpublished writings are marked as such and the source is always given. Where I have consulted the work of others this is always clearly attributed. Where the thesis is based on work done by myself jointly with others, I have made clear exactly what was done by others and what I have contributed myself.

This Master's thesis has not yet been submitted in the same or similar form or in excerpts elsewhere for the fulfilment of any other qualification. I hereby certify that the submitted electronic version corresponds completely to the submitted printed version.

I am aware of the indictability of a false affidavit.

Athens, July 21, 2023

References

- [1] Acquaviva, V., Gawiser, E., & Guaita, L. (2011). Spectral Energy Distribution Fitting with Markov Chain Monte Carlo: Methodology and Application to $z = 3.1$ Ly α -emitting Galaxies. *The Astrophysical Journal*, 737(2), 47.
- [2] Adams, N. J., Bowler, R. A. A., Jarvis, M. J., Häußler, B., & Lagos, C. D. P. (2021). Evolution of the galaxy stellar mass function: evidence for an increasing M^* from $z = 2$ to the present day. *Monthly Notices of the Royal Astronomical Society*, 506(4), 4933–4951.
- [3] Adelman-McCarthy, J. K., Agüeros, M. A., Allam, S. S., Allende Prieto, C., Anderson, K. S. J., Anderson, S. F., Annis, J., Bahcall, N. A., Bailer-Jones, C. A. L., Baldry, I. K., Barentine, J. C., Bassett, B. A., Becker, A. C., Beers, T. C., Bell, E. F., Berlind, A. A., Bernardi, M., Blanton, M. R., Bochanski, J. J., Boroski, W. N., Brinchmann, J., Brinkmann, J., Brunner, R. J., Budavári, T., Carliles, S., Carr, M. A., Castander, F. J., Cinabro, D., Cool, R. J., Covey, K. R., Csabai, I., Cunha, C. E., Davenport, J. R. A., Dilday, B., Doi, M., Eisenstein, D. J., Evans, M. L., Fan, X., Finkbeiner, D. P., Friedman, S. D., Frieman, J. A., Fukugita, M., Gänsicke, B. T., Gates, E., Gillespie, B., Glazebrook, K., Gray, J., Grebel, E. K., Gunn, J. E., Gurbani, V. K., Hall, P. B., Harding, P., Harvanek, M., Hawley, S. L., Hayes, J., Heckman, T. M., Hendry, J. S., Hindsley, R. B., Hirata, C. M., Hogan, C. J., Hogg, D. W., Hyde, J. B., Ichikawa, S.-i., Ivezić, Ž., Jester, S., Johnson, J. A., Jorgensen, A. M., Jurić, M., Kent, S. M., Kessler, R., Kleinman, S. J., Knapp, G. R., Kron, R. G., Krzesiński, J., Kuropatkin, N., Lamb, D. Q., Lampeitl, H., Lebedeva, S., Lee, Y. S., French Leger, R., Lépine, S., Lima, M., Lin, H., Long, D. C., Loomis, C. P., Loveday, J., Lupton, R. H., Malanushenko, O., Malanushenko, V., Mandelbaum, R., Margon, B., Marriner, J. P., Martínez-Delgado, D., Matsubara, T., McGehee, P. M., McKay, T. A., Meiksin, A., Morrison, H. L., Munn, J. A., Nakajima, R., Neilson, Eric H., Newberg, H. J., Nichol, R. C., Nicinski, T., Nieto-Santisteban, M., Nitta, A., Okamura, S., Owen, R., Oyaizu, H., Padmanabhan, N., Pan, K., Park, C., Peoples, John, J., Pier, J. R., Pope, A. C., Purger, N., Raddick, M. J., Re Fiorentin, P., Richards, G. T., Richmond, M. W., Riess, A. G., Rix, H.-W., Rockosi, C. M., Sako, M.,

Schlegel, D. J., Schneider, D. P., Schreiber, M. R., Schwone, A. D., Seljak, U., Sesar, B., Sheldon, E., Shimasaku, K., Sivarani, T., Allyn Smith, J., Snedden, S. A., Steinmetz, M., Strauss, M. A., SubbaRao, M., Suto, Y., Szalay, A. S., Szapudi, I., Szkody, P., Tegmark, M., Thakar, A. R., Tremonti, C. A., Tucker, D. L., Uomoto, A., Vanden Berk, D. E., Vandenberg, J., Vidrih, S., Vogeley, M. S., Voges, W., Vogt, N. P., Wadadekar, Y., Weinberg, D. H., West, A. A., White, S. D. M., Wilhite, B. C., Yanny, B., Yocom, D. R., York, D. G., Zehavi, I., & Zucker, D. B. (2008). The Sixth Data Release of the Sloan Digital Sky Survey. *The Astrophysical Journal Supplement Series*, 175(2), 297–313.

- [4] Albareti, F. D., Allende Prieto, C., Almeida, A., Anders, F., Anderson, S., Andrews, B. H., Aragón-Salamanca, A., Argudo-Fernández, M., Armengaud, E., Aubourg, E., Avila-Reese, V., Badenes, C., Bailey, S., Barbuy, B., Barger, K., Barrera-Ballesteros, J., Bartosz, C., Basu, S., Bates, D., Battaglia, G., Baumgarten, F., Baur, J., Bautista, J., Beers, T. C., Belfiore, F., Bershadsky, M., Bertran de Lis, S., Bird, J. C., Bizyaev, D., Blanc, G. A., Blanton, M., Blomqvist, M., Bolton, A. S., Borissova, J., Bovy, J., Brandt, W. N., Brinkmann, J., Brownstein, J. R., Bundy, K., Burtin, E., Busca, N. G., Camacho Chavez, H. O., Cano Díaz, M., Cappellari, M., Carrera, R., Chen, Y., Cherinka, B., Cheung, E., Chiappini, C., Chojnowski, D., Chuang, C.-H., Chung, H., Cirolini, R. F., Clerc, N., Cohen, R. E., Comerford, J. M., Comparat, J., Correa do Nascimento, J., Cousinou, M.-C., Covey, K., Crane, J. D., Croft, R., Cunha, K., Darling, J., Davidson, James W., J., Dawson, K., Da Costa, L., Da Silva Ilha, G., Deconto Machado, A., Delubac, T., De Lee, N., De la Macorra, A., De la Torre, S., Diamond-Stanic, A. M., Donor, J., Downes, J. J., Drory, N., Du, C., Du Mas des Bourboux, H., Dwelly, T., Ebelke, G., Eigenbrot, A., Eisenstein, D. J., Elsworth, Y. P., Emsellem, E., Eracleous, M., Escoffier, S., Evans, M. L., Falcón-Barroso, J., Fan, X., Favole, G., Fernandez-Alvar, E., Fernandez-Trincado, J. G., Feuillet, D., Fleming, S. W., Font-Ribera, A., Freischlad, G., Frinchaboy, P., Fu, H., Gao, Y., Garcia, R. A., Garcia-Dias, R., Garcia-Hernández, D. A., Garcia Pérez, A. E., Gaulme, P., Ge, J., Geisler, D., Gillespie, B., Gil Marin, H., Girardi, L., Goddard, D., Gomez Maqueo Chew, Y., Gonzalez-Perez, V., Grabowski, K., Green, P., Grier, C. J., Grier, T., Guo, H., Guy, J., Hagen, A., Hall, M., Harding, P., Harley, R. E., Hasselquist, S., Hawley, S., Hayes, C. R., Hearty, F., Hekker, S., Hernandez Toledo, H., Ho, S., Hogg, D. W., Holley-Bockelmann, K., Holtzman, J. A., Holzer, P. H., Hu, J., Huber, D., Hutchinson, T. A., Hwang, H. S., Ibarra-Medel, H. J., Ivans, I. I., Ivory, K., Jaehnig, K., Jensen, T. W., Johnson, J. A., Jones, A., Jullo,

E., Kallinger, T., Kinemuchi, K., Kirkby, D., Klaene, M., Kneib, J.-P., Kollmeier, J. A., Lacerna, I., Lane, R. R., Lang, D., Laurent, P., Law, D. R., Leauthaud, A., Le Goff, J.-M., Li, C., Li, C., Li, N., Li, R., Liang, F.-H., Liang, Y., Lima, M., Lin, L., Lin, L., Lin, Y.-T., Liu, C., Long, D., Lucatello, S., MacDonald, N., MacLeod, C. L., Mackereth, J. T., Mahadevan, S., Maia, M. A. G., Maiolino, R., Majewski, S. R., Malanushenko, O., Malanushenko, V., Mallmann, N. D., Manchado, A., Maraston, C., Marques-Chaves, R., Martinez Valpuesta, I., Masters, K. L., Mathur, S., McGreer, I. D., Merloni, A., Merrifield, M. R., Mészáros, S., Meza, A., Miglio, A., Minchev, I., Molaverdikhani, K., Montero-Dorta, A. D., Mosser, B., Muna, D., Myers, A., Nair, P., Nandra, K., Ness, M., Newman, J. A., Nichol, R. C., Nidever, D. L., Nitschelm, C., O'Connell, J., Oravetz, A., Oravetz, D. J., Pace, Z., Padilla, N., Palanque-Delabrouille, N., Pan, K., Parejko, J., Paris, I., Park, C., Peacock, J. A., Peirani, S., Pellejero-Ibanez, M., Penny, S., Percival, W. J., Percival, J. W., Perez-Fournon, I., Petitjean, P., Pieri, M., Pinsonneault, M. H., Pisani, A., Prada, F., Prakash, A., Price-Jones, N., Raddick, M. J., Rahman, M., Rai-choor, A., Barboza Rembold, S., Reyna, A. M., Rich, J., Richstein, H., Ridl, J., Riffel, R. A., Riffel, R., Rix, H.-W., Robin, A. C., Rockosi, C. M., Rodríguez-Torres, S., Rodrigues, T. S., Roe, N., Roman Lopes, A., Román-Zúñiga, C., Ross, A. J., Rossi, G., Ruan, J., Ruggeri, R., Runnoe, J. C., Salazar-Albornoz, S., Salvato, M., Sanchez, S. F., Sanchez, A. G., Sanchez-Gallego, J. R., Santiago, B. X., Schiavon, R., Schimoia, J. S., Schlafly, E., Schlegel, D. J., Schneider, D. P., Schönrich, R., Schultheis, M., Schwone, A., Seo, H.-J., Serenelli, A., Sesar, B., Shao, Z., Shetrone, M., Shull, M., Silva Aguirre, V., Skrutskie, M. F., Slosar, A., Smith, M., Smith, V. V., Sobeck, J., Somers, G., Souto, D., Stark, D. V., Stassun, K. G., Steinmetz, M., Stello, D., Storch Bergmann, T., Strauss, M. A., Streblanska, A., Stringfellow, G. S., Suarez, G., Sun, J., Taghizadeh-Popp, M., Tang, B., Tao, C., Tayar, J., Tembe, M., Thomas, D., Tinker, J., Tojeiro, R., Tremonti, C., Troup, N., Trump, J. R., Unda-Sanzana, E., Valenzuela, O., Van den Bosch, R., Vargas-Magaña, M., Vazquez, J. A., Villanova, S., Vivek, M., Vogt, N., Wake, D., Walterbos, R., Wang, Y., Wang, E., Weaver, B. A., Weijmans, A.-M., Weinberg, D. H., Westfall, K. B., Whelan, D. G., Wilcots, E., Wild, V., Williams, R. A., Wilson, J., Wood-Vasey, W. M., Wylezalek, D., Xiao, T., Yan, R., Yang, M., Ybarra, J. E., Yeche, C., Yuan, F.-T., Zakamska, N., Zamora, O., Zasowski, G., Zhang, K., Zhao, C., Zhao, G.-B., Zheng, Z., Zheng, Z., Zhou, Z.-M., Zhu, G., Zinn, J. C., & Zou, H. (2017). The 13th Data Release of the Sloan Digital Sky Survey: First Spectroscopic Data from the SDSS-IV Survey Mapping Nearby Galaxies at Apache Point Observatory. *The Astrophysical Journal Sup-*

plement Series, 233(2), 25.

- [5] Allison, J. R., Sadler, E. M., & Meekin, A. M. (2014). A search for H I absorption in nearby radio galaxies using HIPASS. *Monthly Notices of the Royal Astronomical Society*, 440(1), 696–718.
- [6] Antonucci, R. (1993). Unified models for active galactic nuclei and quasars. *Annual Review of Astronomy and Astrophysics*, 31, 473–521.
- [7] Astropy Collaboration, Robitaille, T. P., Tollerud, E. J., Greenfield, P., Droettboom, M., Bray, E., Aldcroft, T., Davis, M., Ginsburg, A., Price-Whelan, A. M., Kerzendorf, W. E., Conley, A., Crighton, N., Barbary, K., Muna, D., Ferguson, H., Grollier, F., Parikh, M. M., Nair, P. H., Unther, H. M., Deil, C., Woillez, J., Conseil, S., Kramer, R., Turner, J. E. H., Singer, L., Fox, R., Weaver, B. A., Zabalza, V., Edwards, Z. I., Azalee Bostroem, K., Burke, D. J., Casey, A. R., Crawford, S. M., Dencheva, N., Ely, J., Jenness, T., Labrie, K., Lim, P. L., Pierfederici, F., Pontzen, A., Ptak, A., Refsdal, B., Servillat, M., & Streicher, O. (2013). Astropy: A community Python package for astronomy. *Astronomy & Astrophysics*, 558, A33.
- [8] Audibert, A., Dasyra, K. M., Papachristou, M., Fernández-Ontiveros, J. A., Ruffa, I., Bisigello, L., Combes, F., Salomé, P., & Gruppioni, C. (2022). CO in the ALMA Radio-source Catalogue (ARC): The molecular gas content of radio galaxies as a function of redshift. *Astronomy & Astrophysics*, 668, A67.
- [9] Avni, Y. & Bahcall, J. N. (1980). On the simultaneous analysis of several complete samples. The V/Vmax and Ve/Va variables, with applications to quasars. *The Astrophysical Journal*, 235, 694–716.
- [10] Barvainis, R. (1993). The Case for an Optically Thin Thermal Big Blue Bump. *The Astrophysical Journal*, 412, 513.
- [11] Beasley, A. J., Gordon, D., Peck, A. B., Petrov, L., MacMillan, D. S., Fomalont, E. B., & Ma, C. (2002). The VLBA Calibrator Survey-VCS1. *The Astrophysical Journal Supplement Series*, 141(1), 13–21.
- [12] Bertelli, G., Bressan, A., Chiosi, C., Fagotto, F., & Nasi, E. (1994). Theoretical isochrones from models with new radiative opacities. *Astronomy & Astrophysics Supplement*, 106, 275–302.

- [13] Best, P. N. & Heckman, T. M. (2012). On the fundamental dichotomy in the local radio-AGN population: accretion, evolution and host galaxy properties. *Monthly Notices of the Royal Astronomical Society*, 421(2), 1569–1582.
- [14] Best, P. N., Kauffmann, G., Heckman, T. M., Brinchmann, J., Charlot, S., Ivezić, Ž., & White, S. D. M. (2005). The host galaxies of radio-loud active galactic nuclei: mass dependences, gas cooling and active galactic nuclei feedback. *Monthly Notices of the Royal Astronomical Society*, 362(1), 25–40.
- [15] Betancourt, M. (2012). Cruising the simplex: Hamiltonian Monte Carlo and the Dirichlet distribution. In P. Goyal, A. Giffin, K. H. Knuth, & E. Vrscay (Eds.), *Bayesian Inference and Maximum Entropy Methods in Science and Engineering: 31st International Workshop on Bayesian Inference and Maximum Entropy Methods in Science and Engineering*, volume 1443 of *American Institute of Physics Conference Series* (pp. 157–164).
- [16] Bonzini, M., Padovani, P., Mainieri, V., Kellermann, K. I., Miller, N., Rosati, P., Tozzi, P., & Vattakunnel, S. (2013). The sub-mJy radio sky in the Extended Chandra Deep Field-South: source population. *Monthly Notices of the Royal Astronomical Society*, 436(4), 3759–3771.
- [17] Bottinelli, L., Durand, N., Fouque, P., Garnier, R., Gouguenheim, L., Loulergue, M., Paturel, G., Petit, C., & Teerikorpi, P. (1993). VizieR Online Data Catalog: Radial Velocities of the local universe (Bottinelli+ 1993). *VizieR Online Data Catalog*, (pp. J/A+AS/102/57).
- [18] Brammer, G. B., Sánchez-Janssen, R., Labbé, I., da Cunha, E., Erb, D. K., Franx, M., Fumagalli, M., Lundgren, B., Marchesini, D., Momcheva, I., Nelson, E., Patel, S., Quadri, R., Rix, H.-W., Skelton, R. E., Schmidt, K. B., van der Wel, A., van Dokkum, P. G., Wake, D. A., & Whitaker, K. E. (2012). 3D-HST Grism Spectroscopy of a gravitationally Lensed, Low-metallicity Starburst Galaxy at $z = 1.847$. *The Astrophysical Journal Letters*, 758(1), L17.
- [19] Bruzual, G. & Charlot, S. (2003). Stellar population synthesis at the resolution of 2003. *Monthly Notices of the Royal Astronomical Society*, 344(4), 1000–1028.
- [20] Buchner, J. (2016). A statistical test for Nested Sampling algorithms. *Statistics and Computing*, 26(1-2), 383–392.

- [21] Buchner, J. (2019). Collaborative Nested Sampling: Big Data versus Complex Physical Models. *Publications of the Astronomical Society of the Pacific*, 131(1004), 108005.
- [22] Buchner, J. (2021a). Nested Sampling Methods. *arXiv e-prints*, (pp. arXiv:2101.09675).
- [23] Buchner, J. (2021b). UltraNest - a robust, general purpose Bayesian inference engine. *The Journal of Open Source Software*, 6(60), 3001.
- [24] Calzetti, D., Armus, L., Bohlin, R. C., Kinney, A. L., Koornneef, J., & Storchi-Bergmann, T. (2000). The Dust Content and Opacity of Actively Star-forming Galaxies. *The Astrophysical Journal*, 533(2), 682–695.
- [25] Cava, A., Bettoni, D., Poggianti, B. M., Couch, W. J., Moles, M., Varela, J., Biviano, A., D’Onofrio, M., Dressler, A., Fasano, G., Fritz, J., Kjærgaard, P., Ramella, M., & Valentiniuzzi, T. (2009). WINGS-SPE Spectroscopy in the WIde-field Nearby Galaxy-cluster Survey. *Astronomy & Astrophysics*, 495(3), 707–719.
- [26] Chabrier, G. (2003). Galactic Stellar and Substellar Initial Mass Function. *The Publications of the Astronomical Society of the Pacific*, 115(809), 763–795.
- [27] Cheng, X. P., An, T., Frey, S., Hong, X. Y., He, X., Kellermann, K. I., Lister, M. L., Lao, B. Q., Li, X. F., Mohan, P., Yang, J., Wu, X. C., Zhang, Z. L., Zhang, Y. K., & Zhao, W. (2020). Compact Bright Radio-loud AGNs. III. A Large VLBA Survey at 43 GHz. *The Astrophysical Journal Supplement Series*, 247(2), 57.
- [28] Colless, M., Peterson, B. A., Jackson, C., Peacock, J. A., Cole, S., Norberg, P., Baldry, I. K., Baugh, C. M., Bland-Hawthorn, J., Bridges, T., Cannon, R., Collins, C., Couch, W., Cross, N., Dalton, G., De Propris, R., Driver, S. P., Efstathiou, G., Ellis, R. S., Frenk, C. S., Glazebrook, K., Lahav, O., Lewis, I., Lumsden, S., Maddox, S., Madgwick, D., Sutherland, W., & Taylor, K. (2003). The 2dF Galaxy Redshift Survey: Final Data Release. *arXiv e-prints*, (pp. astro-ph/0306581).
- [29] Condon, J. J., Cotton, W. D., Greisen, E. W., Yin, Q. F., Perley, R. A., Taylor, G. B., & Broderick, J. J. (1998). The NRAO VLA Sky Survey. *The Astronomical Journal*, 115(5), 1693–1716.

- [30] Conroy, C. (2013). Modeling the Panchromatic Spectral Energy Distributions of Galaxies. *Annual Review of Astronomy and Astrophysics*, 51(1), 393–455.
- [31] Costa, E. & Loyola, P. (1996). Optical astrometry of Benchmark radio sources. III. Positions of 35 southern extragalactic radio sources with respect to the International Reference Stars catalogue. *Astronomy & Astrophysics Supplement*, 115, 75.
- [32] Dale, D. A., Helou, G., Magdis, G. E., Armus, L., Díaz-Santos, T., & Shi, Y. (2014). A Two-parameter Model for the Infrared/Submillimeter/Radio Spectral Energy Distributions of Galaxies and Active Galactic Nuclei. *The Astrophysical Journal*, 784(1), 83.
- [33] Douglas, J. N., Bash, F. N., Bozian, F. A., Torrence, G. W., & Wolfe, C. (1996). The Texas Survey of Radio Sources Covering -35.5 degrees $<$ declination $<$ 71.5 degrees at 365 MHz. *The Astronomical Journal*, 111, 1945.
- [34] Drinkwater, M. J., Jurek, R. J., Blake, C., Woods, D., Pimbblet, K. A., Glazebrook, K., Sharp, R., Pracy, M. B., Brough, S., Colless, M., Couch, W. J., Croom, S. M., Davis, T. M., Forbes, D., Forster, K., Gilbank, D. G., Gladders, M., Jelliffe, B., Jones, N., Li, I. H., Madore, B., Martin, D. C., Poole, G. B., Small, T., Wisnioski, E., Wyder, T., & Yee, H. K. C. (2010). The WiggleZ Dark Energy Survey: survey design and first data release. *Monthly Notices of the Royal Astronomical Society*, 401(3), 1429–1452.
- [35] Drinkwater, M. J., Webster, R. L., Francis, P. J., Condon, J. J., Ellison, S. L., Jauncey, D. L., Lovell, J., Peterson, B. A., & Savage, A. (1997). The Parkes Half-Jansky Flat-Spectrum Sample. *Monthly Notices of the Royal Astronomical Society*, 284(1), 85–125.
- [36] Driver, S. P., Bellstedt, S., Robotham, A. S. G., Baldry, I. K., Davies, L. J., Liske, J., Obreschkow, D., Taylor, E. N., Wright, A. H., Alpaslan, M., Bamford, S. P., Bauer, A. E., Bland-Hawthorn, J., Bilicki, M., Bravo, M., Brough, S., Casura, S., Cluver, M. E., Colless, M., Conselice, C. J., Croom, S. M., de Jong, J., D'Eugenio, F., De Propris, R., Dogruel, B., Drinkwater, M. J., Dvornik, A., Farrow, D. J., Frenk, C. S., Giblin, B., Graham, A. W., Grootes, M. W., Gunawardhana, M. L. P., Hashemizadeh, A., Häußler, B., Heymans, C., Hildebrandt, H., Holwerda, B. W., Hopkins, A. M., Jarrett, T. H., Heath Jones, D., Kelvin, L. S., Koushan, S., Kuijken, K., Lara-López, M. A., Lange, R., López-Sánchez, Á. R., Loveday, J., Mahajan, S., Meyer, M., Moffett, A. J., Napolitano, N. R., Norberg, P., Owers, M. S., Radovich, M., Raouf, M., Peacock, J. A., Phillipps, S., Pimbblet, K. A., Popescu, C., Said, K., Sansom, A. E., Seibert, M., Sutherland, W. J.,

Thorne, J. E., Tuffs, R. J., Turner, R., van der Wel, A., van Kampen, E., & Wilkins, S. M. (2022). Galaxy And Mass Assembly (GAMA): Data Release 4 and the $z < 0.1$ total and $z < 0.08$ morphological galaxy stellar mass functions. *Monthly Notices of the Royal Astronomical Society*, 513(1), 439–467.

- [37] Driver, S. P., Norberg, P., Baldry, I. K., Bamford, S. P., Hopkins, A. M., Liske, J., Loveday, J., Peacock, J. A., Hill, D. T., Kelvin, L. S., Robotham, A. S. G., Cross, N. J. G., Parkinson, H. R., Prescott, M., Conselice, C. J., Dunne, L., Brough, S., Jones, H., Sharp, R. G., van Kampen, E., Oliver, S., Roseboom, I. G., Bland-Hawthorn, J., Croom, S. M., Ellis, S., Cameron, E., Cole, S., Frenk, C. S., Couch, W. J., Graham, A. W., Proctor, R., De Propris, R., Doyle, I. F., Edmondson, E. M., Nichol, R. C., Thomas, D., Eales, S. A., Jarvis, M. J., Kuijken, K., Lahav, O., Madore, B. F., Seibert, M., Meyer, M. J., Staveley-Smith, L., Phillipps, S., Popescu, C. C., Sansom, A. E., Sutherland, W. J., Tuffs, R. J., & Warren, S. J. (2009). GAMA: towards a physical understanding of galaxy formation. *Astronomy and Geophysics*, 50(5), 5.12–5.19.
- [38] Dwek, E. (2005). Interstellar dust: what is it, how does it evolve, and what are its observational consequences? In C. C. Popescu & R. J. Tuffs (Eds.), *The Spectral Energy Distributions of Gas-Rich Galaxies: Confronting Models with Data*, volume 761 of *American Institute of Physics Conference Series* (pp. 103–122).
- [39] Earl, D. J. & Deem, M. W. (2005). Parallel tempering: Theory, applications, and new perspectives. *Physical Chemistry Chemical Physics (Incorporating Faraday Transactions)*, 7(23), 3910.
- [40] Elbaz, D., Daddi, E., Le Borgne, D., Dickinson, M., Alexander, D. M., Chary, R. R., Starck, J. L., Brandt, W. N., Kitzbichler, M., MacDonald, E., Nonino, M., Popesso, P., Stern, D., & Vanzella, E. (2007). The reversal of the star formation-density relation in the distant universe. *Astronomy & Astrophysics*, 468(1), 33–48.
- [41] Elitzur, M. & Shlosman, I. (2006). The AGN-obsuring Torus: The End of the “Doughnut” Paradigm? *The Astrophysical Journal Letters*, 648(2), L101–L104.
- [42] Evans, I. N., Primini, F. A., Glotfelty, K. J., Anderson, C. S., Bonaventura, N. R., Chen, J. C., Davis, J. E., Doe, S. M., Evans, J. D., Fabbiano, G., Galle, E. C., Gibbs, Danny G., I., Grier, J. D., Hain, R. M., Hall, D. M., Harbo, P. N., He, X. H., Houck, J. C., Karovska, M., Kashyap, V. L., Lauer, J., McCollough, M. L., McDowell, J. C., Miller,

J. B., Mitschang, A. W., Morgan, D. L., Mossman, A. E., Nichols, J. S., Nowak, M. A., Plummer, D. A., Refsdal, B. L., Rots, A. H., Siemiginowska, A., Sundheim, B. A., Tibbetts, M. S., Van Stone, D. W., Winkelman, S. L., & Zografou, P. (2010). The Chandra Source Catalog. *The Astrophysical Journal Supplement Series*, 189(1), 37–82.

- [43] Falcón-Barroso, J., Sánchez-Blázquez, P., Vazdekis, A., Ricciardelli, E., Cardiel, N., Cenarro, A. J., Gorgas, J., & Peletier, R. F. (2011). An updated MILES stellar library and stellar population models. *Astronomy & Astrophysics*, 532, A95.
- [44] Falkendal, T., De Breuck, C., Lehnert, M. D., Drouart, G., Vernet, J., Emonts, B., Lee, M., Nesvadba, N. P. H., Seymour, N., Béthermin, M., Kolwa, S., Gullberg, B., & Wylezalek, D. (2019). Massive galaxies on the road to quenching: ALMA observations of powerful high redshift radio galaxies. *Astronomy & Astrophysics*, 621, A27.
- [45] Ferland, G. J., Chatzikos, M., Guzmán, F., Lykins, M. L., van Hoof, P. A. M., Williams, R. J. R., Abel, N. P., Badnell, N. R., Keenan, F. P., Porter, R. L., & Stancil, P. C. (2017). The 2017 Release Cloudy. *Revista Mexicana de Astronomía y Astrofísica*, 53, 385–438.
- [46] Fey, A. L., Ma, C., Arias, E. F., Charlot, P., Feissel-Vernier, M., Gontier, A. M., Jacobs, C. S., Li, J., & MacMillan, D. S. (2004). The Second Extension of the International Celestial Reference Frame: ICRF-EXT.1. *The Astronomical Journal*, 127(6), 3587–3608.
- [47] Fey, A. L., Ojha, R., Quick, J. F. H., Nicolson, G. D., Lovell, J. E. J., Reynolds, J. E., Ellingsen, S. P., McCulloch, P. M., Johnston, K. J., Jauncey, D. L., & Tzioumis, A. K. (2006). Milliarcsecond-Accurate Astrometry of 34 Southern Hemisphere Radio Sources. *The Astronomical Journal*, 132(5), 1944–1949.
- [48] Fomalont, E. B., Petrov, L., MacMillan, D. S., Gordon, D., & Ma, C. (2003). The Second VLBA Calibrator Survey: VCS2. *The Astronomical Journal*, 126(5), 2562–2566.
- [49] Foreman-Mackey, D., Hogg, D. W., Lang, D., & Goodman, J. (2013). emcee: The MCMC Hammer. *Publications of the Astronomical Society of the Pacific*, 125(925), 306.
- [50] Fritz, J., Franceschini, A., & Hatziminaoglou, E. (2006). Revisiting the infrared spectra of active galactic nuclei with a new torus emission model. *Monthly Notices of the Royal Astronomical Society*, 366(3), 767–786.

- [51] García-Burillo, S., Combes, F., Neri, R., Fuente, A., Usero, A., Leon, S., & Lim, J. (2007). Fueling the central engine of radio galaxies. I. The molecular/dusty disk of 4C 31.04. *Astronomy & Astrophysics*, 468(3), L71–L75.
- [52] García-González, J., Alonso-Herrero, A., Hönig, S. F., Hernán-Caballero, A., Ramos Almeida, C., Levenson, N. A., Roche, P. F., González-Martín, O., Packham, C., & Kishimoto, M. (2017). A mid-infrared statistical investigation of clumpy torus model predictions. *Monthly Notices of the Royal Astronomical Society*, 470(3), 2578–2598.
- [53] Gattano, C., Lambert, S. B., & Le Bail, K. (2018). Extragalactic radio source stability and VLBI celestial reference frame: insights from the Allan standard deviation. *Astronomy & Astrophysics*, 618, A80.
- [54] Genzel, R., Tacconi, L. J., Lutz, D., Saintonge, A., Berta, S., Magnelli, B., Combes, F., García-Burillo, S., Neri, R., Bolatto, A., Contini, T., Lilly, S., Boissier, J., Boone, F., Bouché, N., Bournaud, F., Burkert, A., Carollo, M., Colina, L., Cooper, M. C., Cox, P., Feruglio, C., Förster Schreiber, N. M., Freundlich, J., Gracia-Carpio, J., Juneau, S., Kovac, K., Lippa, M., Naab, T., Salome, P., Renzini, A., Sternberg, A., Walter, F., Weiner, B., Weiss, A., & Wuyts, S. (2015). Combined CO and Dust Scaling Relations of Depletion Time and Molecular Gas Fractions with Cosmic Time, Specific Star-formation Rate, and Stellar Mass. *The Astrophysical Journal*, 800(1), 20.
- [55] Ginsburg, A., Sipőcz, B. M., Brasseur, C. E., Cowperthwaite, P. S., Craig, M. W., Deil, C., Guillochon, J., Guzman, G., Liedtke, S., Lian Lim, P., Lockhart, K. E., Mommert, M., Morris, B. M., Norman, H., Parikh, M., Persson, M. V., Robitaille, T. P., Segovia, J.-C., Singer, L. P., Tollerud, E. J., de Val-Borro, M., Valtchanov, I., Woillez, J., Astroquery Collaboration, & a subset of astropy Collaboration (2019). astroquery: An Astronomical Web-querying Package in Python. *The Astronomical Journal*, 157(3), 98.
- [56] Girardi, L., Bressan, A., Bertelli, G., & Chiosi, C. (2000). Evolutionary tracks and isochrones for low- and intermediate-mass stars: From 0.15 to 7 M_{sun} , and from $Z=0.0004$ to 0.03. *Astronomy & Astrophysics Supplement*, 141, 371–383.
- [57] Goodman, J. & Weare, J. (2010). Ensemble samplers with affine invariance. *Communications in Applied Mathematics and Computational Science*, 5(1), 65–80.
- [58] Grazian, A., Fontana, A., Santini, P., Dunlop, J. S., Ferguson, H. C., Castellano, M., Amorin, R., Ashby, M. L. N., Barro, G., Behroozi, P., Boutsia, K., Caputi, K. I.,

Chary, R. R., Dekel, A., Dickinson, M. E., Faber, S. M., Fazio, G. G., Finkelstein, S. L., Galametz, A., Giallongo, E., Giavalisco, M., Grogin, N. A., Guo, Y., Kocevski, D., Koekemoer, A. M., Koo, D. C., Lee, K. S., Lu, Y., Merlin, E., Mobasher, B., Nonino, M., Papovich, C., Paris, D., Pentericci, L., Reddy, N., Renzini, A., Salmon, B., Salvato, M., Sommariva, V., Song, M., & Vanzella, E. (2015). The galaxy stellar mass function at $3.5 \leq z \leq 7.5$ in the CANDELS/UDS, GOODS-South, and HUDF fields. *Astronomy & Astrophysics*, 575, A96.

- [59] Handley, W. J., Hobson, M. P., & Lasenby, A. N. (2015). polychord: nested sampling for cosmology. *Monthly Notices of the Royal Astronomical Society*, 450, L61–L65.
- [60] Harris, C. R., Millman, K. J., van der Walt, S. J., Gommers, R., Virtanen, P., Cournapeau, D., Wieser, E., Taylor, J., Berg, S., Smith, N. J., Kern, R., Picus, M., Hoyer, S., van Kerkwijk, M. H., Brett, M., Haldane, A., del Río, J. F., Wiebe, M., Peterson, P., Gérard-Marchant, P., Sheppard, K., Reddy, T., Weckesser, W., Abbasi, H., Gohlke, C., & Oliphant, T. E. (2020). Array programming with NumPy. *Nature*, 585(7825), 357–362.
- [61] Healey, S. E., Romani, R. W., Taylor, G. B., Sadler, E. M., Ricci, R., Murphy, T., Ulvestad, J. S., & Winn, J. N. (2007). CRATES: An All-Sky Survey of Flat-Spectrum Radio Sources. *The Astrophysical Journal Supplement Series*, 171(1), 61–71.
- [62] Hearin, A. P., Chaves-Montero, J., Alarcon, A., Becker, M. R., & Benson, A. (2023). DSPS: Differentiable stellar population synthesis. *Monthly Notices of the Royal Astronomical Society*, 521(2), 1741–1756.
- [63] Hensley, B. S. & Draine, B. T. (2023). The Astrodust+PAH Model: A Unified Description of the Extinction, Emission, and Polarization from Dust in the Diffuse Interstellar Medium. *The Astrophysical Journal*, 948(1), 55.
- [64] Higson, E., Handley, W., Hobson, M., & Lasenby, A. (2019). Dynamic nested sampling: an improved algorithm for parameter estimation and evidence calculation. *Statistics and Computing*, 29(5), 891–913.
- [65] Hill, G. J., Goodrich, R. W., & Depoy, D. L. (1996). Observations of Paschen alpha in a Complete Sample of Radio Galaxies. *The Astrophysical Journal*, 462, 163.

- [66] Hogg, D. W. (1999). Distance measures in cosmology. *arXiv e-prints*, (pp. astro-ph/9905116).
- [67] Hogg, D. W., Baldry, I. K., Blanton, M. R., & Eisenstein, D. J. (2002a). The K correction. *arXiv e-prints*, (pp. astro-ph/0210394).
- [68] Hogg, D. W., Baldry, I. K., Blanton, M. R., & Eisenstein, D. J. (2002b). The K correction. *arXiv e-prints*, (pp. astro-ph/0210394).
- [69] Holt, J., Tadhunter, C. N., & Morganti, R. (2003). Highly extinguished emission line outflows in the young radio source PKS 1345+12. *Monthly Notices of the Royal Astronomical Society*, 342(1), 227–238.
- [70] Höning, S. F. & Kishimoto, M. (2010). The dusty heart of nearby active galaxies. II. From clumpy torus models to physical properties of dust around AGN. *Astronomy & Astrophysics*, 523, A27.
- [71] Hopkins, P. F., Strauss, M. A., Hall, P. B., Richards, G. T., Cooper, A. S., Schneider, D. P., Vanden Berk, D. E., Jester, S., Brinkmann, J., & Szokoly, G. P. (2004). Dust Reddening in Sloan Digital Sky Survey Quasars. *The Astronomical Journal*, 128(3), 1112–1123.
- [72] Huchra, J. P., Vogeley, M. S., & Geller, M. J. (1999). The CfA Redshift Survey: Data for the South Galactic CAP. *The Astrophysical Journal Supplement Series*, 121(2), 287–368.
- [73] Hunter, J. D. (2007). Matplotlib: A 2d graphics environment. *Computing in Science Engineering*, 9(3), 90–95.
- [74] Iyer, K. & Gawiser, E. (2017). Reconstruction of Galaxy Star Formation Histories through SED Fitting: The Dense Basis Approach. *The Astrophysical Journal*, 838(2), 127.
- [75] Iyer, K. G., Gawiser, E., Faber, S. M., Ferguson, H. C., Kartaltepe, J., Koekemoer, A. M., Pacifici, C., & Somerville, R. S. (2019). Nonparametric Star Formation History Reconstruction with Gaussian Processes. I. Counting Major Episodes of Star Formation. *The Astrophysical Journal*, 879(2), 116.

- [76] Iyer, K. G., Speagle, J. S., Caplar, N., Forbes, J. C., Gawiser, E., Leja, J., & Tacchella, S. (2022). Stochastic Modelling of Star Formation Histories III. Constraints from Physically-Motivated Gaussian Processes. *arXiv e-prints*, (pp. arXiv:2208.05938).
- [77] Jackson, N., Battye, R. A., Browne, I. W. A., Joshi, S., Muxlow, T. W. B., & Wilkinson, P. N. (2007). A survey of polarization in the JVAs/CLASS flat-spectrum radio source surveys - I. The data and catalogue production. *Monthly Notices of the Royal Astronomical Society*, 376(1), 371–377.
- [78] Johnston, K. J., Fey, A. L., Zacharias, N., Russell, J. L., Ma, C., de Vegt, C., Reynolds, J. E., Jauncey, D. L., Archinal, B. A., Carter, M. S., Corbin, T. E., Eubanks, T. M., Florkowski, D. R., Hall, D. M., McCarthy, D. D., McCulloch, P. M., King, E. A., Nicolson, G., & Shaffer, D. B. (1995). A Radio Reference Frame. *The Astronomical Journal*, 110, 880.
- [79] Johnston, R., Teodoro, L., & Hendry, M. (2007). Completeness - I. Revisited, reviewed and revived. *Monthly Notices of the Royal Astronomical Society*, 376(4), 1757–1766.
- [80] Jones, D. H., Read, M. A., Saunders, W., Colless, M., Jarrett, T., Parker, Q. A., Fairall, A. P., Mauch, T., Sadler, E. M., Watson, F. G., Burton, D., Campbell, L. A., Cass, P., Croom, S. M., Dawe, J., Fiegert, K., Frankcombe, L., Hartley, M., Huchra, J., James, D., Kirby, E., Lahav, O., Lucey, J., Mamon, G. A., Moore, L., Peterson, B. A., Prior, S., Proust, D., Russell, K., Safouris, V., Wakamatsu, K.-I., Westra, E., & Williams, M. (2009). The 6dF Galaxy Survey: final redshift release (DR3) and southern large-scale structures. *Monthly Notices of the Royal Astronomical Society*, 399(2), 683–698.
- [81] Jones, D. H., Saunders, W., Colless, M., Read, M. A., Parker, Q. A., Watson, F. G., Campbell, L. A., Burkey, D., Mauch, T., Moore, L., Hartley, M., Cass, P., James, D., Russell, K., Fiegert, K., Dawe, J., Huchra, J., Jarrett, T., Lahav, O., Lucey, J., Mamon, G. A., Proust, D., Sadler, E. M., & Wakamatsu, K.-i. (2004). The 6dF Galaxy Survey: samples, observational techniques and the first data release. *Monthly Notices of the Royal Astronomical Society*, 355(3), 747–763.
- [82] Kennicutt, R. C. & Evans, N. J. (2012). Star Formation in the Milky Way and Nearby Galaxies. *Annual Review of Astronomy and Astrophysics*, 50, 531–608.

- [83] Kwon, K. J., Hahn, C., & Alsing, J. (2023). Neural Stellar Population Synthesis Emulator for the DESI PROVABGS. *The Astrophysical Journal Supplement Series*, 265(1), 23.
- [84] Laigle, C., McCracken, H. J., Ilbert, O., Hsieh, B. C., Davidzon, I., Capak, P., Hasinger, G., Silverman, J. D., Pichon, C., Coupon, J., Aussel, H., Le Borgne, D., Caputi, K., Cassata, P., Chang, Y. Y., Civano, F., Dunlop, J., Fynbo, J., Kartaltepe, J. S., Koekemoer, A., Le Fèvre, O., Le Floc'h, E., Leauthaud, A., Lilly, S., Lin, L., Marchesi, S., Milvang-Jensen, B., Salvato, M., Sanders, D. B., Scoville, N., Smolcic, V., Stockmann, M., Taniguchi, Y., Tasca, L., Toft, S., Vaccari, M., & Zabl, J. (2016). The COSMOS₂₀₁₅ Catalog: Exploring the $1 < z < 6$ Universe with Half a Million Galaxies. *The Astrophysical Journal Supplement Series*, 224(2), 24.
- [85] Leja, J., Carnall, A. C., Johnson, B. D., Conroy, C., & Speagle, J. S. (2019). How to Measure Galaxy Star Formation Histories. II. Nonparametric Models. *The Astrophysical Journal*, 876(1), 3.
- [86] Leja, J., Speagle, J. S., Johnson, B. D., Conroy, C., van Dokkum, P., & Franx, M. (2020). A New Census of the $0.2 < z < 3.0$ Universe. I. The Stellar Mass Function. *The Astrophysical Journal*, 893(2), 111.
- [87] Leja, J., Speagle, J. S., Ting, Y.-S., Johnson, B. D., Conroy, C., Whitaker, K. E., Nelson, E. J., van Dokkum, P., & Franx, M. (2022). A New Census of the $0.2 < z < 3.0$ Universe. II. The Star-forming Sequence. *The Astrophysical Journal*, 936(2), 165.
- [88] Leja, J., van Dokkum, P., & Franx, M. (2013). Tracing Galaxies through Cosmic Time with Number Density Selection. *The Astrophysical Journal*, 766(1), 33.
- [89] Leja, J., van Dokkum, P. G., Franx, M., & Whitaker, K. E. (2015). Reconciling the Observed Star-forming Sequence with the Observed Stellar Mass Function. *The Astrophysical Journal*, 798(2), 115.
- [90] Leslie, S. K., Schinnerer, E., Liu, D., Magnelli, B., Algera, H., Karim, A., Davidzon, I., Gozaliasl, G., Jiménez-Andrade, E. F., Lang, P., Sargent, M. T., Novak, M., Groves, B., Smolčić, V., Zamorani, G., Vaccari, M., Battisti, A., Vardoulaki, E., Peng, Y., & Kartaltepe, J. (2020). The VLA-COSMOS 3 GHz Large Project: Evolution of Specific Star Formation Rates out to $z \sim 5$. *The Astrophysical Journal*, 899(1), 58.

- [91] Lower, S., Narayanan, D., Leja, J., Johnson, B. D., Conroy, C., & Davé, R. (2020). How Well Can We Measure the Stellar Mass of a Galaxy: The Impact of the Assumed Star Formation History Model in SED Fitting. *The Astrophysical Journal*, 904(1), 33.
- [92] Lower, S., Narayanan, D., Li, Q., & Davé, R. (2023). Cosmic Sands: The Origin of Dusty, Star-forming Galaxies in the Epoch of Reionization. *The Astrophysical Journal*, 950(2), 94.
- [93] Ma, C., Arias, E. F., Eubanks, T. M., Fey, A. L., Gontier, A. M., Jacobs, C. S., Sovers, O. J., Archinal, B. A., & Charlot, P. (1998). The International Celestial Reference Frame as Realized by Very Long Baseline Interferometry. *The Astronomical Journal*, 116(1), 516–546.
- [94] Madau, P. & Dickinson, M. (2014). Cosmic Star-Formation History. *Annual Review of Astronomy and Astrophysics*, 52, 415–486.
- [95] Mahony, E. K., Croom, S. M., Boyle, B. J., Edge, A. C., Mauch, T., & Sadler, E. M. (2010). The RASS-6dFGS catalogue: a sample of X-ray selected AGN from the 6dF Galaxy Survey. *Monthly Notices of the Royal Astronomical Society*, 401(2), 1151–1165.
- [96] Malkan, M. A. (1983). The ultraviolet excess of luminous quasars. II. Evidence for massive accretion disks. *The Astrophysical Journal*, 268, 582–590.
- [97] Marigo, P., Girardi, L., Bressan, A., Groenewegen, M. A. T., Silva, L., & Granato, G. L. (2008). Evolution of asymptotic giant branch stars. II. Optical to far-infrared isochrones with improved TP-AGB models. *Astronomy & Astrophysics*, 482(3), 883–905.
- [98] McCarthy, P. J., Kapahi, V. K., van Breugel, W., Persson, S. E., Athreya, R., & Subrahmanya, C. R. (1996). The Molonglo Reference Catalog/1 Jansky Radio Source Survey. I. Radio Galaxy Identifications. *The Astrophysical Journal Supplement Series*, 107, 19.
- [99] McCarthy, P. J., Kapahi, V. K., van Breugel, W., & Subrahmanya, C. R. (1990). High-Redshift Radio Galaxies from the Molonglo Catalogue. *The Astronomical Journal*, 100, 1014.
- [100] McCarthy, P. J., van Breughel, W., Kapahi, V. K., & Subrahmanya, C. R. (1991). High Redshift Radio Galaxies From the Molonglo Catalogue.II. *The Astronomical Journal*, 102, 522.

- [101] Momcheva, I. G., Brammer, G. B., van Dokkum, P. G., Skelton, R. E., Whitaker, K. E., Nelson, E. J., Fumagalli, M., Maseda, M. V., Leja, J., Franx, M., Rix, H.-W., Bezançon, R., Da Cunha, E., Dickey, C., Förster Schreiber, N. M., Illingworth, G., Kriek, M., Labbé, I., Ulf Lange, J., Lundgren, B. F., Magee, D., Marchesini, D., Oesch, P., Pacifici, C., Patel, S. G., Price, S., Tal, T., Wake, D. A., van der Wel, A., & Wuyts, S. (2016). The 3D-HST Survey: Hubble Space Telescope WFC3/G141 Grism Spectra, Redshifts, and Emission Line Measurements for $\sim 100,000$ Galaxies. *The Astrophysical Journal Supplement Series*, 225(2), 27.
- [102] Narayanan, D., Lower, S., Torrey, P., Brammer, G., Cui, W., Dave, R., Iyer, K., Li, Q., Lovell, C., Sales, L., Stark, D. P., Marinacci, F., & Vogelsberger, M. (2023). Outshining by Recent Star Formation Prevents the Accurate Measurement of High-z Galaxy Stellar Masses. *arXiv e-prints*, (pp. arXiv:2306.10118).
- [103] Nesvadba, N. P. H., De Breuck, C., Lehnert, M. D., Best, P. N., & Collet, C. (2017). The SINFONI survey of powerful radio galaxies at $z \approx 2$: Jet-driven AGN feedback during the Quasar Era. *Astronomy & Astrophysics*, 599, A123.
- [104] Noeske, K. G., Weiner, B. J., Faber, S. M., Papovich, C., Koo, D. C., Somerville, R. S., Bundy, K., Conselice, C. J., Newman, J. A., Schiminovich, D., Le Floc'h, E., Coil, A. L., Rieke, G. H., Lotz, J. M., Primack, J. R., Barmby, P., Cooper, M. C., Davis, M., Ellis, R. S., Fazio, G. G., Guhathakurta, P., Huang, J., Kassin, S. A., Martin, D. C., Phillips, A. C., Rich, R. M., Small, T. A., Willmer, C. N. A., & Wilson, G. (2007). Star Formation in AEGIS Field Galaxies since $z=1.1$: The Dominance of Gradually Declining Star Formation, and the Main Sequence of Star-forming Galaxies. *The Astrophysical Journal Letters*, 660(1), L43–L46.
- [105] Ocvirk, P., Pichon, C., Lançon, A., & Thiébaut, E. (2006). STECMAP: STEllar Content from high-resolution galactic spectra via Maximum A Posteriori. *Monthly Notices of the Royal Astronomical Society*, 365(1), 46–73.
- [106] O'Donnell, J. H., Wilkinson, R. D., Diehl, H. T., Aros-Bunster, C., Bechtol, K., Birrer, S., Buckley-Geer, E. J., Carnero Rosell, A., Carrasco Kind, M., da Costa, L. N., Gonzalez Lozano, S. J., Gruendl, R. A., Hilton, M., Lin, H., Lindgren, K. A., Martin, J., Pieres, A., Rykoff, E. S., Sevilla-Noarbe, I., Sheldon, E., Sifón, C., Tucker, D. L., Yanny, B., Abbott, T. M. C., Aguena, M., Allam, S., Andrade-Oliveira, F., Annis, J.,

Bertin, E., Brooks, D., Burke, D. L., Carretero, J., Costanzi, M., De Vicente, J., Desai, S., Dietrich, J. P., Eckert, K., Everett, S., Ferrero, I., Flaugher, B., Fosalba, P., Frieman, J., García-Bellido, J., Gaztanaga, E., Gerdes, D. W., Gruen, D., Gschwend, J., Gill, M. S. S., Gutierrez, G., Hinton, S. R., Hollowood, D. L., Honscheid, K., James, D. J., Jeltema, T., Kuehn, K., Lahav, O., Lima, M., Maia, M. A. G., Marshall, J. L., Melchior, P., Menanteau, F., Miquel, R., Morgan, R., Nord, B., Ogando, R. L. C., Paz-Chinchón, F., Pereira, M. E. S., Plazas Malagón, A. A., Rodriguez-Monroy, M., Romer, A. K., Roodman, A., Sanchez, E., Scarpine, V., Schubnell, M., Serrano, S., Smith, M., Suchyta, E., Swanson, M. E. C., Tarle, G., Thomas, D., To, C., & Varga, T. N. (2022). The Dark Energy Survey Bright Arcs Survey: Candidate Strongly Lensed Galaxy Systems from the Dark Energy Survey 5000 Square Degree Footprint. *The Astrophysical Journal Supplement Series*, 259(1), 27.

- [107] Ogando, R. L. C., Maia, M. A. G., Pellegrini, P. S., & da Costa, L. N. (2008). Line Strengths of Early-Type Galaxies. *The Astronomical Journal*, 135(6), 2424–2445.
- [108] Pacifici, C., Kassin, S. A., Weiner, B., Charlot, S., & Gardner, J. P. (2013). The Rise and Fall of the Star Formation Histories of Blue Galaxies at Redshifts $0.2 < z < 1.4$. *The Astrophysical Journal Letters*, 762(1), L15.
- [109] pandas development team, T. (2023). pandas-dev/pandas: Pandas. If you use this software, please cite it as below.
- [110] Perryman, M. A. C., Lilly, S. J., Longair, M. S., & Downes, A. J. B. (1984). Redshifts of faint 3 CR radio sources. *Monthly Notices of the Royal Astronomical Society*, 209, 159–167.
- [111] Petropoulou, M., Dimitrakoudis, S., Padovani, P., Mastichiadis, A., & Resconi, E. (2015). Photohadronic origin of γ -ray BL Lac emission: implications for IceCube neutrinos. *Monthly Notices of the Royal Astronomical Society*, 448(3), 2412–2429.
- [112] Petrov, L., Kovalev, Y. Y., Fomalont, E., & Gordon, D. (2005). The Third VLBA Calibrator Survey: VCS3. *The Astronomical Journal*, 129(2), 1163–1170.
- [113] Pollack, L. K., Taylor, G. B., & Allen, S. W. (2005). VLA polarimetry observations of PKS2322-123: estimating magnetic fields in the Abell 2597 cluster. *Monthly Notices of the Royal Astronomical Society*, 359(4), 1229–1236.

- [114] Prevot, M. L., Lequeux, J., Maurice, E., Prevot, L., & Rocca-Volmerange, B. (1984). The typical interstellar extinction in the Small Magellanic Cloud. *Astronomy & Astrophysics*, 132, 389–392.
- [115] Puglisi, A., Rodighiero, G., Franceschini, A., Talia, M., Cimatti, A., Baronchelli, I., Daddi, E., Renzini, A., Schawinski, K., Mancini, C., Silverman, J., Gruppioni, C., Lutz, D., Berta, S., & Oliver, S. J. (2016). Dust attenuation in $z \sim 1$ galaxies from Herschel and 3D-HST H α measurements. *Astronomy & Astrophysics*, 586, A83.
- [116] Rauzy, S., Hendry, M. A., & D'Mellow, K. (2001). A test for assessing the goodness-of-fit of luminosity function models to magnitude-redshift data. *Monthly Notices of the Royal Astronomical Society*, 328(4), 1016–1026.
- [117] Reddy, K., Georganopoulos, M., & Meyer, E. T. (2021). X-Ray-to-radio Offset Inference from Low-count X-Ray Jets. *The Astrophysical Journal Supplement Series*, 253(2), 37.
- [118] Renzini, A. & Peng, Y.-j. (2015). An Objective Definition for the Main Sequence of Star-forming Galaxies. *The Astrophysical Journal Letters*, 801(2), L29.
- [119] Richards, G. T., Lacy, M., Storrie-Lombardi, L. J., Hall, P. B., Gallagher, S. C., Hines, D. C., Fan, X., Papovich, C., Vanden Berk, D. E., Trammell, G. B., Schneider, D. P., Vestergaard, M., York, D. G., Jester, S., Anderson, S. F., Budavári, T., & Szalay, A. S. (2006). Spectral Energy Distributions and Multiwavelength Selection of Type 1 Quasars. *The Astrophysical Journal Supplement Series*, 166(2), 470–497.
- [Rush et al.] Rush, B., McCarthy, P. J., Athreya, R. M., & Persson, S. E. The High-Redshift Radio Galaxy MRC 0406-244. *The Astrophysical Journal*, keywords = Galaxies: Evolution, Galaxies: Individual: Alphanumeric: MRC 0406-244, Galaxies: Photometry, Galaxies: Structure, Radio Continuum: Galaxies, year = 1997, month = jul, volume = 484, number = 1, pages = 163-179, doi = 10.1086/304307, adsurl = <https://ui.adsabs.harvard.edu/abs/1997ApJ...484..163R>, adsnote = Provided by the SAO/NASA Astrophysics Data System.
- [121] Saintonge, A. & Catinella, B. (2022). The Cold Interstellar Medium of Galaxies in the Local Universe. *Annual Review of Astronomy and Astrophysics*, 60, 319–361.

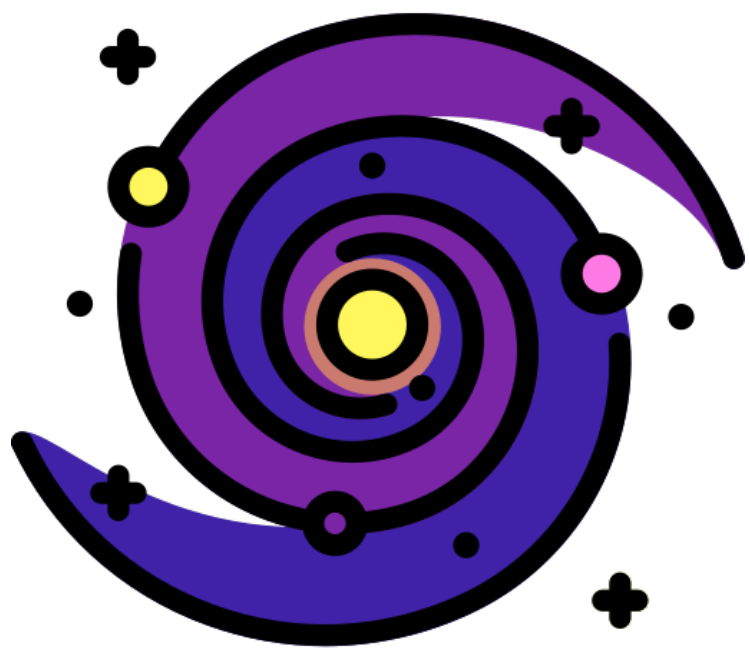
- [122] Salim, S. & Narayanan, D. (2020). The Dust Attenuation Law in Galaxies. *Annual Review of Astronomy and Astrophysics*, 58, 529–575.
- [123] Sambridge, M. (2014). A Parallel Tempering algorithm for probabilistic sampling and multimodal optimization. *Geophysical Journal International*, 196(1), 357–374.
- [124] Sánchez-Blázquez, P., Peletier, R. F., Jiménez-Vicente, J., Cardiel, N., Cenarro, A. J., Falcón-Barroso, J., Gorgas, J., Selam, S., & Vazdekis, A. (2006). Medium-resolution Isaac Newton Telescope library of empirical spectra. *Monthly Notices of the Royal Astronomical Society*, 371(2), 703–718.
- [125] Sandage, A., Tammann, G. A., & Yahil, A. (1979). The velocity field of bright nearby galaxies. I. The variation of mean absolute magnitude with redshift for galaxies in a magnitude-limited sample. *The Astrophysical Journal*, 232, 352–364.
- [126] Scarlata, C., Carollo, C. M., Lilly, S., Sargent, M. T., Feldmann, R., Kampczyk, P., Porciani, C., Koekemoer, A., Scoville, N., Kneib, J. P., Leauthaud, A., Massey, R., Rhodes, J., Tasca, L., Capak, P., Maier, C., McCracken, H. J., Mobasher, B., Renzini, A., Taniguchi, Y., Thompson, D., Sheth, K., Ajiki, M., Aussel, H., Murayama, T., Sanders, D. B., Sasaki, S., Shioya, Y., & Takahashi, M. (2007). COSMOS Morphological Classification with the Zurich Estimator of Structural Types (ZEST) and the Evolution Since $z = 1$ of the Luminosity Function of Early, Disk, and Irregular Galaxies. *The Astrophysical Journal Supplement Series*, 172(1), 406–433.
- [127] Schaye, J., Crain, R. A., Bower, R. G., Furlong, M., Schaller, M., Theuns, T., Dalla Vecchia, C., Frenk, C. S., McCarthy, I. G., Helly, J. C., Jenkins, A., Rosas-Guevara, Y. M., White, S. D. M., Baes, M., Booth, C. M., Camps, P., Navarro, J. F., Qu, Y., Rahmati, A., Sawala, T., Thomas, P. A., & Trayford, J. (2015). The EAGLE project: simulating the evolution and assembly of galaxies and their environments. *Monthly Notices of the Royal Astronomical Society*, 446(1), 521–554.
- [128] Schechter, P. (1976). An analytic expression for the luminosity function for galaxies. *The Astrophysical Journal*, 203, 297–306.
- [129] Schmidt, M. (1968). Space Distribution and Luminosity Functions of Quasi-Stellar Radio Sources. *The Astrophysical Journal*, 151, 393.

- [130] Skilling, J. (2005). Bayesics. In K. H. Knuth, A. E. Abbas, R. D. Morris, & J. P. Castle (Eds.), *Bayesian Inference and Maximum Entropy Methods in Science and Engineering*, volume 803 of *American Institute of Physics Conference Series* (pp. 3–24).
- [131] Skilling, J. (2006). Skilling, j.: Nested sampling for general bayesian computation. *bayesian anal.* 1(4), 833–860. *Bayesian Analysis*, 1, 833–860.
- [132] Skrutskie, M. F., Cutri, R. M., Stiening, R., Weinberg, M. D., Schneider, S., Carpenter, J. M., Beichman, C., Capps, R., Chester, T., Elias, J., Huchra, J., Liebert, J., Lonsdale, C., Monet, D. G., Price, S., Seitzer, P., Jarrett, T., Kirkpatrick, J. D., Gizis, J. E., Howard, E., Evans, T., Fowler, J., Fullmer, L., Hurt, R., Light, R., Kopan, E. L., Marsh, K. A., McCallon, H. L., Tam, R., Dyk, S. V., & Wheelock, S. (2006). The two micron all sky survey (2mass). *The Astronomical Journal*, 131(2), 1163.
- [133] Smith, R. J., Lucey, J. R., Hudson, M. J., Schlegel, D. J., & Davies, R. L. (2000). Streaming motions of galaxy clusters within 1200 km s^{-1} - I. New spectroscopic data. *Monthly Notices of the Royal Astronomical Society*, 313(3), 469–490.
- [134] Snellen, I. A. G., Zhang, M., Schilizzi, R. T., Roettgering, H. J. A., de Bruyn, A. G., & Miley, G. K. (1995). Faint radio sources with peaked spectra. I. VLA observations of a new sample with intermediate flux-densities. *Astronomy & Astrophysics*, 300, 359.
- [135] Speagle, J. S. (2020). DYNESTY: a dynamic nested sampling package for estimating Bayesian posteriors and evidences. *Monthly Notices of the Royal Astronomical Society*, 493(3), 3132–3158.
- [136] Speagle, J. S., Steinhardt, C. L., Capak, P. L., & Silverman, J. D. (2014). A Highly Consistent Framework for the Evolution of the Star-Forming “Main Sequence” from $z \sim 0\text{--}6$. *The Astrophysical Journal Supplement Series*, 214(2), 15.
- [137] Spoon, H. W. W., Hernán-Caballero, A., Rupke, D., Waters, L. B. F. M., Lebouteiller, V., Tielens, A. G. G. M., Loredo, T., Su, Y., & Viola, V. (2022). The Infrared Database of Extragalactic Observables from Spitzer. II. The Database and Diagnostic Power of Crystalline Silicate Features in Galaxy Spectra. *The Astrophysical Journal Supplement Series*, 259(2), 37.

- [138] Tacchella, S., Forbes, J. C., & Caplar, N. (2020). Stochastic modelling of star-formation histories II: star-formation variability from molecular clouds and gas inflow. *Monthly Notices of the Royal Astronomical Society*, 497(1), 698–725.
- [139] Tal, T., Dekel, A., Oesch, P., Muzzin, A., Brammer, G. B., van Dokkum, P. G., Franx, M., Illingworth, G. D., Leja, J., Magee, D., Marchesini, D., Momcheva, I., Nelson, E. J., Patel, S. G., Quadri, R. F., Rix, H.-W., Skelton, R. E., Wake, D. A., & Whitaker, K. E. (2014). Observations of Environmental Quenching in Groups in the 11 GYR since $z = 2.5$: Different Quenching for Central and Satellite Galaxies. *The Astrophysical Journal*, 789(2), 164.
- [140] Taylor, G. B., Barton, E. J., & Ge, J. (1994). Searching for Cluster Magnetic Fields in the Cooling Flows of o745-191, A2029, and A4059. *The Astronomical Journal*, 107, 1942.
- [141] Titov, O., Jauncey, D. L., Johnston, H. M., Hunstead, R. W., & Christensen, L. (2011). Optical Spectra of Candidate Southern Hemisphere International Celestial Reference Frame (ICRF) Radio Sources. *The Astronomical Journal*, 142(5), 165.
- [142] Tomczak, A. R., Quadri, R. F., Tran, K.-V. H., Labb  , I., Straatman, C. M. S., Papovich, C., Glazebrook, K., Allen, R., Brammer, G. B., Kacprzak, G. G., Kawinwanichakij, L., Kelson, D. D., McCarthy, P. J., Mehrtens, N., Monson, A. J., Persson, S. E., Spitler, L. R., Tilvi, V., & van Dokkum, P. (2014). Galaxy Stellar Mass Functions from ZFOURGE/CANDELS: An Excess of Low-mass Galaxies since $z = 2$ and the Rapid Buildup of Quiescent Galaxies. *The Astrophysical Journal*, 783(2), 85.
- [143] Trager, S. C., Faber, S. M., Worthey, G., & Gonz  lez, J. J. (2000). The Stellar Population Histories of Local Early-Type Galaxies. I. Population Parameters. *The Astronomical Journal*, 119(4), 1645–1676.
- [144] Triani, D. P., Sinha, M., Croton, D. J., Pacifici, C., & Dwek, E. (2020). The origin of dust in galaxies across cosmic time. *Monthly Notices of the Royal Astronomical Society*, 493(2), 2490–2505.
- [145] Urry, C. M. & Padovani, P. (1995). Unified Schemes for Radio-Loud Active Galactic Nuclei. *The Publications of the Astronomical Society of the Pacific*, 107, 803.

- [146] van den Bosch, R. C. E., Gebhardt, K., Gültekin, K., Yıldırım, A., & Walsh, J. L. (2015). Hunting for Supermassive Black Holes in Nearby Galaxies With the Hobby-Eberly Telescope. *The Astrophysical Journal Supplement Series*, 218(1), 10.
- [147] Vazdekis, A., Sánchez-Blázquez, P., Falcón-Barroso, J., Cenarro, A. J., Beasley, M. A., Cardiel, N., Gorgas, J., & Peletier, R. F. (2010). Evolutionary stellar population synthesis with MILES - I. The base models and a new line index system. *Monthly Notices of the Royal Astronomical Society*, 404(4), 1639–1671.
- [148] Venkatesan, T. C. A., Batuski, D. J., Hanisch, R. J., & Burns, J. O. (1994). Why Do Head-Tail Sources Exist in Poor Clusters of Galaxies? *The Astrophysical Journal*, 436, 67.
- [149] Virtanen, P., Gommers, R., Oliphant, T. E., Haberland, M., Reddy, T., Cournapeau, D., Burovski, E., Peterson, P., Weckesser, W., Bright, J., van der Walt, S. J., Brett, M., Wilson, J., Millman, K. J., Mayorov, N., Nelson, A. R. J., Jones, E., Kern, R., Larson, E., Carey, C. J., Polat, İ., Feng, Y., Moore, E. W., VanderPlas, J., Laxalde, D., Perktold, J., Cimrman, R., Henriksen, I., Quintero, E. A., Harris, C. R., Archibald, A. M., Ribeiro, A. H., Pedregosa, F., van Mulbregt, P., & SciPy 1.0 Contributors (2020). SciPy 1.0: Fundamental Algorithms for Scientific Computing in Python. *Nature Methods*, 17, 261–272.
- [150] Vousden, W. D., Farr, W. M., & Mandel, I. (2016). Dynamic temperature selection for parallel tempering in Markov chain Monte Carlo simulations. *Monthly Notices of the Royal Astronomical Society*, 455(2), 1919–1937.
- [151] Walcher, J., Groves, B., Budavári, T., & Dale, D. (2011). Fitting the integrated spectral energy distributions of galaxies. *Astrophysics and Space Science*, 331, 1–52.
- [152] Wegner, G., Bernardi, M., Willmer, C. N. A., da Costa, L. N., Alonso, M. V., Pellegrini, P. S., Maia, M. A. G., Chaves, O. L., & Rité, C. (2003). Redshift-distance survey of early-type galaxies: Spectroscopic data. *The Astronomical Journal*, 126(5), 2268.
- [153] Weigel, A. K., Schawinski, K., & Bruderer, C. (2016). Stellar mass functions: methods, systematics and results for the local Universe. *Monthly Notices of the Royal Astronomical Society*, 459(2), 2150–2187.
- [154] Weinberg, S. (2008). *Cosmology*.

- [155] Witt, A. N. & Gordon, K. D. (2000). Multiple Scattering in Clumpy Media. II. Galactic Environments. *The Astrophysical Journal*, 528(2), 799–816.
- [156] Wong, O. I., Ryan-Weber, E. V., Garcia-Appadoo, D. A., Webster, R. L., Staveley-Smith, L., Zwaan, M. A., Meyer, M. J., Barnes, D. G., Kilborn, V. A., Bhathal, R., de Blok, W. J. G., Disney, M. J., Doyle, M. T., Drinkwater, M. J., Ekers, R. D., Freeman, K. C., Gibson, B. K., Gurovich, S., Harnett, J., Henning, P. A., Jerjen, H., Kesteven, M. J., Knezek, P. M., Koribalski, B. S., Mader, S., Marquarding, M., Minchin, R. F., O'Brien, J., Putman, M. E., Ryder, S. D., Sadler, E. M., Stevens, J., Stewart, I. M., Stootman, F., & Waugh, M. (2006). The Northern HIPASS catalogue - data presentation, completeness and reliability measures. *Monthly Notices of the Royal Astronomical Society*, 371(4), 1855–1864.
- [157] Wright, A. & Otrupcek, R. (1990). Parkes Catalog, 1990, Australia telescope national facility. *PKS Catalog (1990)*, (pp. 5).



THIS THESIS WAS TYPESET using L^AT_EX, originally developed by Leslie Lamport and based on Donald Knuth's T_EX. The body text is set in 11 point Egenolff-Berner Garamond, a revival of Claude Garamont's humanist typeface. The above illustration is attributed to flaticon.com/authors/freepik. A template that can be used to format a dissertation with this look & feel has been released under the permissive AGPL license, and can be found online at github.com/suchow/Dissertate or from its lead author, Jordan Suchow, at suchow@post.harvard.edu.

